Measuring the high redshift space density of FRI radio galaxies: investigating the nature of the FRI/II divide

EMMA ELIZABETH RIGBY

Institute for Astronomy

School of Physics

Doctor of Philosophy

The University of Edinburgh

2007

Abstract

The results are presented here of multi–wavelength observations centred on two fields of the Leiden–Berkeley Deep Survey, which form the basis for a study of the population and cosmic evolution of the high redshift, low power, Fanaroff & Riley class I (FRI) radio galaxies. These fields, Hercules.1 and Lynx.2, contain a complete sample of 81 radio sources with $S_{1.4\mathrm{GHz}} > 0.5$ mJy within 0.6 square degrees. Wide–field, $\sim$1.5″ resolution, radio observations, along with near infra–red and optical imaging, and some multi–object spectroscopy, are used to select the best high–redshift FRI candidates, giving 37 in total. Currently, the host galaxy identification fraction is 86% with 11 sources remaining unidentified at a level of $r \geqslant 25.2$ (Hercules; 4 sources) or $r \geqslant 24.4$ (Lynx; 7 sources) and $K \gtrsim 20$. Spectroscopic redshifts are determined for 49% of the sample and photometric redshift estimates are presented for the sample sources without spectra or previously published results.

95% of the 37 best FRI high-redshift candidate sources were then observed using sub–arcsecond radio resolution, with the aim of detecting extended emission with respect to compact core features – vital for unambiguous morphological classification. The nature of the radio observations meant that 10 extra sample sources could also be included in the data. Lower resolution data were also taken for the Lynx.2 field sources to provide a comparison with the 1.5″ data.

The classification of the entire radio sample is done in two stages. Sources which showed clear extension are classified by morphology alone, whereas sources with no obvious or weak extension were classified using a combination of morphology and flux density loss in the higher resolution data indicative of resolved out extended emission. Five groups are used for this – ‘Certain FRIs’, ‘Likely FRIs’, ‘Possible FRIs’, ‘Unclassifiable sources’ (for those not included in the higher resolution observations) and ‘Not FRIs’. The final group numbers are 8, 10, 24, 33 and 6 for groups 1–5 respectively.

The space densities of the maximum, probable and minimum FRIs are then calculated and compared to two previously published measurements of the local value, and with the behaviour of

the strongest FRII sources. The results for all three groups show density enhancements of factors of 5–9 at $z \sim 1.0$ which implies cosmic evolution of the FRI population; this enhancement is also in very good agreement with that predicted by previous models. The behaviour of the FRI/FRII dividing luminosity, as a function of host galaxy absolute magnitude, at the different cosmic epochs of the sample, and for two different star formation histories, is also investigated. A shift to brighter absolute magnitudes is found to be inconsistent with the data but this conclusion is weak due to the lack of knowledge of the host galaxy stellar populations, and the small number of sources in the sample.

Declaration

I hereby declare that this thesis entitled “Measuring the high redshift space density of FRI radio galaxies: investigating the nature of the FRI/FRII divide” is not substantially the same as any that I have submitted for a degree or diploma or other qualification at any other University. I further state that no part of my thesis has already been or is being concurrently submitted for any such degree, diploma or other qualification.

This thesis is the outcome of my own work except where specifically indicated in the text.

Emma Elizabeth Rigby
Edinburgh,
February 2007.

Acknowledgements

This thesis would not have been possible without the help and support of a large number of people. Firstly, I would like to thank my supervisors Ignas Snellen and Philip Best whose guidance and patience over the past three(ish) years made the whole thing so much easier. Sorry for making you read so many drafts!

Next, I have to thank my fellow students at the ROE who were always available for a moan, a laugh or a biscuit. Particular mention must go to my officemates (at one time or another), Caz Francis, Niall Deacon, Tom Kitching, Rita Tojeiro, Barney Rowe, Rachel Smith, Matt Hollister, Tom Targett and Anita Schael, who all provided excellent distractions from work, and to Michael Davidson, Rachel Dowsett, Emma Taylor, Miller Crawford, Jess Skelton, Mairi Brookes and Olivia Johnson who led the way and showed that there's life after graduation! They all also always knew the answers, even if the question came from Info. Office. Thanks also to John Barrow, Horst Meyerdierks and the other members of the computing staff, who always managed to sort my computer out whenever I broke it.

Thanks also to my parents, Judith and John, and my brother, Mark, for all their love and support over the years. Without their belief in me I could never have achieved all that I have. Thanks must also go to all my teachers over the years, especially Mr Shotbolt, who once memorably noted that I was "...good at physics, for a girl".

Finally, all my thanks and love to my boyfriend Bruce who has been there throughout this time, cheering me up, making me laugh, explaining the hard bits, and just generally being indispensable and irreplaceable. It is to him, even though he still hasn't fully read it, that I dedicate this thesis.

Contents

List of Figures

List of Tables

CHAPTER 1

Introduction

1.1 An overview of Active Galactic Nuclei

Observations have shown that, for a small but significant fraction of galaxies, the bulk of their emission is due to non-stellar processes and is concentrated in a central region of small angular size (e.g. Peterson, 1997). It is thought that this emission is due to accretion onto a $\gtrsim 10^6$ $M_\odot$, supermassive, black hole, which is why these objects are referred to as Active Galactic Nuclei or AGN.

AGN are historically divided into several different subclasses including Seyfert galaxies, Broad and Narrow Line Radio Galaxies, Quasars, BL Lac Objects and Optically Violently Variables (OVVs). In Seyfert galaxies the host, spiral, galaxy is clearly visible, even if the central, bright, nucleus can also be seen, and their AGN luminosity is lower than in other classes. They can be further sub-divided into two types, depending on the emission lines seen in their spectra; Type 1 Seyfert spectra show both narrow and broad lines, whereas Type 2s show narrow lines only. Broad and Narrow Line Radio Galaxies (BLRG and NLRG) can be thought of as the radio–loud counterparts to Seyfert Type 1 and 2 galaxies respectively, except that their host galaxies are ellipticals, instead of spirals. In quasars, the host galaxy is completely outshone by the high luminosity nuclear emission and they appear as stellar–like point–sources. They can be either radio–loud or radio–quiet (at $z \sim$2 Miller et al. (1990) found that radio–loud have $L_{5\mathrm{GHz}} > 10^{25}$ WHz^{-1}sr^{-1}, whereas radio–quiet have $L_{5\mathrm{GHz}} < 10^{24}$ WHz^{-1}sr^{-1}) and their

spectra also show similar broad and narrow line features as the Seyfert 1 spectra. The final two subclasses, BL Lac Objects and OVVs, are highly variable, over very short timescales and are also radio loud sources. OVVs also show high polarization whereas the main characteristic of BL Lacs is the lack of strong emission or absorption lines in their spectra.

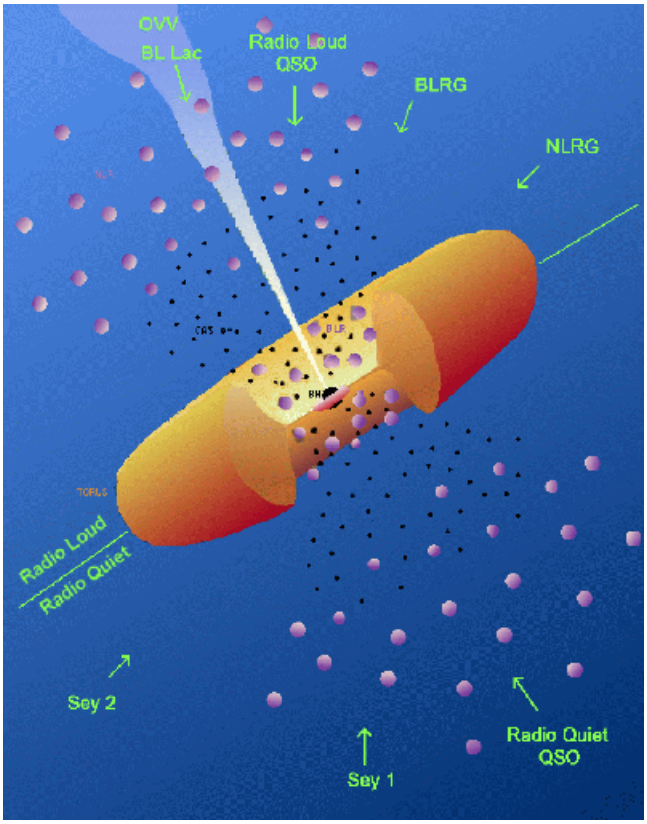

Figure 1.1: The standard model for an AGN, illustrating the viewing angles which give rise to the different subclasses in the AGN 'zoo'. The top portion of the diagram shows a radio loud model whereas the bottom portion shows radio quiet. If the view of the central nucleus and BLR is obscured by the torus then NLRGs and Seyfert type 2 galaxies are seen; if it is visible then the AGN will appear as a BLRG, a Quasar (QSO), both radio loud and quiet, or a Seyfert type 1, depending on the presence of a radio jet. Finally, if the viewing angle is such that the observer looks directly down the radio jet, an OVV or BL Lac is seen (Dunn, 2005).

When these different subclasses were first detected, their lack of shared characteristics led to the assumption that they were unrelated. It was later proposed that many of these differences are the result of observing similar objects at varying orientation angles, with varying amounts of obscuration. Figure 1.1 illustrates this model: the aforementioned central black hole and corresponding accretion disk, is surrounded by a large, dusty region, the exact shape of which is unknown; for simplicity, it is usually shown and referred to as a 'torus'. Within this torus, there are also many fast moving clouds of gas, which give rise to the broad emission lines seen in the spectra of some AGN. These broad lines are for permitted transitions only which implies that the density in these clouds is high enough to suppress forbidden transitions. Outside the

central regions, there also exists a larger region of slower moving, lower density, clouds of gas which in turn result in the narrow emission lines, both forbidden and permitted, seen in other spectra. These two areas are known as the Broad Line Region (BLR) and the Narrow Line Region (NLR) respectively. Additionally, less than 10% of AGN are radio–loud and emit highly collimated radio jets from their nuclei (Mushotzky, 2004).

1.1.1 Characteristics of AGN radio emission

For some radio–loud AGN, the majority of the radio emission comes from kiloparsec–scale lobes, located either side of the host galaxy and aligned with the inner jets (extended, BLRG and NLRG sources), whereas in others the emission is unresolved and confined to the central, core, region (compact sources). The lobes, if present, are generally observed to be steep spectrum, with $\alpha \sim 0.5$ – 1.0[1], and the core and inner jet are observed to be flat spectrum with $\alpha \sim 0$ – 0.5. In both cases however, the emission is synchrotron in origin.

Fanaroff & Riley Class I and II radio galaxies

The lobe–dominated sources can be further subdivided into Fanaroff & Riley Class I and II galaxies (Fanaroff, 1974), depending on their morphology. Class I (FRI) are 'edge–darkened' with the majority of their emission confined to their central regions and lobes that flare out close to the nucleus. On the other hand, the FRII, class II, galaxies are 'edge–brightened' meaning the bulk of their emission originates from hotspots at the lobe ends. The FRII galaxies are the more luminous of the two classes and typically have $P_{178\mathrm{MHz}} > 10^{24-25}$ WHz^{-1}sr^{-1} but there is significant overlap at the break luminosity. Examples of the two types can be found in Figures 1.2 and 1.3.

The differences between the two FR classes are not confined to the lobe morphology. Zirbel & Baum (1995) found that the FRIIs produce 10-50 times more emission line luminosity than the FRIs at a particular radio core power. These results led Baum et al (1995) to suggest that this may be due to qualitative, intrinsic, differences in the central engines of the two types, with the FRI sources having a lower accretion rate and a slower black-hole spin than the FRII sources which results in lower power, less collimated jets. The low FRI accretion rate suggested by Baum et al. (1995) led to the theory that FRI accretion disks were in an advection dominated accretion flow (ADAF) state (Ghisellini and Celotti, 2001), where most of the released gravi-

[1]The spectral energy distribution of an AGN can be expressed as a power law, $S_\nu \propto \nu^{-\alpha}$, where S_ν is the flux density at a frequency ν and α is the spectral energy index.

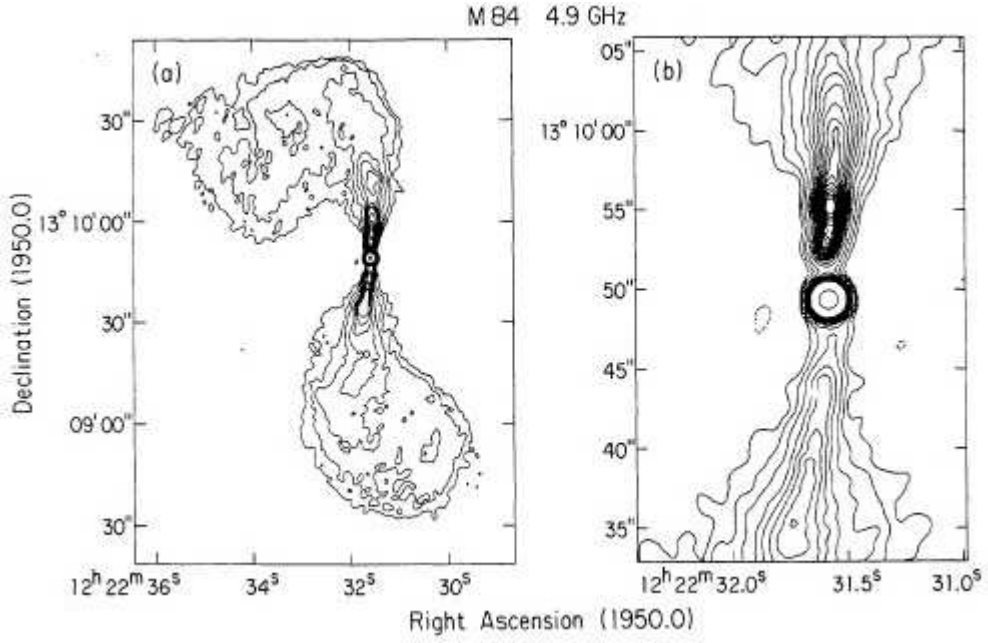

Figure 1.2: The elliptical galaxy M84 – a FRI object. The right–hand panel shows an enlargement of the central bright region (Bridle and Perley, 1984).

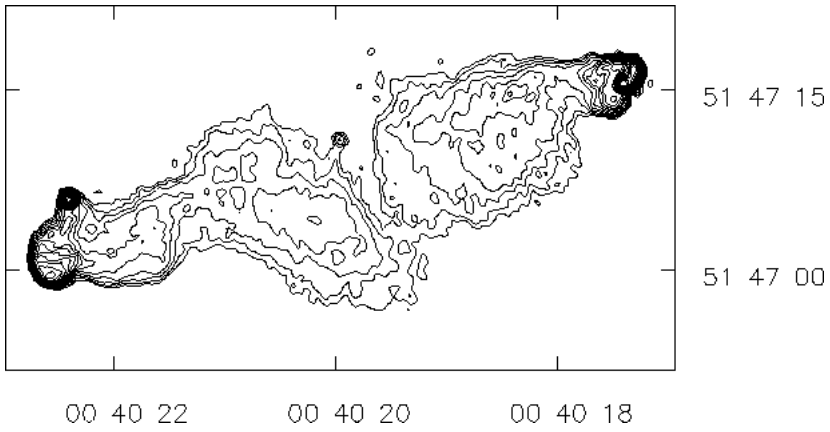

Figure 1.3: 3C20, a FRII radio galaxy clearly showing the edge–brightening (Hardcastle, 1995).

tational energy from the accreting matter is transported into the black hole. This results in very inefficient radiation by the disk. More recently, however, work by Cao & Rawlings (2004) concluded that there was no difference in accretion mode between the FRI and FRII populations, for a significant fraction of their sample (all of which were high luminosity FRIs). They suggest that the apparent radiative inefficiency, for the higher luminosity FRIs at least, may be due to obscuration of the central accretion disk.

The ‘intrinsic difference’ models have one main problem:- the existence of objects that show both FRI and FRII morphologies, introduced by Gopal-Krishna & Wiita (2000) and supported by Gawroński et al. (2006). An example of this rare type of object can be seen in Figure 1.4. These sources cannot be explained in the context of the Baum et al. (1995) model as the same central engine could not give rise to both FRI and FRII morphologies concurrently. This led Gopal-Krishna & Wiita (2000) to argue for an extrinsic model, in which it is the environment around the galaxies that causes the observed differences; a jet in a relatively calm environment would remain collimated and retain its hotspots for far longer than one in a more turbulent environment. Additionally, if a galaxy is denser than average, or is located in a denser region, the chance of jet disruption is significantly increased.

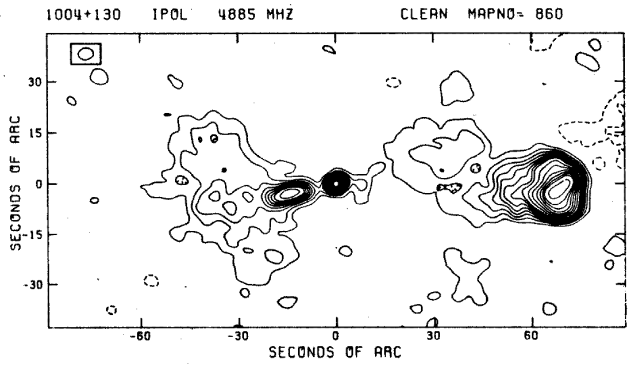

Figure 1.4: 1004+130 – a source showing both FRI and FRII morphologies (Gopal-Krishna and Wiita, 2000).

Initially, optical observations of the FRI and FRII sources appeared to support the Baum et al. (1995) intrinsic model with Owen & Laing (1989) finding that the host galaxies of FRIs tended to be larger and more luminous than those of FRIIs. Later work by Ledlow & Owen (1996) suggested however, that this result was caused firstly by a sample selection effect due to observing galaxies near the FRI/FRII break, and secondly by only observing a small range in radio power. Since they found that the FRI/II break is a function of the absolute magnitude of the host galaxy as well as the radio power (Figure 1.5), a small range in power led Owen & Laing to the conclusion that the FRII host galaxies were less luminous.

Ledlow & Owen (1996) concluded that all radio galaxies live in similar large–scale environments, and that the host galaxy luminosity and properties are most important in determining the evolution of radio sources. Incidentally it should be noted that since the mass of the central black hole is correlated with the host galaxy luminosity (McLure and Dunlop, 2002), the FRI/FRII break is correlated with it also, suggesting that the properties of the black hole cannot be completely ruled out of the debate.

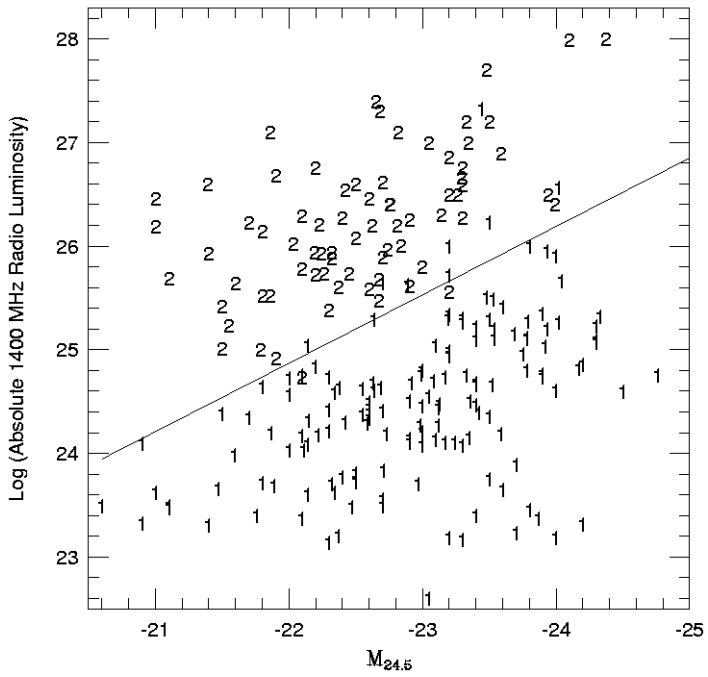

Figure 1.5: Radio power against host galaxy absolute isophotal magnitude, measured to 24.5 magnitudes arcsec^{-2}, for the FRI (1) and FRII (2) galaxies (Ledlow & Owen (1996) and references therein). It should be noted that there are FRI sources above the break and FRII sources below it further suggesting that the two populations may not be distinct.

The lobe–dominated population could alternatively be divided up depending on their source emission line strength. In this scheme, the low power, weak emission line objects encompass both FRI and certain FRIIs (those with low–excitation spectra in which lines such as [OIII] are very weak or undetectable (Laing et al., 1994)), whereas the high power, strong emission line objects are mainly FRIIs. As a result, this grouping does not correspond exactly with that obtained using the FRI/II classification scheme. In an attempt to investigate possible intrinsic differences, Willott et al. (2001) used this new dual population scheme for their sample, instead of the usual FRI/II split, since the line strength is a direct probe of the central engine, whereas radio luminosity could be modified by the surrounding environment; they found that this new model fitted their data well, thus suggesting further links between the two FR types.

As has been shown by the results outlined above, it is still unclear whether the observed morphological differences between the two FR classes are the result of fundamental differences in the properties of the central engine, or differences in the interactions of the jets with their environments, or some combination of the two. This intrinsic/extrinsic question is of vital importance for understanding the relationship between these objects; if the intrinsic difference

model is correct then the FRIs and FRIIs are two discrete classes of object, however if the evidence suggests the other model is correct, the underlying properties of the classes would be the same. In the latter case the two classes may simply represent different stages in the evolution of a radio galaxy, i.e. it starts out as a powerful, high–luminosity FRII and as it ages its jets become less powerful and it becomes an FRI (e.g. Willott et al. 2001).

1.2 The cosmic evolution of FRI/II radio sources

One of the key ways in which the observed differences can be investigated is through the cosmic evolution of the two types; any similarities in behaviour detected lends weight to the extrinsic difference model, and vice versa. The following sections outline the current observational evidence for evolution of the FRI population. It should be noted that the choice of survey observing frequency has a major effect on the resulting source populations detected. For example, at low frequencies, the majority of the radio sources detected will be steep spectrum, lobe–dominated, objects, whereas at high frequencies the flat spectrum, compact, objects will dominate.

Determining the cosmic evolution of FRI radio galaxies is also important because of the impact that they may have on galaxy formation and evolution. Models of galaxy formation are increasingly turning to these objects to solve the problem of massive galaxy over–growth (e.g. Bower et al., 2006). It is predominantly the lower luminosity sources that provide the necessary feedback for this, (Best et al., 2006), and may possibly be limited to the FRI population alone. As such, understanding the little studied FRI sources and their evolution could be critical to deciphering this mechanism.

1.2.1 Radio results

Ryle & Clarke (1961) were among the first to attempt to infer the cosmic evolution of radio sources through the use of number count statistics. Their results suggested that the evolution is confined to the higher powered sources only, and this was supported by the similar findings of Longair (1966).

The luminosity dividing the strongly evolving population of radio sources from those showing little or no evolution was subsequently found to be very close to that dividing FRI from

FRII galaxies. This led Wall (1980) to suggest a correspondence between the two groups. In his model the FRIs have constant space density whereas the FRIIs undergo strong cosmic evolution. Jackson & Wall (1999) extended these ideas and attempted to construct a dual–population unification scheme linking FRI galaxies with BL Lac objects and FRII galaxies with flat-spectrum quasars. They also tested for evolution in their sample by calculating the $V/V_{\rm max}$ statistic which is expected to have a value of 0.5 if the sample sources are uniformly distributed over the survey volume and >0.5 if the source number density is higher at larger distances, suggesting evolution. (Full details of this method can be found in Appendix A). The 26 FRI sources were found to have $\langle V/V_{\rm max}\rangle = 0.314 \pm 0.0577$ rising to 0.507 ± 0.144 for the highest luminosity objects. Conversely $\langle V/V_{\rm max}\rangle = 0.664 \pm 0.025$ for the 137 FRII sources with a range of $0.415 \leq \langle V/V_{\rm max}\rangle \leq 0.807$ as the luminosity increases. These results strongly supported the hypothesis of Wall (1980). Jackson & Wall (1999) also modelled this evolution and their fit indicated that the space density of FRII sources was enhanced by $> 10^4$ at $z = 2.8$.

These results were disputed by Snellen & Best (2001; 2003). They pointed out that since the sample of Jackson & Wall (1999) was flux density limited, the high luminosity FRII sources could be detected out to much higher redshifts ($z < 2$ compared to $z < 0.2$ for the FRIs). Indeed if the individual FRI and FRII plots of $V/V_{\rm max}$ versus radio power are combined (Figure 1.6), no difference can be seen between the two populations at a particular power. The overall trend is for $V/V_{\rm max}$ to increase with radio power, possibly indicating luminosity dependent but population independent evolution.

1.2.2 The evolving radio luminosity function

The distribution of source number density with radio luminosity, known as the radio luminosity function or RLF, is an important tool for studying the behaviour of the two FR populations: studying the changes it undergoes with increasing redshift highlights the evolution in the source space density. The local RLF is well fitted by a dual–power law function, with a break luminosity roughly equivalent to that dividing the FRI and FRII galaxies, as illustrated by that derived by Best et al. (2005) for a sample of radio galaxies in the Sloan Digital Sky Survey, together with that determined for two previous surveys for comparison, shown in Figure 1.7.

Dunlop & Peacock (1990, hereafter DP90) modelled the RLF evolution using the redshift distributions of four, complete, 2.7 GHz, samples, alongside local RLF measurements and additional source count determinations at fainter flux limits. To do this they used both ‘free–form’ models, in which there were no preconceived assumptions about the evolution, and parametric models, which assumed either pure luminosity or a combination of luminosity and density evolution (PLE, LDE); these were then extrapolated to cover those radio powers and redshifts for

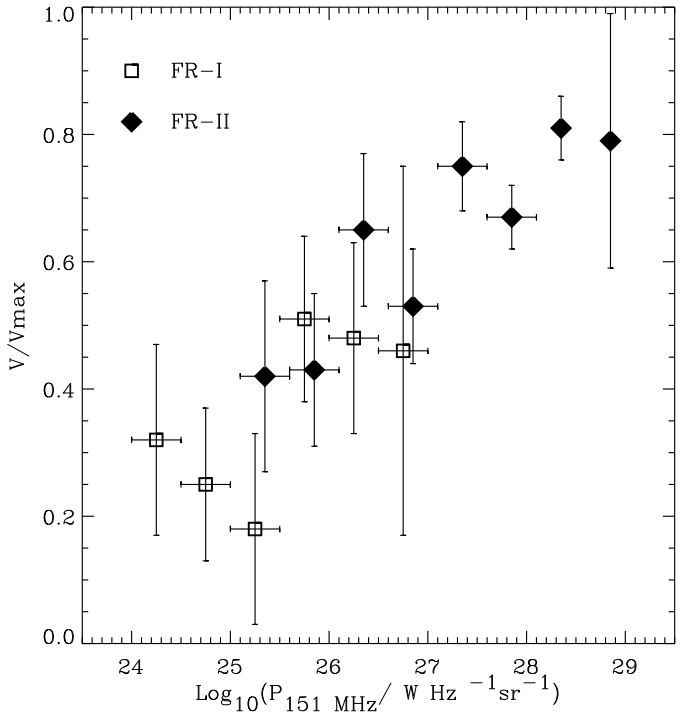

Figure 1.6: Average $V/V_{\rm max}$ values from Snellen & Best (2001) using values from Jackson & Wall (1999). Squares represent FRIs and diamonds represent FRIIs. At a particular radio power, no difference can be seen between the two populations.

which no data existed. In contrast to the evolving/non–evolving, dual–population, paradigm discussed above, the parametric models assumed the radio galaxy sample was a single population, made up of a low luminosity, weakly evolving, component and a higher luminosity, strongly evolving component. Both of these model ensembles found evidence for a cut–off in the comoving number density of the radio population between $z = 2 - 4$, as illustrated, for the pure luminosity model, by Figure 1.8. The pure luminosity and luminosity/density evolution models also predict density enhancements for sources with typical FRI radio powers of a factor of $\sim$6 out to $z = 2$ which, it should be noted, is less than that predicted for the more luminous, FRII–type, objects.

Waddington et al. (2001) investigated the model predictions of DP90 using a lower flux density, 1.4 GHz sample, of mJy radio sources. They found that two of the 'free–form' models, both of which incorporated an enforced decline in the RLF above redshifts of 2, were consistent with their data, whereas the parametric models fit well at low redshift but overestimate the numbers of sources at $z \gtrsim 0.5$. However, Willott et al. (2001) performed a similar luminosity function calculation for their sample and found that their data were consistent with the pure luminosity

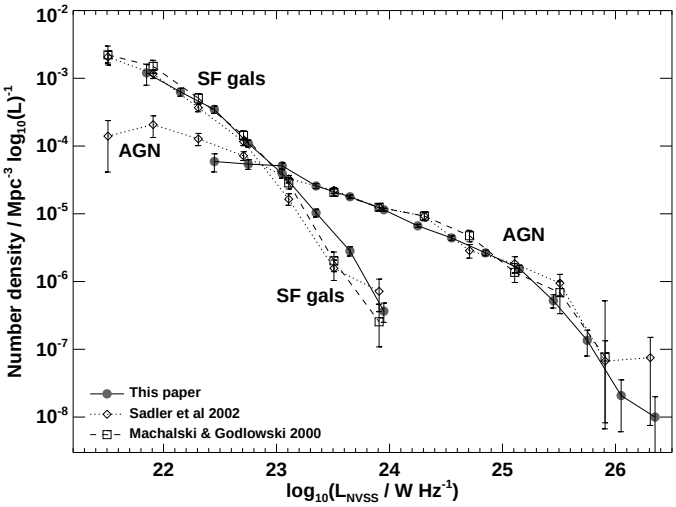

Figure 1.7: The local RLF calculated by Best et al. (2005) (solid circles) for a sample of radio–galaxies drawn from the Sloan Digital Sky Survey, separated into AGN and starburst galaxies, together with two previous versions taken from the literature.

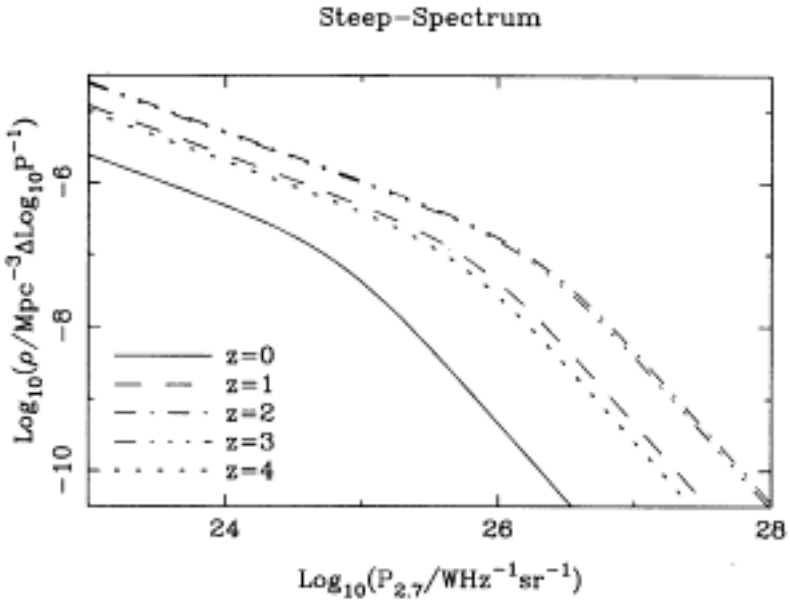

Figure 1.8: The evolution of the RLF as predicted by the pure luminosity evolution model of DP90, calculated using Einstein de Sitter cosmology.

evolution model out to $z = 2$.

Since the lifetime of a radio source is typically 10^7–10^8 yr, the evolution of the RLF is not that of individual sources, but of the population of a whole (Waddington et al., 2001). This suggests that the simple PLE model, in which the same set of objects merely fade with cosmic time, has a weak physical basis, whilst still fitting the observations well. Similarly, a model

of pure density evolution, in which objects have a constant luminosity but different lifetimes, also seems unlikely (Peacock, 1999). Willott et al. (2001) though, point out that their dual–population model, which has a better physical basis, replicates the PLE results well.

1.3 Measuring the high redshift space density of FRIs

It is clear from the number count statistics that higher luminosity sources undergo stronger evolution, but whether this is sufficient to define a dual population scheme involving FRI and FRII galaxies is not yet clear, especially without reliable $V/V_{\max}$ tests. Many of the current set of observations produce contradictory results, leaving the question of whether the FRIs are intrinsically different to the FRIIs open. What is needed is a direct measurement of the high redshift space density of these objects; this has only just become feasible because of the difficulties involved in observing sources out to $z\sim1$ at the sub-arcsecond resolutions that are required to accurately morphologically classify a source.

The first attempt at determining the high–redshift space density of morphologically selected FRIs was carried out by Snellen & Best (2001) using the Hubble Deep Field and Flanking Fields (HDF+FF). This area of sky has been well studied in the radio and contains two FRI sources. There may be more FRIs present, but with the existing data only objects above mJy levels can be reliably identified. The first of these sources, HDF123644+621133 (Figure 1.9, left), has a redshift of $z = 1.013$ arising from its optical identification with a elliptical galaxy, and a total radio power of $P_{1.4\mathrm{GHz}} = 10^{25.0}$ WHz^{-1}. The second FRI source, HDF123725+621128 (Figure 1.9, right), is optically identified with a faint compact galaxy of undetermined redshift. However Snellen & Best (2001) argue that the galaxy must be at $z > 1$ because of its faintness and its red optical to near–infrared colours. A photometric redshift of 1.2 was subsequently calculated for it by Donley et al. (2005), confirming this and giving it a 1.4 GHz radio power of $P_{1.4\mathrm{GHz}} = 10^{25.7}$WHz^{-1}.

With only two FRIs, Snellen & Best were unable to directly calculate the high–redshift space density of FRIs, but they were able to investigate any possible evolution of the FRI population by calculating the statistical significance of finding the two aforementioned sources in the HDF+FF area, if a constant number density is assumed. The derivation of this comes from the Poisson distribution:

$$P_\nu(n) = \frac{\nu^n e^{-\nu}}{n!}, \tag{1.1}$$

where $P_\nu(n)$ is the probability of obtaining exactly n successes giving an expected number of

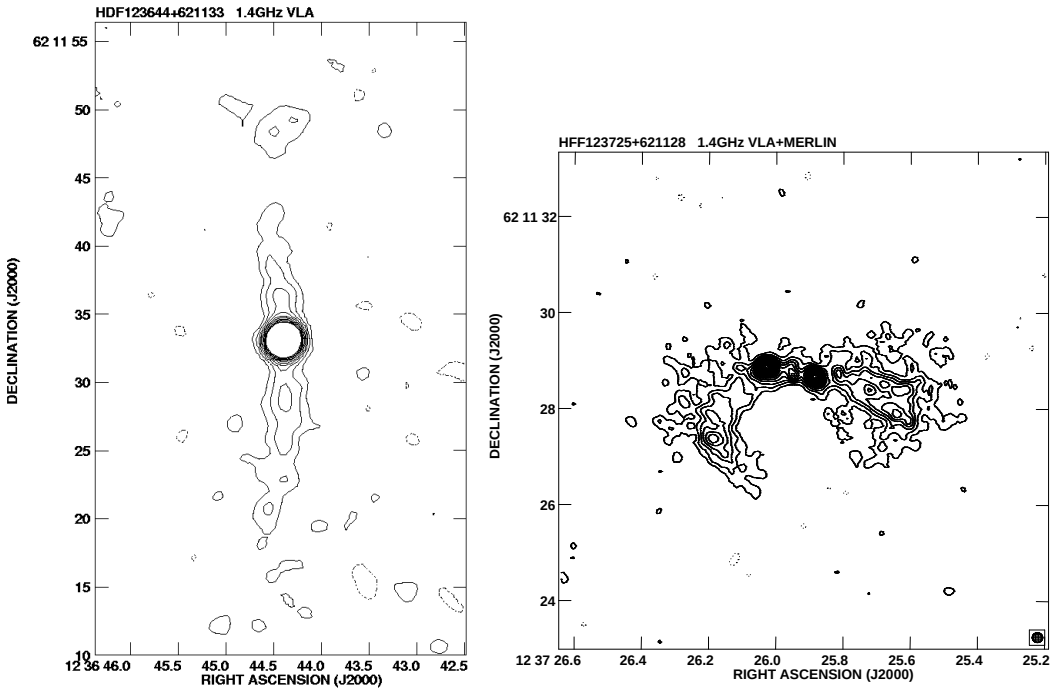

Figure 1.9: The two FRI sources HDF123644+621133 (left) and HDF123725+621128 (right) found in the HDF+HFF (Muxlow et al., 2005; Snellen and Best, 2001)

successes ν.

In this case though, it is not the probability of detecting exactly n objects that is required, but rather the probability of detecting $\geq n$. Therefore the expression

$$P(\geq n) = \sum_{n}^{\infty} \frac{\nu^n e^{-\nu}}{n!}, \tag{1.2}$$

was needed.

With $n = 2$ this becomes

$$P(\geq 2) = \sum_{n=2}^{\infty} \frac{\nu^n e^{-\nu}}{n!} = e^{-\nu} \sum_{n=2}^{\infty} \frac{\nu^n}{n!} = e^{-\nu}(e^{\nu} - 1 - \nu), \tag{1.3}$$

using the expansion of e^x:

$$e^x = \sum_{n=0}^{\infty} \frac{x^n}{n!} = 1 + x + \sum_{n=2}^{\infty} \frac{x^n}{n!} \tag{1.4}$$

In summary then, the chance of finding 2 or more FRI sources in a particular volume if the

expected number in that volume is ν is

$$P(\geq 2) = e^{-\nu}(e^{\nu} - 1 - \nu). \tag{1.5}$$

The local space density was found by Snellen & Best in two ways: firstly a value of 200 FRIs per Gpc^3 was obtained using the local RLF of DP90, and secondly a similar value of 170 FRIs per Gpc^3 was directly measured from a complete subsample of 3CR radio galaxies (Laing et al., 1994). Using the first density result, 200 FRIs per Gpc^3, they then calculated various values of ν for different volumes. These volumes arise from the maximum redshifts at which the sources could have been detected and still classed as FRIs. For the fainter source, this maximum was given as $z_{\max} \approx 1.7$ at $> 3\sigma$. Since the other source had, in their work, an assumed redshift in the range $1 < z < 1.5 \sim 2$, its maximum redshift had a range $1.5 < z_{\max} < 3.0$, and thus led them to use values of $z_{\max}$ =1.5, 2.0, 2.5 and 3.0 in the calculations. Their results showed a probability of $< 1\%$ for the non-evolution scenario. They repeated their calculations using the density enhancements predicted by the pure luminosity evolution and luminosity/density evolution models of DP90 which do not differentiate between FR type. The resulting probabilities varied from 2% – ∼20% for both types of evolution, meaning that the observations can be consistent with those models, again supporting a possible evolution for the FRI sources. However, with only two detected FRIs the uncertainties in this result are clearly large.

This luminosity dependent evolution is further supported by the work of Jamrozy (2004) who constructed two complete, morphologically classified, radio source samples at 1.4 GHz and 408 MHz using several different radio surveys. They find that a positive cosmic evolution for the most luminous FRI sources is needed to fit their observational data out to $z \sim 2$. On the other hand, Clewley & Jarvis (2004) find no evidence for a density enhancement out to $z = 0.8$ for their FRI sample, constructed by cross–matching two deep radio surveys (the Westerbork Northern Sky Survey, WENSS, Faint Images of the Radio Sky at Twenty Centimetres, FIRST, and NRAO VLA Sky Survey, NVSS) with the optical Sloan Digital Sky Survey. They conclude that Snellen & Best's findings were a result of using two FRI galaxies with luminosities at or near the FRI/FRII break. However, they selected the FRIs in their sample using a luminosity cut; this could lead to FRIs being missed (particularly the more luminous FRIs which may evolve the most, c.f. Figure 1.6) since the FRI/FRII break luminosity is not fixed, but is a function of host galaxy magnitude as described in §1.1.1. It should also be noted that Sadler et. al. (2007), using a sample selected in a very similar way to that of Clewley & Jarvis (2004), find that the FRI no–evolution scenario can be ruled out at a significance level of $>6\sigma$. All these studies, which seem to have a wide range of different results, are actually in reasonable agreement when all the factors are taken into account (e.g. when the radio luminosities each work at are converted to the same radio frequency). It is clear therefore that to obtain an

accurate picture of the high redshift behaviour of FRIs, radio morphological classification is a necessity.

This thesis aims to directly measure the space density of a sample of properly (i.e. morphologically) classified sample of high redshift FRIs with the aim of constraining the cosmic evolution of these objects. This will provide a valuable insight into the observed differences between the two classes. However, before the thesis contents are outlined a brief overview of some useful cosmological results, which will be needed for the later density calculations, are outlined.

1.4 Useful cosmological results

The expansion of the Universe means that the distances between objects does not remain constant and therefore, cosmological factors need to be taken into account for the calculation of accurate results. In this section, three different distance measures, comoving, angular and luminosity distance, and the cosmological volume element are described for a flat Universe with a non–zero cosmological constant, Λ. For further details, see Hogg (1999), Peacock (1999), Peebles (1993) and references therein.

Firstly, some definitions of key parameters are needed:

- The cosmic scale factor, $a(t)$, is the size of the Universe relative to the size of the Universe at a particular time. It is normalised such that $a = a_0 = 1$ at the current epoch
- The Hubble parameter, H, defined as $\dot{a}/a$, is the constant of proportionality of the expansion of the Universe. Locally, $H = H_0$ and has a value of $100h$km s^{-1}Mpc^{-1}; h is currently thought to be ~ 0.7 (e.g. Spergel et al., 2006) .
- Redshift, z, is defined as the observed wavelength, λ, of an object's light relative to $\lambda_{\rm e}$, the wavelength at which the light was emitted: $z = (\lambda/\lambda_{\rm e}) - 1$. It is related to the scale factor by $a(t) = (1 + z)^{-1}$.

1.4.1 Comoving distance, $\mathrm{d_c}$

In a flat, isotropic and homogeneous Universe the variation with time of the cosmic scale factor, is given by the Friedmann equation:

$$\left(\frac{\dot{a}}{a}\right)^2 = \frac{8\,\pi\,G\,\rho}{3}, \tag{1.6}$$

where G is the Gravitational constant and ρ is the density of the Universe, which itself is the sum of $\rho_{\rm m}$ and ρ_Λ, the densities due to matter and vacuum energy respectively. It can be shown that $\rho_{\rm m} = \rho_{0,{\rm m}}\ a^{-3}$ and $\rho_\Lambda = \rho_{0,\Lambda}$ where the subscript 0 denotes a value at the current epoch. Substituting this into Equation 1.6 gives

$$\left(\frac{\dot{a}}{a}\right)^2 = \frac{8\,\pi\,G}{3}\left(\rho_{\rm m,0}\ a^{-3} + \rho_{\Lambda,0}\right). \tag{1.7}$$

$\rho_{\rm m,0}$ and $\rho_{\Lambda,0}$ can be converted to the dimensionless quantities, Ω_m and Ω_Λ, by dividing them by $3\ H_0^2/8\ \pi\ G$, a quantity referred to as the critical density, $\rho_{\rm c}$. Remembering that $a = (1+z)^{-1}$ and $H = \dot{a}/a$, Equation 1.6 can be written as

$$H = H_0\ \sqrt{\left(\Omega_{\rm m}\ (1+z)^3 + \Omega_\Lambda\right)} = H_0\ E(z). \tag{1.8}$$

For a photon travelling radially towards an observer $d\ (\mathbf{d}_{\rm c})/dz = c/H$ where $\mathbf{d}_{\rm c}$ is the comoving distance between the two points (i.e. the proper distance scaled by the ratio of the two scale factors) and c is the speed of light. Therefore,

$$\mathbf{d}_{\rm c} = \frac{c}{H_0}\int_0^z \frac{dz'}{E(z')}. \tag{1.9}$$

1.4.2 Angular diameter distance, $\mathbf{d}_{\rm a}$

In an Euclidean universe, the angular size, θ, (in radians) of an object is related to its actual physical size, $\mathbf{d}_{\rm p}$ by

$$\mathbf{d}_{\rm a} = \frac{\mathbf{d}_{\rm p}}{\theta} \tag{1.10}$$

The size of this object in a non–Euclidean geometry is $\mathbf{d}_{\rm p} = a\ \mathbf{d}_{\rm c}\ \theta$ so Equation 1.10 becomes

$$\mathbf{d}_{\rm a} = \frac{\mathbf{d}_{\rm c}}{(1+z)} \tag{1.11}$$

At $z \gtrsim 1$, this begins to decrease which means that objects at larger distances have smaller values of $\mathbf{d}_{\rm a}$, and hence larger angular sizes. In other words, if there are two objects with the same physical size located at $z = 2.0$ and $z = 1.0$, the one at higher redshift will appear to be larger.

1.4.3 Luminosity distance, $\mathbf{d}_\mathrm{l}$

If photons were emitted by a distant source at some frequency ν_1 then they would be detected by an observer at a frequency $\nu_0 = \nu_1/(1+z)$. Since the energy of the photon is $h\nu$, then the measured photon energy flux density is

$$S'_\nu(\nu_0) = h\,\nu'_0\,n'_\nu\,(\nu_0) = h\,\frac{\nu_1}{1+z}\,n_\nu(\nu_1) = \frac{S_\nu(\nu_1)}{1+z}, \tag{1.12}$$

where $'$ denotes measurements in the observers frame and n is the total number of photons. The total energy flux received over all frequencies is therefore

$$S' = \int \frac{S_\nu(\nu_1)}{(1+z)}\frac{d\nu_1}{(1+z)} = \frac{S}{(1+z)^2}. \tag{1.13}$$

The two factors of $(1+z)$ in this equation represent the effects of redshift on the frequency and the arrival rate of the incoming photons.

For an object at co–moving distance $\mathbf{d}_\mathrm{c}$ and with emitted luminosity L, the flux measured in the emitted reference frame would be $S = L/(4\pi\,(a_0\mathbf{d}_\mathrm{c})^2)$ where $a_0 = 1$ is the cosmic scale factor at the present epoch. Using the previous result, the flux measured by the observer would be

$$S' = \frac{S}{(1+z)^2} = \frac{L}{4\pi\,(1+z)^2\,{\mathbf{d}_\mathrm{c}}^2} = \frac{L}{4\pi\mathbf{d}_l^2}, \tag{1.14}$$

where $\mathbf{d}_l = (1+z)\mathbf{d}_c$ is the luminosity distance.

Similarly, the observed flux density of a source is given by

$$S'_\nu(\nu_0) = \frac{(1+z)\,L_\nu(\nu_0[1+z])}{4\,\pi\,\mathbf{d}_\mathrm{l}^2}, \tag{1.15}$$

where the extra factor of $(1+z)$ takes into account the change in bandwidth due to the redshift. For radio galaxies, in which photons are emitted with a power law spectrum of the form $S_\nu \propto \nu^{-\alpha}$, this can therefore be rewritten as

$$S'_\nu(\nu_0) = \frac{L'_\nu(\nu_0)}{4\,\pi\,{\mathbf{d}_\mathrm{l}}^2\,(1+z)^{\alpha-1}} \tag{1.16}$$

1.4.4 Comoving volume, $V_{\rm c}$

For a flat Universe the comoving volume element in solid angle $d\Omega$ is given by

$$d\,V_{\rm c} = \frac{\mathbf{d_c}^3}{3}\,d\Omega. \tag{1.17}$$

Integrating this over solid angle gives the total comoving volume out to a redshift of z

$$V_{\rm c} = \frac{4\,\pi}{3}\,\mathbf{d_c}^3. \tag{1.18}$$

Additionally, the comoving volume between two redshifts, z_a and z_b is

$$V_{\rm c}(z) = \frac{c}{H_0}\int_{z_a}^{z_b}\frac{\mathbf{d_c}^2}{E(z')}d\Omega\,dz \tag{1.19}$$

1.5 Thesis outline

The outline of this thesis is as follows. Chapter 2 defines the complete sample of 81 radio galaxies and describes the new radio observations that were taken to initially select FRI candidates. Chapter 3 describes the optical and infra–red observations of the sample, and the resulting host galaxy identifications. The spectroscopic observations of a subset of the sample can be found in Chapter 4, along with the redshift estimation methods used for the sample sources with no redshift information. Chapter 5 describes the high–resolution radio observations taken of the best high–redshift FRI candidates and the subsequent classification of the entire sample. The space density of the FRIs in the sample can be found in Chapter 6 along with an investigation into the behaviour of the FRI/FRII break luminosity at the different redshifts of the sample. Finally, conclusions about the cosmic evolution of the FRI population are outlined in Chapter 7. For the remainder of this thesis, values for the cosmological parameters of $H_0 = 71$ km s^{-1}Mpc^{-1}, $\Omega_{\rm m} = 0.27$ and $\Omega_\Lambda = 0.73$ are used.

CHAPTER 2

A new radio sample

The area of sky used in the analysis of Snellen & Best (2001) was only large enough to give a first estimate of the high redshift space density of FRIs. This work, therefore, uses a deep, wide–field, Very Large Array (VLA) A–array survey an order of magnitude larger than the HDF+HFF. This survey was split over two fields – one in the constellation of Lynx at $\alpha = 8h41$, $\delta = +44.8^{\circ}$ and one in Hercules at $\alpha = 17h18$, $\delta = +49.9^{\circ}$ – which were chosen because of the existence of previous optical and low resolution radio observations by Windhorst et al. (1984) and, for Hercules only, by Waddington et al. (2000). Alongside this, the Lynx field is also covered by the Sloan Digital Sky Survey (York et al., 2000; Stoughton et al., 2002).

The two fields were originally observed as part of the Leiden–Berkeley Deep Survey (LBDS) in which they were referred to as Lynx.2 and Hercules.1. For the remainder of this thesis they will be referred to as Lynx and Hercules respectively. This section outlines the previous work in the two fields along with the new A–array observations that form the basis of this work.

2.1 Sample definition and previous radio work

The LBDS survey was constructed to provide photometry for faint galaxies and quasars via multicolour plates obtained with the 4m Mayall Telescope at Kitt Peak (Kron, 1980; Koo &

Kron 1982). Radio follow–up of nine of the LBDS fields (including Hercules and Lynx that are used here) was performed subsequently using the 3 km Westerbork Synthesis Radio Telescope (WSRT) at 1.4 GHz at a resolution of 12.5″ (Windhorst et al., 1984), reaching a rms noise level, at the field centre, of 0.12–0.28 mJy. Their radio sample consists of 306 sources which satisfied the sample selection criteria of peak signal to noise (S_P/N) $\geq 5\sigma$ out to an attenuation factor, $A(r)$, ≤ 5 (for WSRT this corresponds to a radius of $\leq 0.464^\circ$ or $\leq 28'$).

The Hercules and Lynx fields were reobserved by Oort & van Langevelde (1987) and Oort & Windhorst (1985) respectively, again using the 3km WSRT at 1.4 GHz with a 12.5″ beam. These two sets of observations were a factor 2–3 deeper than the original Windhorst et al. (1984) ones, reaching a 5σ flux limit of 0.45 mJy for Hercules and 0.30 mJy for Lynx at the pointing centre.

The sample used in this work is a subset of the combined Hercules and Lynx sources as it is limited by the field of view size of the optical imaging described in Chapter 3; this is illustrated in Figure 2.1. A flux limit of 0.5 mJy was also imposed to remove the faintest, most poorly detected sources and provide a more uniform limiting flux density across the two fields. Table 2.2 gives the Oort & van Langevelde (1987) Hercules and Table 2.3 the Oort & Windhorst (1985) Lynx flux densities for the sources included in this work. These, and other source parameters, were measured using an elliptical Gaussian fitting method in two dimensions. Table 2.1 gives the 1.4 GHz flux densities of sources which were not covered by the optical observations but were included in the subsequent infra–red imaging; consequently they are not part of the complete sample but are included here for completeness.

2.2 Sample completeness

The selection criteria of the LBDS meant that source weighting was necessary to make the sample complete. This incompleteness arises from two factors: the attenuation of the WSRT primary beam and the resolution bias. The effect of the first of these factors, the decreasing sensitivity at increasing radial distance from the pointing centre, is to make the probability of detecting a source depend on where it is located in the map; a source which just satisfies the selection criteria at the centre would have been missed if it was located at the map edge. To correct for this each source was assigned a weight that was inversely proportional to the area over which it would have met the selection criteria and hence, have been included in the original sample (Windhorst et al., 1984). The total sample area for the current work is limited by the size of the optical imaging, so the attenuation weights for the sources considered here were recalculated to account for this.

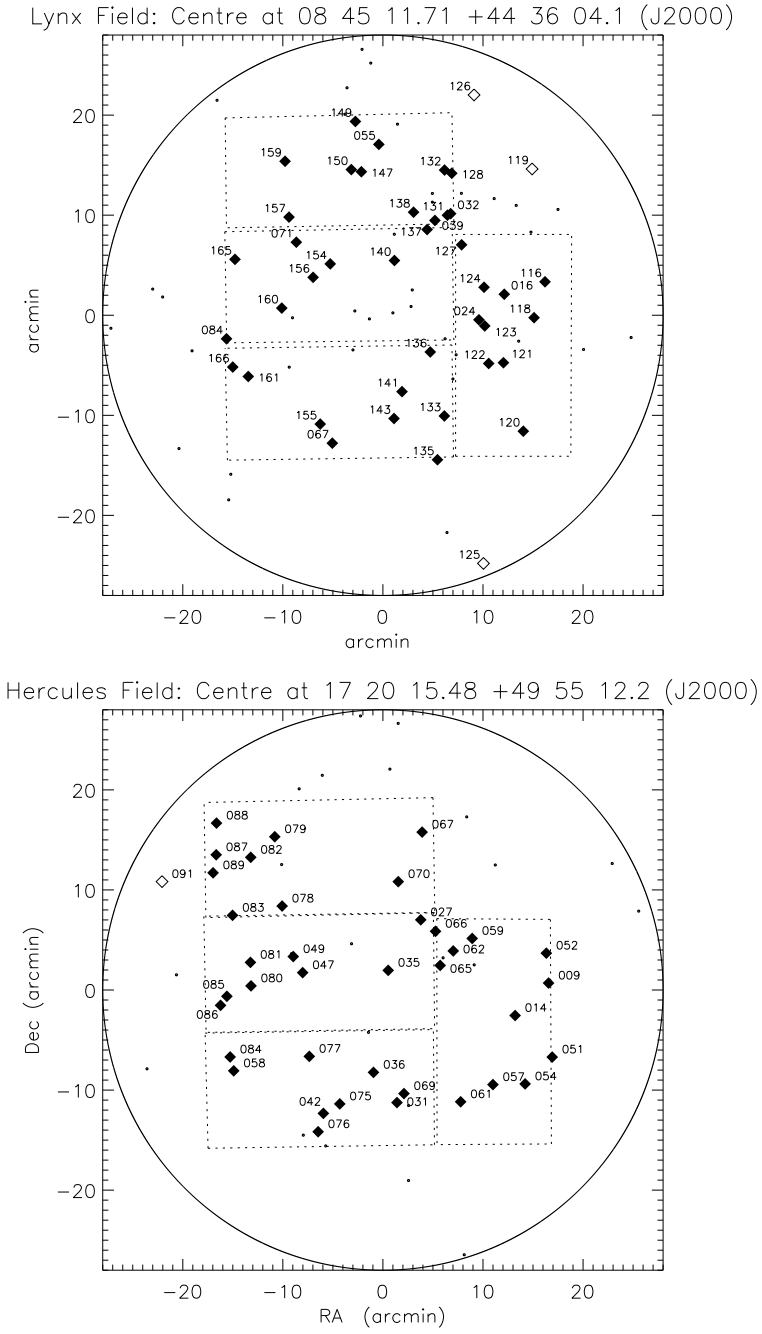

Figure 2.1: The distribution of the radio sources in the Lynx and Hercules fields; the labels correspond to the last 3 characters of the source names. The large circle in both plots represents the 0.464° radius of the previous WSRT observations of e.g. Windhorst et al. (1984); this is also approximately the 30′ primary beam of the VLA at 1.4 GHz. The dotted line represents the area of the sample (0.29 sq. degree for each field) which is defined by the field of view of the optical imaging. Dots indicate the positions of the additional sources which were not included in the sample because they either fell below the flux density limit of 0.5 mJy or they are not covered by the optical imaging. Open diamonds indicate sources not included in the complete sample but which were included in the infra–red observations.

The corrections for the incompleteness due to the resolution bias (the fact that a resolved source will be more difficult to detect than a point source of the same total flux) were found, by Windhorst et al. (1984), through detailed modelling of the source detection algorithms. It was subsequently found that sources with higher flux densities were also those with a large angular size which, as Windhorst, Mathis & Neuschaefer (1990) showed, meant that the original weights were overestimated. The revised equation for the weights due to the resolution bias, as calculated by Waddington et al. (2000) is

$$w_{res} = 1 + \frac{58}{HPBW}\, e^{-2.71\frac{S/N_{tot}}{5}} \tag{2.1}$$

where $HPBW = 12'$ is the half power beam width of the observations and $S/N_{\rm tot}$ is the total signal to noise of the sources. It is the values calculated using this revised method that are used here.

These two correction factors, the attenuation weight and resolution weight, were then multiplied together, $w_{\rm tot} = w_{\rm atten} \times w_{\rm res}$, to give the final weights. For further details of the source weighting methods used in the LBDS see Windhorst et al. (1984) and Waddington et al. (2000).

2.3 New radio observations

2.3.1 The observations

The VLA data were taken with the array in A configuration, on 22nd April 2002 for the Hercules field, and 15th February 2002 for the Lynx field. Both sets of observations were taken at a frequency of 1.4 GHz (L–band), in spectral line mode to enable wide field imaging, using 16 channels of width 781.25 kHz. The Intermediate Frequencies were centred on 1391.3 and 1471.1 MHz observing dual polarization. Both the Hercules and the Lynx fields were observed for 8.5 hours each.

The calibration of the data was carried out by Ignas Snellen, using the NRAO AIPS package (a full explanation of the techniques used to reduce wide–field radio imaging can be found in Chapter 5). For each of the Hercules and Lynx fields, 256 by 256 pixel facets (with $0.35''$ per pixel) were centred on all the sources that were already known from the imaging of Windhorst, Oort and collaborators, discussed above. These sub-fields were cleaned and self-calibrated using the AIPS tasks IMAGR and CALIB. The self calibration consisted of multiple phase–only cycles followed by one final amplitude and phase calibration. The resulting maps have a

resolution of 1.6″, and reach a noise limit of 15 μJy.

2.3.2 Source detection and flux density measurements

The Hercules sources of Oort & van Langevelde (1987) and Lynx sources of Oort & Windhorst (1985) were all detected in our VLA observations. This gives a sample of 81 sources, evenly spread over the two fields; the distribution on the sky can be seen in Figure 2.1. Flux densities were measured for these sources using the aips task *imfit* to fit a Gaussian, if they were pointlike, or the task *tvstat* to sum within a defined area, if they showed significant extension; the method used for each individual source is indicated in Tables 2.2 and 2.3. The values were then corrected for the attenuation of the VLA primary beam. It should be noted that for some objects, where previously one source was detected, these higher resolution observations have resolved it into more than one component each associated with a different host galaxy. In these cases, the sub–components are labelled *a*, *b*, etc. and the low resolution flux density has been assigned to each new component according to the A–array flux density ratio. These components are only retained in the sample if they remain above the 0.5 mJy flux density limit.

The positions of the detected sources are given in Tables 2.2 and 2.3 along with the measured flux densities and primary beam correction factors, $C_{\rm PB}$, (i.e. $S_{\rm Cor} = C_{\rm PB}\ S_{\rm Meas}$) used. The corresponding radio contour images can be found in Figures 2.2 and 2.3. The Oort et al. and A–array flux densities are brought together with the subsequent radio observations of the sample and discussed in Chapter 5. Consequently, a flux density comparison of the two radio datasets described here can be found in §5.5.

Name	RA/DEC (J2000)		$S_{\rm Oort}$ (mJy)	$S_{1.4\rm GHz}$ (mJy)	W	$C_{\rm PB}$	M
53w091	17 22 32.73	50 06 01.9	22.6 ± 1.1	37.93 ± 6.62	0.00	7.43	T
55w119	08 43 47.98	44 50 41.4	1.78 ± 0.16	1.78 ± 0.30	0.00	3.86	I
55w125	08 44 15.28	44 11 16.2	22.2 ± 1.20	12.15 ± 2.30	0.00	12.01	I
55w126	08 44 20.56	44 58 05.0	3.20 ± 0.24	4.19 ± 0.76	0.00	6.37	I

Table 2.1: The Hercules and Lynx field radio source A–array positions for sources which did not fall within the optical field but were included in the infra–red observations. They are given a weight, W, of 0.00 as they are not part of the complete sample. They are included here for completeness. For full details see text. An 'I' in the final, measurement, column indicates an *imfit* measured flux density; a 'T' indicates a *tvstat* measurement. A primary beam correction error of 20% of the difference between the corrected and un–corrected flux density has been incorporated into the quoted errors.

Hercules							
Name	RA/DEC (J2000)		$S_{\rm Oort}$ (mJy)	$S_{\rm 1.4GHz}$ (mJy)	W	$C_{\rm PB}$	M
53w052	17 18 34.14	49 58 53.0	8.00 ± 0.34	9.31 ± 1.17	1.00	2.26	I
53w054a	17 18 47.30	49 45 49.0	2.07 ± 0.19	2.14 ± 0.35	1.00	2.34	I
53w054b	17 18 49.97	49 46 12.2	2.08 ± 0.19	2.44 ± 0.32	1.00	2.20	I
53w057	17 19 07.29	49 45 44.8	1.96 ± 0.14	1.95 ± 0.21	1.00	1.82	I
53w059	17 19 20.18	50 00 21.2	19.40 ± 1.0	23.81 ± 1.21	1.00	1.34	T
53w061	17 19 27.34	49 44 01.9	4.76 ± 0.43	1.44 ± 0.18	1.02	1.69	I
53w062	17 19 31.93	49 59 06.2	0.73 ± 0.10	1.08 ± 0.07	1.42	1.19	I
53w065	17 19 40.05	49 57 39.2	5.54 ± 0.20	5.89 ± 0.14	1.00	1.11	I
53w066	17 19 42.96	50 01 03.9	4.27 ± 0.17	4.53 ± 0.15	1.00	1.18	I
53w067	17 19 51.27	50 10 58.7	21.9 ± 0.90	36.68 ± 3.97	1.00	2.15	T
53w069	17 20 02.52	49 44 51.0	3.82 ± 0.17	5.25 ± 0.31	1.00	1.36	T
53w070	17 20 06.07	50 06 01.7	2.56 ± 0.14	2.61 ± 0.17	1.00	1.39	I
53w075	17 20 42.37	49 43 49.1	96.8 ± 3.3	99.82 ± 6.83	1.00	1.51	I
53w076	17 20 55.82	49 41 02.2	1.94 ± 0.17	6.93 ± 0.92	1.00	2.21	T
53w077	17 21 01.32	49 48 34.0	6.51 ± 0.39	18.11 ± 1.01	1.00	1.31	T
53w078	17 21 18.17	50 03 35.2	0.74 ± 0.12	1.84 ± 0.20	1.40	1.62	T
53w079	17 21 22.75	50 10 31.0	11.7 ± 0.5	11.1 ± 1.68	1.00	2.87	I
53w080	17 21 37.48	49 55 36.8	25.9 ± 0.9	31.11 ± 2.42	1.00	1.63	T
53w081	17 21 37.86	49 57 57.6	12.1 ± 0.5	12.93 ± 1.08	1.00	1.68	I
53w082	17 21 37.64	50 08 27.4	2.50 ± 0.19	2.97 ± 0.47	1.00	2.86	I
53w083	17 21 48.95	50 02 39.7	5.01 ± 0.25	5.06 ± 0.64	1.00	2.28	I
53w084	17 21 50.43	49 48 30.5	0.68 ± 0.12	1.01 ± 0.19	1.51	2.53	I
53w085	17 21 52.48	49 54 34.1	4.52 ± 0.22	4.94 ± 0.66	1.00	2.02	I
53w086a	17 21 56.42	49 53 39.8	1.62 ± 0.30	4.06 ± 0.54	1.09	2.17	T
53w086b	17 21 57.65	49 53 33.8	2.44 ± 0.30	6.13 ± 0.74	1.00	2.22	T
53w087	17 21 59.10	50 08 42.9	5.58 ± 0.35	14.35 ± 2.23	1.00	4.23	T
53w088	17 21 58.90	50 11 52.7	14.1 ± 0.7	14.52 ± 2.92	1.00	6.07	I
53w089	17 22 01.05	50 06 54.7	3.04 ± 0.26	3.58 ± 0.62	1.00	3.71	T
66w009a	17 18 32.76	49 55 53.4	1.14 ± 0.21	1.50 ± 0.22	1.23	2.22	I
66w009b	17 18 33.73	49 56 03.2	0.70 ± 0.21	0.91 ± 0.16	5.69	2.19	I
66w014	17 18 53.51	49 52 39.1	3.34 ± 0.51	0.60 ± 0.09	1.18	1.66	I
66w027	17 19 52.11	50 02 12.7	0.57 ± 0.11	0.67 ± 0.13	3.75	1.19	I
66w031	17 20 06.87	49 43 57.0	0.76 ± 0.14	0.97 ± 0.12	2.32	1.43	I
66w035	17 20 12.32	49 57 09.7	0.63 ± 0.09	0.71 ± 0.06	1.77	1.01	I
66w036	17 20 21.46	49 46 58.3	0.78 ± 0.11	3.70 ± 0.29	1.57	1.20	T
66w042	17 20 52.59	49 42 52.4	0.78 ± 0.14	1.99 ± 0.26	1.61	1.70	T
66w047	17 21 05.43	49 56 56.0	0.60 ± 0.10	1.16 ± 0.10	2.32	1.20	T
66w049	17 21 11.25	49 58 32.4	1.38 ± 0.27	2.17 ± 0.22	3.09	1.28	I
66w058	17 21 48.23	49 47 07.3	1.89 ± 0.16	1.72 ± 0.24	1.01	2.33	I

Table 2.2: The Hercules radio source positions from the VLA A–array observations along with the A–array and Oort et al. (1987) 1.4 GHz primary beam corrected flux densities, source weights, W, and primary beam correction factor, $C_{\rm PB}$ (see text for full details). An 'I' in the final measurement column indicates an *imfit* measured flux density; a 'T' indicates a *tvstat* measurement. A primary beam correction error of 20% of the difference between the corrected and un–corrected flux density has been incorporated into the quoted errors.

Lynx Name	RA/DEC (J2000)		$S_{\rm Oort}$ (mJy)	$S_{\rm 1.4GHz}$ (mJy)	W	$C_{\rm PB}$	M
55w116	08 43 40.72	44 39 24.7	1.36 ± 0.12	1.52 ± 0.25	1.00	2.22	I
55w118	08 43 46.86	44 35 49.7	0.91 ± 0.09	0.74 ± 0.11	1.03	1.92	I
55w120	08 43 52.89	44 24 29.0	1.83 ± 0.16	1.67 ± 0.29	1.00	2.68	I
55w121	08 44 04.06	44 31 19.4	1.21 ± 0.09	1.04 ± 0.11	1.00	1.60	I
55w122	08 44 12.33	44 31 14.9	0.56 ± 0.08	0.66 ± 0.12	1.27	1.45	I
55w123	08 44 14.54	44 35 00.2	2.01 ± 0.10	1.17 ± 0.08	1.00	1.33	I
55w124	08 44 14.93	44 38 52.2	4.67 ± 0.17	2.79 ± 0.16	1.00	1.35	I
55w127	08 44 27.55	44 43 07.4	1.81 ± 0.10	1.64 ± 0.11	1.00	1.36	I
55w128	08 44 33.05	44 50 15.3	3.34 ± 0.18	4.77 ± 0.54	1.00	2.05	T
55w131	08 44 35.51	44 46 04.1	1.01 ± 0.10	0.74 ± 0.11	1.01	1.48	T
55w132	08 44 37.12	44 50 34.7	1.10 ± 0.11	1.66 ± 0.23	1.01	2.05	T
55w133	08 44 37.24	44 26 00.4	2.20 ± 0.11	2.25 ± 0.16	1.00	1.47	I
55w135	08 44 41.10	44 21 37.7	2.60 ± 0.14	3.86 ± 0.44	1.00	1.98	T
55w136	08 44 45.14	44 32 23.9	1.02 ± 0.07	0.92 ± 0.08	1.00	1.10	T
55w137	08 44 46.90	44 44 37.9	1.60 ± 0.09	1.66 ± 0.11	1.00	1.29	T
55w138	08 44 54.51	44 46 22.0	1.82 ± 0.10	1.99 ± 0.15	1.00	1.37	I
55w140	08 45 06.06	44 40 41.2	0.79 ± 0.08	0.55 ± 0.06	1.25	1.06	I
55w141	08 45 03.29	44 28 15.1	0.87 ± 0.07	0.43 ± 0.06	1.01	1.19	I
55w143a	08 45 05.49	44 25 45.0	2.41 ± 0.11	2.19 ± 0.13	1.00	1.34	I
55w143b	08 45 04.25	44 25 53.3	0.57 ± 0.09	0.33 ± 0.06	1.58	1.33	I
55w147	08 45 23.83	44 50 24.6	1.72 ± 0.11	1.97 ± 0.19	1.00	1.82	I
55w149	08 45 27.17	44 55 25.9	7.10 ± 0.32	7.82 ± 1.11	1.00	3.20	T
55w150	08 45 29.47	44 50 37.4	0.95 ± 0.10	0.63 ± 0.10	1.02	1.88	I
55w154	08 45 41.30	44 40 11.9	12.1 ± 0.40	13.71 ± 0.40	1.00	1.13	T
55w155	08 45 46.89	44 25 11.6	1.83 ± 0.10	1.70 ± 0.14	1.00	1.55	I
55w156	08 45 50.92	44 39 51.5	4.14 ± 0.16	4.78 ± 0.21	1.00	1.19	T
55w157	08 46 04.44	44 45 52.7	1.37 ± 0.10	1.24 ± 0.12	1.00	1.68	I
55w159a	08 46 06.67	44 51 27.5	6.70 ± 0.29	6.49 ± 0.82	1.00	2.69	I
55w159b	08 46 06.82	44 50 54.1	0.75 ± 0.13	1.00 ± 0.19	1.00	2.55	T
55w160	08 46 08.50	44 36 47.1	0.94 ± 0.08	0.81 ± 0.07	1.01	1.32	I
55w161	08 46 27.32	44 29 56.9	1.34 ± 0.14	1.25 ± 0.15	1.02	1.87	I
55w165a	08 46 34.76	44 41 39.2	18.12 ± 0.54	18.88 ± 1.54	1.00	2.06	T
55w165b	08 46 33.37	44 41 24.4	0.78 ± 0.40	0.92 ± 0.14	1.47	1.99	I
55w166	08 46 36.02	44 30 53.5	2.46 ± 0.14	2.31 ± 0.26	1.00	2.07	I
60w016	08 44 03.58	44 38 10.2	0.62 ± 0.08	0.88 ± 0.13	1.14	1.52	I
60w024	08 44 17.83	44 35 36.9	0.51 ± 0.09	0.37 ± 0.05	2.06	1.29	I
60w032	08 44 33.69	44 46 13.0	0.54 ± 0.09	0.46 ± 0.08	1.58	1.51	I
60w039	08 44 42.50	44 45 32.5	0.65 ± 0.09	0.72 ± 0.16	1.26	1.38	I
60w055	08 45 14.00	44 53 08.7	0.51 ± 0.08	0.62 ± 0.13	1.42	2.34	I
60w067	08 45 40.47	44 23 20.1	0.56 ± 0.09	0.69 ± 0.15	1.31	1.70	T
60w071	08 46 00.34	44 43 22.1	0.50 ± 0.08	0.60 ± 0.07	1.44	1.42	I
60w084	08 46 39.86	44 33 44.5	0.85 ± 0.17	1.80 ± 0.37	1.38	2.08	T

Table 2.3: The Lynx radio source positions from the VLA A–array observations along with the A–array and Oort et al. (1985) 1.4 GHz primary beam corrected flux densities, source weights, W, and primary beam correction factor, $C_{\rm PB}$ (see text for full details). An 'I' in the final, measurement, column indicates an *imfit* measured flux density; a 'T' indicates a *tvstat* measurement. A primary beam correction error of 20% of the difference between the corrected and un–corrected flux density has been incorporated into the quoted errors.

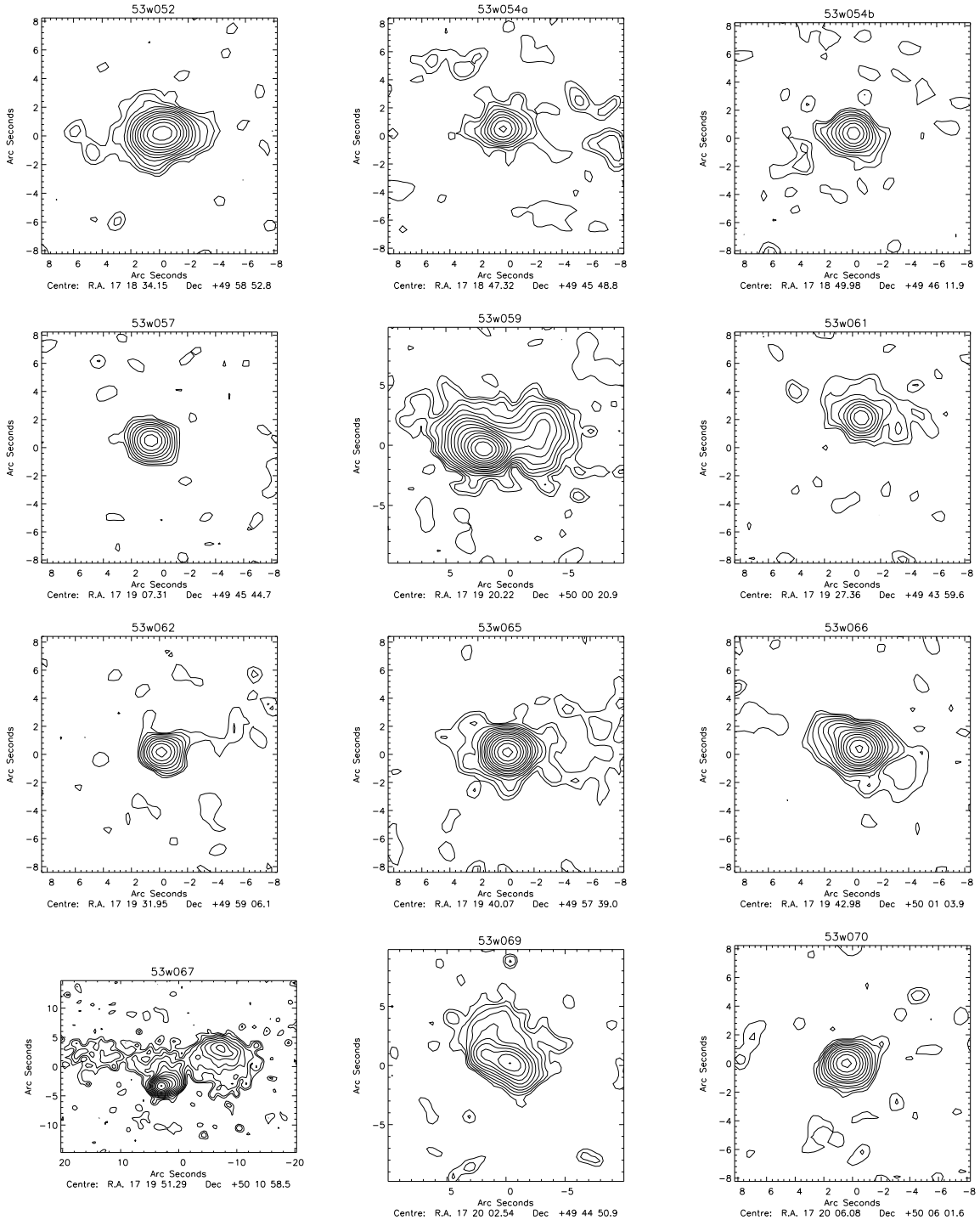

Figure 2.2: The radio contour images, for the Hercules field, from the VLA 1.4GHz A–array observations. The beam size is $1.5'' \times 1.5''$. Contours start at 24μJy/beam and are separated by factors of $\sqrt{2}$. The images are centred on the optical host galaxy positions from Chapter 3 if available.

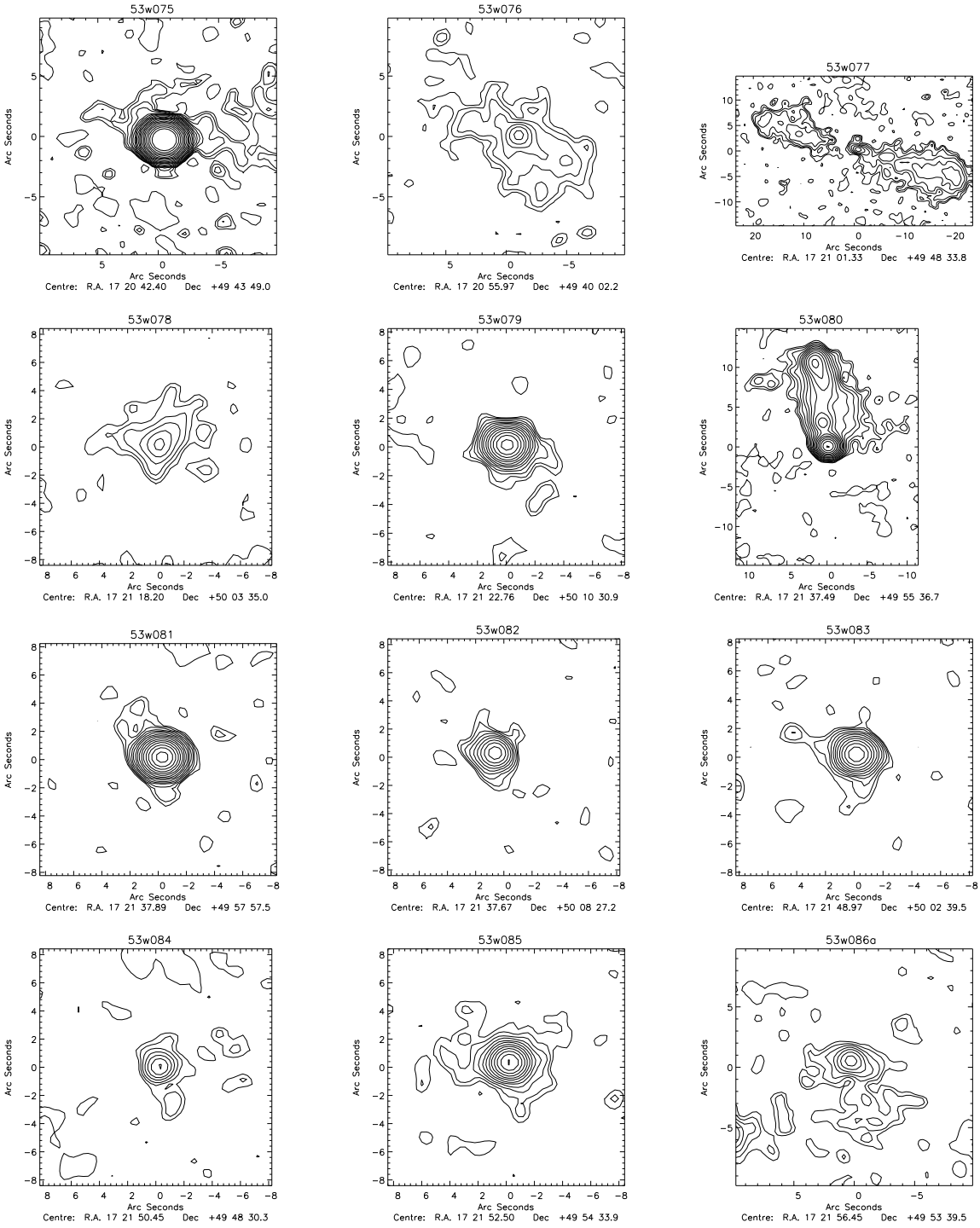
53w075
Arc Seconds
Centre: R.A. 17 20 42.40 Dec +49 43 49.0
53w076
Arc Seconds
Centre: R.A. 17 20 55.97 Dec +49 40 02.2
53w077
Arc Seconds
Centre: R.A. 17 21 01.33 Dec +49 48 33.8
53w078
Arc Seconds
Centre: R.A. 17 21 18.20 Dec +50 03 35.0
53w079
Arc Seconds
Centre: R.A. 17 21 22.76 Dec +50 10 30.9
53w080
Arc Seconds
Centre: R.A. 17 21 37.49 Dec +49 55 36.7
53w081
Arc Seconds
Centre: R.A. 17 21 37.89 Dec +49 57 57.5
53w082
Arc Seconds
Centre: R.A. 17 21 37.67 Dec +50 08 27.2
53w083
Arc Seconds
Centre: R.A. 17 21 48.97 Dec +50 02 39.5
53w084
Arc Seconds
Centre: R.A. 17 21 50.45 Dec +49 48 30.3
53w085
Arc Seconds
Centre: R.A. 17 21 52.50 Dec +49 54 33.9
53w086a
Arc Seconds
Centre: R.A. 17 21 56.45 Dec +49 53 39.5

Figure 2.2

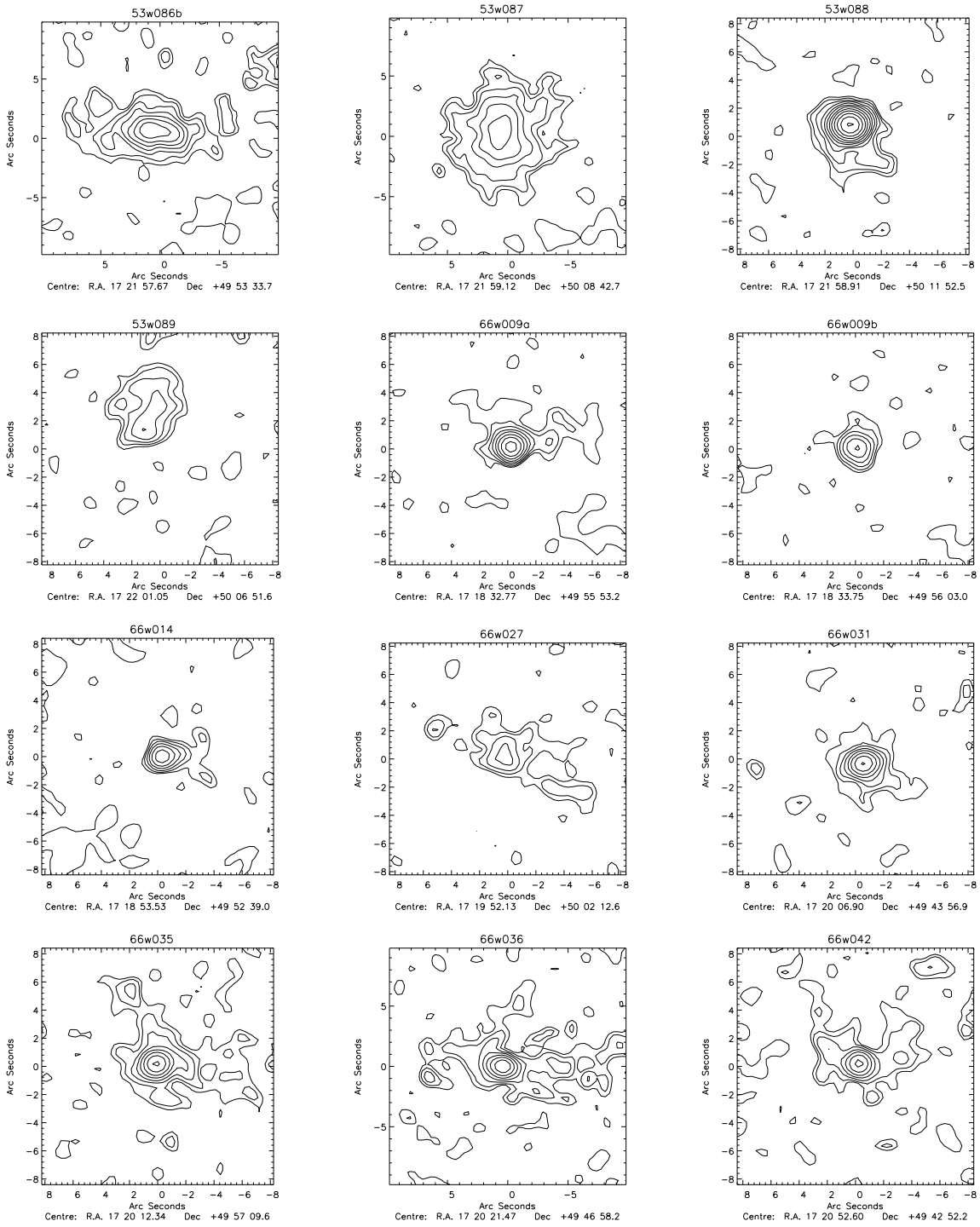
53w086b
Arc Seconds
Centre: R.A. 17 21 57.67 Dec +49 53 33.7
53w087
Arc Seconds
Centre: R.A. 17 21 59.12 Dec +50 08 42.7
53w088
Arc Seconds
Centre: R.A. 17 21 58.91 Dec +50 11 52.5
53w089
Arc Seconds
Centre: R.A. 17 22 01.05 Dec +50 06 51.6
66w009a
Arc Seconds
Centre: R.A. 17 18 32.77 Dec +49 55 53.2
66w009b
Arc Seconds
Centre: R.A. 17 18 33.75 Dec +49 56 03.0
66w014
Arc Seconds
Centre: R.A. 17 18 53.53 Dec +49 52 39.0
66w027
Arc Seconds
Centre: R.A. 17 19 52.13 Dec +50 02 12.6
66w031
Arc Seconds
Centre: R.A. 17 20 06.90 Dec +49 43 56.9
66w035
Arc Seconds
Centre: R.A. 17 20 12.34 Dec +49 57 09.6
66w036
Arc Seconds
Centre: R.A. 17 20 21.47 Dec +49 46 58.2
66w042
Arc Seconds
Centre: R.A. 17 20 52.60 Dec +49 42 52.2

Figure 2.2

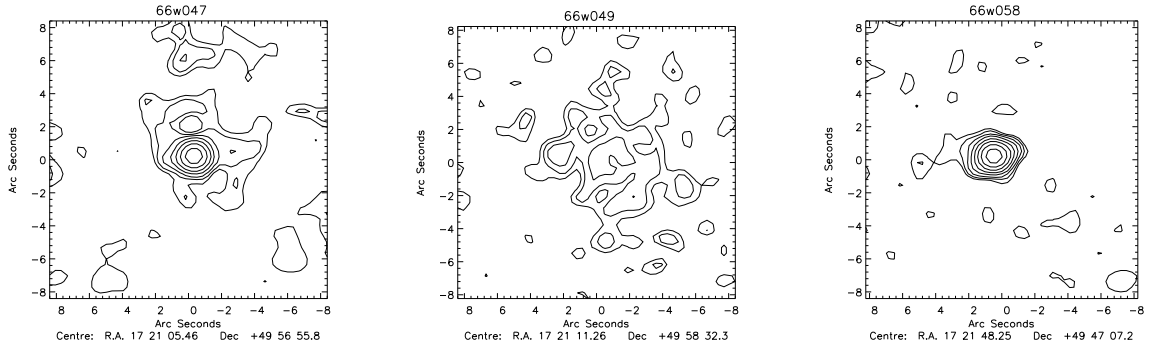
66w047
Arc Seconds
Arc Seconds
Centre: R.A. 17 21 05.46 Dec +49 56 55.8
66w049
Arc Seconds
Arc Seconds
Centre: R.A. 17 21 11.26 Dec +49 58 32.3
66w058
Arc Seconds
Arc Seconds
Centre: R.A. 17 21 48.25 Dec +49 47 07.2

Figure 2.2

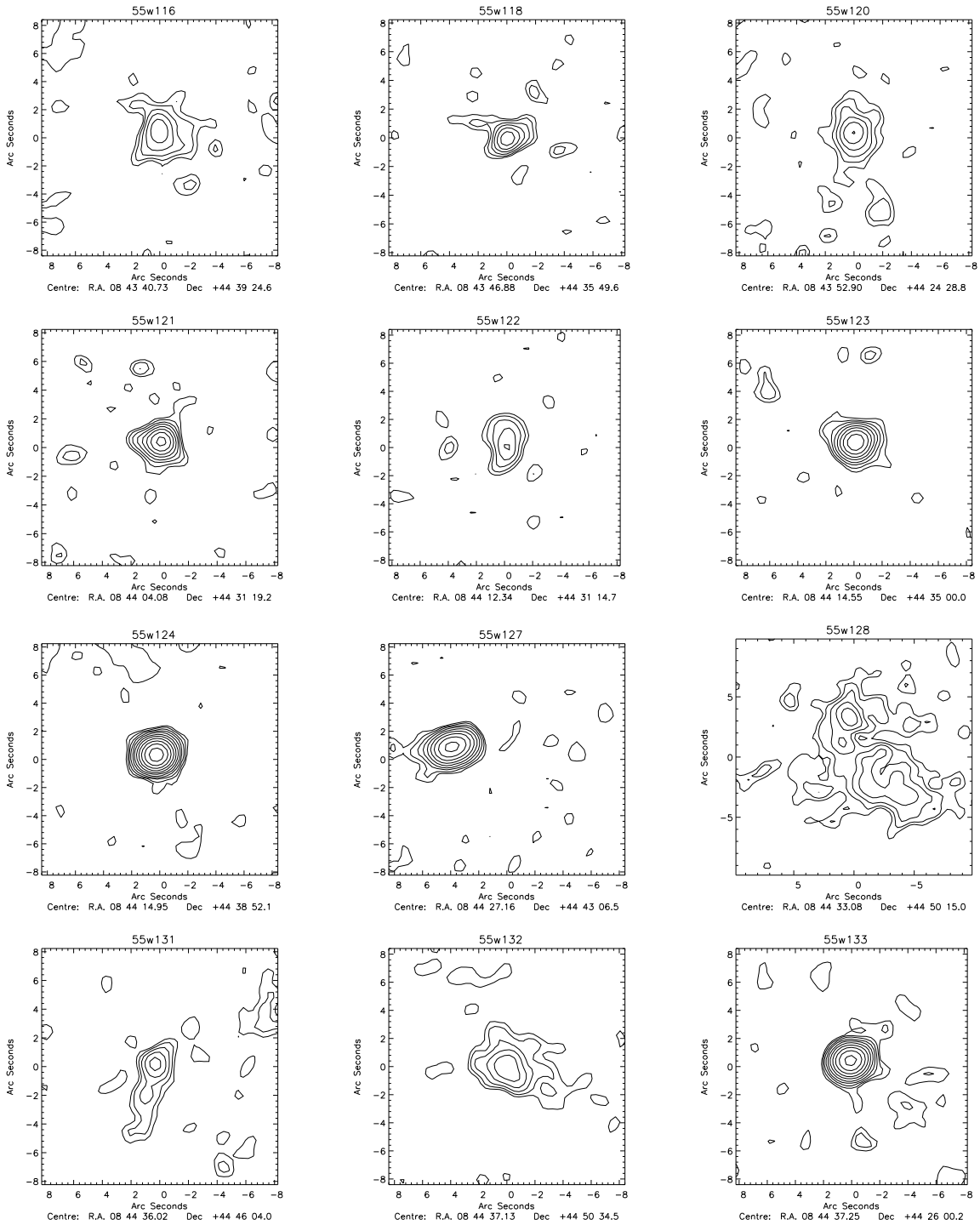

Figure 2.3: The radio contour images, for the Lynx field, from the VLA 1.4 Ghz A–array observations. The beam size is $1.5'' \times 1.5''$. Contours start at 24μJy/beam and are separated by factors of $\sqrt{2}$. The images are centred on the optical host galaxy positions from Chapter 3 if available.

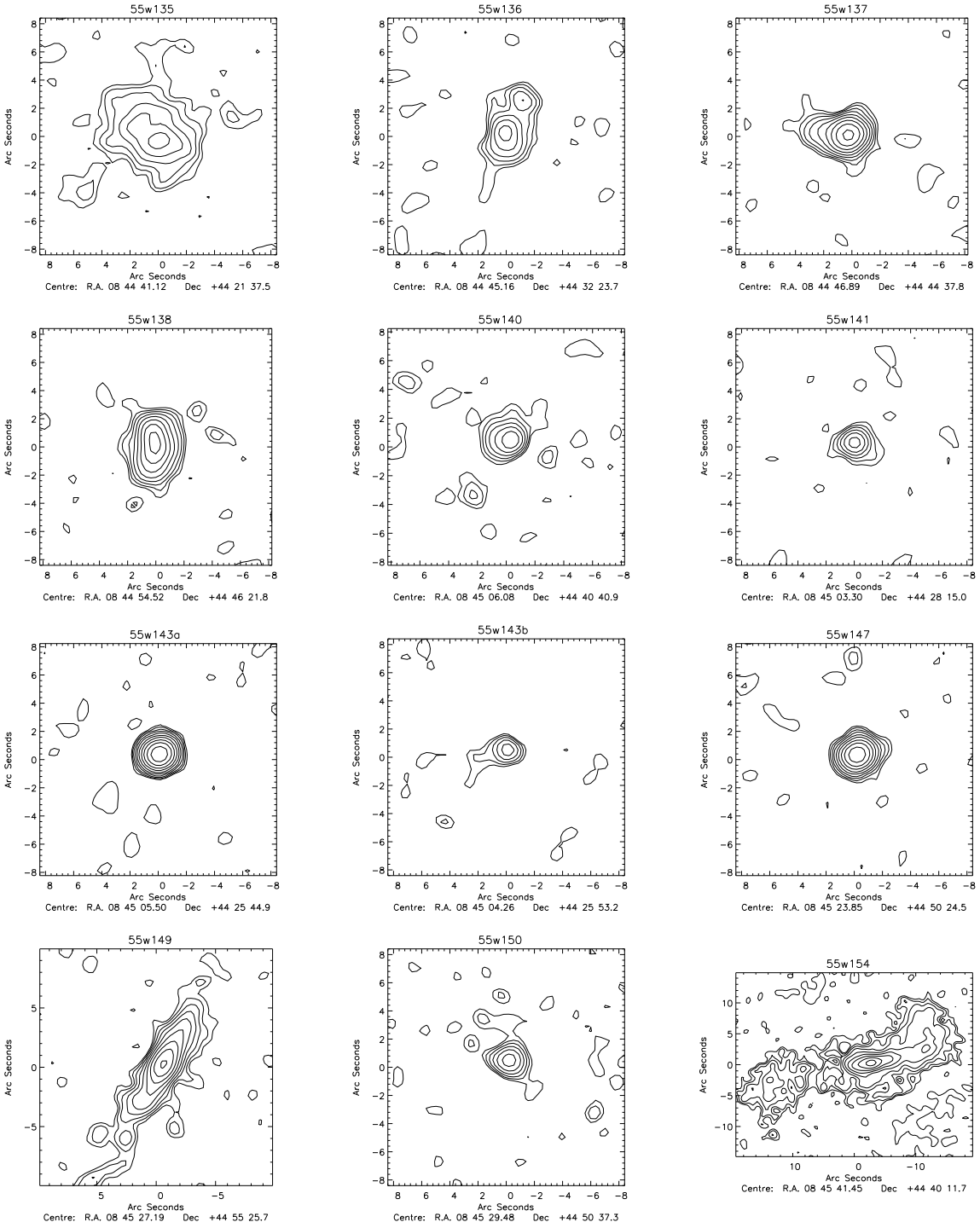
55w135
Arc Seconds
Arc Seconds
Centre: R.A. 08 44 41.12 Dec +44 21 37.5
55w136
Arc Seconds
Arc Seconds
Centre: R.A. 08 44 45.16 Dec +44 32 23.7
55w137
Arc Seconds
Arc Seconds
Centre: R.A. 08 44 46.89 Dec +44 44 37.8
55w138
Arc Seconds
Arc Seconds
Centre: R.A. 08 44 54.52 Dec +44 46 21.8
55w140
Arc Seconds
Arc Seconds
Centre: R.A. 08 45 06.08 Dec +44 40 40.9
55w141
Arc Seconds
Arc Seconds
Centre: R.A. 08 45 03.30 Dec +44 28 15.0
55w143a
Arc Seconds
Arc Seconds
Centre: R.A. 08 45 05.50 Dec +44 25 44.9
55w143b
Arc Seconds
Arc Seconds
Centre: R.A. 08 45 04.26 Dec +44 25 53.2
55w147
Arc Seconds
Arc Seconds
Centre: R.A. 08 45 23.85 Dec +44 50 24.5
55w149
Arc Seconds
Arc Seconds
Centre: R.A. 08 45 27.19 Dec +44 55 25.7
55w150
Arc Seconds
Arc Seconds
Centre: R.A. 08 45 29.48 Dec +44 50 37.3
55w154
Arc Seconds
Arc Seconds
Centre: R.A. 08 45 41.45 Dec +44 40 11.7

Figure 2.3

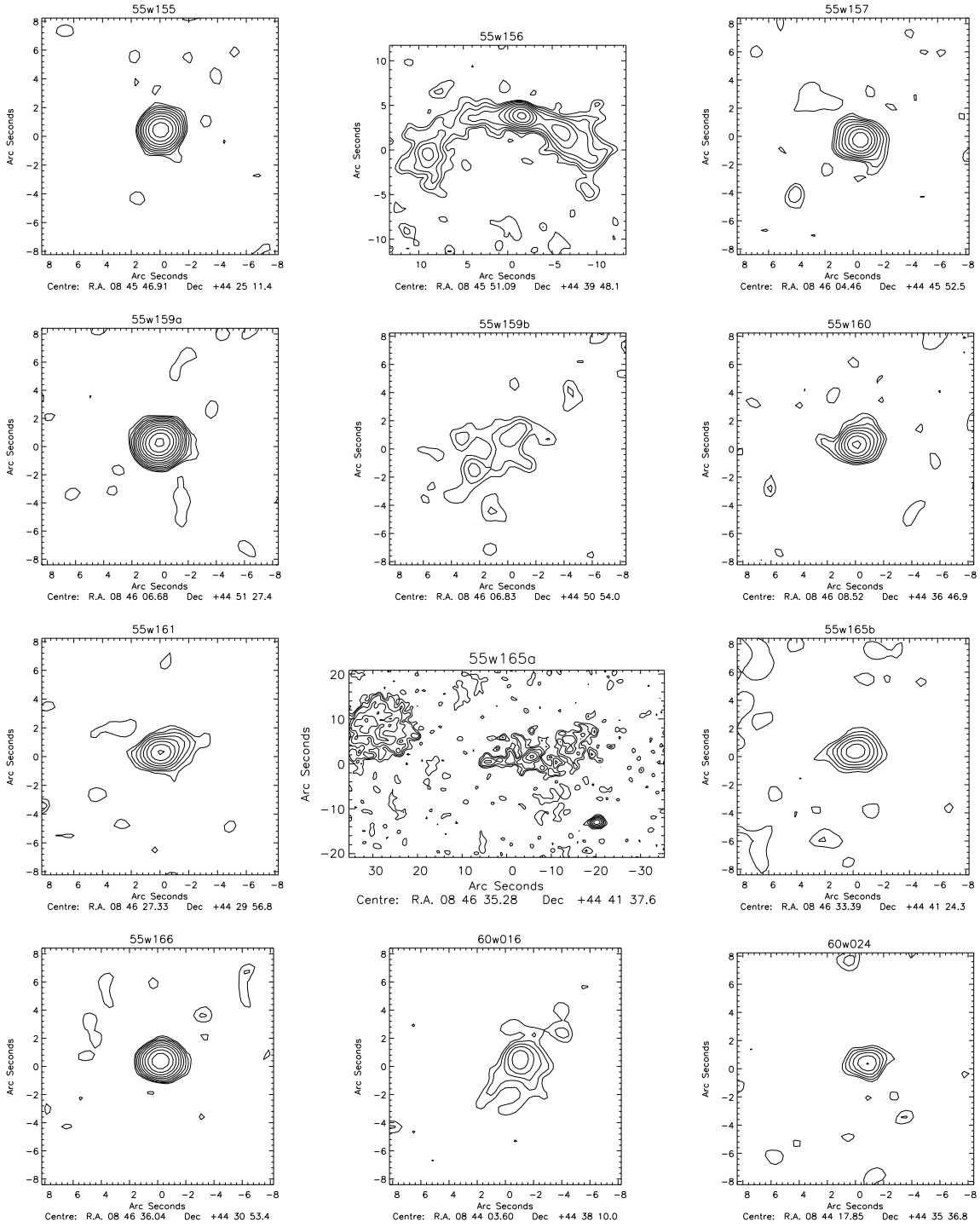
55w155
Arc Seconds
Arc Seconds
Centre: R.A. 08 45 46.91 Dec +44 25 11.4
55w156
Arc Seconds
Arc Seconds
Centre: R.A. 08 45 51.09 Dec +44 39 48.1
55w157
Arc Seconds
Arc Seconds
Centre: R.A. 08 46 04.46 Dec +44 45 52.5
55w159a
Arc Seconds
Arc Seconds
Centre: R.A. 08 46 06.68 Dec +44 51 27.4
55w159b
Arc Seconds
Arc Seconds
Centre: R.A. 08 46 06.83 Dec +44 50 54.0
55w160
Arc Seconds
Arc Seconds
Centre: R.A. 08 46 08.52 Dec +44 36 46.9
55w161
Arc Seconds
Arc Seconds
Centre: R.A. 08 46 27.33 Dec +44 29 56.8
55w165a
Arc Seconds
Arc Seconds
Centre: R.A. 08 46 35.28 Dec +44 41 37.6
55w165b
Arc Seconds
Arc Seconds
Centre: R.A. 08 46 33.39 Dec +44 41 24.3
55w166
Arc Seconds
Arc Seconds
Centre: R.A. 08 46 36.04 Dec +44 30 53.4
60w016
Arc Seconds
Arc Seconds
Centre: R.A. 08 44 03.60 Dec +44 38 10.0
60w024
Arc Seconds
Arc Seconds
Centre: R.A. 08 44 17.85 Dec +44 35 36.8

Figure 2.3

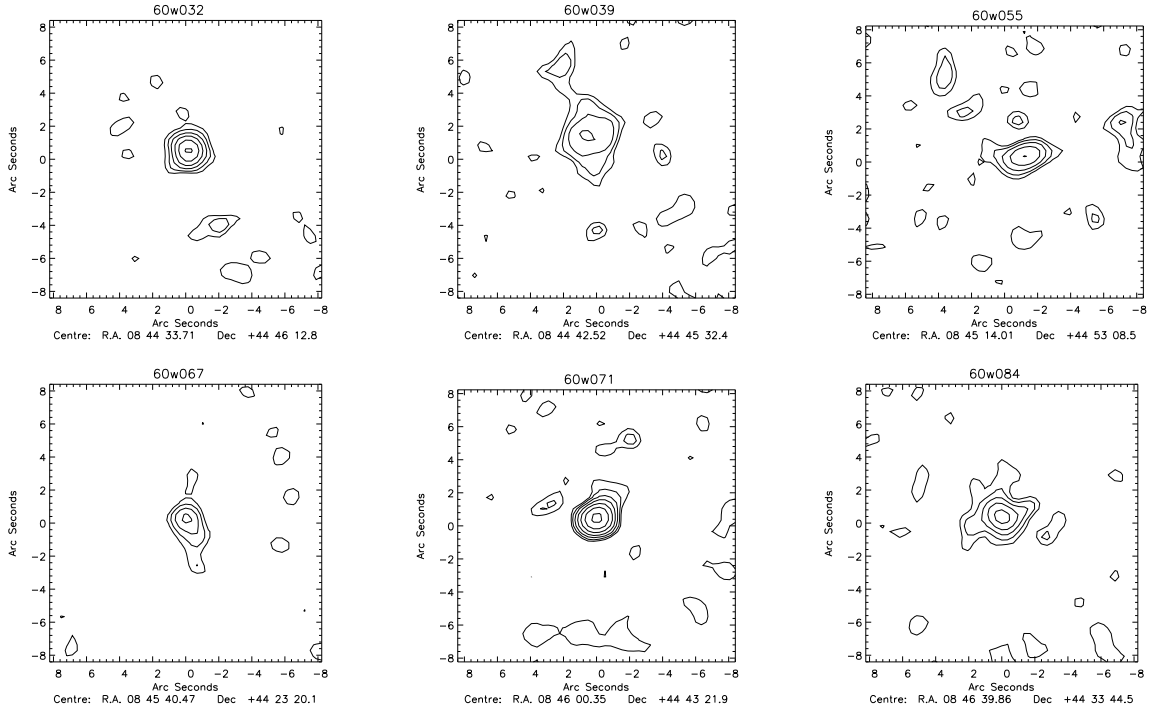

Figure 2.3

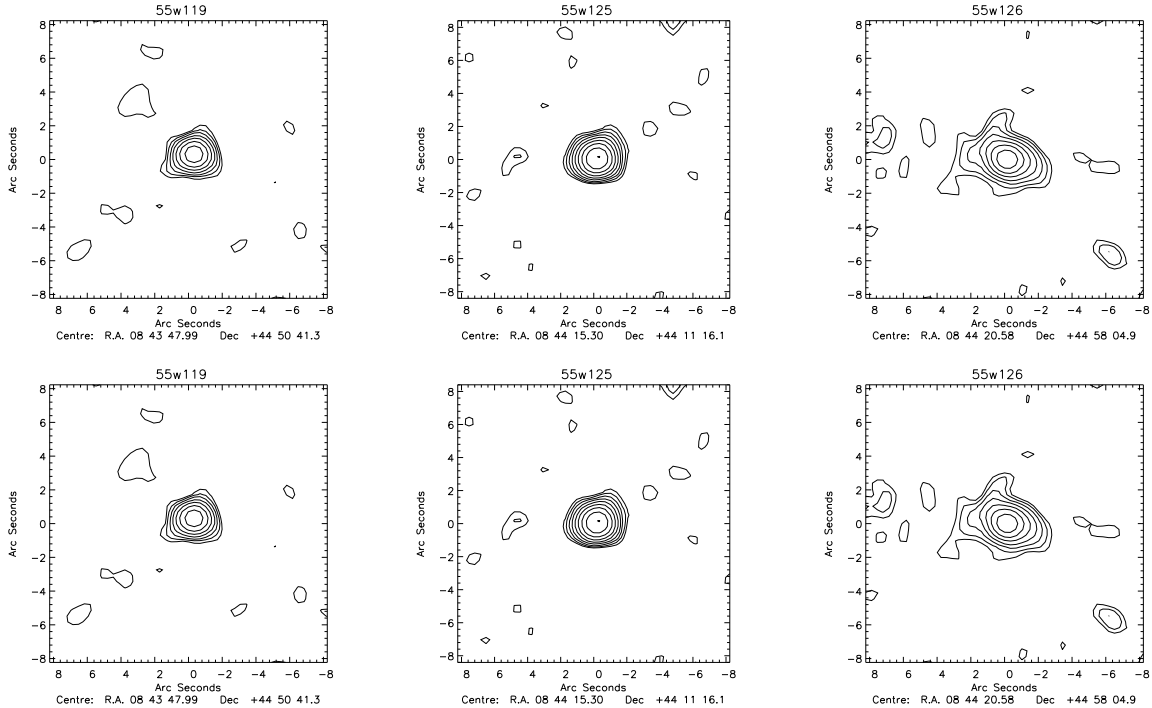

Figure 2.4: The radio contour images, for the sources not included in the complete sample, from the VLA 1.4GHz A–array observations. The beam size is $1.5'' \times 1.5''$. Contours start at 24μJy/beam and are separated by factors of $\sqrt{2}$. The images are centred on the optical host galaxy positions from Chapter 3 if available.

2.4 Chapter summary

In this Chapter the radio sample, which forms the basis of this thesis, was defined. It consists of 81 radio sources, above the limiting flux density of $S_{1.4\mathrm{GHz}} > 0.5$ mJy, located over two fields in the constellations of Lynx and Hercules and, with the application of the individually calculated source weights, is complete. The total area covered by the sample is 0.58 sq. degrees (0.29 sq. degrees per field).

CHAPTER 3

Imaging: Optical and IR

3.1 Introduction

The FRI space density calculation depends on successful measurements of the redshifts of the radio galaxies in the survey. To obtain these spectroscopically would have been very time consuming, so the original aim was to obtain 5–band optical photometry of the two fields; this would then provide photometric redshifts for all the sources. These would then be supplemented with some additional spectroscopic redshifts for the best candidates (Chapter 4). However, the optical observations, carried out using the Wide Field Camera (WFC) on the 2.5m Isaac Newton Telescope (INT) in La Palma, were partly weathered out and only two photometric bands could be used. To improve the photometric information and identification fraction, further observations of a subsample of sources were made using the UKIRT Fast Track Imager (UFTI) on UKIRT, the 3.8m UK Infra–red Telescope located in Hawaii. The sections below outline the data reduction processes and results from the WFC and UFTI observations.

3.2 INT observations and data reduction

The WFC consists of 4 thinned EEV 2kx4k CCDs with a pixel size of 13.5μm, resulting in a scale of $0.33\ ''$/pixel and a combined field of view of $\sim$34x34 arcmin^2. This large field of

view made the WFC an ideal instrument for observing the two fields which are of comparable size (as shown previously in Figure 2.1). For later use, a detector is defined as one of the four WFC CCDs that together are used to make one exposure. The layout of the 4 CCDs is shown in Figure 3.1 for reference.

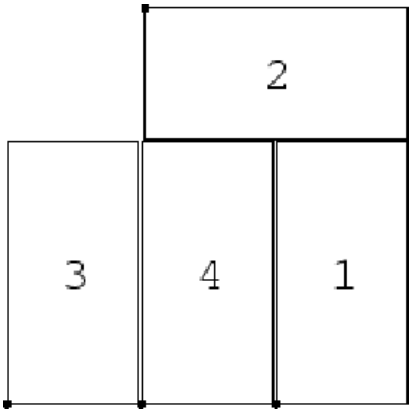

Figure 3.1: The schematic CCD layout in the WFC.(Taylor, 2000)

The WFC observations were split over two separate runs in April 2003 and April 2004. Unfortunately these were both largely weathered out so observations through two filters only were obtained - sloan *r* and *i*. The telescope was offset by 30″ after every third 300s or 600s exposure to avoid saturation of the CCD and ensure that the whole of each field was covered; there were 5 different telescope pointings in total. Full details of the observations can be found in Table 3.1.

Field	Band	Observation Date	Exposure Time	Photometric?	Seeing (″)
Hercules	r	07/04/03	24x300s	No	2.5
	i	”	10x300s	No	1.9
	r	15/04/04	15x600s	Yes	1.5
	i	”	15x300s	Yes	1.5
Lynx	i	07/04/03	9x300s	No	2.1
	r	15/04/04	6x300s	Yes	1.5
	i	06/01/05	1x300s	Yes	3.0

Table 3.1: Summary of INT observations

The April 2003 run took data on one night only; the 7th. Conditions were non–photometric, so these data have only been used to determine optical identifications for the radio objects. For the April 2004 run, observations were only taken on the 15th and 17th. On the 15th standard star fields were observed throughout the night and this is also when the bulk of the imaging was done; the night was photometric. Three Lynx observations were taken on the 17th, but they were non-photometric with significantly worse seeing than those taken on the 15th. They have

therefore been excluded and are not included in Table 3.1.

One further observation of the Lynx field of 300s in *i* was kindly obtained by Rachel Dowsett and Philip Best on 6th January 2005. This was needed because of the lack of photometric *i*–band data in the Lynx field. The night was photometric but the seeing was very poor ($\sim 3''$). Standard star fields were again observed throughout the night. This image was only used to photometrically calibrate the Lynx field; the identifications were done with the previous *r* and *i*–band images.

All the images were processed using the IRAF software package. Bias frames, taken at the beginning of each night, were averaged together to make a master–bias for each detector which was then subtracted from the remaining data. A flat–field was made for the four detectors, in each field and filter, by median combining the separate science frames and rejecting pixels according to the readnoise and gain of the CCD. Next the individual science frames were divided by the corresponding sky–flat, which had been normalised using its pixel mean. The only deviation from this method was the *r*–band images of 15th April. For these, twilight–flats from the morning and evening were available. These were also median–combined and normalised and then the science frames were divided in the same way. The twilight flats were also edited, using the IRAF task *imedit*, to remove a small number of stars that remained after combining.

The *i*–band detectors were also affected by fringing. These fringes occur when light from night sky emission lines is partially reflected within the CCD and subsequently interferes with the incoming radiation, resulting in a thin–film interference pattern in the image. The *r*–band images are not contaminated in this way because the night sky lines are more numerous at *i*–band wavelengths. In general, subtraction of a fringe map is needed to correct for this but, since the fringing was not dominant, division by the sky–flat was sufficient.

The final step in the reduction is to combine the individual science frames for each filter and field. Since the observations were offset with a minimum of 3 different telescope pointings the frames were registered using $\sim$10 stars and shifted. They were then median combined and clipped using the CCD noise properties as before. The offsets were sufficiently small that it was not necessary to account for distortions in this process.

3.2.1 INT astrometry

The simplest method of astrometrical calibration for the INT observations uses a database image of the two fields from the Digitized Sky Survey (DSS). The objects in the DSS image

are then identified with their counterparts in the original images and, using the starlink image–manipulation package *gaia*, a co–ordinate system can then be established by fitting pixel size, x and y position, and plate rotation. To improve the accuracy of the fit the calibration is then 'tweaked' (i.e. only RA and DEC varied) using the positions of objects in the USNO (United States Naval Observatory) B1.0 catalogue (Monet et al., 2003); these objects are less common but their astrometry is in the International Celestial Reference Frame (ICRF). Unfortunately this method proved unsuccessful for the INT observations; residual offsets between object positions remained after calibration (Figure 3.2).

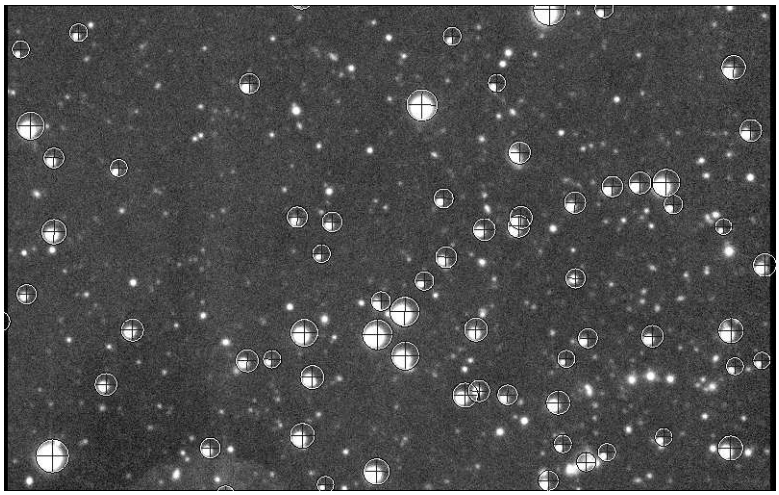

Figure 3.2: A slice through an *r*–band, CCD1, image in the Hercules field showing the offset between the USNO star positions (circles) and the objects in the field.

This offset was caused by the distortion of the WFC across its 4 CCDs. This distortion can be modelled as

$$r' = r(1 + Dr^2), \tag{3.1}$$

(Taylor, 2000), where D is the distortion co–efficient, r is the measured distance and r' is the idealised angular distance from the optical axis. D is given as 220.0 rad^{-2} by Irwin (2002), however, as described below, the best value for each CCD was determined individually here.

To correct for this distortion the starlink package *astrom* was used. *astrom* takes an input list of x and y positions, their corresponding α and δ co–ordinates and an approximate value for the distortion co–efficient, D, and uses this information to carry out a nine–parameter fit; this consists of 6 parameters to determine the co–ordinate transforms, 2 parameters to determine the image centre and 1 parameter to determine the distortion co–efficient. It then outputs a FITS[1] header containing the astrometric solution. It can also calculate x and y positions corre-

[1]Flexible Image Transport System – the normal format for the image files

sponding to a set of WCS co–ordinates.

The x and y positions of a large number of objects in the two fields were obtained using the Object Detection function in *gaia*. These were then associated with the positions of the USNO objects using an IDL script which searched the two lists until a match was obtained. Occasionally a USNO position would be mistakenly aligned with more than one field object; therefore the list was checked by hand to remove these duplicates. The original FITS header for the images was then updated with the astrometric solution. The aim of this process was to achieve average rms offsets of $< 1.00''$ across the four CCDs and over the two fields. The most inaccurate area of calibration was at and near the outer edges of CCDs 1 to 4 where the distortion was originally greatest.

The resulting errors in the astrometry for the April 2003 observations were $0.90''$ for Hercules and $1.22''$ for Lynx. The slightly higher Lynx result was due to the comparative shallowness of the data. For the April 2004 observations astrometric calibration was only applied to the *r*–band data as it was felt that no further radio host–galaxy identifications would be obtained from considering the significantly shallower *i*–band data also. However, the *i*–band images were tweaked locally to each *r*–band detection to ensure that the images lined up. The calculated errors were $\sim 0.3''$ for all CCDs in both fields; the improvements resulted from including the reference star proper motions along with allowing *astrom* more freedom in its fit.

astrom can also use the calculated astrometric solution, along with a list of RA and DEC co–ordinates, to output their corresponding x and y positions in the field. This was done for the VLA radio positions, and the resulting x and y values were used to extract a sub–image square centred on each object for later overlay purposes.

3.3 UKIRT observations and data reduction

In contrast, UFTI consists of one 1024x1024 HgCdTe array with a plate scale of $0.091''$/pixel. This results in a field of view of $92''$ which is significantly smaller than that of the WFC. This meant that it could only be used to obtain images of, mainly, individual sources rather than the complete–field observations done with the INT.

The UFTI observations were done in a combination of service and visitor mode, spread over the period July 2004 to January 2005. All the observations were done using the *K*–band filter; details of the observations, along with the sources observed can be found in Table 3.2. The sources selected for these observations were those with a faint optical detection or no optical detection at all.

Field	Date	Target Source	Exposure Time	Seeing (″)
Hercules	25/07/04	53w054	54x60s	0.7
	28/07/04	53w084	36x60s	0.5
	”	53w087	36x60s	”
	22/08/04	53w089	36x60s	0.9
	”	66w031	36x60s	”
	12/09/04	66w009	36x60s	0.8
	11/09/04	53w091	36x60s	0.7
	14/09/04	66w035	36x60s	1.1
	20/09/04	66w036	36x60s	0.9
Lynx	15/01/05	55w119	36x60s	0.9
	21/01/05	55w128	36x60s	0.7
	”	55w132	36x60s	”
	”	55w120	36x60s	”
	”	55w125	27x60s	”
	”	55w126	36x60s	”
	”	55w133	36x60s	”
	23/01/05	55w135	36x60s	0.7
	”	55w138	36x60s	”
	”	55w147	36x60s	”
	24/01/05	55w155	36x60s	0.5
	”	55w136	36x60s	”
	”	55w128	36x60s	”
	”	55w132	36x60s	”
	16/02/05	55w133	18x60s	0.9
	17/02/05	55w121	36x60s	1.4
	”	55w123	36x60s	”
	”	55w156	36x60s	”
	”	55w143	36x60s	”

Table 3.2: Summary of UKIRT observations.

The sources were observed using a 9–point dither pattern with offsets of 10″ and an exposure time of 60s per dither position. In general this was repeated 4 times resulting in a total of 36 exposures. The exceptions to this were 53w054 where the observation had to be re–started due to high humidity and 55w125 where software problems meant the observation had to be halted after 27 exposures (3 repeats of the dither pattern). Also, because some observations were done in service, two sources which were not detected after 36 exposures were able to be re–observed for a further 18 exposures at a later date. The observations of 55w128 and 55w132 were also repeated since the originals were taken at a very high airmass which resulted in significant elongation of the objects in the field. The seeing for each observation can be found in Table 3.2.

Appropriate standard stars (FS125 for Lynx and FS27 for Hercules) were observed multiple times throughout the night if multiple sources were also observed, but only observed once on other nights. All nights were photometric.

The infra–red, UKIRT, data reduction method is similar to that already described for the optical, INT, data; again the IRAF software was used to process the images, but each individual source observation was reduced independently. The first step was the subtraction of the appropriate dark frame from each image. One dark frame was observed immediately prior to the observation of each source, giving each image a 'personal' dark. Flat–fields were then made for each source by median combining the first 9 observations only, rejecting pixels according to the noise properties of the detector. Only 9 observations were used due to the variability of the sky over the full length of the exposure. The images were then divided by the flat–field which had been normalised using its pixel median value. (The mean pixel value was not used as it may be affected by bright artefacts in the image.)

The final steps in the reduction process – sky–subtraction, cosmic ray removal and image combining – were done using the IRAF package *dimsum*, by P. Eisenhardt, M. Dickinson and S.A. Stanford, and, in particular, the task *reduce*. The images were again registered using on average 10 stars. For the source with 2 separate observations (55w133) the sky–subtraction was done for the two nights separately but then all the images were registered and combined together to produce a single final image.

3.3.1 UKIRT astrometry

The astrometrical calibration of the UKIRT images was done where possible using the INT images as references, since the small size of the UKIRT images meant that they cover only a small area of sky and therefore, do not contain many DSS stars. If a USNO star was available the calibration was also 'tweaked' to further improve the fit. For the sources with no corresponding INT data, an image with rough astrometry, derived from the telescope pointing position, was created using the UKIRT orac-dr reduction software[2]. The USNO catalogue was then overlaid onto the rough image allowing the right ascension and declination of a star near the image centre to be identified. The x and y co–ordinates of the star were then measured in the original image and the calibration was performed using *gaia*.

[2]This software takes the raw telescope data and passes it through a reduction pipeline to create a 'first–look' image.

3.4 Aperture photometry and source identification

The source host–galaxy positions were found by overlaying the VLA A–array radio contour maps with the optical and infra–red data. For the optical images this was done in the *r*–band; sources with no *r*–band detection would also lack a detection in the *i*–band due to the comparative shallowness of the observation. Figure 3.4 shows the radio/optical and, where appropriate, radio/infra–red overlays resulting from the UKIRT and April 2004 observations; the corresponding host galaxy positions can be found in Tables 3.5 and 3.6.

The aperture photometry of all the sources was done using *gaia*. The counts received for each source in *r*, *i*, and *K*–band (if available), were measured in one of 4 different sized apertures – 1.5″, 2.5″, 4.0″ and 8.0″ radius – depending on the extent of the source. The aperture chosen for each source was the same in the three bands to enable colours to be accurately determined. The resulting magnitudes were then aperture corrected to ensure that the sources were measured out to the same physical radius (see §3.4.3 for details). The sky–value was determined either using an annulus around the object or, in cases where this could not be done because of the proximity of other objects, using a sky–aperture placed nearby. This sky–value could then be subtracted from the measured counts leaving only the counts from the source itself.

The instrumental magnitudes, $m_{\rm inst}$ of the sources were then calculated from the measured counts, C using

$$m_{\rm inst} = -2.5\ \log\left[\frac{C}{t_{\rm exp}}\right], \tag{3.2}$$

where t_{exp} is the exposure time of the observation. The instrumental magnitude is related to the apparent magnitude $m_{\rm app}$ by

$$m_{\rm app} = m_{\rm inst} + m_{\rm zpt} + \kappa X, \tag{3.3}$$

where $m_{\rm zpt}$ is the zeropoint magnitude, κ is the extinction co–efficient determined for the filter and X is the airmass of the observation.

3.4.1 Optical standard star calibration

For the optical data the unknown quantities in Equation 3.3 were determined using the standard star observations. Since their apparent magnitudes were known and their instrumental

magnitudes could be measured, κ and $m_{\rm zpt}$ could be found graphically.

The standard star observations were reduced in the same way as the science observations. The fields used were from the Landolt Faint Equatorial Standards catalogue (Landolt, 1992), each containing an average of 10 standard stars. The April 2004 standard field was SA104 in *r*–band only and SA107 in *r* and *i* whereas the January 2005 standard fields were SA104 and SA98. The April 2003 observations were not photometric. Source counts were measured using a 5″ radius aperture for all standards, with the *gaia* package; the only exception to this was for the January 2005 standards, where high seeing meant a larger aperture (15″ radius) was needed and stars with near neighbours were ignored to minimise errors.

The Landolt Faint Equatorial Standards were originally observed using the Johnson–Kron–Cousins photometric system. Therefore the $m_{\rm app}$ for the Landolt standard stars needed to be transformed to the Sloan photometric system before the calibration co–efficients could be determined. This transformation was done using the following two relations from Smith et al, (2002):

$$r = V - 0.84(V - R) + 0.13 \tag{3.4}$$

$$r - i = 1.00(R - I) - 0.21 \tag{3.5}$$

In the above equations lowercase letters indicate the Sloan photometric system and uppercase letters the Johnson system.

Once the transformations had been applied, the calibration coefficients, zeropoint magnitude, $m_{\rm zpt}$, and extinction co–efficient, κ, were determined for the photometry. These are summarised in Table 3.3 and are in good agreement with previously published values for INT extinction. The appropriate values of κ and $m_{\rm zpt}$ were then used to calibrate the optical source instrumental magnitudes; these are given in Tables 3.5 and 3.6. Only one aperture–size result (either 1.5″, 2.5″, 4″or 8″) is listed for each source; this is the 'ideal' size which gives the best magnitude measurement.

	Filter	κ (mag/airmass)	$m_{\rm zpt}$
April 2004	i	-0.03	24.24 ± 0.05
	r	-0.07	24.68 ± 0.05
January 2005	i	-0.01	24.31 ± 0.05

Table 3.3: The calibration co–efficients for the two observations

3.4.2 Infra–red standard star calibration

The UKIRT standard star observations were reduced in a similar way to the science images; the one difference being that all 5 observations for each standard were used to make the flat–field image. In contrast to the INT Landolt standard star fields, which contained many stars, only one star was used for Hercules (FS27) and one for Lynx (FS125). These were both from the UKIRT Faint *JHK* Standards catalogue (Casali, 1992). The aperture size used to measure the standards was 2.5″ radius.

The graphical method for determining the co–efficients in Equation 3.3 cannot be used for these observations as there is only one star per field and, for dates where one source only was observed, just one standard star observation per night. The extinction co–efficient, κ, was therefore taken to be 0.05 mags/airmass, the published value for UFTI (Leggett, 2005). The zeropoint magnitudes for each observing night were then calculated using the published $m_{\rm app}$ for each standard (Table 3.4). For nights where more than one source and hence more than one standard, were observed the mean value for $m_{\rm zpt}$ was used. The derived values of the zeropoint magnitude are in good agreement with previous values given for UKIRT. These were then used to calibrate the source instrumental magnitudes and are again given in Tables 3.5 and 3.6. Additionally, the *K*–band magnitudes for sources observed with UKIRT but not included in the complete sample are given in Table 3.7.

3.4.3 Aperture corrections

The next step was to correct all the calculated source apparent magnitudes to a metric aperture of 63.9 kpc diameter, thus allowing accurate comparisons to be made between sources at all redshifts. The 63.9 kpc aperture, which corresponds to an aperture of $\sim$8″ at $z = 1$, was used as it has become a standard metric size following previous work by Eales et al. (1997) and others.

At low redshift ($z < 0.6$) this correction is carried out using the curve of growth for elliptical galaxies tabulated by Sandage (1972); this method assumes that the hosts of radio galaxies are all giant ellipticals and that they share the same intensity profile. This assumption is a good approximation at low redshift but is not valid for higher redshift radio galaxies which can exhibit very different structure due to the ‘alignment effect’ (e.g. McCarthy et al., 1987), where the optical emission aligns with the radio jets of a source. For radio galaxies located at $z > 0.6$ therefore, the measured emission, within an aperture of radius r, was assumed to be proportional to r^{α} where $\alpha = 0.35$ (Eales et al., 1997).

Date	$m_{\rm zpt}$
25/07/04	22.38 ± 0.02
”	22.26 ± 0.02
28/07/04	22.36 ± 0.02
22/08/04	22.37 ± 0.02
”	22.37 ± 0.02
12/09/04	22.39 ± 0.02
11/09/04	22.34 ± 0.02
14/09/04	22.33 ± 0.02
20/09/04	22.36 ± 0.02
”	22.35 ± 0.02
15/01/05	22.41 ± 0.02
21/01/05	22.34 ± 0.02
”	22.40 ± 0.02
”	22.38 ± 0.02
”	22.38 ± 0.02
23/01/05	22.38 ± 0.02
”	22.40 ± 0.02
24/01/05	22.35 ± 0.02
”	22.35 ± 0.02
”	22.35 ± 0.02
”	22.37 ± 0.02
16/02/05	22.40 ± 0.02
17/02/05	22.21 ± 0.02
”	22.37 ± 0.02
18/02/05	22.31 ± 0.02

Table 3.4: The zeropoint magnitudes for the UKIRT observations. The anomalous magnitude value of 22.21 on 17/02/05 was the result of bad seeing; it was therefore ignored.

The magnitude corrections from the Sandage (1972) curve of growth are given as a function of a parameter β which is defined as

$$\beta = \frac{\theta z}{(1+z)^2}, \tag{3.6}$$

where z is the source redshift and θ the angular diameter of the aperture in arcseconds. β was so defined as it provides a measure of the physical diameter of the aperture for the cosmology used by Sandage. However, β varies for other cosmologies and so will not be the standard 63.9 Kpc aperture needed. Thus for galaxies with $z < 0.6$ the magnitude correction was done twice; firstly to the Sandage system and then to the 63.9 Kpc aperture,

$$m(63.9\mathrm{Kpc}) = m(\theta_{\rm m}) + (\Delta m(\beta_{\rm m}) - \Delta m(\beta_{63.9\mathrm{Kpc}})). \tag{3.7}$$

In the above equation $m(63.9\mathrm{Kpc})$ is the corrected magnitude, $m(\theta_{\mathrm{m}})$ is the magnitude as measured in the original aperture, m, $\Delta m(\beta_{\mathrm{m}})$ and $\Delta m(\beta_{63.9\mathrm{Kpc}})$ are the magnitude corrections for both apertures measured from the curve of growth. It should be noted that θ_{m} is the aperture diameter whereas the apertures used to measure the magnitudes were given in terms of their radius. In other words, $\theta_{\mathrm{m}} = 2\theta_{\mathrm{mes}}$ where θ_{mes} is the aperture size used for the measurements.

The alternative magnitude corrections for the galaxies at redshifts greater than 0.6 were calculated using

$$m(63.9\mathrm{Kpc}) = m(\theta_{\mathrm{m}}) - 2.5 \cdot 0.35 \log \frac{63.9}{D(\theta_{\mathrm{m}})}, \tag{3.8}$$

where $D(\theta_{\mathrm{m}})$ is the diameter of the original aperture in Kpc.

These aperture correction methods obviously depend on the redshifts for the sources being known; only a small fraction of the sample satisfied this condition. For the remaining objects redshifts were estimated iteratively using the K–z and r–z relations. The methods used for this estimation are outlined in §4.5 and full details of the redshifts, both estimated and spectroscopic can be found in §4. The calculated magnitude corrections for the *r*, *i* and *K*–band magnitudes can be found in Tables 3.5 and 3.6. The corrections range from +0.15 to -0.52 magnitudes.

3.4.4 Magnitude error

The magnitude error on these results is made up of four parts: (i) the error on the received counts, (ii) the error in the determination of m_{zpt} (κ is assumed to have negligible error), (iii) the error on the background subtraction and (iv), for the aperture corrected magnitudes, the error in the aperture correction, which is taken as 50% of the correction value. If the source is bright (i) dominates; (iii) is most important for the infra–red observations where the background is very high.

The sky–background error was determined by placing 10 apertures on empty regions in the fields. If the background subtraction process was perfect then the counts measured in these apertures will all be zero, therefore the sky–error can be determined by calculating the standard deviation of any counts measured. This was repeated for the other aperture sizes.

The error on the counts, ΔC, arises from the Poisson error on the number of arriving photons, ΔN_{P}, which are related to the measured counts by $C = N_{\mathrm{P}}/g$ where g is the gain of the CCD (e^{-}/DN). In other words

$$\Delta C = \Delta N_{\mathrm{P}}/g \tag{3.9}$$

and

$$\Delta N_{\rm P} = \sqrt{N_{\rm P}} = \sqrt{C\ g} \tag{3.10}$$

It would however, be more useful to calculate the error on the counts per second (C/S) instead of just counts as this is the quantity that was used in the magnitude calculations:

$$\begin{aligned} (C/S) &= \frac{N_{\rm P}}{g\ t_{\rm exp}} \\ \implies \Delta(C/S) &= \frac{\Delta N_{\rm P}}{g\ t_{\rm exp}} = \sqrt{\frac{(C/S)}{g\ t_{\rm exp}}}. \end{aligned} \tag{3.11}$$

The instrumental magnitude error due to the error on the counts, $\Delta m_{\rm inst}$, is therefore

$$\Delta m_{\rm inst} = \frac{-2.5}{\ln 10}\left[\frac{\Delta(C/S)}{C/S}\right] = \frac{-2.5}{\ln 10}\sqrt{\frac{1}{(C/S)\ g\ t_{\rm exp}}} \tag{3.12}$$

In practice, the sky background error was combined in quadrature with the error on the counts before the instrumental error was calculated using Equation (3.12). The zeropoint error was found from the spread of the calibration graph (for the optical data) or by combining the error on the published magnitude with the error calculated from the standard star instrumental magnitudes (for the infra–red data); these values are quoted in Tables 3.3 and 3.4 respectively. The final error was then found by combining in quadrature the instrumental magnitude error with the error on the zeropoint magnitude and the error on the aperture correction where appropriate.

3.5 Imaging results

The April 2003 optical data resulted in an identification fraction of 53% and 63% for Lynx and Hercules fields respectively. These numbers rose to 76% and 87% with the inclusion of the optical data from April 2004. 80% of the Hercules sources observed in the infra–red were identified, compared with 57% of the sources observed in the Lynx field. Combining these figures with the optical identification fraction gives a final result for the Lynx field of 83% and 90% for Hercules.

In total, out of the complete sample, 4 radio sources in the Hercules field and 7 radio sources in the Lynx field remain unidentified after the *r*, *i* and *K*–band observations. The observations reached optical 3σ limiting magnitudes of $r < 25.17$ and $i < 23.76$ for Hercules and $r < 24.38$ and $i < 23.46$ for Lynx; the infra–red 3σ limiting magnitudes were $K < 19.85$, $K <$

19.98 and $K < 20.16$ for the 36x60s, 54x60s and 72x60s observations respectively. The complete sample *r*, *i* and *K*–band host galaxy images can be found in Figures 3.4 and 3.5 and the corresponding positions and magnitudes are given in Tables 3.5 and 3.6. Additionally, the *K*–band images, positions and magnitudes for the sources not included in the complete sample are shown in Figure 3.3 and Table 2.1 respectively.

3.5.1 Notes on individual sources

This section provides further details on certain sources, whose results require further explanation.

53w054a and 53w054b – Windhorst et al. (1984) classified these two sources as radio galaxy lobes but, in agreement with Waddington et al. (2000), optical identifications were found for both sources indicating they are two separate radio galaxies. However, the Waddington et al. identification of 53w054b seems incorrect – a faint source is detected in the *K*–band which is more closely associated with the radio position.

53w089 – The presence of a bright source to the west of this source makes the identification appear misleading; it is in fact aligned with the centre of the radio position.

66w009a – The presence of a nearby bright source partially obscures the optical identification in the *r* and *i*–band images, though it is clearly visible in the *K*–band.

66w014 – The optically identified host galaxy for this source is partially obscured by a large, bright nearby galaxy.

66w042 – Whilst the centre of this source does not appear to align with the indicated optical galaxy, the identification is valid as the faint radio core is offset to the west.

55w133 and 55w143a/b – The *r*–band magnitudes measured for these three sources are all around the 1σ level. They therefore should be treated as unreliable.

55w135 – The slightly different telescope pointing used in the 2004 INT observations compared to that used in 2003, meant that the *r*–band image of this source is only partially present.

55w136 – Whilst the centre of this source does not appear to align with the indicated optical galaxy, the identification is valid as the faint radio core is offset to the north.

55w137 and 60w032 – The slightly different telescope pointing used in the 2004 INT observations, compared to that used in 2003, meant that these sources were not present on the 2004 images.

55w159b – The magnitude measured for this source should be treated as less reliable due to the presence of two other objects in close proximity to it.

55w165a – Whilst the core of this source appears to be to the west of the optical identification, inspection of Figure 2.3 shows that this is in reality part of the jet structure.

60w084 – This source is shown on a different scale to the rest of the sample due to its proximity to the edge of the observing area.

Hercules								
Name	RA (J2000)	DEC (J2000)	r	r (63.9 kpc)	i	i (63.9 kpc)	K	K (63.9 kpc)
53w052	17 18 34.07	49 58 50.2	21.31 ± 0.05 (4)	21.19 ± 0.08	20.86 ± 0.07 (4)	20.74 ± 0.09	–	–
53w054a	17 18 47.30	49 45 49.0	23.74 ± 0.14 (2.5)	23.58 ± 0.16	23.62 ± 0.26 (2.5)	23.46 ± 0.27	18.32 ± 0.13 (2.5)	18.17 ± 0.15
53w054b	17 18 49.97	49 46 12.2	>25.17	–	>23.76	–	19.95 ± 0.59 (2.5)	19.75 ± 0.60
53w057	17 19 07.29	49 45 44.8	24.69 ± 0.31 (2.5)	24.53 ± 0.32	>23.76	–	–	–
53w059	17 19 20.26	50 00 19.6	24.32 ± 0.22 (2.5)	24.17 ± 0.23	>23.76	–	–	–
53w061	17 19 27.34	49 43 59.7	21.13 ± 0.05 (4)	21.13 ± 0.05	20.77 ± 0.07 (4)	20.77 ± 0.07	–	–
53w062	17 19 32.07	49 59 06.8	21.91 ± 0.06 (2.5)	21.67 ± 0.14	21.04 ± 0.06 (2.5)	20.80 ± 0.14	–	–
53w065	17 19 40.07	49 57 40.8	23.00 ± 0.08 (2.5)	22.84 ± 0.11	23.31 ± 0.20 (2.5)	23.14 ± 0.22	–	–
53w066	–		>25.17	–	>23.76	–	–	–
53w067	17 19 51.27	50 10 58.5	22.15 ± 0.06 (2.5)	21.94 ± 0.12	21.43 ± 0.06 (2.5)	21.22 ± 0.12	–	–
53w069	17 20 02.54	49 44 51.0	25.12 ± 0.46 (2.5)	24.97 ± 0.47	>23.76	–	–	–
53w070	17 20 06.07	50 06 01.7	22.20 ± 0.06 (2.5)	22.05 ± 0.10	21.37 ± 0.06 (2.5)	21.21 ± 0.10	–	–
53w075	17 20 42.36	49 43 49.2	21.10 ± 0.05 (4)	21.12 ± 0.05	20.67 ± 0.06 (4)	20.69 ± 0.06	–	–
53w076	17 20 55.78	49 41 03.1	19.57 ± 0.05 (4)	19.41 ± 0.10	18.91 ± 0.05 (4)	18.75 ± 0.10	–	–
53w077	17 21 01.32	49 48 34.1	21.71 ± 0.05 (4)	21.69 ± 0.05	20.82 ± 0.07 (4)	20.80 ± 0.07	–	–
53w078	17 21 18.17	50 03 34.9	18.28 ± 0.05 (8)	18.29 ± 0.05	17.54 ± 0.05 (8)	17.54 ± 0.05	–	–
53w079	17 21 22.62	50 10 31.2	20.62 ± 0.05 (4)	20.54 ± 0.07	19.71 ± 0.05 (4)	19.62 ± 0.07	–	–
53w080	17 21 37.46	49 55 36.9	18.22 ± 0.05 (8)	18.37 ± 0.09	17.85 ± 0.05 (8)	18.00 ± 0.09	–	–
53w081	17 21 37.81	49 57 56.9	23.99 ± 0.13 (1.5)	23.64 ± 0.19	23.36 ± 0.26 (1.5)	23.01 ± 0.31	–	–
53w082	17 21 37.64	50 08 27.4	25.01 ± 0.42 (2.5)	24.86 ± 0.43	>23.76	–	–	–
53w083	17 21 48.93	50 02 39.8	22.18 ± 0.06 (2.5)	21.94 ± 0.13	21.52 ± 0.06 (2.5)	21.28 ± 0.13	–	–
53w084	17 21 50.43	49 48 30.5	24.78 ± 0.34 (2.5)	24.61 ± 0.35	>23.76	–	19.46 ± 0.38 (2.5)	19.29 ± 0.39
53w085	17 21 52.47	49 54 34.0	22.17 ± 0.06 (2.5)	22.01 ± 0.10	21.93 ± 0.07 (2.5)	21.77 ± 0.10	–	–
53w086a	17 21 56.42	49 53 39.8	20.22 ± 0.05 (4)	20.10 ± 0.08	19.44 ± 0.05 (4)	19.32 ± 0.08	–	–
53w086b	17 21 57.65	49 53 33.8	22.08 ± 0.06 (2.5)	21.69 ± 0.12	20.95 ± 0.06 (2.5)	20.56 ± 0.12	–	–
53w087	–		>25.17	–	>23.76	–	>19.85	–

Table 3.5: The host galaxy positions and magnitudes for the Hercules field. The radius (in $''$) of the aperture used for photometry is given in brackets. Sources which were unmeasurable due to the presence of a nearby bright object are labelled with a * and 3σ limits are given for undetected sources. The corresponding radio positions can be found in Table 2.2.

Hercules								
Name	RA (J2000)	DEC (J2000)	r	r (63.9 kpc)	i	i (63.9 kpc)	K	K (63.9 kpc)
53w088	–		>25.17	–	>23.76	–	–	–
53w089	17 22 01.02	50 06 51.7	24.27 ± 0.16 (1.5)	23.84 ± 0.22	>23.76	–	>19.85	–
66w009a	17 18 32.87	49 55 53.9	23.11 ± 0.08 (1.5)	22.68 ± 0.22	22.36 ± 0.11 (1.5)	21.93 ± 0.24	16.94 ± 0.02 (1.5)	16.51 ± 0.21
66w009b	17 18 33.80	49 56 02.2	17.71 ± 0.05 (4)	17.19 ± 0.26	17.19 ± 0.05 (4)	16.67 ± 0.26	13.79 ± 0.01 (4)	13.26 ± 0.26
66w014	17 18 53.49	49 52 39.3	*	–	*	–	–	–
66w027	17 19 52.11	50 02 12.7	18.33 ± 0.05 (8)	17.99 ± 0.19	17.81 ± 0.05 (8)	17.46 ± 0.19	–	–
66w031	17 20 06.87	49 43 57.0	22.65 ± 0.07 (2.5)	22.45 ± 0.12	22.43 ± 0.10 (2.5)	22.23 ± 0.14	17.96 ± 0.10 (2.5)	17.76 ± 0.14
66w035	17 20 12.41	49 57 08.7	23.47 ± 0.11 (2.5)	23.31 ± 0.14	23.12 ± 0.17 (2.5)	22.95 ± 0.19	19.10 ± 0.29 (2.5)	18.94 ± 0.30
66w036	17 20 21.46	49 46 58.3	22.79 ± 0.07 (2.5)	22.60 ± 0.12	21.82 ± 0.07 (2.5)	21.63 ± 0.12	17.45 ± 0.06 (2.5)	17.26 ± 0.11
66w042	17 20 52.20	49 42 49.2	21.21 ± 0.05 (4)	21.16 ± 0.06	21.01 ± 0.07 (4)	20.96 ± 0.08	–	–
66w047	17 21 05.48	49 56 55.9	19.30 ± 0.05 (8)	19.38 ± 0.06	18.80 ± 0.06 (8)	18.87 ± 0.07	–	–
66w049	17 21 11.21	49 58 32.9	22.59 ± 0.07 (2.5)	22.41 ± 0.11	22.16 ± 0.08 (2.5)	21.98 ± 0.12	–	–
66w058	–		>25.17	–	>23.76	–	–	–

Table 3.5

Lynx								
Name	RA (J2000)	DEC (J2000)	r	r (63.9 kpc)	i	i (63.9 kpc)	K	K (63.9 kpc)
55w116	08 43 40.79	44 39 25.5	22.03 ± 0.07 (2.5)	21.84 ± 0.12	21.16 ± 0.10 (2.5)	20.97 ± 0.14	–	–
55w118	08 43 46.86	44 35 49.7	21.29 ± 0.06 (4)	21.24 ± 0.07	20.89 ± 0.08 (4)	20.84 ± 0.08	–	–
55w120	08 43 52.87	44 24 29.1	>24.38	–	>23.46	–	18.12 ± 0.10 (2.5)	17.96 ± 0.13
55w121	08 44 04.01	44 31 20.3	23.15 ± 0.14 (2.5)	22.98 ± 0.16	>23.46	–	19.35 ± 0.35 (2.5)	19.17 ± 0.36
55w122	08 44 12.10	44 31 17.5	20.74 ± 0.05 (4)	20.66 ± 0.07	20.56 ± 0.08 (4)	20.47 ± 0.09	–	–
55w123	08 44 14.54	44 35 00.2	22.90 ± 0.12 (2.5)	22.71 ± 0.15	22.98 ± 0.36 (2.5)	22.79 ± 0.37	17.30 ± 0.06 (2.5)	17.10 ± 0.11
55w124	08 44 14.93	44 38 52.2	21.22 ± 0.06 (4)	21.16 ± 0.07	21.28 ± 0.10 (4)	21.22 ± 0.10	–	–
55w127	08 44 27.15	44 43 08.0	14.18 ± 0.05 (8)	13.45 ± 0.37	14.12 ± 0.07 (8)	13.39 ± 0.37	–	–
55w128	–		>24.38	–	>23.46	–	>20.16	–
55w131	08 44 35.51	44 46 04.1	23.18 ± 0.15 (2.5)	23.02 ± 0.17	21.79 ± 0.14 (2.5)	21.62 ± 0.16	–	–
55w132	–		>24.38	–	>23.46	–	>20.16	–
55w133	08 44 37.24	44 26 00.4	25.51 ± 1.03 (1.5)	25.15 ± 1.05	>23.46	–	>19.98	–
55w135	08 44 41.10	44 21 37.7	>24.38	–	>23.46	–	13.23 ± 0.02 (10)	13.12 ± 0.23
55w136	08 44 45.09	44 32 27.3	23.80 ± 0.22 (1.5)	23.45 ± 0.28	>23.46	–	19.17 ± 0.16 (1.5)	18.81 ± 0.24
55w137	–		>24.38	–	>23.46	–	–	–
55w138	08 44 54.45	44 26 22.0	>24.38	–	>23.46	–	19.72 ± 0.25 (1.5)	19.34 ± 0.31
55w140	08 45 06.06	44 40 41.2	20.72 ± 0.05 (4)	20.75 ± 0.05	20.94 ± 0.08 (4)	20.96 ± 0.08	–	–
55w141	–		>24.38	–	>23.46	–	–	–
55w143a	08 45 05.62	44 25 42.9	25.38 ± 0.92 (1.5)	25.03 ± 1.00	>23.46	–	>19.85	–
55w143b	08 45 04.25	44 25 53.3	25.46 ± 0.98 (1.5)	25.11 ± 0.98	>23.46	–	>19.85	–
55w147	08 45 23.83	44 50 24.6	23.07 ± 0.13 (2.5)	22.90 ± 0.16	>23.46	–	17.68 ± 0.07 (2.5)	17.51 ± 0.11
55w149	08 45 27.17	44 55 25.9	16.49 ± 0.05 (8)	16.34 ± 0.09	15.94 ± 0.07 (8)	15.80 ± 0.10	–	–
55w150	08 45 29.47	44 50 37.4	20.82 ± 0.05 (4)	20.70 ± 0.08	20.12 ± 0.07 (4)	20.00 ± 0.09	–	–
55w154	08 45 41.30	44 40 11.9	19.19 ± 0.05 (8)	19.25 ± 0.06	18.59 ± 0.08 (8)	18.64 ± 0.08	–	–
55w155	–		>24.38	–	>23.46	–	>19.85	–
55w156	08 45 50.92	44 39 51.5	22.75 ± 0.10 (2.5)	22.56 ± 0.14	23.03 ± 0.37 (2.5)	22.84 ± 0.38	17.27 ± 0.05 (2.5)	17.07 ± 0.11
55w157	08 46 04.44	44 45 52.7	22.07 ± 0.07 (2.5)	21.77 ± 0.16	21.45 ± 0.11 (2.5)	21.15 ± 0.18	–	–
55w159a	08 46 06.67	44 51 27.5	23.54 ± 0.08 (2.5)	23.38 ± 0.22	>23.46	–	–	–

Table 3.6: The host galaxy positions and magnitudes for the Lynx field. The radius (in $''$) of the aperture used for photometry is given in brackets and 3σ limits are given for undetected sources. The corresponding radio positions can be found in Table 2.3.

Lynx								
Name	RA (J2000)	DEC (J2000)	r	r (63.9 kpc)	i	i (63.9 kpc)	K	K (63.9 kpc)
55w159b	08 46 06.66	44 50 53.8	18.70 ± 0.05 (8)	18.74 ± 0.05	18.11 ± 0.07 (8)	18.15 ± 0.07		
55w160	08 46 08.57	44 36 47.4	21.40 ± 0.06 (4)	21.33 ± 0.07	20.24 ± 0.07 (4)	20.17 ± 0.08	–	–
55w161	08 46 27.46	44 29 57.1	20.07 ± 0.05 (4)	19.94 ± 0.08	19.46 ± 0.07 (4)	19.33 ± 0.10	–	–
55w165a	08 46 34.78	44 41 37.6	21.36 ± 0.06 (4)	21.31 ± 0.06	20.31 ± 0.07 (4)	20.26 ± 0.07	–	–
55w165b	08 46 33.37	44 41 24.4	21.65 ± 0.07 (4)	21.62 ± 0.07	20.89 ± 0.08 (4)	20.86 ± 0.08	–	–
55w166	08 46 36.02	44 30 53.5	22.72 ± 0.10 (2.5)	22.54 ± 0.13	21.99 ± 0.16 (2.5)	21.81 ± 0.18	–	–
60w016	08 44 03.58	44 38 10.2	22.74 ± 0.10 (2.5)	22.55 ± 0.14	21.58 ± 0.12 (2.5)	21.38 ± 0.15	–	–
60w024	08 44 17.83	44 35 36.9	21.97 ± 0.08 (4)	21.94 ± 0.08	20.81 ± 0.08 (4)	20.78 ± 0.08	–	–
60w032	–		>24.38	–	>23.46	–	–	–
60w039	08 44 42.50	44 45 32.5	17.23 ± 0.05 (8)	17.08 ± 0.08	16.78 ± 0.07 (8)	16.63 ± 0.10	–	–
60w055	08 45 14.00	44 53 08.7	21.85 ± 0.06 (2.5)	21.63 ± 0.12	20.79 ± 0.08 (2.5)	20.57 ± 0.13	–	–
60w067	–		>24.38	–	>23.46	–	–	–
60w071	08 46 00.34	44 43 22.1	23.44 ± 0.18 (2.5)	23.28 ± 0.20	>23.46	–	–	–
60w084	08 46 40.23	44 33 44.7	17.79 ± 0.05 (8)	17.58 ± 0.11	17.06 ± 0.07 (8)	16.85 ± 0.12		

Table 3.6

Name	RA (J2000)	DEC (J2000)	K	K (63.9 kpc)
53w091	17 22 32.73	50 06 01.9	18.40 ± 0.15 (2.5)	18.25 ± 0.17
55w119	08 43 47.98	44 50 41.4	19.54 ± 0.37 (2.5)	19.36 ± 0.38
55w125	08 44 15.25	44 11 16.7	17.44 ± 0.06 (2.5)	17.26 ± 0.11
55w126	–		>19.85	–

Table 3.7: The host galaxy positions and *K*–band magnitudes for the sources not included in the complete sample. The radius (in $''$) of the aperture used for photometry is given in brackets and 3σ limits are given for undetected sources. The corresponding radio positions can be found in Table 2.1.

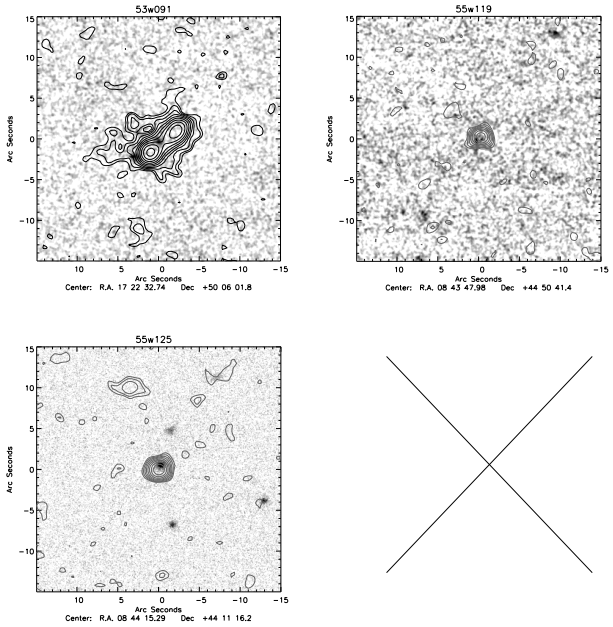

Figure 3.3: The radio images and infra–red identifications, if present, for the sources not included in the complete sample. Radio contours start at 24μJy/beam and are separated by factors of $\sqrt{2}$. The primary beam correction has not been applied to the radio maps so that uniform images can be presented.

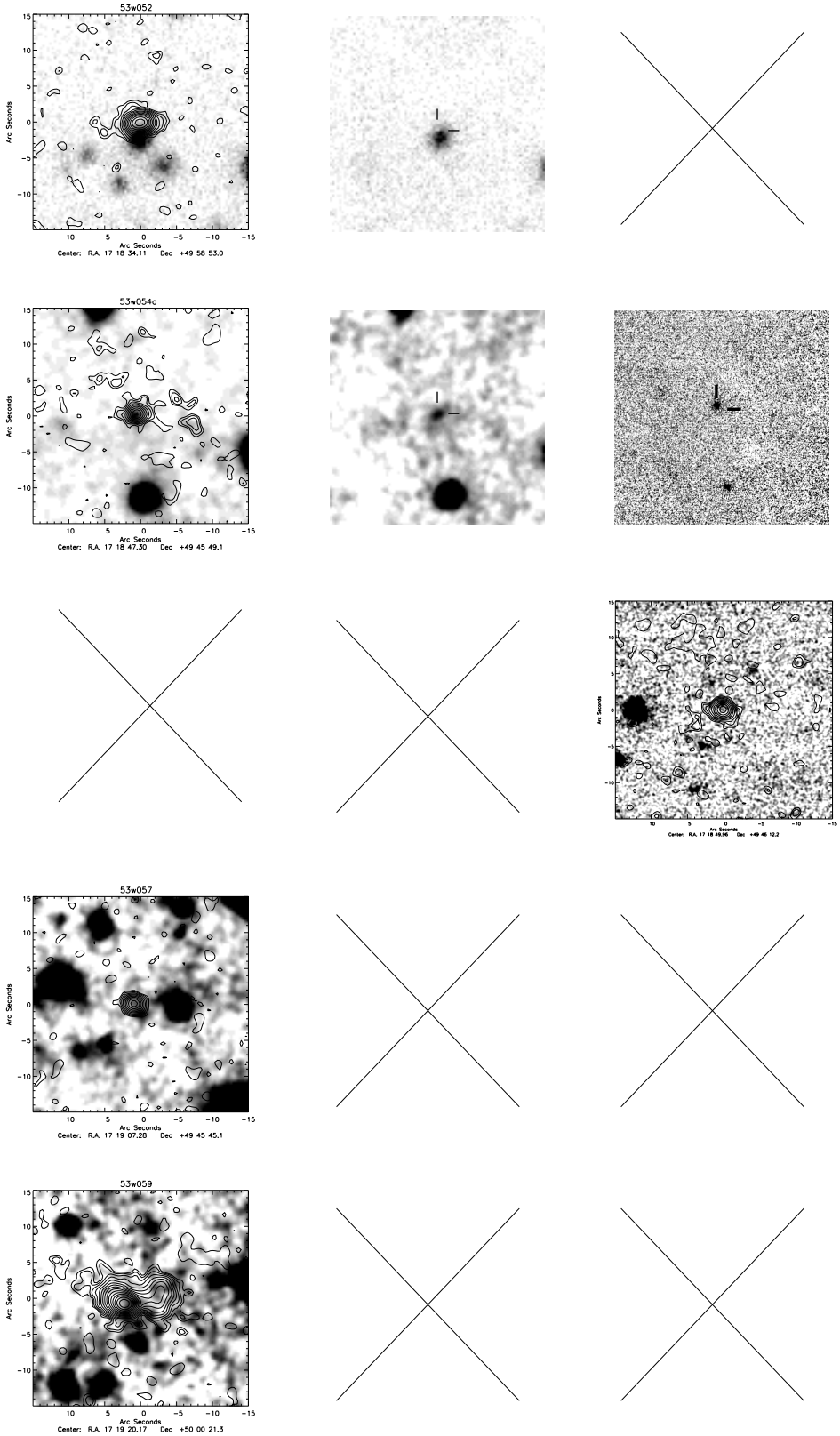

Figure 3.4: The identifications for the Hercules field; from left, *r* overlayed with the radio contour map if present, *i* and *K* with overlay if there is no *r* detection ; where necessary, host galaxy positions are marked with crosshairs. Some images have been guassian smoothed for clarity. Radio contours start at 24μJy/beam and are separated by factors of $\sqrt{2}$. The primary beam correction has not been applied to the radio maps so that uniform images can be presented.

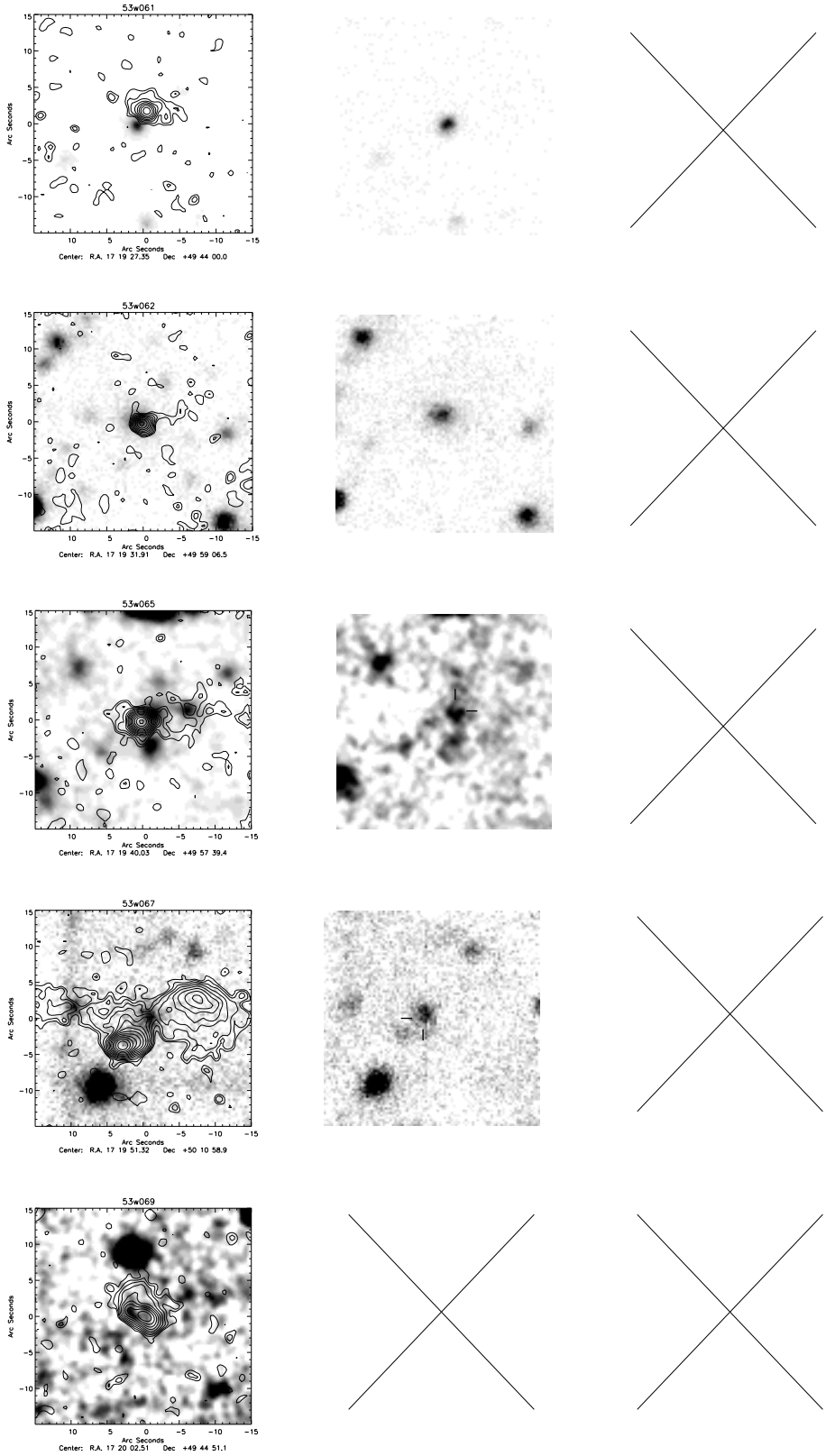
53w061
Arc Seconds
Center: R.A. 17 19 27.35 Dec +49 44 00.0
53w062
Arc Seconds
Center: R.A. 17 19 31.91 Dec +49 59 06.5
53w065
Arc Seconds
Center: R.A. 17 19 40.03 Dec +49 57 39.4
53w067
Arc Seconds
Center: R.A. 17 19 51.32 Dec +50 10 58.9
53w069
Arc Seconds
Center: R.A. 17 20 02.51 Dec +49 44 51.1

Figure 3.4

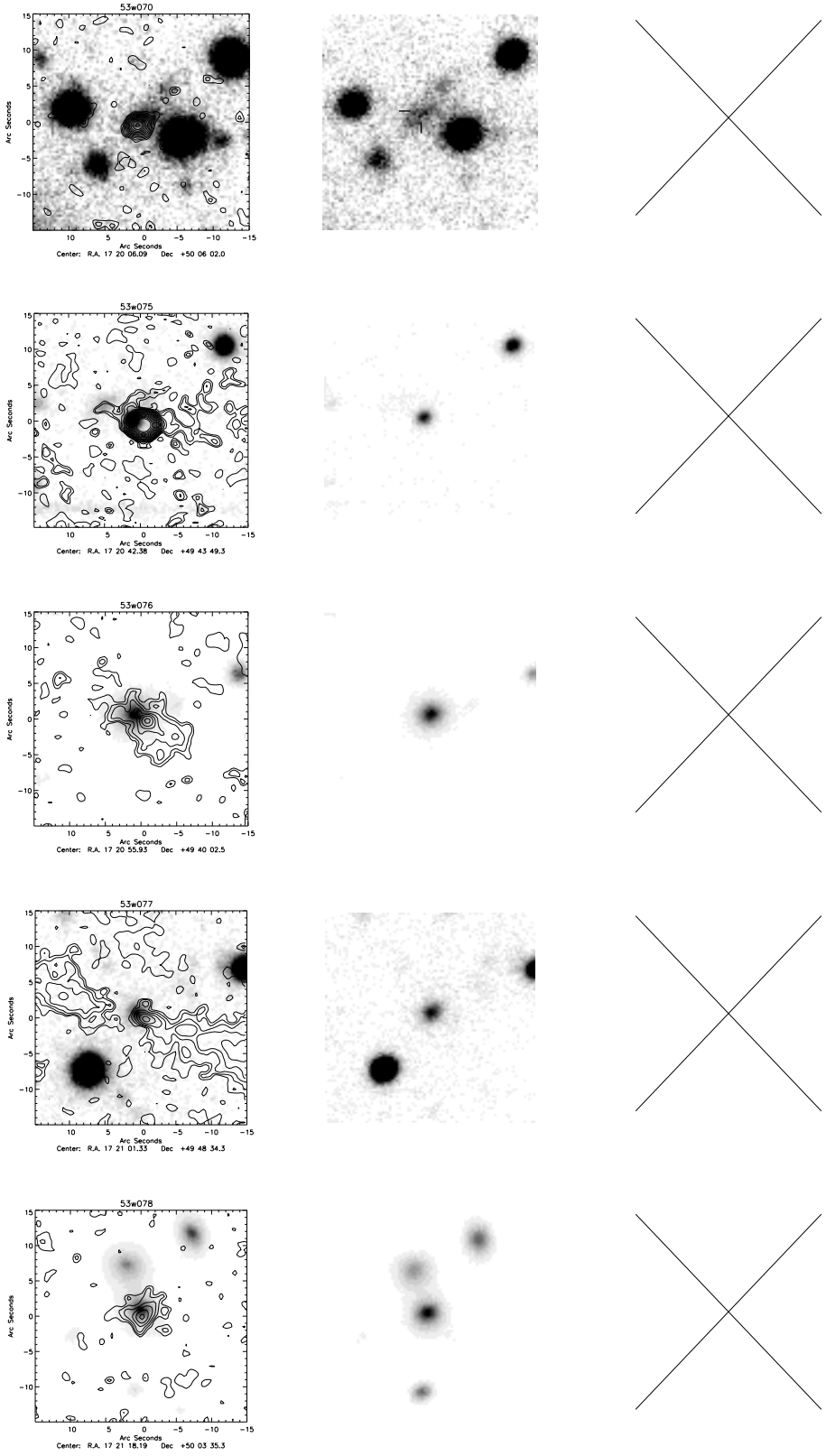
53w070
Arc Seconds
Arc Seconds
Center: R.A. 17 20 08.09 Dec +50 06 02.0
53w075
Arc Seconds
Arc Seconds
Center: R.A. 17 20 42.38 Dec +49 43 49.3
53w076
Arc Seconds
Arc Seconds
Center: R.A. 17 20 55.93 Dec +49 40 02.5
53w077
Arc Seconds
Arc Seconds
Center: R.A. 17 21 01.33 Dec +49 48 34.3
53w078
Arc Seconds
Arc Seconds
Center: R.A. 17 21 18.19 Dec +50 03 35.3

Figure 3.4

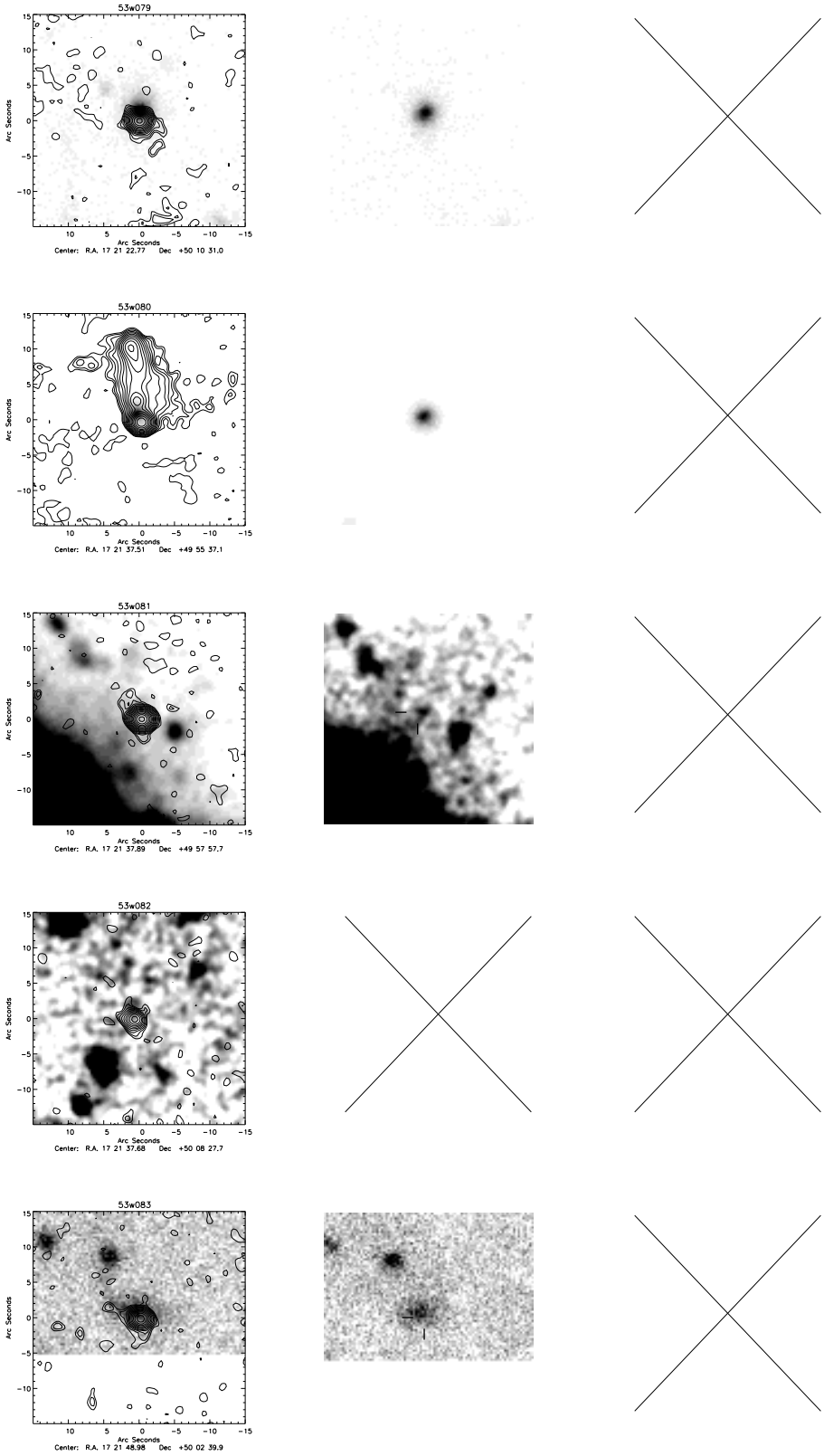
53w079
Arc Seconds
Center: R.A. 17 21 22.77 Dec +50 10 31.0
53w080
Arc Seconds
Center: R.A. 17 21 37.51 Dec +49 55 37.1
53w081
Arc Seconds
Center: R.A. 17 21 37.89 Dec +49 57 57.7
53w082
Arc Seconds
Center: R.A. 17 21 37.68 Dec +50 08 27.7
53w083
Arc Seconds
Center: R.A. 17 21 48.98 Dec +50 02 39.9

Figure 3.4

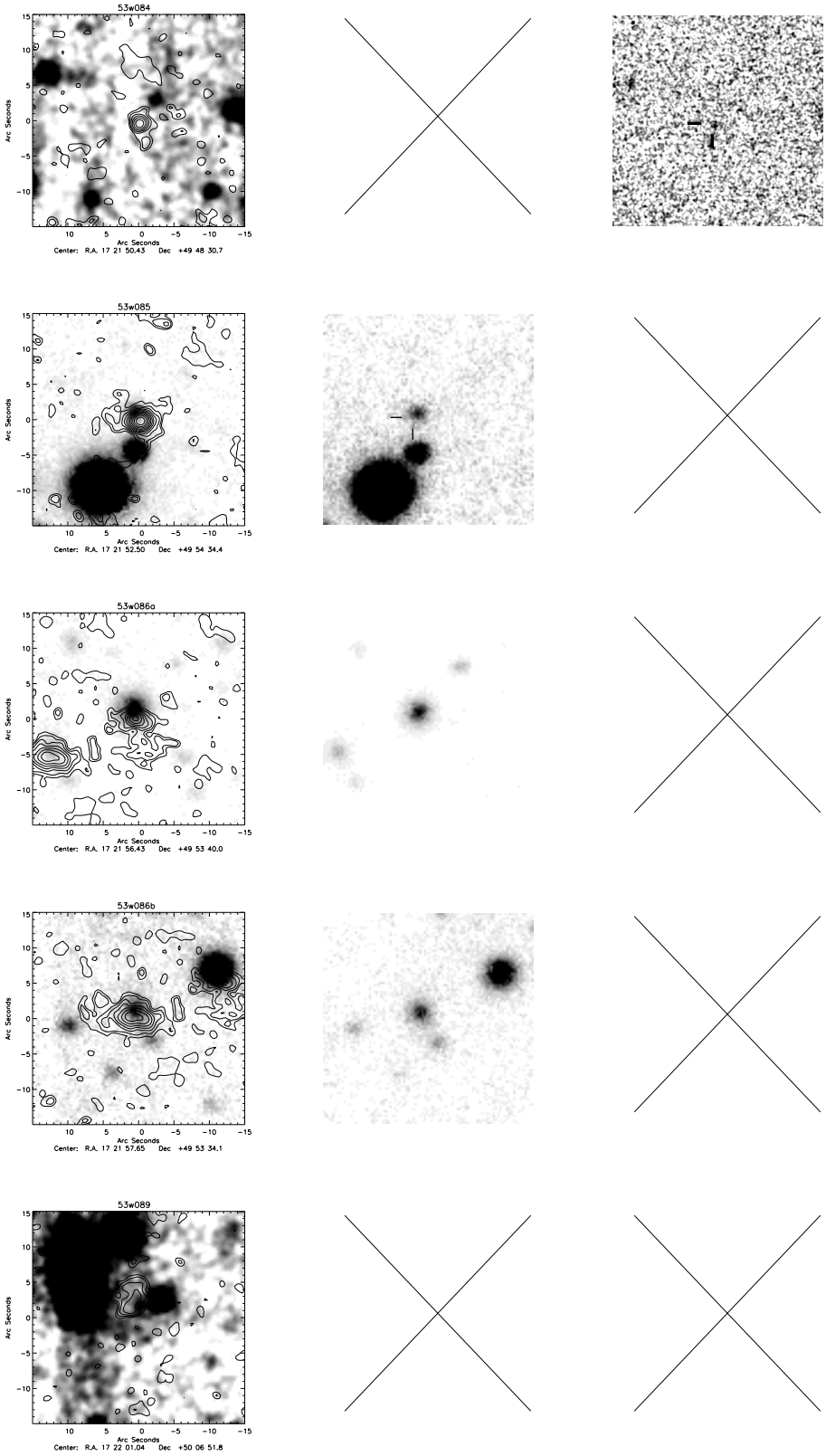
53w084
Arc Seconds
Center: R.A. 17 21 50.43 Dec +49 48 30.7
53w085
Arc Seconds
Center: R.A. 17 21 52.50 Dec +49 54 34.4
53w086a
Arc Seconds
Center: R.A. 17 21 56.43 Dec +49 53 40.0
53w086b
Arc Seconds
Center: R.A. 17 21 57.65 Dec +49 53 34.1
53w089
Arc Seconds
Center: R.A. 17 22 01.04 Dec +50 06 51.8

Figure 3.4

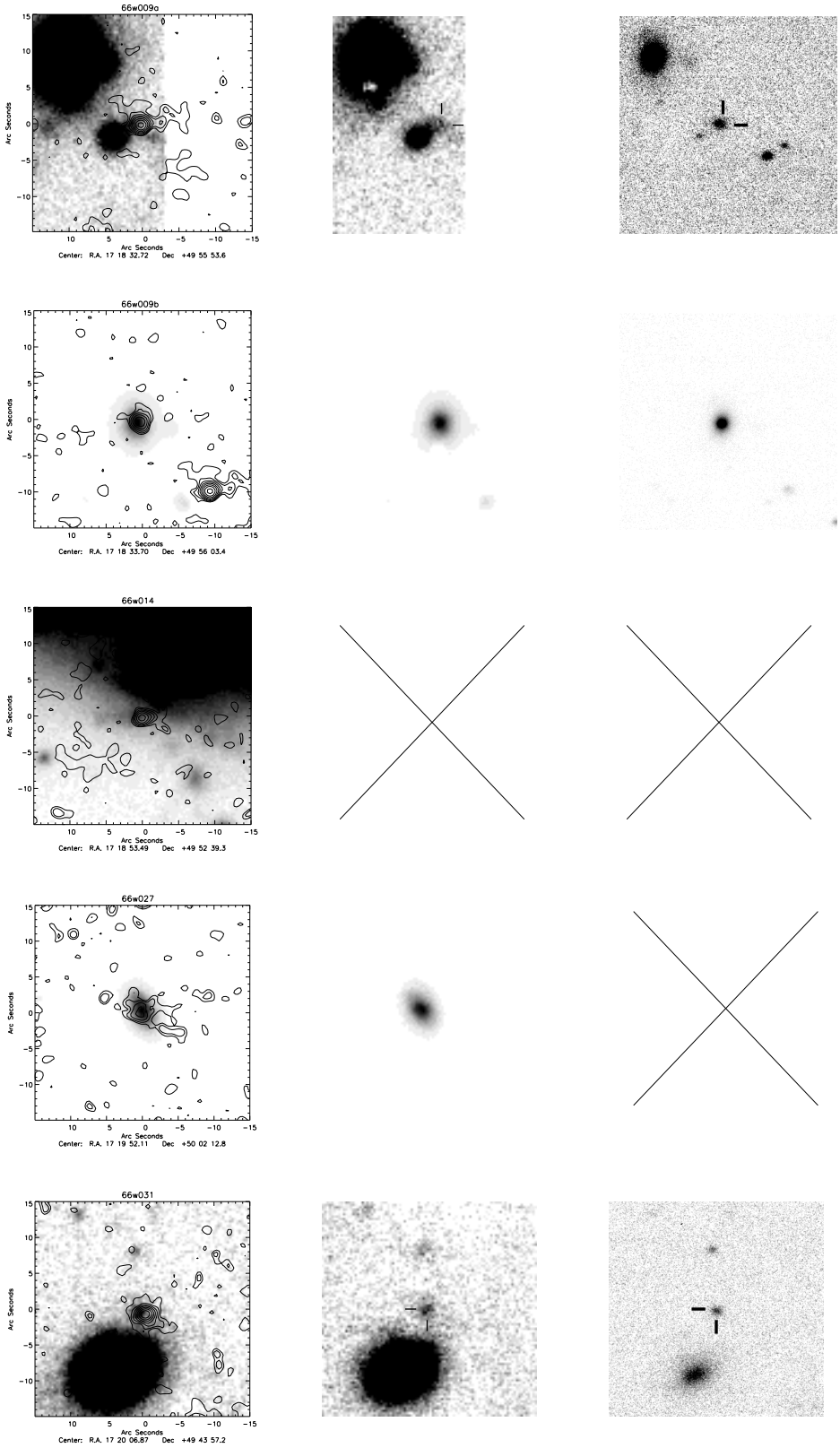
66w009a
Arc Seconds
Center: R.A. 17 18 32.72 Dec +49 55 53.6
66w009b
Arc Seconds
Center: R.A. 17 18 33.70 Dec +49 56 03.4
66w014
Arc Seconds
Center: R.A. 17 18 53.49 Dec +49 52 39.3
66w027
Arc Seconds
Center: R.A. 17 19 52.11 Dec +50 02 12.8
66w031
Arc Seconds
Center: R.A. 17 20 06.87 Dec +49 43 57.2

Figure 3.4

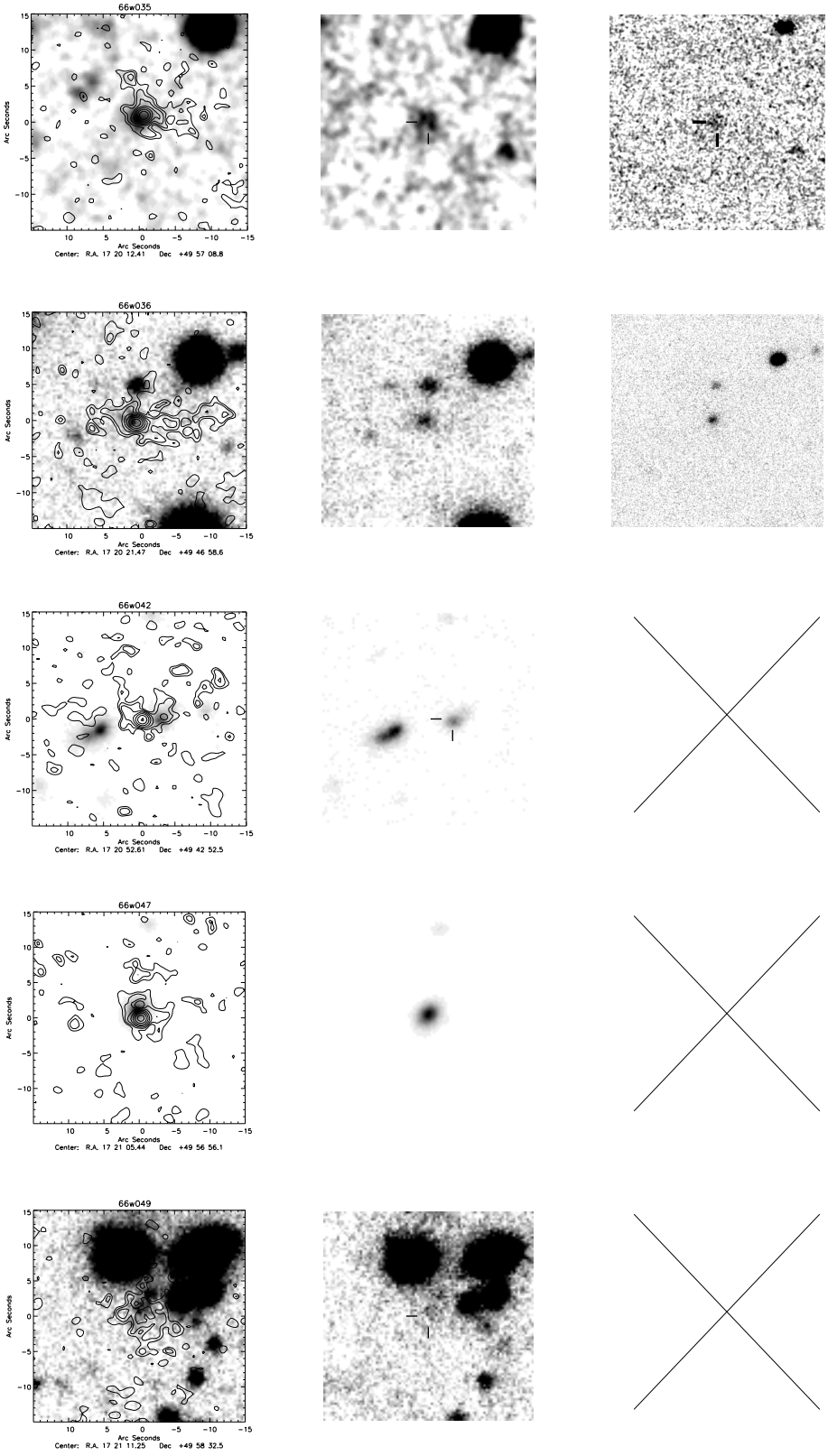
66w035
Arc Seconds
Arc Seconds
Center: R.A. 17 20 12.41 Dec +49 57 08.8
66w036
Arc Seconds
Arc Seconds
Center: R.A. 17 20 21.47 Dec +49 46 58.6
66w042
Arc Seconds
Arc Seconds
Center: R.A. 17 20 52.61 Dec +49 42 52.5
66w047
Arc Seconds
Arc Seconds
Center: R.A. 17 21 05.44 Dec +49 56 56.1
66w049
Arc Seconds
Arc Seconds
Center: R.A. 17 21 11.25 Dec +49 58 32.5

Figure 3.4

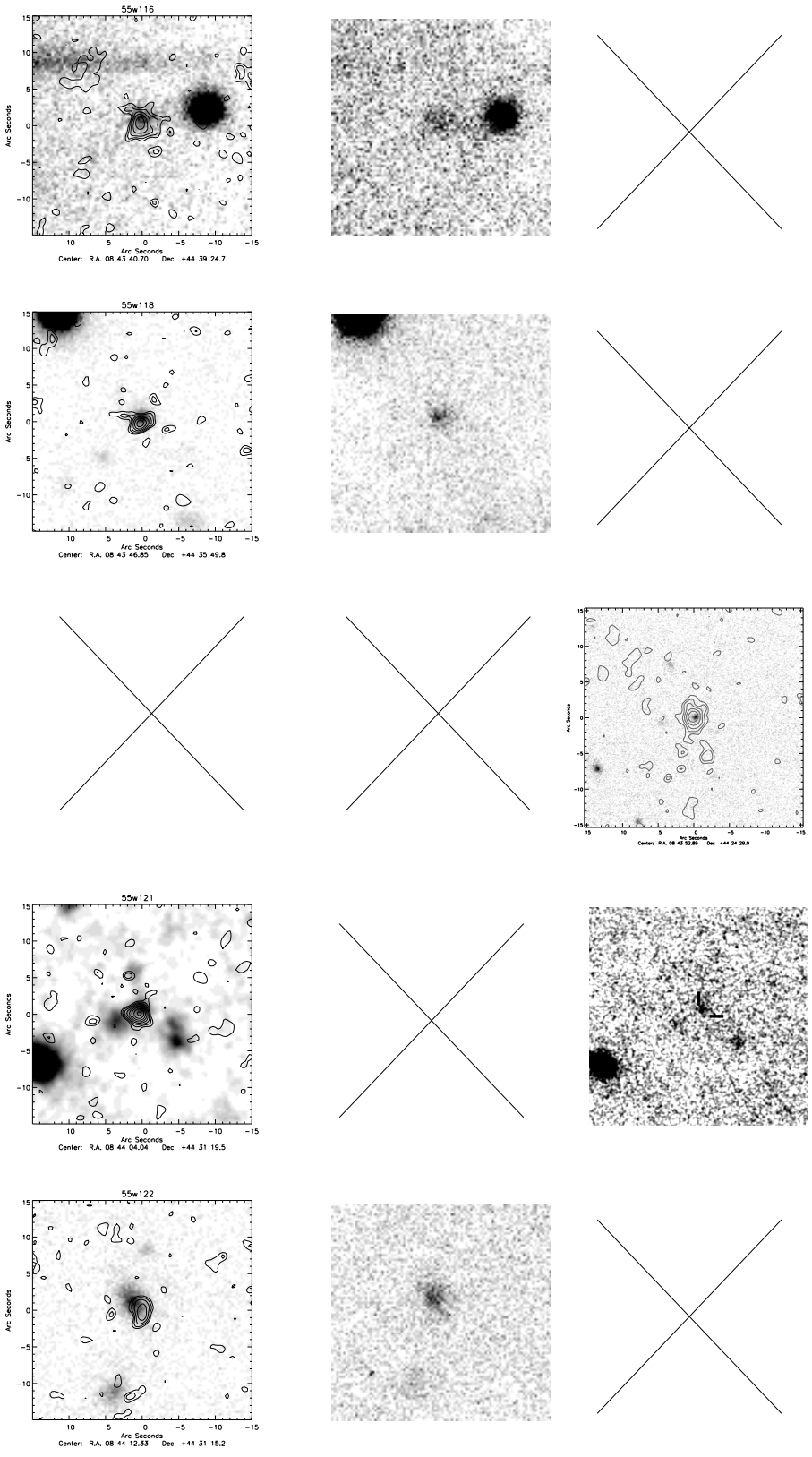

Figure 3.5: Similarly, the identifications for the Lynx field. From left, 1.4GHz radio contour map, *r* with overlay if present, *i* and *K* with overlay if there is no *r* detection. Radio contours start at 24μJy/beam and are separated by factors of $\sqrt{2}$. The primary beam correction has not been applied to the radio maps so that uniform images can be presented.

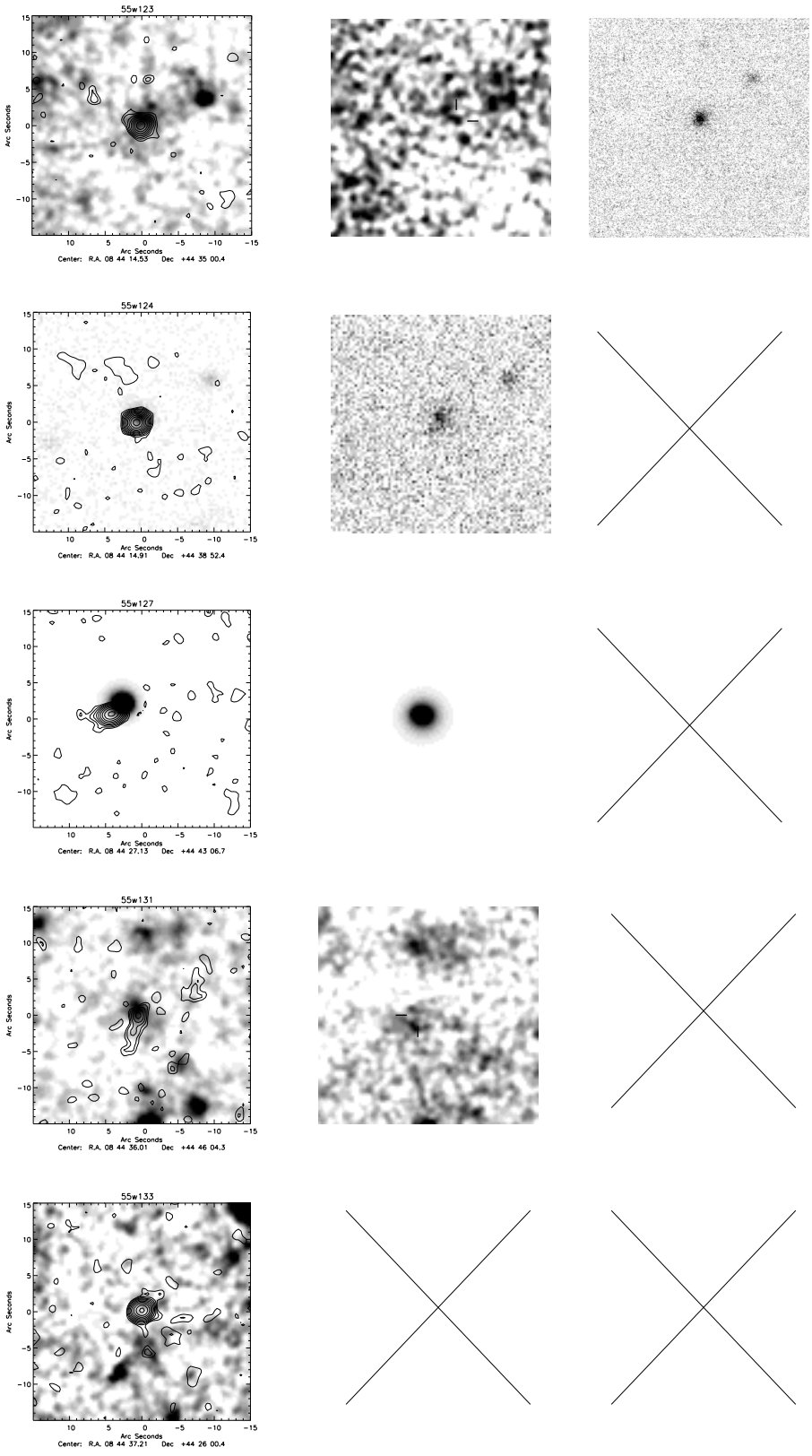
55w123
Arc Seconds
Arc Seconds
Center: R.A. 08 44 14.53 Dec +44 35 00.4
55w124
Arc Seconds
Arc Seconds
Center: R.A. 08 44 14.91 Dec +44 38 52.4
55w127
Arc Seconds
Arc Seconds
Center: R.A. 08 44 27.13 Dec +44 43 06.7
55w131
Arc Seconds
Arc Seconds
Center: R.A. 08 44 36.01 Dec +44 46 04.3
55w133
Arc Seconds
Arc Seconds
Center: R.A. 08 44 37.21 Dec +44 26 00.4

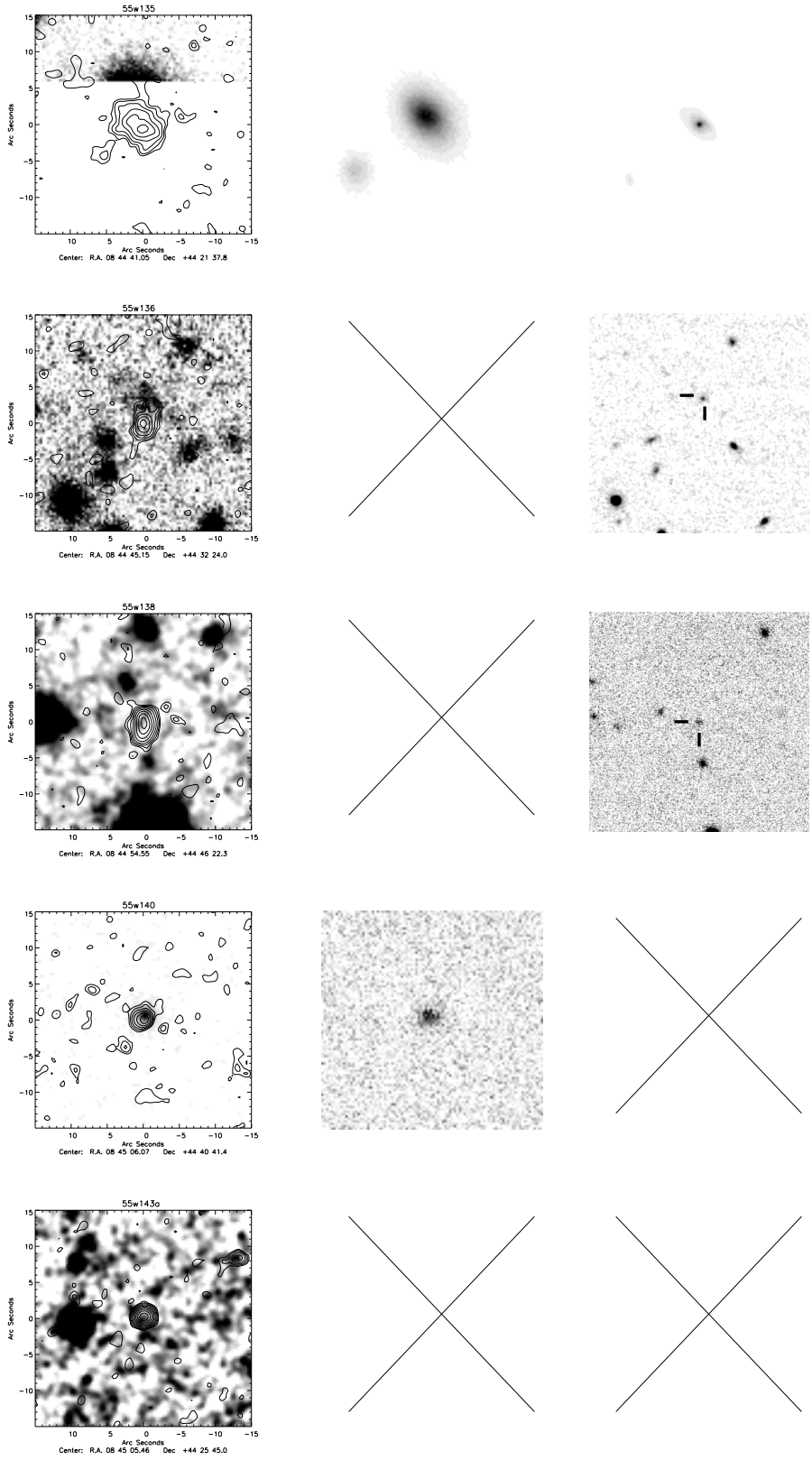
55w135
Arc Seconds
Center: R.A. 08 44 41.05 Dec +44 21 37.8
55w136
Arc Seconds
Center: R.A. 08 44 45.15 Dec +44 32 24.0
55w138
Arc Seconds
Center: R.A. 08 44 54.55 Dec +44 46 22.3
55w140
Arc Seconds
Center: R.A. 08 45 06.07 Dec +44 40 41.4
55w143a
Arc Seconds
Center: R.A. 08 45 05.46 Dec +44 25 45.0

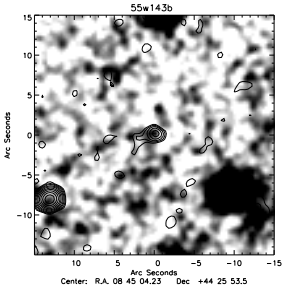
55w143b
Arc Seconds
Arc Seconds
Center: R.A. 08 45 04.23 Dec +44 25 53.5

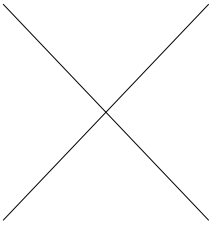

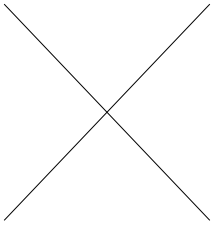

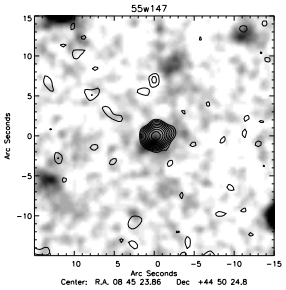
55w147
Arc Seconds
Arc Seconds
Center: R.A. 08 45 23.86 Dec +44 50 24.8

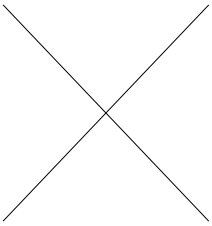

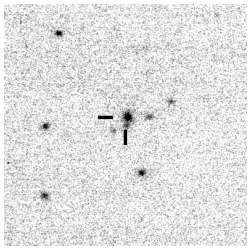

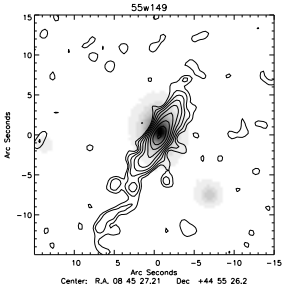
55w149
Arc Seconds
Arc Seconds
Center: R.A. 08 45 27.21 Dec +44 55 26.2

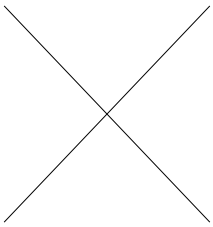

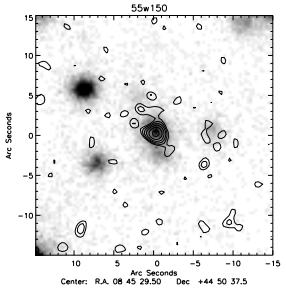
55w150
Arc Seconds
Arc Seconds
Center: R.A. 08 45 29.50 Dec +44 50 37.5

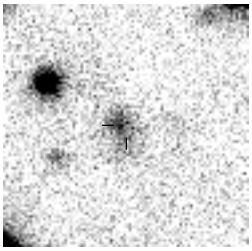

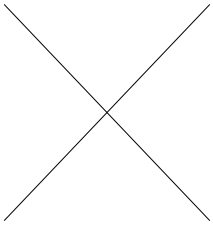

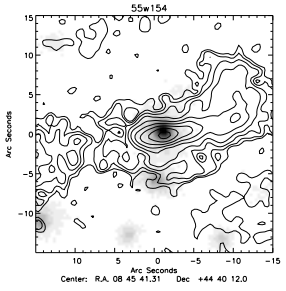
55w154
Arc Seconds
Arc Seconds
Center: R.A. 08 45 41.31 Dec +44 40 12.0

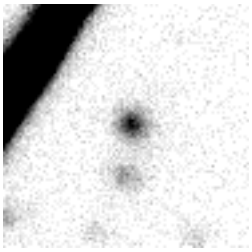

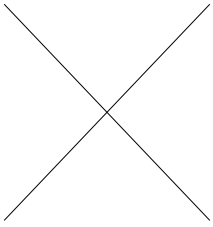

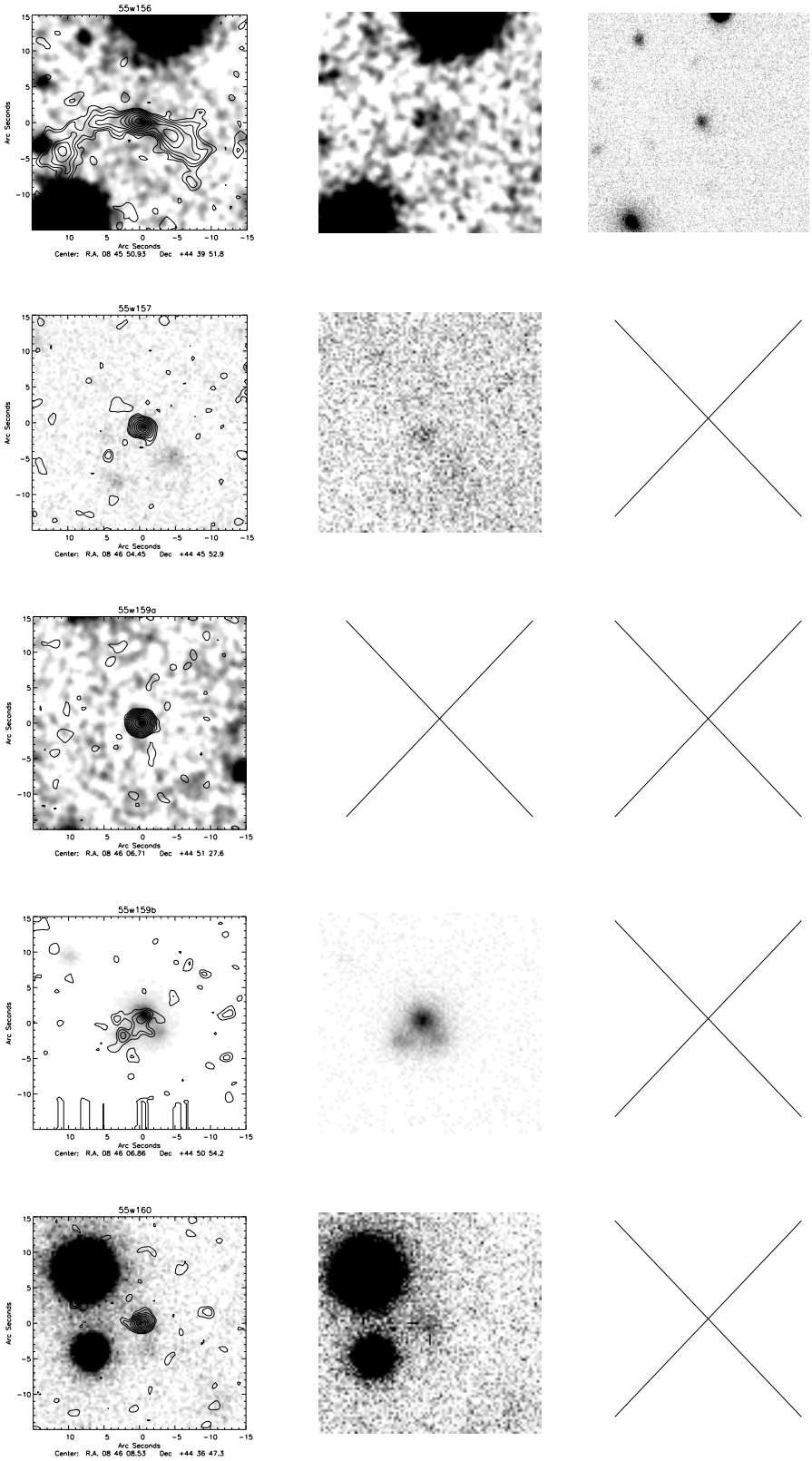
55w156
Arc Seconds
Center: R.A. 08 45 50.93 Dec +44 39 51.8
55w157
Arc Seconds
Center: R.A. 08 46 04.45 Dec +44 45 52.9
55w159a
Arc Seconds
Center: R.A. 08 46 06.71 Dec +44 51 27.6
55w159b
Arc Seconds
Center: R.A. 08 46 06.86 Dec +44 50 54.2
55w160
Arc Seconds
Center: R.A. 08 46 08.53 Dec +44 36 47.3

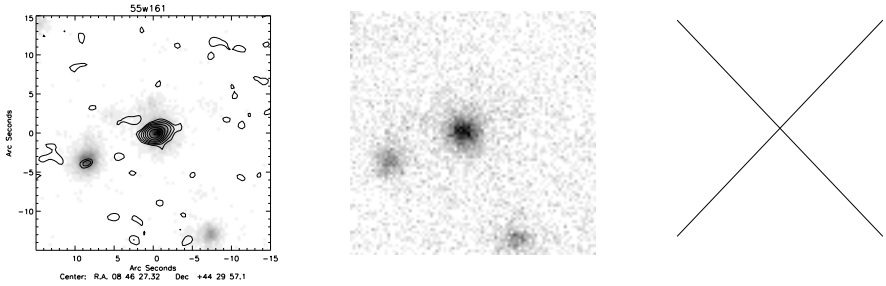
55w161
Arc Seconds
Arc Seconds
Center: R.A. 08 46 27.32 Dec +44 29 57.1

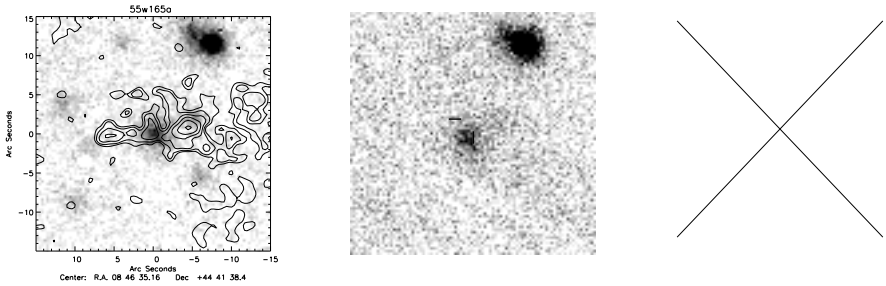
55w165a
Arc Seconds
Arc Seconds
Center: R.A. 08 46 35.16 Dec +44 41 38.4

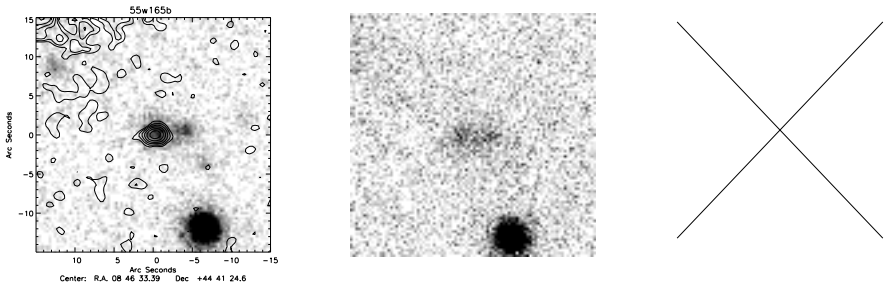
55w165b
Arc Seconds
Arc Seconds
Center: R.A. 08 46 33.39 Dec +44 41 24.6

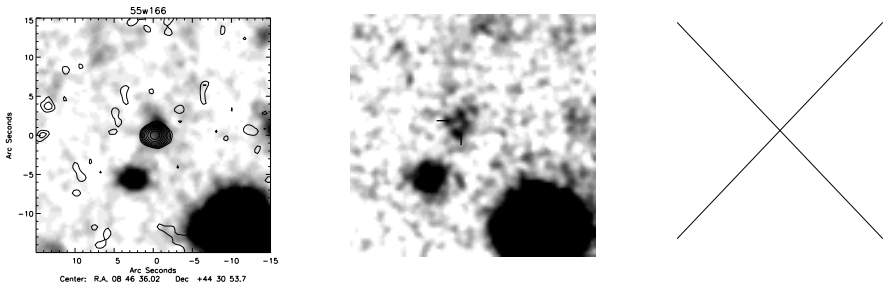
55w166
Arc Seconds
Arc Seconds
Center: R.A. 08 46 36.02 Dec +44 30 53.7

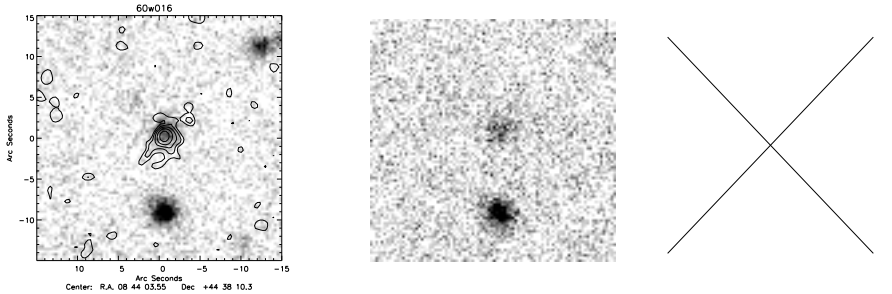
60w016
Arc Seconds
Arc Seconds
Center: R.A. 08 44 03.55 Dec +44 38 10.3

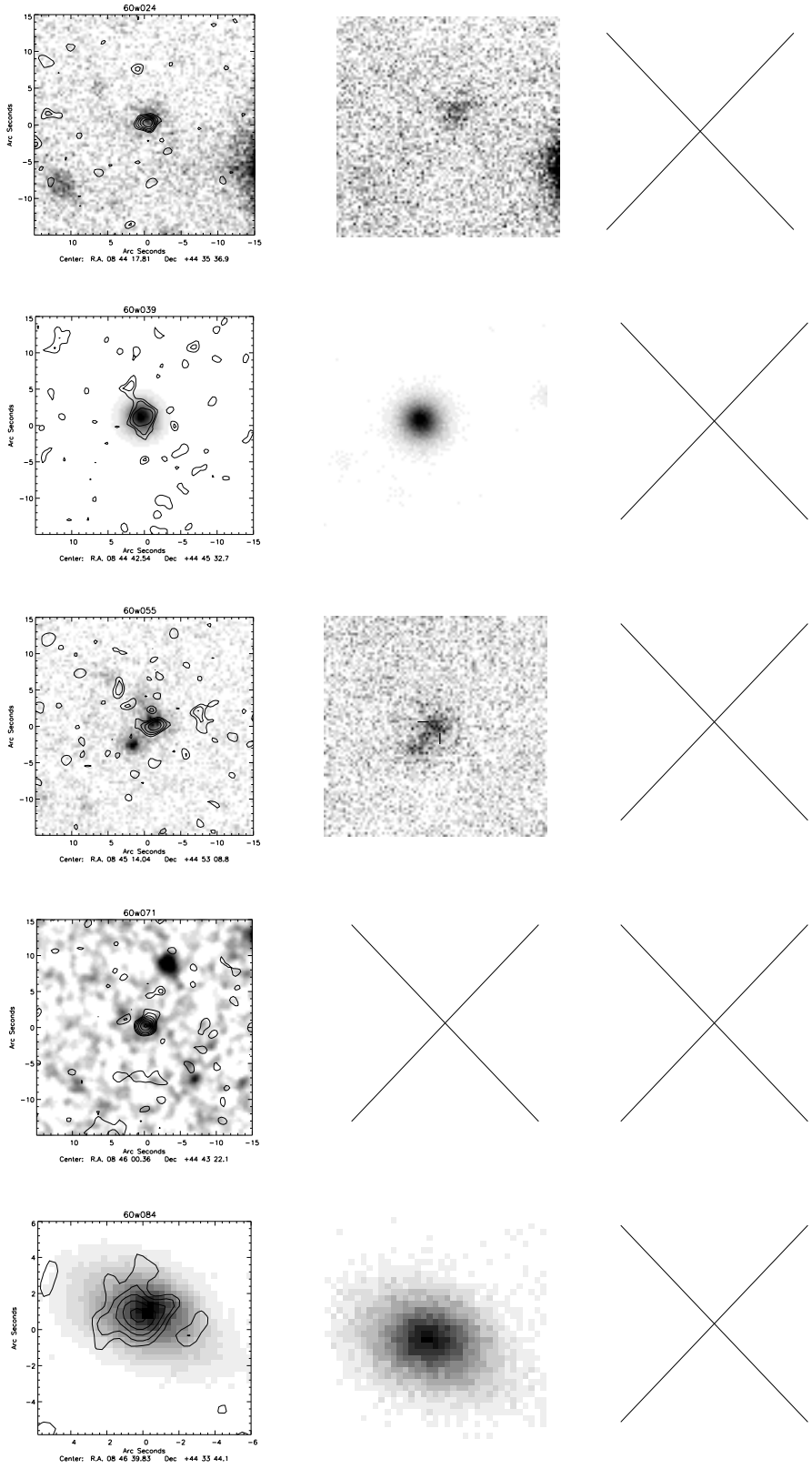
60w024
Arc Seconds
Arc Seconds
Center: R.A. 08 44 17.81 Dec +44 35 36.9
60w039
Arc Seconds
Arc Seconds
Center: R.A. 08 44 42.54 Dec +44 45 32.7
60w055
Arc Seconds
Arc Seconds
Center: R.A. 08 45 14.04 Dec +44 53 08.8
60w071
Arc Seconds
Arc Seconds
Center: R.A. 08 46 00.36 Dec +44 43 22.1
60w084
Arc Seconds
Arc Seconds
Center: R.A. 08 46 39.83 Dec +44 33 44.1

Figure 3.5

3.5.2 Magnitude comparison

Many of the sources in the Hercules field were also observed by Waddington et al (2000) with Thuan–Gunn $r_{\rm g}$ and $i_{\rm g}$–band filters using the 4–Shooter CCD camera on the 200–inch Hale telescope at Palomar Observatory, and in *K*–band using the infra–red cameras IRCAM and IRCAM3 on UKIRT. Their optical results were used to give a 'first–glance' at the accuracy of the calculated apparent magnitudes for this field (Figure 3.6). A lack of infra–red magnitudes made the comparison unfeasible in *K*.

The two sets of magnitudes appear to be in reasonable agreement. The apertures used by Waddington et al. (2000) are slightly different (4.0, 7.5 or 10″ square diameter) to the ones I used; they also do not specify which aperture a particular source was measured with. These factors, along with the differences in filter sets used, may account for the slight discrepancy between the results.

The Lynx field is covered by the Sloan Digital Sky Survey (SDSS; York et al. 2000, Stoughton et al. 2002), a multiwavelength survey carried out using the 2.5m telescope in Apache Point, New Mexico. The 'first–glance' accuracy comparison for the Lynx calculated magnitudes using the SDSS results can be seen in Figure 3.7. Again, the two sets of magnitudes appear to be in reasonable agreement with the discrepancies likely to be caused by the different magnitude measuring methods. No further host galaxy detections resulted from this comparison which is not surprising given the shallowness of the SDSS compared to these observations.

The complete SDSS magnitudes for the included Lynx sources can be found in Table 3.8.

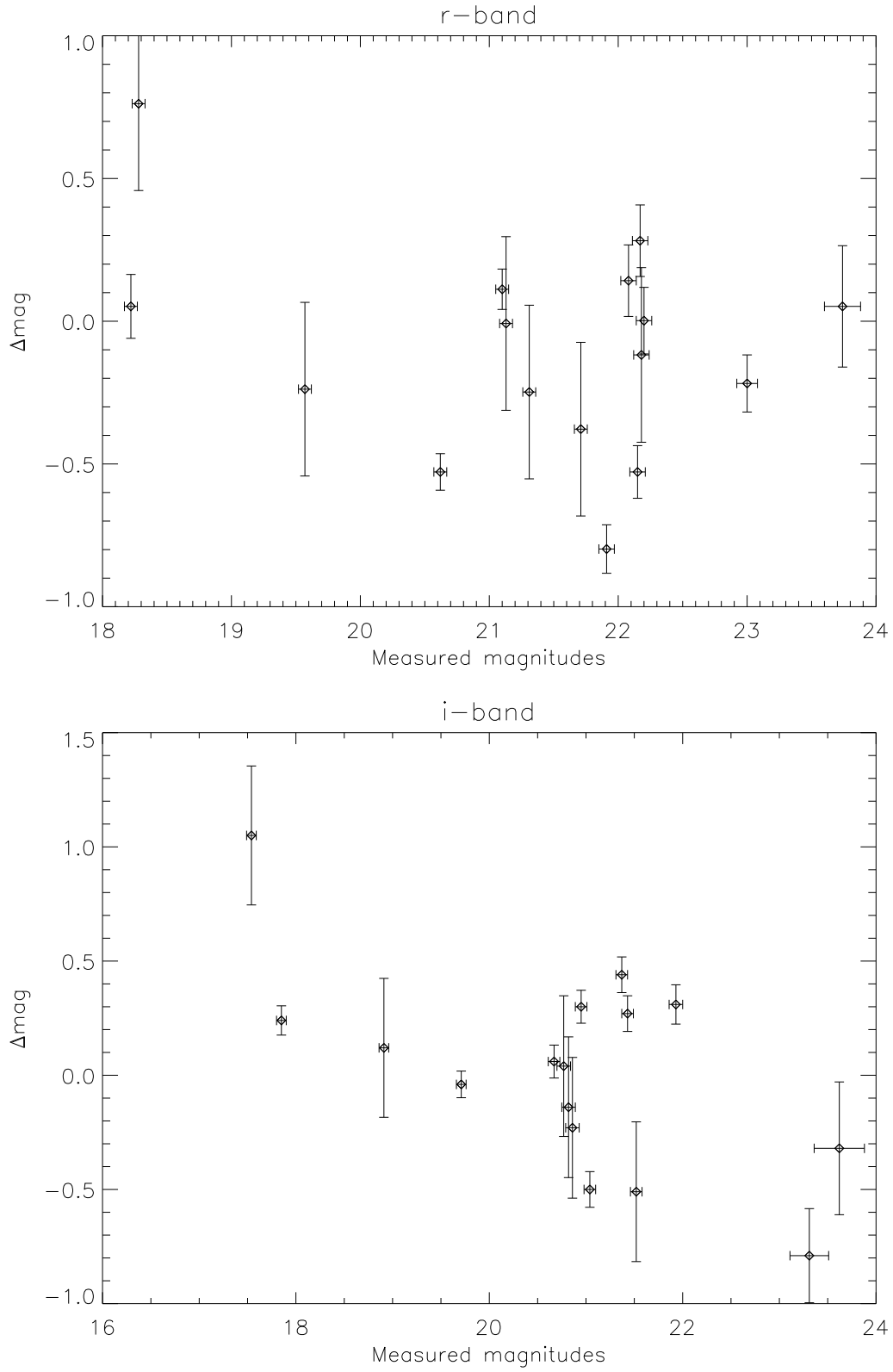

Figure 3.6: A comparison with the *r* and *i*–band magnitudes of Waddington et al. (2000). ($\Delta\mathrm{mag} = m_{\mathrm{Waddington}} - m_{\mathrm{Here}}$)

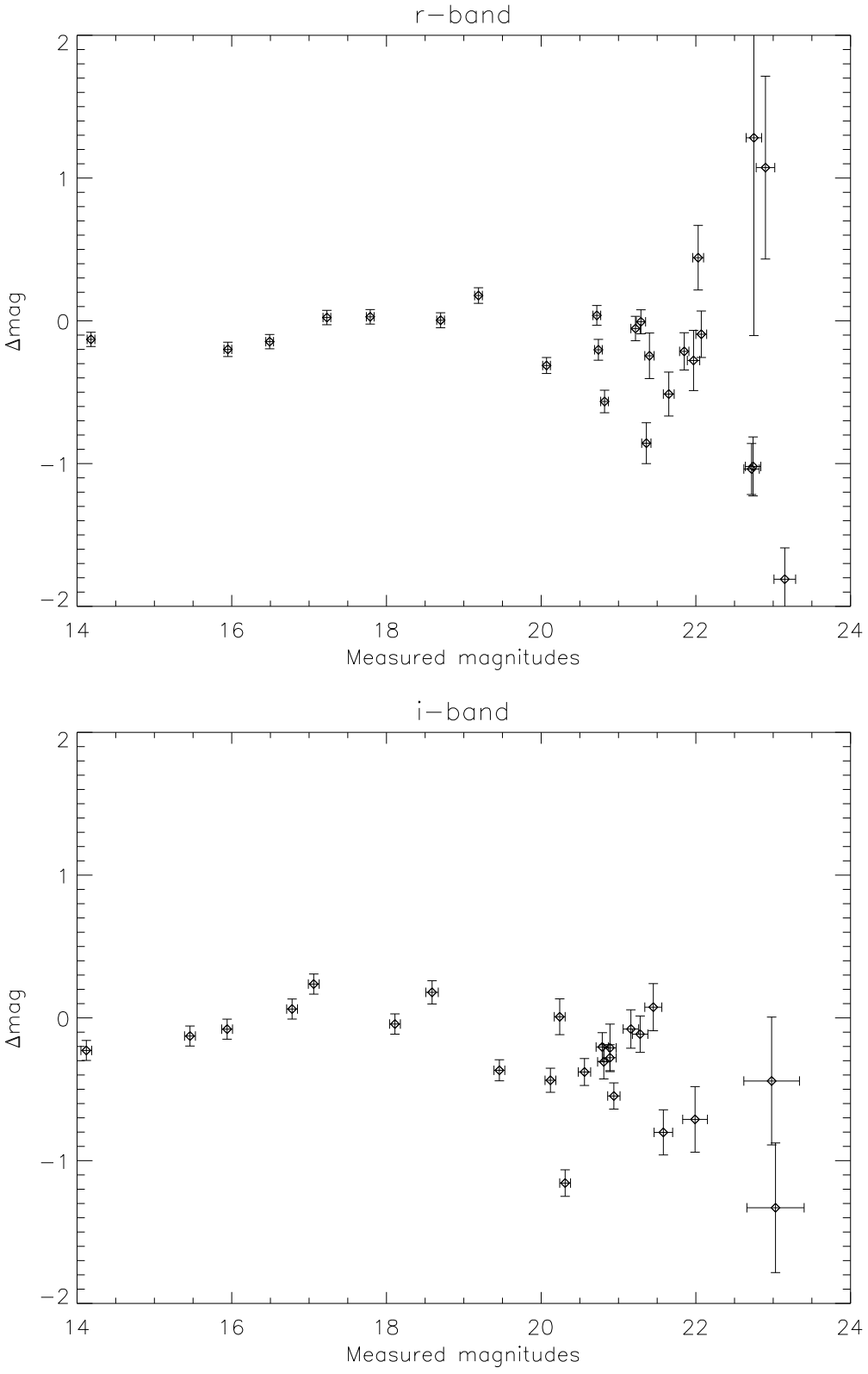

Figure 3.7: A comparison with the *r* and *i*–band magnitudes of the SDSS. ($\Delta\mathrm{mag} = m_{\mathrm{SDSS}} - m_{\mathrm{Here}}$)

Name	u	g	r	i	z
55w116	25.51 ± 1.08	24.48 ± 0.65	22.46 ± 0.22	21.08 ± 0.22	20.23 ± 0.16
55w118	24.42 ± 1.08	22.60 ± 0.12	21.28 ± 0.06	20.60 ± 0.06	20.12 ± 0.10
55w121	21.78 ± 0.45	22.14 ± 0.23	21.34 ± 0.17	21.67 ± 0.17	20.35 ± 0.32
55w122	23.40 ± 1.11	22.23 ± 0.16	20.53 ± 0.05	20.18 ± 0.05	19.57 ± 0.10
55w123	24.56 ± 1.35	24.66 ± 0.69	23.96 ± 0.63	22.53 ± 0.63	20.91 ± 0.22
55w124	21.46 ± 0.16	21.37 ± 0.06	21.17 ± 0.06	21.17 ± 0.06	20.80 ± 0.20
55w127	15.66 ± 0.01	14.47 ± 0.01	14.05 ± 0.01	13.89 ± 0.01	13.85 ± 0.01
55w140	21.03 ± 0.11	20.69 ± 0.03	20.76 ± 0.05	20.39 ± 0.05	20.68 ± 0.19
55w149	19.58 ± 0.08	17.50 ± 0.01	16.34 ± 0.01	15.86 ± 0.01	15.49 ± 0.01
55w150	25.07 ± 2.56	21.77 ± 0.16	20.25 ± 0.06	19.68 ± 0.06	19.18 ± 0.11
55w154	21.59 ± 0.20	21.23 ± 0.06	20.25 ± 0.04	19.85 ± 0.04	19.37 ± 0.07
55w156	22.84 ± 0.94	25.75 ± 1.20	24.03 ± 1.3	21.69 ± 1.30	19.89 ± 0.18
55w157	25.44 ± 1.07	22.62 ± 0.18	21.98 ± 0.15	21.52 ± 0.15	21.30 ± 0.34
55w160	23.50 ± 1.69	22.87 ± 0.59	21.16 ± 0.15	20.25 ± 0.15	19.60 ± 0.21
55w161	26.03 ± 1.10	21.44 ± 0.09	19.76 ± 0.03	19.09 ± 0.03	18.71 ± 0.05
55w165a	26.83 ± 1.08	21.62 ± 0.29	20.50 ± 0.13	19.15 ± 0.13	18.53 ± 0.12
55w165b	21.71 ± 0.34	21.83 ± 0.22	21.14 ± 0.14	20.68 ± 0.14	19.51 ± 0.18
55w166	25.10 ± 2.26	26.62 ± 0.60	21.68 ± 0.15	21.28 ± 0.15	20.42 ± 0.25
60w016	22.67 ± 0.76	24.62 ± 1.20	21.71 ± 0.18	20.78 ± 0.18	19.60 ± 0.14
60w024	22.71 ± 0.86	25.64 ± 1.30	21.69 ± 0.19	20.50 ± 0.19	19.51 ± 0.13
60w039	19.00 ± 0.03	17.89 ± 0.01	17.25 ± 0.01	16.84 ± 0.01	16.64 ± 0.02
60w055	25.03 ± 1.51	23.03 ± 0.26	21.64 ± 0.12	20.59 ± 0.12	19.98 ± 0.14

Table 3.8: SDSS magnitudes for included Lynx sources.

3.5.3 Colours and magnitude distribution

The $(r - i)$ and $(r - K)$ colour–magnitude diagrams for both Lynx and Hercules sources are shown in Figure 3.8. The $(r - i)$ plot suggests a slightly greater range in the colours of the sources in the Lynx field, compared to the Hercules field, but this is likely to be the result of the relative shallowness of the Lynx *i*–band data, which would introduce a bias against the fainter, bluer, sources in this field. The $(r - i)$ colours for both fields though, show that the majority of the radio sources are hosted by red galaxies as expected.

The Lynx field sources in the $(r - K)$ plot have a similar colour distribution to the Hercules sources, but the small number of sources in this diagram make a comparison difficult. The small numbers and poor population are the result of the selection criteria used for the *K*–band observations; sources with either an undetected or faint *r*–band detection were those chosen.

The magnitude distribution histograms (Figure 3.9) are useful as they provide a first look at the

redshift distribution of the sample through the magnitude–redshift relations for radio galaxies (these are described in more detail in §4.5.1) which indicate that the optically faintest objects should lie at the largest distances. The *K*–band magnitude distribution is ignored here because the low number of K–magnitudes taken would not result in a meaningful diagram.

Both the colour–magnitude and magnitude distribution diagrams are also in reasonable agreement with those shown in Figures 9 and 10 respectively of Waddington et al. (2000).

3.6 Chapter summary

In this chapter the optical and infra–red observations of the Lynx and Hercules field have been presented, and the host galaxies for 83% and 90% respectively of the field radio sources have been identified and their magnitudes have been measured. The magnitudes, colours and magnitude distributions of these objects are in good agreement with previous work and with expectations.

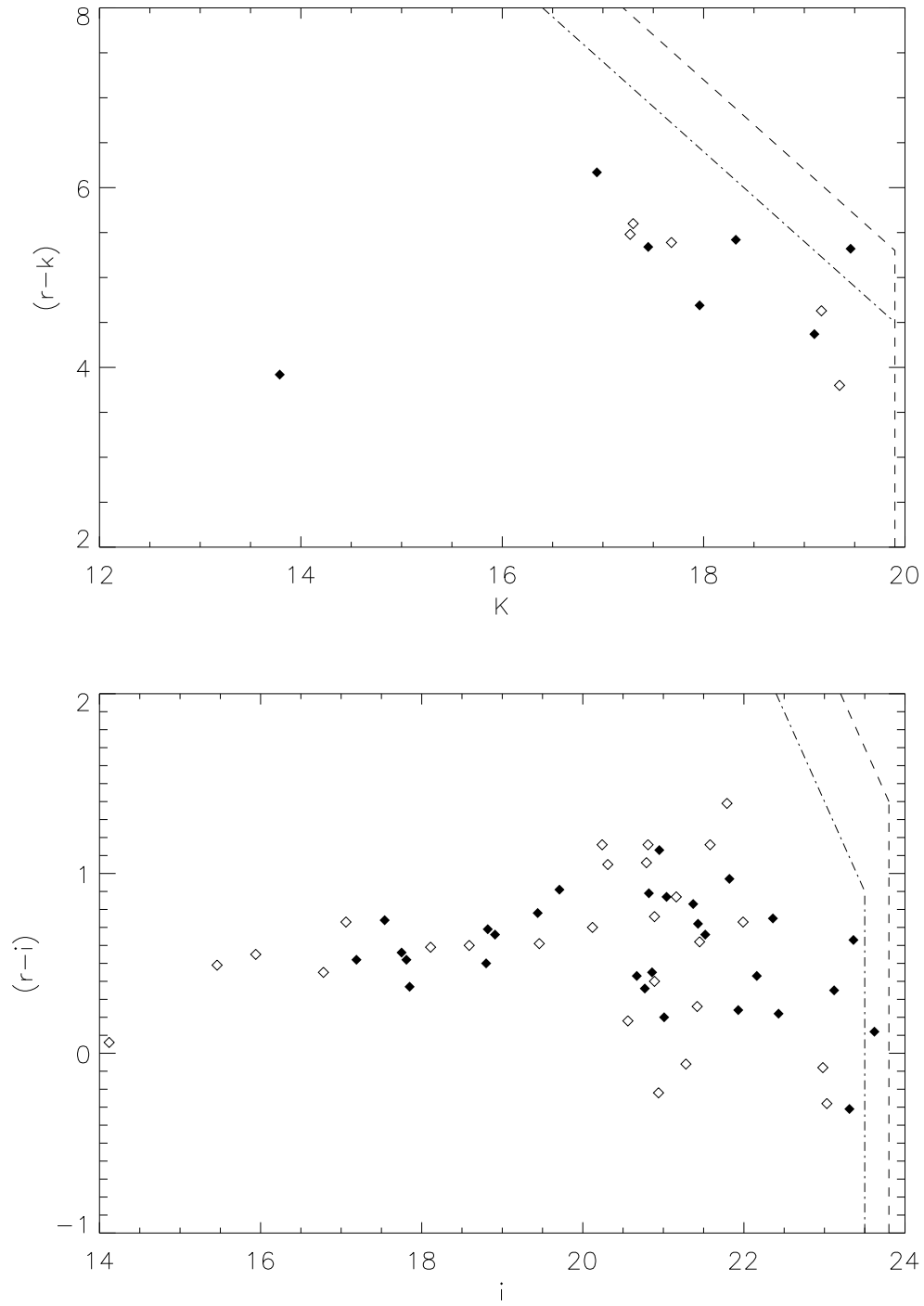

Figure 3.8: Colour magnitude diagrams and completeness limits for the Lynx (open diamonds; dot–dashed lines) and Hercules (filled diamonds; dashed lines) results.

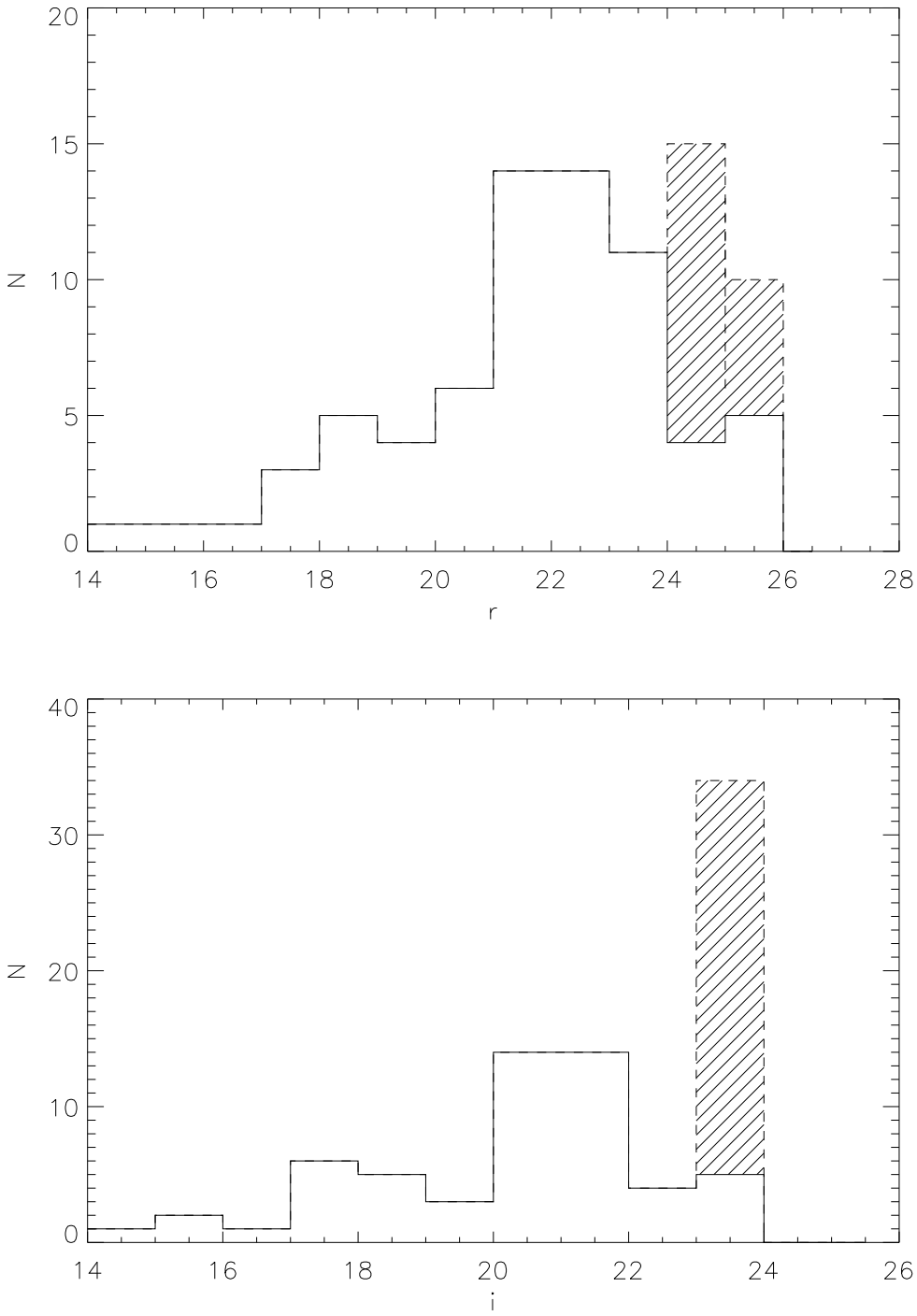

Figure 3.9: Magnitude distribution for the combined Lynx and Hercules sample in *r* (top) and *i* (bottom). Shaded regions show the magnitude limits.

CHAPTER 4

Spectroscopy and redshift estimation

4.1 Introduction

The redshifts for the radio sources identified in the Lynx and Hercules fields are vital in determining their cosmic evolution. Previously published spectroscopic or photometric redshifts (Waddington et al. 2000 and references therein; Bershady et al. 1994) already exist for 19 of the Hercules field sources, and 3 of the Lynx field sources had spectroscopic redshifts from the SDSS; the remaining sources had no previous redshift information. This section covers the spectroscopic observations made of a selection of the sample with the multi–object spectrograph DOLORES on the 3.58m Telescopio Nazionale Galileo (TNG), along with the redshift estimation methods used for the remaining sources.

4.2 TNG observations

DOLORES, the Device Optimized for the LOw RESolution, consists of one Loral back–illuminated and thinned 2048x2048 pixel CCD, with a scale of $0.275''$/pixel, resulting in a field of view of $9.4'$x $9.4'$. For multi–object spectroscopy (MOS) observations, rectangular masks with dimensions $6.0'$x $7.7'$, are used. Vertical slits of constant width (either $1.1''$ or $1.6''$) but varying length are drilled in the masks according to the positions of the various sources for

which spectra are required. These slits must not overlap along the y–axis; this would result in overlapping spectra.

Since some uncertainties in the astrometry, remained the 1.6″ slit was used for the observations. Only 10 masks were permitted per observing run, so it was decided to create 5 masks of varying position angle for each for the two fields, thus covering as many sources as possible. §4.2.1 below describes the mask creation and source selection process.

The DOLORES observations took place from 18th to 20th April 2004. All nights were photometric and the standard star Feige 34 was observed (with the 5″ slit) at regular intervals. Each mask observation consisted of several long exposures to avoid saturation of the CCD and to allow cosmic ray hits to be identified in the final spectra. The good weather conditions also allowed two observations with the 1.5″ longslit of three sources, (two in Hercules and one in Lynx) which were not included on the masks. All observations were carried out using the LR-R grism which has a wavelength range of 4470–10360Å and a resolution of 11.0Å. Full details of the observations can found in Table 4.1.

The masks for the Lynx field were, on average, observed for less time than those for Hercules due to the early setting time of the Lynx field.

Date	Mask	Exposure Time	Seeing (″)
18/04/04	L4	3x1200s	1.27
”	L5	3x1500s	1.27
”	H1	4x1500s	1.27
”	H3	3x1800s, 1x492s	1.27
19/04/04	L1	4x1500s	1.30
”	L3	2x1800s	1.30
”	H2	4x1800s	1.30
”	H5	3x1800s, 1x100s, 1x1200s	1.30
20/04/04	L2	3x1800s	0.76
”	H4	4x1800s	0.76
”	53w066 (Longslit)	3x1500s	0.76
”	55w160 (Longslit)	3x1000s	0.76

Table 4.1: Summary of TNG observations. L and H indicate a mask for the Lynx and Hercules fields respectively.

4.2.1 MOS Mask Creation

The mask limitations meant that not all the radio sources could be included in the observations, therefore a ranking system was introduced to ensure that the optimum number of interesting, high–redshift, sources were included. First, *r*–band magnitudes were estimated for all the sources using a rough $m_{\rm zpt}$ and ignoring the airmass and extinction corrections. These magnitudes could only be estimated as, at the time these observations were being prepared, only the non–photometric April 2003 WFC data were available.

The resulting magnitudes were then used to give an indication of the source redshifts through the r–z relation (Snellen et al., 1996), allowing those at high–redshift to be identified. All r–band magnitudes $\gtrsim$21 were therefore assumed to be at a redshift $\gtrsim$0.5. First rank sources were those with *r*–band magnitudes 21–22, which could be expected to have redshifts around 1.0; second rank were faint sources with *r*–magnitudes $>$22 which, whilst at higher redshift, were also comparatively less likely to be detected in the observation. Third and fourth ranks were applied to the remaining brightest sources at lower redshift. Those sources with previously published redshifts were obviously excluded from the rankings. Table 4.2 gives the full details of the ranking scheme.

The masks were then arranged such that the maximum number of first rank sources would be observed. This was done using an IDL script which allowed possible combinations of objects to be rotated, to determine the best fit parameters for each mask; Table 4.3 gives the final determined parameters. In the Lynx field 56% of all the sources were included, and of these 30% were first rank and 78% were second rank or above. The Hercules field was slightly better with 62% of the total number included; 80% classed as second rank or higher and 11% first rank.

Redshift	*r* magnitude	Rank
z$>$0.5	21-22	1
	$>$22	2
z$<$0.5	$<$21	3
	$<$15	4

Table 4.2: The ranking scheme for the radio sources.

Mask	Position Angle (°)	Centre (J2000)	Slit Length (″)
L1	0	8 45 53.78 +44 43 01.8	12
L2	20	8 45 24.20 +44 53 43.4	12
L3	0	8 44 55.98 +44 44 04.8	12
L4	-5	8 44 36.14 +44 46 50.1	10
L5	-95	8 44 00.00 +44 37 08.0	12
H1	-40	17 21 51.57 +49 50 31.3	11
H2	10	17 21 52.74 +50 09 11.4	12
H3	-15	17 20 14.86 +49 47 20.3	12
H4	-45	17 20 09.00 +50 01 33.6	12
H5	-90	17 19 05.97 +49 45 59.4	12

Table 4.3: The position angles and slit lengths determined for the masks. H and L again refer to the Hercules and Lynx fields respectively.

4.2.2 Data reduction

The initial data reduction of the DOLORES observations was very similar to the WFC reduction process; again the IRAF software package was used throughout. First a master bias was constructed for each night by averaging all the appropriate bias frames together; this was then subtracted from the rest of the exposures. The science, flat–field and arc data were then grouped according to mask. The calibration arc–lamp used was HeNeAr.

Next, an un–reduced science image for each mask was made by combining all the science exposures for an observation and rejecting pixels according to the readnoise and gain of the CCD. Flat–field images were made from the individual flat–field exposures in the same way. Two–dimensional strips, corresponding to each observed source, were then cut out of the combined science image, the combined flat–field and the original arc images. Each mask had now been sub–divided into the appropriate strips for the individual sources. For the rest of the reduction process the spectra, including the two longslits, were all treated individually.

The flat–field strips were normalised using the IRAF task *response* (part of the package *longslit*). The science strips were then flat–fielded by dividing them by the appropriate normalised flat. The two–dimensional science spectrum for each source was now fully reduced, but before the one–dimensional spectrum could be extracted, the strong, background, sky–lines needed to be removed. This was done using the *background* task; sample areas either side of the central continuum were selected, fit and subtracted, leaving a clean spectrum. This process was not perfect and some background residuals remained; these had to be taken into account when attempting to identify spectral features.

One–dimensional spectra were then extracted for each source. This was done using the task *apsum* to find the aperture (the continuum emission), fit a trace to it and perform the extraction. The arc spectra for each source were then extracted, using the source aperture as a reference in *apsum*. Lines in the arc spectra were then identified and the resulting calibration was applied to the science spectra, thus providing them with wavelength information. However it became obvious that these wavelength calibrations were inaccurate, mainly because there were significant regions in the arc–lamp spectra where there were no strong lines; this led to ambiguous fits to the science spectrum. The solution to this was to add sky–lines ([OI] at 6300.3Å and 5579Å and Na at 5896Å), extracted from the un–background subtracted science spectra, to cover the missing regions. This enhanced arc–line wavelength coverage resulted in a more accurate final calibration for the data.

The spectra were then flux calibrated using the standard star Feige 34. The spectra of the standard were reduced and extracted in the same way as that of the sources. The resulting spectra (one for the first and third nights and two for the second) were passed through the packages *standard* and *sensfunc* to calculate the sensitivity function and form the flux calibration which could then be applied to the science spectra.

The standard star spectra were also used to remove the background sky absorption lines which were present in the data. First a polynomial was fit to the standard star spectrum, excluding the sky–absorption lines, observed closest to the source spectra to be cleaned. Next, the original spectrum was divided by this fit leaving a normalised spectrum containing sky–absorption lines only which was then scaled to the source spectrum. Finally the package *telluric* was used to divide the object spectrum by the scaled, normalised, standard spectrum whilst retaining the flux values. The object spectrum should now be free of sky absorption features. For this process to be most effective a standard star spectrum should have been observed after each mask since the depth and shape of the sky–absorption lines are strongly dependent on airmass and observing conditions, but that level of accuracy was not required for the purposes of these observations and would have introduced unnecessary overheads.

4.3 Spectroscopic Results

The spectroscopic observations included 41 sources in total; 17 in the Hercules field and 24 in the Lynx field. The resulting spectra yielded 3 and 11 definite redshifts in the Hercules and Lynx fields respectively. A single line was detected in a further 4 spectra in Lynx and 2 in Hercules; this mainly provided a redshift ‘best–guess’ only, except where the line identification was obvious (e.g. broad MgII). 65% of the redshifts were from emission lines and the

remainder were from absorption lines only. These results are given more fully in Table 4.4 and the spectra for sources with one or more detected lines or absorption features, are shown in Figure 4.1. The list of sources observed with DOLORES but for which no lines were detected can be found in Table **??**.

4.3.1 Notes on individual sources

53w054b – This spectrum is not of the optical counterpart to the radio source; the optical counterpart was misidentified in the INT imaging and was only detected in the later *K*–band observations. This spectrum was actually of a source 3″ to the north.

53w070 – The single broad line is identified as MgII, giving a redshift of 1.32.

53w086b – The 4000Å break can be seen in this spectrum but no lines are convincingly detected. The redshift of 0.73 is consistent with the *r*–band magnitude estimate of 0.81.

53w089 – Waddington et al. (2000) detect [OII] and [OIII] for this source, giving a redshift of 0.635, but nothing is detected in these (shallower) observations.

66w027 – The strong, clear, lines (such as Hα and [SII]) present give a firm redshift for this source.

66w031 – The identification of single strong line as [OII] at a redshift of 0.81 is consistent with the redshift estimated from the *r*–band magnitude (0.97).

66w036 – No line data are quoted for the G–band absorption line for this source, as the negative extent of the flux density suggests that it is contaminated by noise.

55w116 – The 4000Å break and CaH+K absorption lines present give a firm redshift for this source.

55w124 – The single broad line is identified as MgII, but this is uncertain.

55w128 – The weakly detected single line is identified as [OII], giving a redshift of 1.19, which is consistent with its non–detection in the *K*–band observations.

55w131 – The single line is identified as [OII] giving a redshift of 1.12, which is consistent with the redshift of 1.15 estimated using the r–z relation.

55w137 – The strong, clear, lines (such as Hα and [SII]) present give a firm redshift for this source.

55w140 – The redshift of 1.68 is from a single, broad line, identified as MgII. It should also be noted that a section of the spectrum has been removed due to the presence of residuals from the sky subtraction process.

55w149 – Only one emission line ([OIII]) is detected for this source, but the additional presence of strong absorption lines, such as Na D, mean that the redshift is secure.

55w150 – The detection of the [OIII] doublet gives a firm redshift for this source.

55w154 – No emission lines are detected for this source, but the presence of strong absorption lines such as CaH+K and mg B, indicate that the redshift is secure.

55w157 – A weak 4000Å break, combined with the detection of the CaK and Hγ absorption lines give a firm redshift for this source.

55w160 – The 4000Å break and CaH+K absorption lines detected give a firm redshift for this source.

60w016 – The 4000Å break and CaH+K absorption lines detected give a firm redshift for this source.

60w024 – The detection of the CaH+K absorption lines, along with the [OII] emission line give a firm redshift for this source.

60w039 – The two observations of this source on masks L3 and L4 have been combined together with the *scomb* task in *iraf*.

60w055 – The strong detection of the [OII] emission line, combined with several absorption lines give a firm redshift for this source.

Mask	Source	λ (Å)	Line	Flux ($\times 10^{-16}$erg s^{-1}cm^{-2})	$\Delta_{\rm fwhm}$ (kms^{-1})	W (Å)	z	Final z
Hercules								
H4	53w070	6480.5	MgII	0.48 ± 0.07	–	27 ± 5	1.315 ± 0.001	1.315 ± 0.001
H1	53w086b	–	4000Å break	–	–	–	0.73 ± 0.01	0.73 ± 0.05
H4	66w027	7136.6	Hα	16.9 ± 2.55	1091 ± 228	39 ± 4	0.087 ± 0.001	0.086 ± 0.002
		7136.5	NII	6.9 ± 2.55	1074 ± 228	38 ± 4	0.084 ± 0.001	
		7311.7	[SII]	$\sim$3.94	–	$\sim$6	0.088 ± 0.001	
		6401	NaD	–	–	–	–	
		5282	Hβ	10.77 ± 1.94	–	17 ± 3	–	
H3	66w031	6751.8	[OII]	2.47 ± 0.25	987 ± 251	508 ± 205	0.812 ± 0.001	0.812 ± 0.001
		8822	Hβ	–	–	–		
H3	66w036	8273.4	G–band	–	–	–	0.924 ± 0.001	0.924 ± 0.001
		7581.4	CaH	–	–	–	0.927 ± 0.012	
		7650	CaK	–	–	–	–	
Lynx								
L5	55w116	7281.5	CaH	–	–	–	0.854 ± 0.031	0.851 ± 0.007
		7343.4	CaK	–	–	–	0.851 ± 0.008	
L5	55w124	6536.5	MgII	4.85 ± 0.49	5471 ± 894	39 ± 4	1.335 ± 0.003	1.335 ± 0.003
L4	55w128	8159.3	[OII]	0.17 ± 0.03	–	–	1.189 ± 0.001	1.189 ± 0.001
L4	55w131	7917.1	[OII]	0.75 ± 0.10	409 ± 281	–	1.124 ± 0.001	1.124 ± 0.001
L3	55w137	5755.8	[OIII]	1.64 ± 0.22	–	4 ± 1	0.150 ± 0.001	0.151 ± 0.001
		5703.8	[OIII]	9.94 ± 2.56	–	26 ± 7		
		7567.1	Hα	11.7 ± 2.63	2000 ± 266	37 ± 4	0.153 ± 0.001	
		7575.2	[NII]	13.1 ± 2.56	1975 ± 265	36 ± 4	0.150 ± 0.001	
		7738.4	[SII]	2.77 ± 0.31	–	–	0.152 ± 0.001	
		6778.4	NaD	–	–	–	0.150 ± 0.001	
		7248.8	[OI]	0.57 ± 0.15	–	–	0.151 ± 0.001	

Table 4.4: Spectroscopic redshifts and line information for the Hercules and Lynx fields.

Mask	Source	λ (Å)	Line	Flux ($\times 10^{-16}$erg s^{-1}cm^{-2})	$\Delta_{\rm fwhm}$ (kms^{-1})	W (Å)	z	Final z
L3	55w140	7514.3	MgII	12.10 ± 1.40	6192 ± 2647	36 ± 4	1.685 ± 0.012	1.685 ± 0.012
L2	55w149	6793.7	NaD	–	–	–	0.152 ± 0.001	0.151 ± 0.001
		5950.6	Mgb	–	–	–	0.150 ± 0.001	
		5747.7	[OIII]	–	–	–	–	
		5601.2	Hβ	–	–	–	–	
L2	55w150	7359.3	[OIII]	6.16 ± 0.64	727 ± 233	67 ± 8	0.470 ± 0.001	0.470 ± 0.001
		7292.6	[OIII]	1.65 ± 0.21	–	22 ± 3	0.471 ± 0.001	
		7138.4	Hβ	0.96 ± 0.16	–	21 ± 4	0.469 ± 0.001	
		9660.4	Hα	–	–	–	–	
L1	55w154	6475.6	Hβ	–	–	–	0.332 ± 0.001	0.330 ± 0.001
		6891.1	Mgb	–	–	–	0.332 ± 0.001	
		5717.9	G–band	–	–	–	0.330 ± 0.002	
		5227.3	CaH	–	–	–	0.329 ± 0.001	
		5277.5	CaK	–	–	–	–	
		5456.5	Hδ	–	–	–	–	
L1	55w157	6760.2	Hγ	–	–	–	0.558 ± 0.001	0.559 ± 0.002
		6201.4	CaK	–	–	–	0.563 ± 0.001	
LS	55w160	6292.3	CaH	–	–	–	0.600 ± 0.002	0.600 ± 0.002
		6352.0	CaK	–	–	–	–	
L5	60w016	7237.0	CaH	–	–	–	0.840 ± 0.001	0.840 ± 0.001
		7332.7	CaK	–	–	–	–	
L5	60w024	6609.9	[OII]	0.41 ± 0.06	814 ± 374	13 ± 2	0.774 ± 0.001	0.774 ± 0.001
		6974.2	CaH	–	–	–	–	
		7032.2	CaK	–	–	–	–	

Table 4.4

Mask	Source	λ (Å)	Line	Flux ($\times 10^{-16}$erg s^{-1}cm^{-2})	$\Delta_{\rm fwhm}$ (kms^{-1})	W (Å)	z	Final z
L3/4	60w039	7562.2	Hα	51.0 ± 6.18	939 ± 223	47 ± 5	0.152 ± 0.001	0.151 ± 0.001
		7585.2	[NII]	11.4 ± 6.12	925 ± 223	46 ± 5	0.149 ± 0.001	
		7738.7	[SII]	8.32 ± 1.33	–	–	0.152 ± 0.002	
		6786.8	NaD	–	–	–	0.151 ± 0.001	
		5597.6	Hβ	–	–	–	0.152 ± 0.001	
L2	60w055	6405.0	[OII]	1.40 ± 0.14	529 ± 255	45 ± 5	0.718 ± 0.001	0.718 ± 0.005
		6754.4	CaH	–	–	–	0.717 ± 0.001	
		6818.8	CaK	–	–	–	–	
		7397.9	G–band	–	–	–	–	
		7437.8	Hγ	–	–	–	–	

Table 4.4

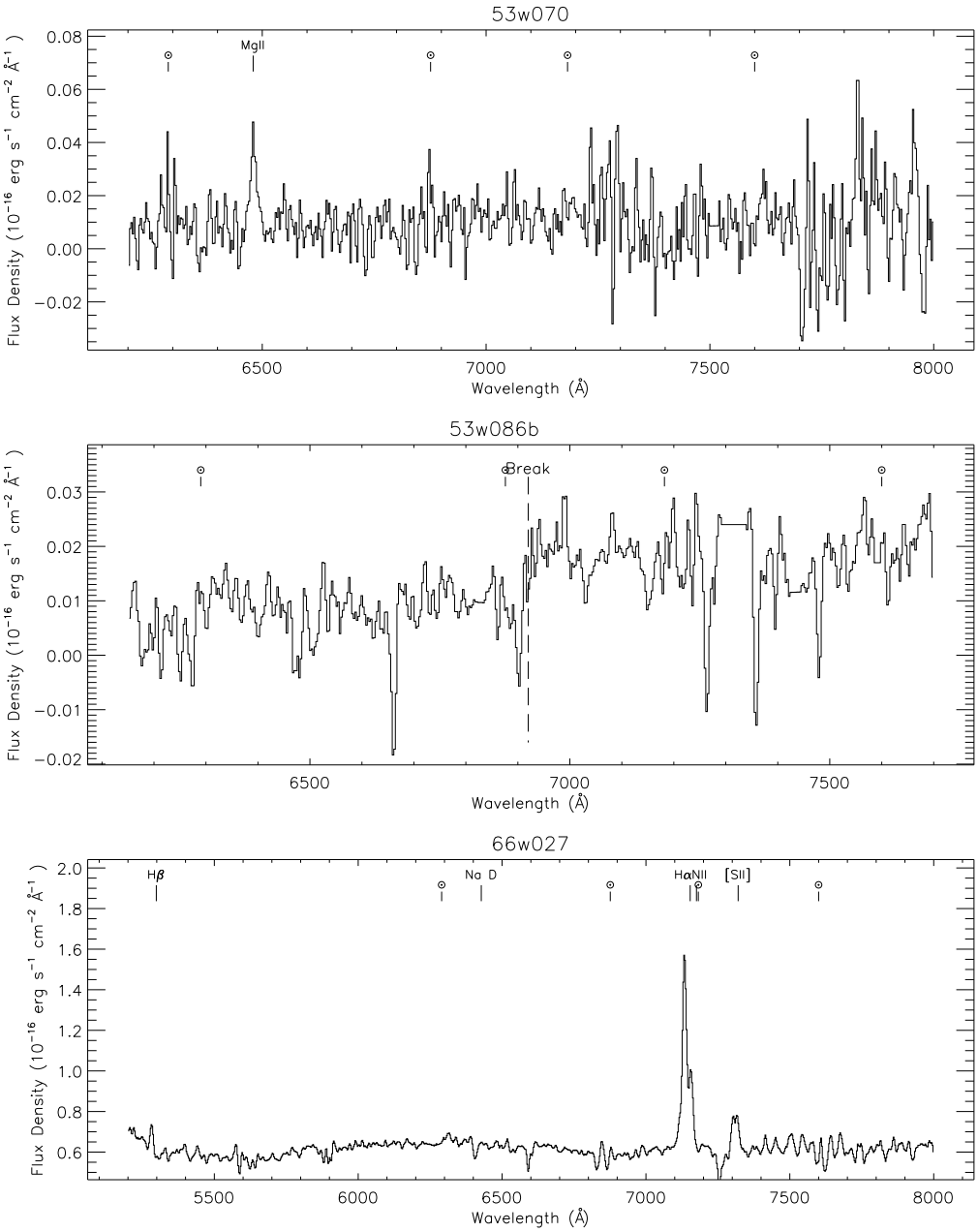

Figure 4.1: The spectra resulting from the MOS observations. Residual sky features are marked with a ⊙ and dashed lines indicate the position of the 4000Å break. 2D spectra are also shown in cases where the line detection is weak.

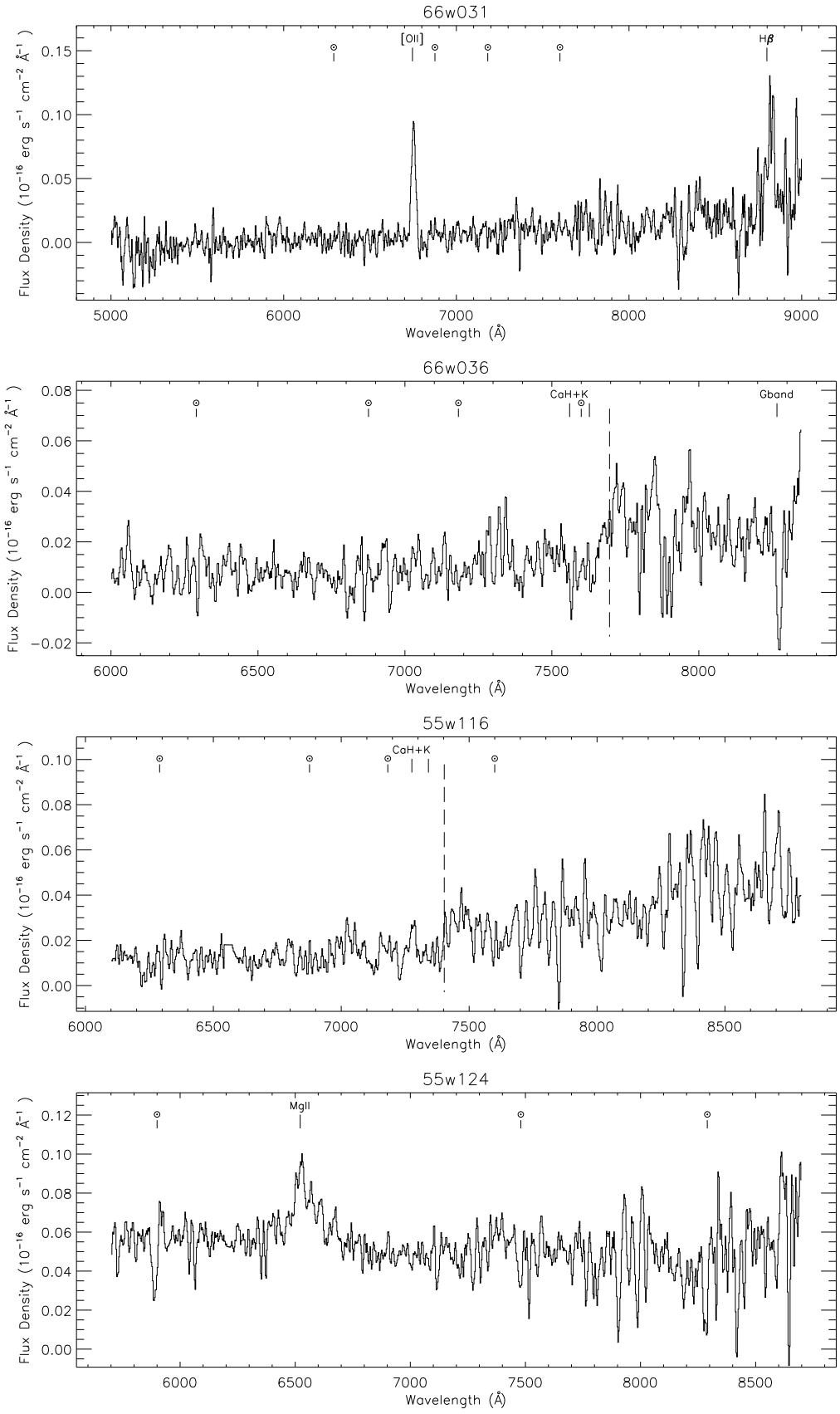
66w031
[OII]
Hβ
Flux Density (10^{-16} erg s^{-1} cm^{-2} Å^{-1})
Wavelength (Å)
66w036
CaH+K
Gband
Flux Density (10^{-16} erg s^{-1} cm^{-2} Å^{-1})
Wavelength (Å)
55w116
CaH+K
Flux Density (10^{-16} erg s^{-1} cm^{-2} Å^{-1})
Wavelength (Å)
55w124
MgII
Flux Density (10^{-16} erg s^{-1} cm^{-2} Å^{-1})
Wavelength (Å)

Figure 4.1

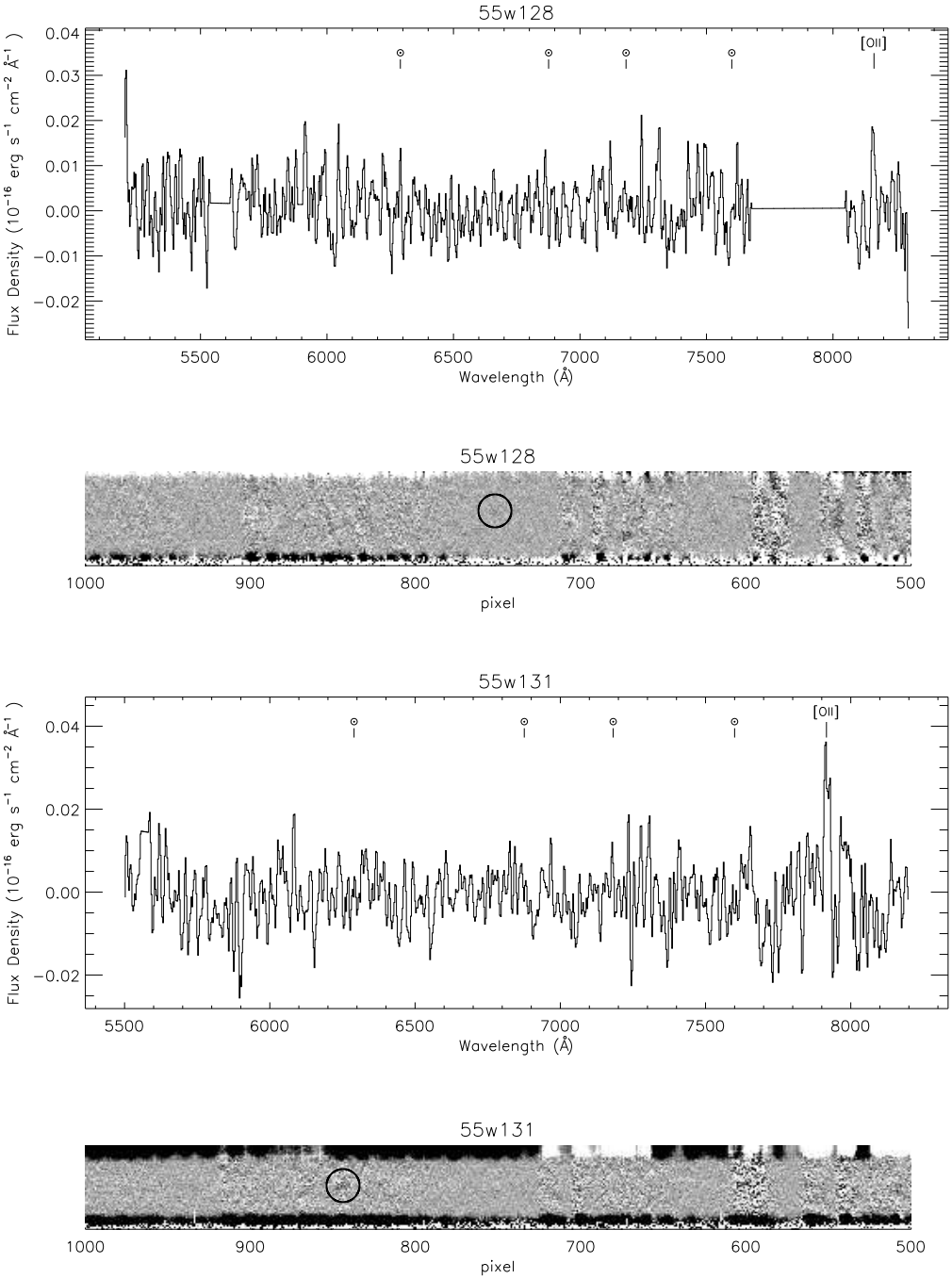
55w128
[OII]
Flux Density (10^{-16} erg s^{-1} cm^{-2} Å^{-1})
0.04
0.03
0.02
0.01
0.00
−0.01
−0.02
5500
6000
6500
7000
7500
8000
Wavelength (Å)
55w128
1000
900
800
700
600
500
pixel
55w131
[OII]
Flux Density (10^{-16} erg s^{-1} cm^{-2} Å^{-1})
0.04
0.02
0.00
−0.02
5500
6000
6500
7000
7500
8000
Wavelength (Å)
55w131
1000
900
800
700
600
500
pixel

Figure 4.1

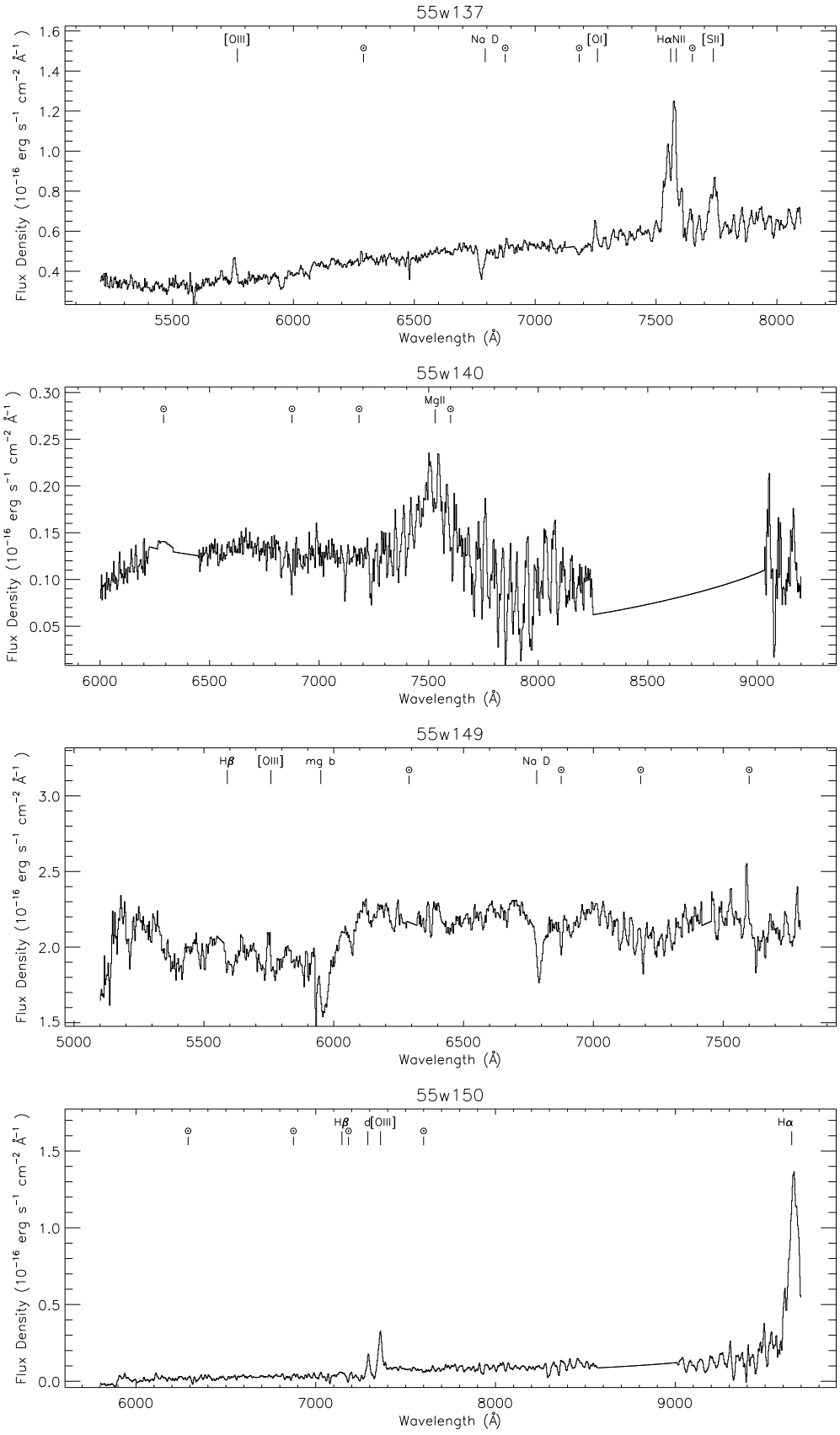
55w137
[OIII]
Na D
[OI]
HαNII
[SII]
Flux Density (10^{-16} erg s^{-1} cm^{-2} Å^{-1})
Wavelength (Å)
55w140
MgII
Flux Density (10^{-16} erg s^{-1} cm^{-2} Å^{-1})
Wavelength (Å)
55w149
Hβ
[OIII]
mg b
Na D
Flux Density (10^{-16} erg s^{-1} cm^{-2} Å^{-1})
Wavelength (Å)
55w150
Hβ
d[OIII]
Hα
Flux Density (10^{-16} erg s^{-1} cm^{-2} Å^{-1})
Wavelength (Å)

Figure 4.1

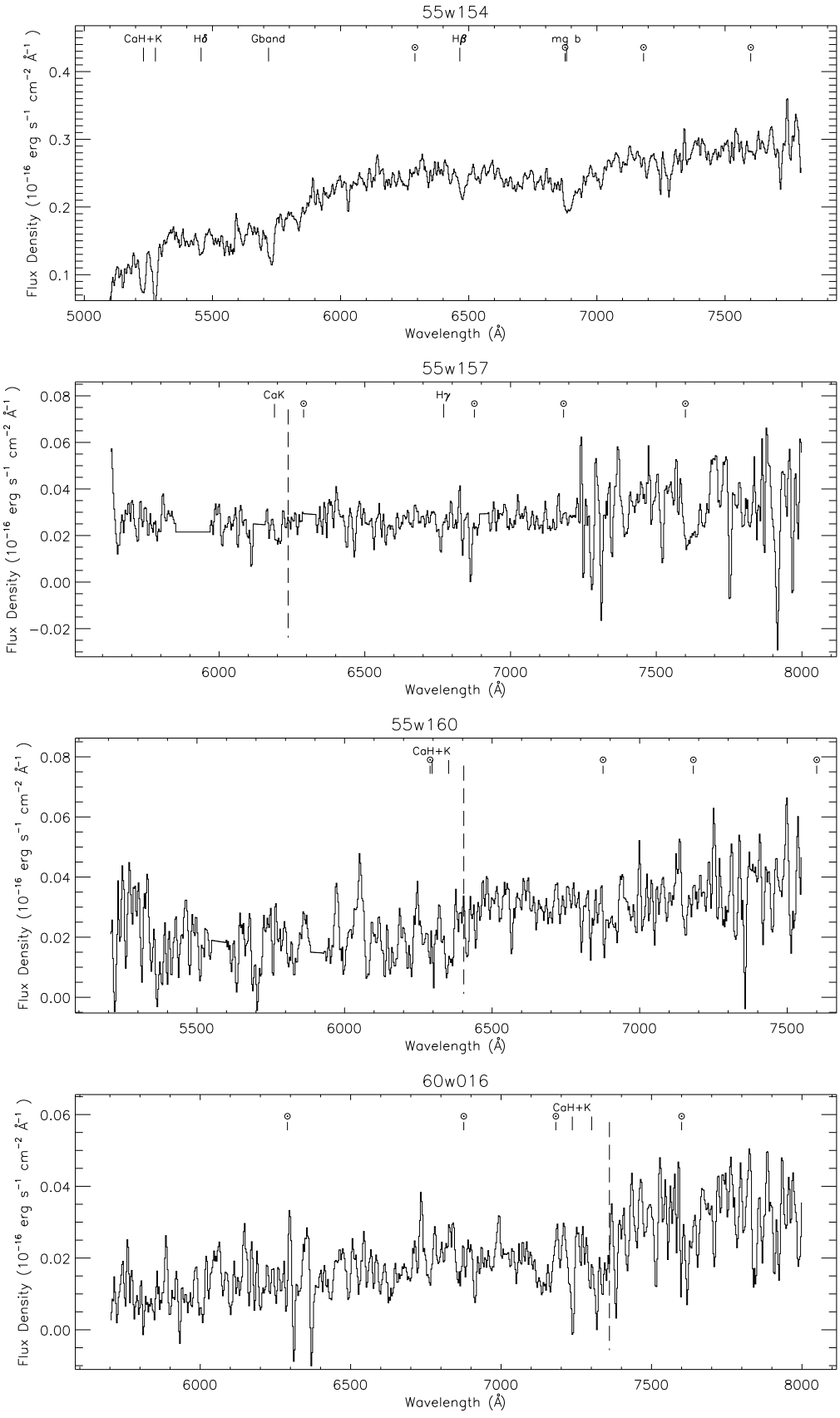
55w154
CaH+K
Hδ
Gband
Hβ
mg b
Flux Density (10^{-16} erg s^{-1} cm^{-2} Å^{-1})
Wavelength (Å)
55w157
CaK
Hγ
Flux Density (10^{-16} erg s^{-1} cm^{-2} Å^{-1})
Wavelength (Å)
55w160
CaH+K
Flux Density (10^{-16} erg s^{-1} cm^{-2} Å^{-1})
Wavelength (Å)
60w016
CaH+K
Flux Density (10^{-16} erg s^{-1} cm^{-2} Å^{-1})
Wavelength (Å)

Figure 4.1

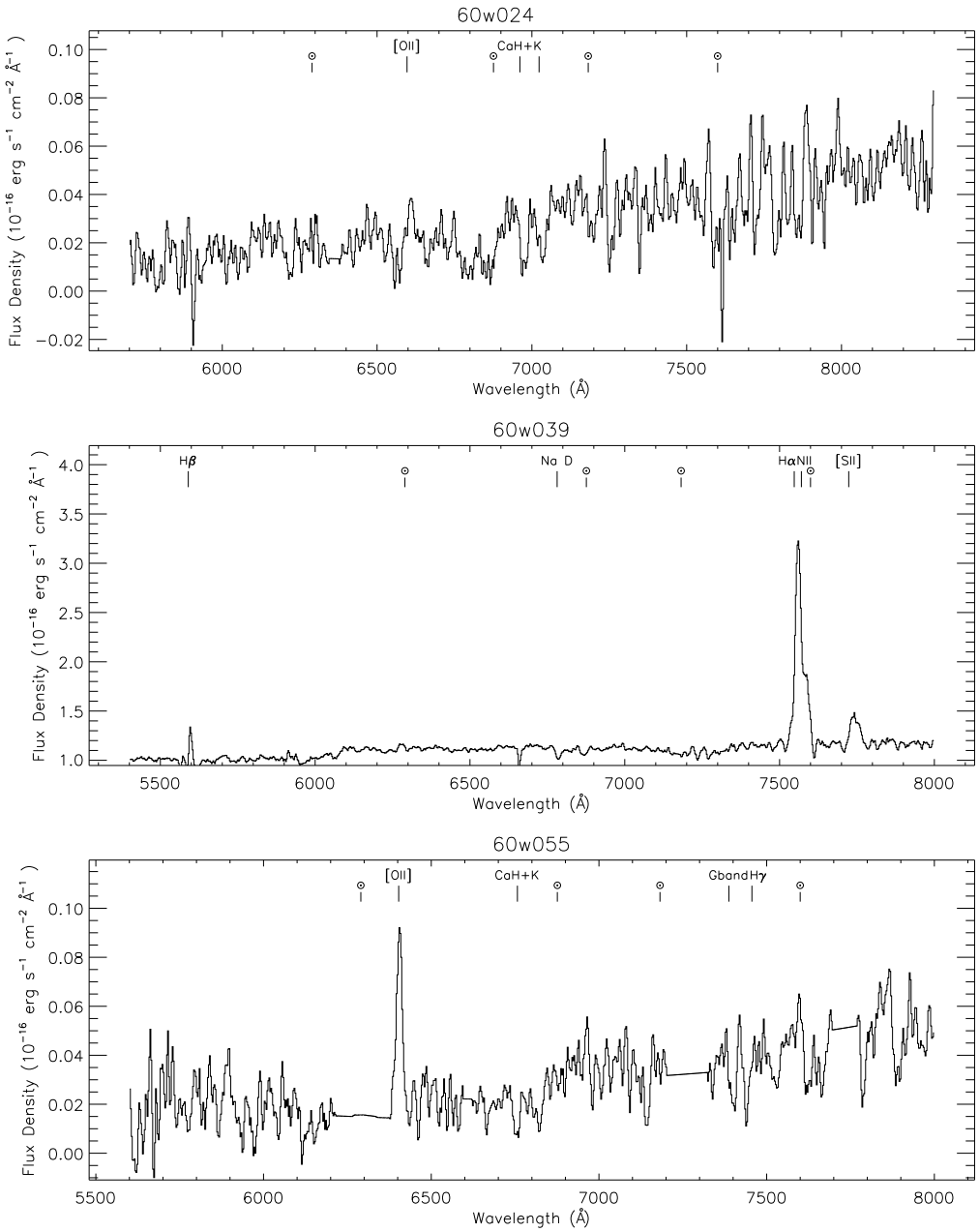
60w024
[OII]
CaH+K
Flux Density (10^{-16} erg s^{-1} cm^{-2} Å^{-1})
Wavelength (Å)
60w039
Hβ
Na D
HαNII
[SII]
Flux Density (10^{-16} erg s^{-1} cm^{-2} Å^{-1})
Wavelength (Å)
60w055
[OII]
CaH+K
GbandHγ
Flux Density (10^{-16} erg s^{-1} cm^{-2} Å^{-1})
Wavelength (Å)

Figure 4.1

Mask	Source
H1	53w084, 53w086a, 66w058
H2	53w082, 53w087, 53w088, 53w089
H3	53w069
H4	66w035
H5	53w054a, 53w057, 53w061
L1	55w156, 60w071
L2	55w147
L3	55w138
L4	55w127, 55w132, 60w032
L5	55w118, 55w123

Table 4.5: The sources targeted in the DOLORES observations with no lines detected.

4.4 Cleaning the sample: identifying quasars and starburst galaxies

Not all the radio sources detected in the two fields will be radio galaxies; some contamination of the sample by quasars and starburst galaxies is inevitable. Jackson & Wall (1999) predicted the radio sample composition for a given flux density limit. Their Figure 17, reproduced here as Figure 4.2, suggests that at the Lynx and Hercules sample limits up to 30% of the radio sources detected may be starburst galaxies and ∼5% may be quasars.

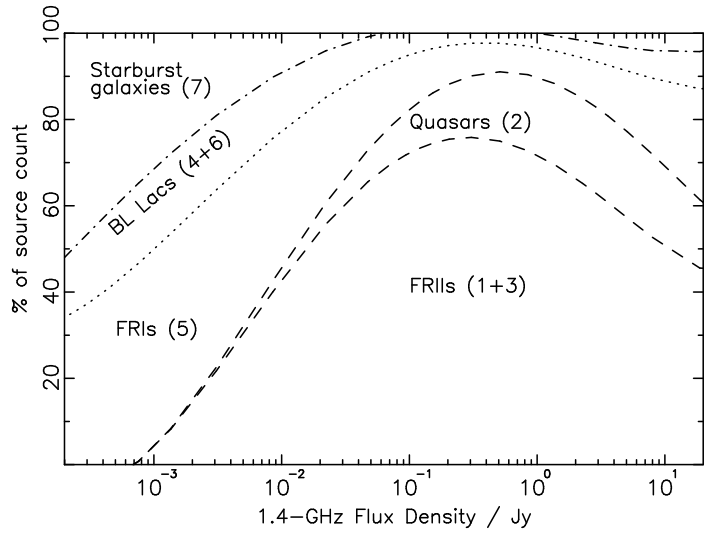

Figure 4.2: Predicted survey composition from Jackson & Wall (1999). The regions associated with each population are indicated by name (e.g. quasars, BL Lacs) and numbers in brackets refer to the different source subpopulations (see Jackson & Wall for details).

These objects need to be identified and, in the case of the starburst galaxies, removed from the

sample. This section describes the methods used for the identification of these objects and the sources found in these ways.

4.4.1 Identifying starburst galaxies

The radio emission from starburst galaxies is mainly due to synchrotron emission from supernovae instead of, as in radio galaxies, accretion onto a supermassive black hole. The radio luminosity function of Best et al. (2005, Figure 1.7 in Chapter 1.1) shows that, in general, the radio power of these galaxies is lower than that of AGN and that it is only at these very low radio powers ($\sim 10^{23}$ WHz^{-1}) that their number density dominates; this suggests that only low–power sources need to be considered here. There were 16 radio sources in the sample which have $P_{\rm rad} \leq 10^{24}$ WHz^{-1} (based on their estimated redshift) and were therefore possible starburst galaxy candidates.

The main way to distinguish between radio and starburst galaxies is through examination of the emission line ratios of their spectra. Kauffmann et al. (2003) classify a source as an AGN if

$$\log(f[\mathrm{OIII}]/f(\mathrm{H}\beta)) > \frac{0.61}{\log(f[\mathrm{NII}]/f(\mathrm{H}\alpha)) - 0.05} + 1.3, \tag{4.1}$$

where $f[\mathrm{OIII}]$, $f(\mathrm{H}\beta)$, $f[\mathrm{NII}]$ and $f(\mathrm{H}\alpha)$ are the fluxes of the respective emission lines; [OIII] (5007Å), [NII] (6583Å), H_β (4861Å) and H_α (6563Å). This is illustrated by their diagnostic diagram, reproduced here as Figure 4.3. This classification method obviously requires a source to have spectroscopic data with the right lines detected. Of the 16 candidates, 11 have DOLORES spectra but none have all four of the necessary emission lines. However, 3 candidates (66w027, 55w137 and 60w039) have both [NII] and Hα detected and one, 55w150, has both [OIII] and Hβ, hence an indication of their classifications is possible; the results of this are outlined below and the fluxes for these lines can be found in Table 4.4. A further two candidates, 55w135 and 60w084, were included in the spectroscopic observations of the SDSS. The resulting spectrum for 55w135 clearly shows it to be a starburst galaxy since $f(\mathrm{H}\alpha) \gg f[\mathrm{NII}]$ and $f(\mathrm{H}\beta) \gg f[\mathrm{OIII}]$ whereas the spectrum for 60w084 suggests that it is an AGN since $f(\mathrm{H}\alpha) \sim f[\mathrm{NII}]$ and $f[\mathrm{OIII}] \gg f(\mathrm{H}\beta)$.

- **66w027** (z=0.086, $\mathrm{P}_{1.4\mathrm{GHz}}$=$10^{22.00}$WHz^{-1}) – $\log(f[\mathrm{NII}]/f(\mathrm{H}\alpha)) = -0.38$ for this source which suggests that it is a starburst galaxy but is not sufficient to be unambiguous. However, the Hβ line was also detected whilst the [OIII] line was not, implying that $\log(f[\mathrm{OIII}]/f(\mathrm{H}\beta)) < 0.0$ and that this source is a starburst galaxy.

- **55w137** (z=0.151, $\mathrm{P}_{1.4\mathrm{GHz}}$=$10^{22.97}$WHz^{-1}) – $\log(f[\mathrm{NII}]/f(\mathrm{H}\alpha)) = 0.05$ for this

source which places it firmly in the AGN region of Figure 4.3. This is further supported by the indication of extended radio emission visible in the radio image.

- **60w039** (z=0.151, $P_{1.4GHz}$=$10^{22.58}$WHz^{-1}) – $\log(f[\mathrm{NII}]/f(\mathrm{H}\alpha)) = -0.65$ for this source which places it firmly in the starburst region of the diagram.
- **55w150** (z=0.470, $P_{1.4GHz}$=$10^{23.86}$WHz^{-1}) – $\log(f[\mathrm{OIII}]/f(\mathrm{H}\beta)) = 0.78$ for this source which, coupled with the high radio power, strongly suggests that it is an AGN.

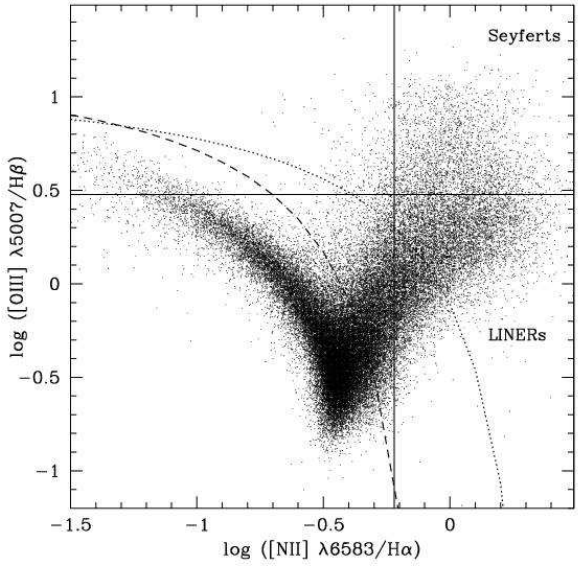

Figure 4.3: The diagnostic diagram for AGN from Kauffmann et al. (2003). The dashed curve marks the demarcation between AGN and starburst galaxies given in Equation 4.1; the dotted curve marks a previous demarcation by Kewley et al. (2001).

The five remaining starburst candidates with spectra can be classified by comparing their $f([\mathrm{OII}])$ and radio fluxes. Best et al. (2002) derive a rough relationship between these two fluxes for starburst galaxies by equating the theoretical correlation between mean star–formation rate and [OII] luminosity (Barbaro and Poggianti, 1997) with that for radio (Condon and Yin, 1990) giving

$$\frac{S_{1.4\mathrm{GHz}}}{\mu\mathrm{Jy}} = 11.0\frac{f[\mathrm{OII}]}{10^{-16}\mathrm{ergs}^{-1}\mathrm{cm}^{-2}}(1+z)^{-0.8} \tag{4.2}$$

where $S_{1.4\mathrm{GHz}}$ is the radio flux of the object in question at a frequency of 1.4GHz and z is the redshift. It should be noted that dust extinction can cause the measurement of the star–formation, from the [OIII] flux, to be underestimated.

The radio–[OII] flux relationship for AGN is an extrapolation of the results of Willott et al. (1999) for powerful radio galaxies to the sub–mJy levels of these sources. This gives, after converting to 1.4 GHz (assuming a spectral index of 0.8),

$$\frac{S_{1.4\mathrm{GHz}}}{\mu\mathrm{Jy}} = 4.7 \times 10^4 \Big(\frac{f[\mathrm{OII}]}{10^{-16}\mathrm{ergs}^{-1}\mathrm{cm}^{-2}} \Big)^{1.45} \tag{4.3}$$

It should be noted however, that AGN show considerable scatter around this line.

Equations 4.2 and 4.3 are shown in Figure 4.4. Overplotted are the [OII] and radio fluxes for 60w055 and 60w024. The remaining 3 sources (60w016, 55w160 and 55w157) lack an [OII] detection so an upper limit for their [OII] flux is plotted instead. It is clear from inspection of this diagram that all these sources lie well below the starburst region, suggesting that they are AGN. This is in accordance with their radio powers, all of which are $> 10^{23.3}$ WHz^{-1}.

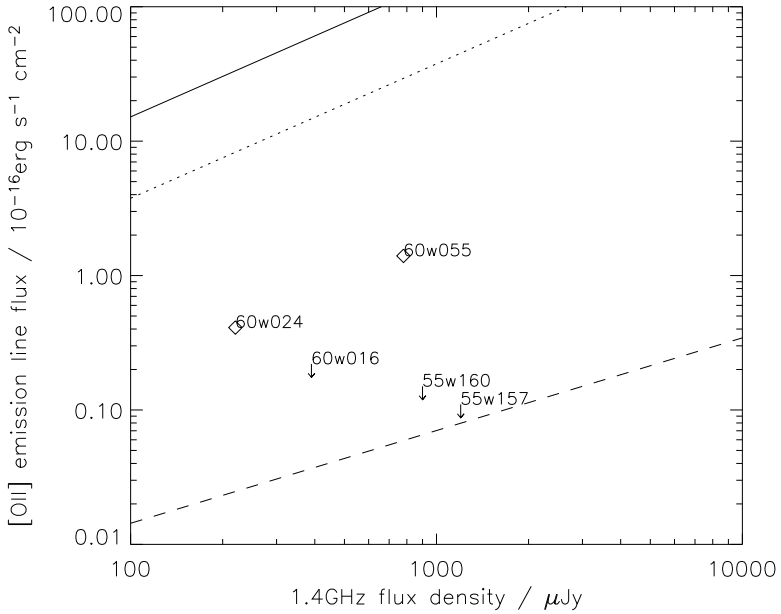

Figure 4.4: Radio–[OII] flux relationships for starburst galaxies (solid line) and radio galaxies (dashed line). The dotted line shows the effect of two magnitudes of dust extinction in the measurement of the star formation rate. Overplotted are the starburst candidate sources for classification.

As a further check on these classifications a similar line–radio flux diagram can be plotted for the combined Hα+[NII] fluxes. The Hα+[NII]–radio flux relation (Equation 4.4) comes from Owen et al. (1999) and is again derived by equating two relations for star formation rate.

$$\frac{S_\nu}{\mu\mathrm{Jy}} = 5.24 \frac{f(\mathrm{H}\alpha + [\mathrm{NII}])}{10^{-16}\mathrm{ergs}^{-1}\mathrm{cm}^{-2}} (1+z)^{-0.8} \tag{4.4}$$

The AGN relation for Hα+[NII] comes from Zirbel & Baum (1995). They derive separate relations for FRI and FRII radio galaxies; their FRI relation, converted to 1.4 GHz, is used here (Equation 4.5) as it is more appropriate for these low power starburst candidates.

$$\frac{S_\nu}{\mu\mathrm{Jy}} = 745.9\Big(\frac{f(\mathrm{H}\alpha + [\mathrm{NII}])}{10^{-16}\mathrm{ergs}^{-1}\mathrm{cm}^{-2}}\Big)^{3.57} \tag{4.5}$$

Figure 4.5 shows the diagram for Hα+[NII] flux with all the sources classified using spectroscopic methods overplotted. The sources with [OII] fluxes or upper limits were converted to Hα+[NII] flux using the ratio (Hα+[NII])/[OII]=4.0 (McCarthy, 1993). As expected the two sources identified as starburst galaxies lie in the starburst region with the remainder below.

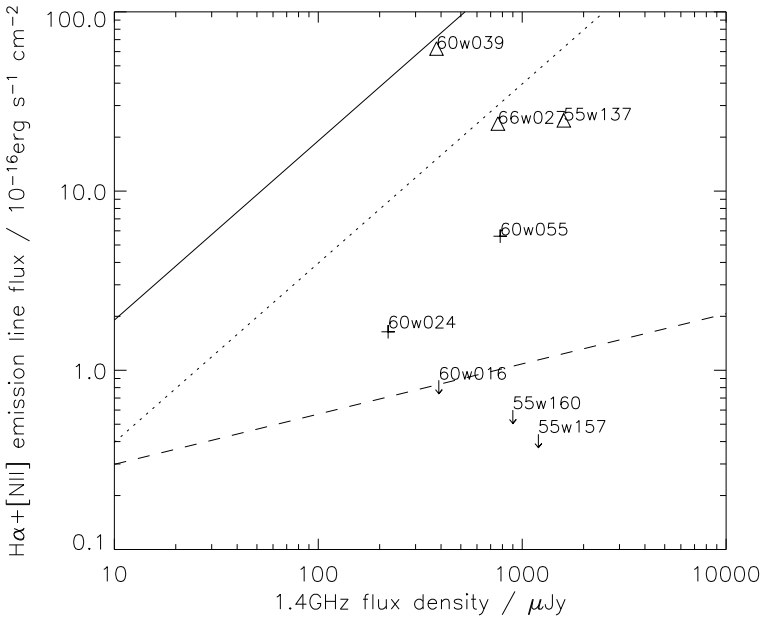

Figure 4.5: Radio–Hα+[NII] flux relationships for starburst galaxies (solid line) and radio galaxies (dashed line) with the dotted line again showing two magnitudes of dust extinction. Overplotted are all the sources classified spectroscopically so far. Crosses and arrows indicate [OII] fluxes and upper limits and triangles indicate Hα+[NII] fluxes.

This leaves 5 candidates still to be classified. Two (66w009b and 55w127) have radio powers that are $\leq 10^{23.01}\mathrm{WHz}^{-1}$ which strongly suggests that these are also starburst galaxies. The final three candidate sources (55w118, 55w122 and 55w161) all have $P \gtrsim 10^{23}\mathrm{WHz}^{-1}$ which is comparable with the powers of candidates already identified as AGN. Therefore, on the balance of probability, these three objects are classified as AGN also.

In summary, therefore, there are five starburst galaxies which need to be removed from the sample: 66w027, 66w009b, 55w127, 55w135 and 60w039.

4.4.2 Identifying quasars

Possible quasars in the sample were identified in three ways; firstly on the basis of their point–like appearance (determined by measuring the FWHM using *gaia*) in the *r*–band images, secondly by looking for broad lines in the available spectra and thirdly by examining their optical $(r-i)$ colours. The spectral method can be misleading as radio galaxies can also have lines as broad as $\sim$1000 kms^{-1} therefore a source is only classified as a quasar here if it has lines which are $\gg$1000 kms^{-1}. The quasar candidates selected in this way are described below.

- **53w061** – This source has a pointlike appearance (FWHM of 1.53″ in *r*–band, c.f. seeing of 1.5″) and a blue $(r-i)$ colour of 0.36. It is also classed as a likely quasar (Q?) by Kron et al. (1985) on the basis of its colour. It was included in the DOLORES observations but no continuum was detected. It is therefore classed as a quasar here.

- **53w065** – This source has a blue $(r-i)$ colour of -0.31 but Waddington et al. (2001) classify it as a galaxy on the basis of the narrow lines seen in its spectrum.

- **53w070** – This source does not have a blue $(r-i)$ colour, and its MgII line is not very broad. It is therefore classed as a galaxy.

- **53w075** – This source is classified as a quasar by Kron et al. (1985) on the basis of its spectrum; this is supported by its pointlike appearance.

- **53w080** – This source is classified as a quasar by Kron et al. (1985) on the basis of its spectrum; this is supported by its pointlike appearance.

- **55w121** – This source is classified as a quasar by Kron et al. (1985) on the basis of its colour. However, whilst its non–detection in *i* does suggest a blue colour, this is not supported by its, not very blue, $(r-K)$ of 3.8, and it does not appear to be pointlike. It is therefore classed as a galaxy here.

- **55w124** – This source is classified as a quasar on the basis of its very broad MgII line and blue $(r-i)$ colour of -0.06.

- **55w140** – This source is classified as a quasar on the basis of its very broad MgII line and very blue $(r-i)$ colour of -0.21.

In summary, therefore, the objects classed as quasars in the sample are 53w061, 53w075, 53w080, 55w124 and 55w140.

4.5 Redshift estimation

Redshifts have now been determined for 44% of sources in the Lynx field and 62% of sources in the Hercules field, either through the observations described above or with previously published results. For the remainder, estimated redshifts were calculated instead using the two different magnitude–redshift relations, K–z and r–z, outlined in §4.5.1 below. The K–z relation, the more accurate of the two, was used for all sources detected in the UKIRT observations; the remaining sources were estimated with the r–z.

It should be noted that the 5–band photometry for the Lynx field sources which were included in the SDSS (as previously given in Table 3.8) could be used to obtain photometric redshifts. This was attempted using the publicly available code `hyperz` (Bolzonella et al., 2000), which works by fitting template galaxy SEDs to input magnitudes, but the results, whilst broadly consistent with the previously found spectroscopic redshifts, were very uncertain. The likely reasons for this are: (1) that the available templates do not describe the radio galaxies well, and (2) above $r \sim 21$ the SDSS *r* and *i*–band magnitudes do not agree well with the measured INT values (as illustrated in Figure 3.7). However, since there are only 10 sources without redshifts, but with SDSS magnitudes, this will have a negligible effect on the results.

4.5.1 The K–z and r–z magnitude–redshift relationships

The K–z relation is a tight correlation between the *K*–band magnitudes and redshifts of radio source host galaxies; it exists because the radio host galaxy population is made up of passively evolving, massive elliptical galaxies.

At high redshift the relation is slightly different for the radio surveys of different flux density limits (Willott et al., 2003), as shown in Figure 4.6, which therefore implies that it is dependent on the flux density of the radio source. The relation used here is that found for the 7C survey as the source fluxes for that sample are the best comparison to those considered here. The relation itself is given by Willott et al. (2003) as,

$$K = 17.37 + 4.53 \log z - 0.31 (\log z)^2. \tag{4.6}$$

The majority of the sources with a host galaxy detection but without redshifts, were also not included in the UKIRT observations so, therefore, the K–z relation outlined above cannot be used for them. Instead, since all these sources have an *r*–band magnitude, the r–z relation was used. This relation describes a correlation between the redshift and *r*–band magnitude of the

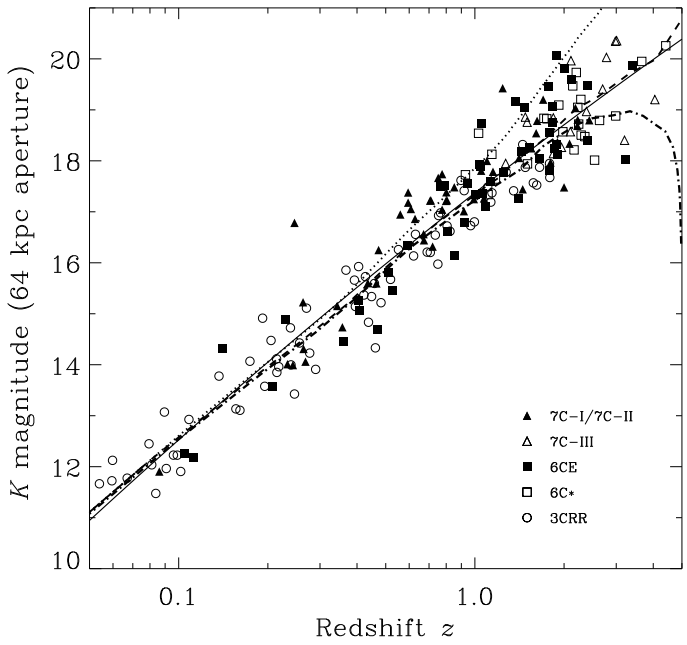

Figure 4.6: The K–z relation for the 7CRS, 6CE, 6C* and 3CRR samples from Willott et al. (2003). The solid line is the best fit to the data as given in Equation 4.6.

host galaxies of radio sources.

In general, redshifts estimated using the r–z relation are not as reliable as those found using the K–z, especially above $z \sim 0.6$ where the *r*–band samples shortward of the 4000Å break. In addition, in powerful radio galaxies there is considerable scatter in magnitudes at these bluer wavelengths due to the 'alignment effect', where the optical structures of the galaxy align with the radio jets (e.g. McCarthy et al., 1987) . However, the low power of the sources in the sample means that there will not be much alignment, so the effect of this will be minimal. To account for these factors, two r–z relations were used: one for low and one for high redshift sources, as illustrated in Figure 4.7. The low redshift relation was for the bright, 3C, radio sample, which is reliable up to $z \sim 0.6$, but then brightens beyond that due to the alignment effect. The high redshift relation, conversely, was that for Gigahertz Peaked Spectrum (GPS) radio sources. These are compact objects with convex radio spectra which peak at about 1 GHz, and are ideal for this as they do not show the alignment effect. The 3C relation is

$$r_{\rm g} = 21.2 + 5.3 \log z, \tag{4.7}$$

and the GPS relation is

$$r_{\rm g} = 22.7 + 7.4 \log z, \tag{4.8}$$

which, it should be noted, is valid up to $z \sim 1$; at higher redshifts it is unreliable due to the scarcity of measurements and the blue rest–frame wavelength range it is sampling.

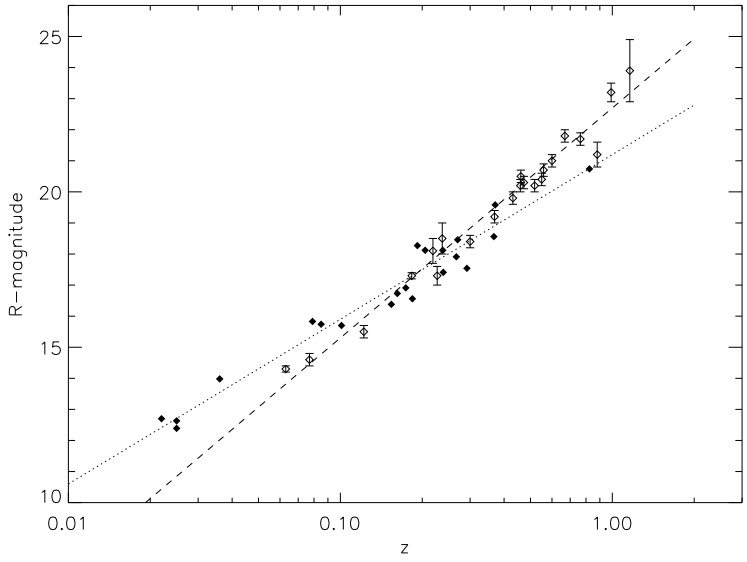

Figure 4.7: The r–z relations for GPS galaxies (empty diamonds; dashed line), and 3C galaxies (filled diamonds; dotted line), from Snellen et al. (1996)

The relations given in Equations 4.8 and 4.7 above assumes that the *r*–band magnitudes used were observed using the Thuan–Gunn filter system. They therefore had to be transformed to the Sloan filter system, via the Johnson filter system, before they could be used. In the following description capital letters indicate the Johnson system, lower–case letters indicate the Sloan system and *g* subscripts indicate the Thuan–Gunn system. To convert from Johnson to Thuan–Gunn, Jorgensen et al. (1994) give:

$$r_{\rm g} = R + 0.111(g_{\rm g} - r_{\rm g}) + 0.317, \tag{4.9}$$

whilst the conversion from Johnson to Sloan comes from rearranging Equation 3.4:

$$r = R + 0.16(V - R) + 0.13. \tag{4.10}$$

Making the assumption that $(V-R) \simeq (g_{\rm g}-r_{\rm g}) \simeq 1$ for radio galaxy hosts, then $r = r_{\rm g} - 0.14$ and the r–z relations become

$$r_{\rm GPS} = 22.56 + 7.4 \log z \tag{4.11}$$

$$r_{\rm 3C} = 21.06 + 5.3 \log z, \tag{4.12}$$

where the subscripts 'GPS' and '3C' refer to the relations for GPS and 3C galaxies respectively. Figure 4.7 shows that the two relations cross at $r = 17.27$ ($r_{\rm g} = 17.41$), so it was decided that only redshift estimates for sources brighter than this would be done using the 3C relation, with the remainder of the sample estimated with the GPS relation. In practice though, there was only one source (55w127) with $r < 17.27$; the rest were all fainter than this.

The magnitude–redshift relations need aperture corrected magnitudes to give reasonable results but the estimated redshift is needed to perform the aperture correction (as described in §3.4.3). To solve this problem an IDL script was written to iterate the redshift estimates and subsequent aperture corrections until they converged on a final value.

Table 4.6 summarises all the redshift information for the sources in the two fields. The quoted redshift for each source is ideally a spectroscopic or previously published one; if neither of those is available then the redshift is one from a K–z estimation and finally, for sources with no K–magnitude or spectrum, the redshift given is an r–z estimate.

4.5.2 Redshift comparison

A valuable test of the redshift estimation comes from comparing the estimates with the DOLORES MOS and the previously published (Waddington et al. 2000; 2001) spectroscopic and photometric redshifts. The results of this comparison for both r–z and K–z redshift estimates are shown in Figure 4.8; in general the agreement between the spectroscopic and estimated results is very good with a 1σ Δz of 0.15. The agreement is also reasonably good for the photometric redshifts.

Additionally, several of the sources in the sample have both r and K–band magnitudes thus providing a useful means of comparing the two methods of redshift estimation. The solid diamonds plotted in Figure 4.8 show the difference in the two estimates ((K–z)- (r–z)) plotted against the K–z value. The two relations give similar redshifts up to $z_{\rm kz}\sim1.5$, but, for the redshifts higher than this, the K–z value is much greater than the r–z further suggesting the lower accuracy of the r–z relation at these values.

4.6 The redshift distribution of the sample

Now that redshift information has been obtained or estimated for a large proportion of the objects in the two fields, redshift histograms can be constructed to compare the radio source

Hercules			Lynx		
Name	z	Origin	Name	z	Origin
53w052	0.46	1a	55w116	0.851	2
53w054a	1.51	3	55w118	0.66	4
53w054b	3.50	3	55w120	1.35	3
53w057	1.85	4	55w121	2.57	3
53w059	1.65	4	55w122	0.55	4
53w061	2.88	1b	55w123	0.87	3
53w062	0.61	1a	55w124	1.335	2
53w065	1.185	1a	55w127	0.04	4
53w066	1.82	1b	55w128	1.189	2
53w067	0.759	1a	55w131	1.124	2
53w069	1.432	1a	55w132	$>$4.4	3
53w070	1.315	2	55w133	2.24	4
53w075	2.150	1a	55w135	0.090	1c
53w076	0.390	1a	55w136	2.12	3
53w077	0.80	1a	55w137	0.151	2
53w078	0.27	1a	55w138	2.81	3
53w079	0.548	1a	55w140	1.685	2
53w080	0.546	1a	55w141	$>$1.8	4
53w081	2.060	1a	55w143a	2.15	4
53w082	2.04	4	55w143b	2.21	4
53w083	0.628	1a	55w147	1.07	3
53w084	2.73	3	55w149	0.151	2
53w085	1.35	1a	55w150	0.470	2
53w086a	0.46	4	55w154	0.330	2
53w086b	0.73	2	55w155	$>$3.7	3
53w087	$>$3.7	3	55w156	0.86	3
53w088	1.773	1a	55w157	0.557	2
53w089	0.635	1a	55w159a	1.29	4
66w009a	0.65	3	55w159b	0.311	1c
66w009b	0.156	1a	55w160	0.600	2
66w014	–	–	55w161	0.44	4
66w027	0.086	2	55w165a	0.68	4
66w031	0.812	2	55w165b	0.75	4
66w035	2.26	3	55w166	0.99	4
66w036	0.924	2	60w016	0.840	2
66w042	0.65	4	60w024	0.773	2
66w047	0.37	4	60w032	$>$1.8	4
66w049	0.95	4	60w039	0.151	2
66w058	$>$2.3	4	60w055	0.718	2
			60w067	$>$1.8	4
			60w071	1.25	4
			60w084	0.127	1c

Table 4.6: The redshifts found for the sources in the complete sample. (1a) and (1b) indicates a previously published value, (a – spectroscopic (Waddington et al., 2000; Bershady et al., 1994), b– photometric (Waddington et al., 2001)), (1c) indicates the redshift came from the SDSS, (2) indicates a DOLORES spectroscopic value, (3) is a K–z estimate, (4) is a r–z estimate.

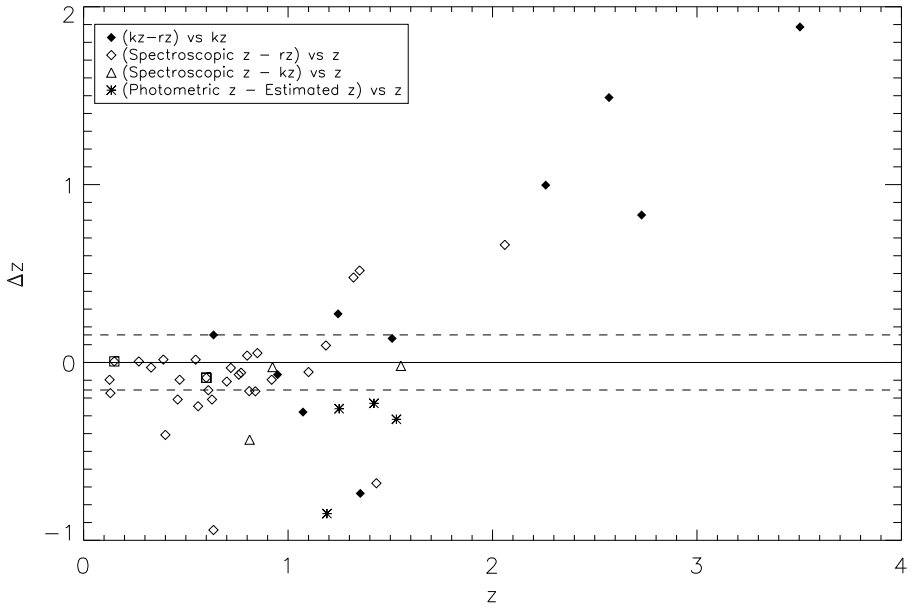

Figure 4.8: A comparison of the different methods used to obtain redshifts. Filled diamonds indicate the comparison between the two redshift estimation methods whilst empty diamonds and triangles indicate the comparison between the spectroscopically determined redshifts and the r–z and K–z estimates respectively. Square outlines indicate redshifts that came from single–line spectra. The dotted lines are the 1σ values of the spectroscopic Δz, ± 0.15.

distributions for the two fields; these are shown, split into the different redshift methods, in Figures 4.9(a) and 4.9(b). Both histograms, peak at redshifts before $z = 1.0$ which is to be expected as higher redshift sources are fainter and therefore harder to detect.

These histograms also illustrate the lack of definite redshifts for the Lynx field, especially at the high end, compared to the Hercules field. Whilst many of the Lynx sources were included in the DOLORES MOS observations, lines in the resulting spectra tended to be detected in the brighter, lower redshift objects. The high–z end of both fields, however, is populated mainly by sources with less accurate redshift estimates.

4.7 Chapter summary

In this Chapter the redshifts of the sample sources, both estimated and spectroscopic, have been presented. The spectroscopic completeness of the sample is now 49%, including the previously published results and MOS spectra and $<$10% of sources across both fields have no redshift, either estimated or determined spectroscopically. 21% of sources in the Hercules and 33% in

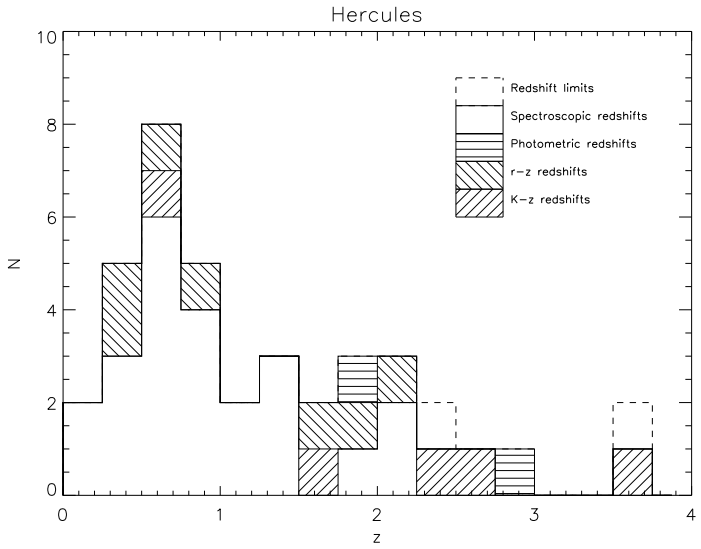

(a)

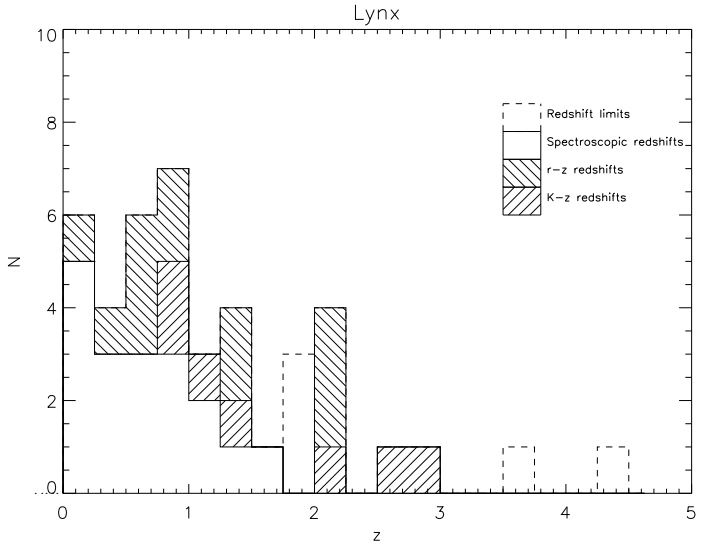

(b)

Figure 4.9: The redshift distribution for sources in the Hercules (a) and Lynx (b) fields subdivided to show the contribution from the different redshift methods.

the Lynx field have r–z estimated redshifts only; these will be treated as the least accurate in the sample.

CHAPTER 5

Radio observations and classifications

This thesis is strongly dependent on radio observations of both low and high resolution. The radio sample has already been defined in Chapter 2; this chapter deals with the selection of the high–redshift FRI candidates and the high–resolution radio observations employed to follow them up.

5.1 An overview of radio data reduction

Since the radio data reduction methods used for the four different radio observations in this chapter have many similarities, a brief overview of the main points is given in this section with observation specific details given in the following sections. The information in this section is mainly taken from the MERLIN User Guide (Diamond et al., 2003) and Synthesis Imaging in Radio Astronomy II, edited by Taylor et al., (1999).

5.1.1 Radio interferometer basics

The angular resolution of any telescope is proportional to λ/D where λ is the wavelength of the observation and D is the telescope diameter. At the $\sim$cm radio wavelengths therefore, to

achieve reasonable resolution, an unfeasibly large single dish would be needed. This problem can be solved by using an array of antennae linked together to form an interferometer.

In a simple two–element interferometer, the radio receiver in each antenna will output a sine wave in response to plane parallel electromagnetic waves from some distant astronomical source, if the source is point–like. These two signals can then be multiplied together to produce an interference pattern which depends only on the geometry of the array in relation to the source. As the Earth rotates, the geometry of the array changes; as a result a series of measurements over time provides additional information about the source. Similarly, if more antennae are added to the array, each pair, or baseline, would also act as a two–element interferometer. If every possible configuration could be measured then the resulting image would be equivalent to that taken with a single, large, dish. In practice, however, there will always be gaps in this synthesized dish, as an array of N antennae can only have a maximum of $N(N-1)/2$ possible baselines; the data must therefore, be interpolated to correct for this. If an object with structure, instead of being a simple, compact, point, is observed by an interferometer then the amplitude and phase of the signal detected by each baseline will depend on this structure as well as the array geometry. However, in practice, it is simpler to consider a complex structure as merely a collection of different point sources.

The radio image, or brightness distribution, of an astronomical source turns out to be a good approximation of the Fourier Transform of the complete set of phase and amplitude measurements taken at each baseline, over the length of the observation. These measurements are known as visibilities, with each visibility being approximately one Fourier component of the image. The baselines themselves are specified by the coordinates (u, v) which are in the directions of East and North respectively. Using this definition the Fourier transform can be written as

$$V(u,v) = \int\int I(l,m) e^{-2\pi\ i(ul+vm)}\ dl\ dm \tag{5.1}$$

where $V(u,v)$ is the complete set of visibilities, known as the visibility function, $I(l,m)$ is the sky brightness function (i.e. the true image of the source), and (l,m) are the sky coordinates which correspond to u and v respectively.

The field of view, or primary beam, of the radio interferometer is simply the field of view of any individual antenna in the array. Since this is diffraction limited, the half power beam width (HPBW) is given by $\sim \lambda/D$ and sources at radii greater then this can generally be ignored due to their strong attenuation. Sources which fall within the HPBW are also affected by the primary beam aberrations which increase at increasing distance from the pointing centre. The three main types of aberration are bandwidth smearing, time–average smearing and that which arises from the non–coplanar nature of the array.

Bandwidth smearing, also known as chromatic aberration, occurs because the response of the radio array is different at different frequencies. A normal radio observation is done using a single bandwidth of width $\Delta\nu$, with some central frequency; the resulting visibility data are averaged over this width and are reduced in amplitude (smeared) if the response over $\Delta\nu$ is not constant. These changes over $\Delta\nu$ are equivalent to the visibilites changing over some finite width in the uv plane, and this effect is greatest at large distances from the pointing centre. If an image of a wide area of the beam is required therefore, the single observing band must be split into enough narrow band channels such that the bandwidth smearing effects within each one are negligible.

Time–average smearing occurs when the visibility data are averaged over time–periods during which they are not constant and as such, it bears many similarities to bandwidth smearing. This effect tends to be strongest on the longest baselines as these move faster through the uv plane, but can be reduced by simply using shorter integration times.

The final cause of aberration, the non–coplanar nature of the array or three–dimensional sky effect, is analogous to field curvature in an optical telescope. The normal, two–dimensional, Fourier transform that is used to recover an image from a set of visibility data assumes that the measurements have been taken on a plane (or that the field of view is sufficiently small that it is a reasonable approximation to a plane). However, this assumption is only always true for arrays in which the antennae are distributed along an East–West line or for arrays located at the Earth's poles. An array like the Very Large Array (VLA) is located on a plane with respect to some astronomical source at any instant, but, as the Earth rotates, the array position continuously changes; this causes the positions of sources far from the pointing centre to alter over the course of the observation, causing them to appear smeared on the final image. The simplest way to correct for this, if a wide–field image is required, is to use a three–dimensional Fourier transform, but this is normally computationally impractical. Instead, the field of view is divided up into small facets, generally corresponding to the positions of the sources in the field if known, which approximate flat, two–dimensional planes. The centre of the image is then shifted to the centre of each facet in turn and a two–dimensional Fourier transform can be performed (Perley, 1999).

The basic data reduction steps, covered in more detail in the following sections, are:

1. Edit the raw visibilities to remove bad measurements due to radio interference or instrument malfunctions (this can be done for the target or calibration sources at any stage of the calibration).

2. Calibrate the edited visibilities using observations of sources whose response to the instruments in the interferometer is known.

3. Fourier transform the calibrated data to produce the raw image which is a convolution of the true source image with the point spread function (PSF), or 'dirty beam', of the array.

4. Deconvolve the raw image from the dirty beam to produce the final image.

The above steps were mainly carried out for all the radio observations using the Astronomical Image Processing System (AIPS) package developed by the National Radio Astronomy Observatory (NRAO). The two key tasks within AIPS are **CALIB** and **IMAGR** which are used to derive the phase and amplitude calibration solutions, and perform the Fourier transform and deconvolution respectively. Further, observation specific, details are given in the relevant sections further on in this Chapter.

5.1.2 Calibration

The calibration of radio data can be thought of as akin to focusing a conventional optical telescope (Burke and Graham-Smith, 2002). The observed visibilities, V, assuming no bad data are present, are related to the true visibilities, $V_{\rm true}$, by

$$V_{\rm true} = G_i G_j^* G_{ij} V_{ij} \tag{5.2}$$

where the subscripts i and j refer to the baseline between antennas i and j respectively and G_i represents the amplitudes and phases of a particular antenna (known as the complex gain). $G_{i,j}$ is a small baseline dependent offset introduced by the correlator. Variations in phase are mainly due to the different refractive indices in the atmosphere which change over timescales of minutes, whilst variations in amplitude are mainly due to the slower, hourly, changes in the radio receiver sensitivity. Each baseline, therefore, provides one equation which can be used to solve for the N total G values, if a set of model values of V is known. These model values come from observations of calibration point sources since V_{ij} is simply given by the source flux density, S in this case.

In practice, three different calibration sources are used; a flux calibrator, a point source calibrator and a phase calibrator. (It should be noted though that the same object is often used for both the point and phase calibrators.) The point source calibrator and the flux calibrator are both targeted once, for typically several minutes each, at some point during the observation, whereas the phase calibrator is targeted for a few minutes at regular intervals interspaced with the target source. The separation of these depends on the array and observing setup used. The point source calibrator data are used to determine the initial values for the instrumental gains and apply these to the target and the phase calibrator; these values tend to vary by $<5\%$ from day to day. The sources typically used for this tend to be variable, so a source of known flux

density, the flux calibrator, is also observed so that the flux scale can be accurately determined. For the observations described below, the flux calibrator used was always 3C286; the flux scale for this is set by the measurements of Baars et al. (1977).

The variations in time from the initial gain values are then determined using the observations of the phase calibrator. The frequent observations of this calibrator are necessary due to the short timescales of these atmospheric phase changes; at the 1.4 GHz frequency at which all these observations were taken, the source of these effects is the ionosphere. If the phase calibrator is not a true point source then self–calibration (see §5.1.3 below) is applied to produce a model of the source which can be used for the calibration.

Finally, if the observations are done in wide–field (or spectral line) mode, with multiple channels, bandpass calibration is also needed. This corrects for the changes in the antenna amplitudes and phases at different frequencies and is done using the point source calibrator observations.

5.1.3 Imaging and deconvolution

After the calibration has been applied to the raw target visibilities they are interpolated to cover regions of incomplete (u, v) coverage and then Fourier transformed to create the 'dirty image'; this is a convolution of the true image with the point spread function, or 'dirty beam', of the interferometer. If the calibration is perfect and the noise is minimal then the dirty beam is the Fourier transform of a function of (u, v) that exists only where there are data.

The true image of the target can now be found by deconvolving it from the dirty beam. This deconvolution is usually done using the CLEAN algorithm (Högbom, 1974) which models the true image as a set of points (the CLEAN components) in an empty sky; these are found iteratively by subtracting the dirty beam from the bright peaks in the dirty map. The components are then convolved with an idealized CLEAN beam to form the CLEANed, final, image. The CLEAN, or restoring, beam is usually an elliptical Gaussian; this step is necessary to suppress the higher spatial frequencies which the algorithm tends to estimate poorly.

The results of the imaging and deconvolution processes can be improved by applying some form of weighting before the data are Fourier transformed. The two main types used are known as Natural, in which every data point is given an equal weight, and Uniform, in which every cell in the uv plane is given equal weight instead. Natural weighting results in a higher density of points towards the centre of the uv plane and maximises the sensitivity. Uniform weighting, on the other hand, results in a higher resolution final image. Weights intermediate between these

two options are also possible. In interferometer arrays in which the antennae are of different sizes, the visibilities can also be re–weighted according to the different instrument sensitivities present.

The final image produced in this process can also, if the target source is strong enough, be used to provide an input model for the gain calibration described earlier. The resulting, improved, calibration is then applied to the target data and imaged and deconvolved again and the process is repeated; this is known as self calibration and it allows gain changes throughout the on–source time to be included. It should be noted however, that no self calibration has been carried out for any of the observations described in this Chapter due to the weakness of the sources in the radio sample.

5.2 Lynx field VLA B–array observations

The aim of the low–resolution Lynx field VLA B–array observations was to provide a measure of the total flux density for each field source and to look for any extended emission that may have been resolved out in the A–array data. In B configuration the longest baseline of the 26 antennas is 10km (compared to 36km for the A configuration). Complimentary observations of the Hercules field in this configuration were not done due to time constraints.

The observations took place on 30th October 2003, in L–band (1.4 GHz), using the wide–field mode to minimise bandwidth smearing effects. The flux, point and phase calibrators used were 3C286, 3C147 and 0828+493 respectively and the total exposure time on the field was 7000s; this was split into 5 sections which were interspersed with $\sim$120s visits to the phase calibrator. 8 channels, with a total bandwidth of 25 MHz, were used, along with two intermediate frequencies of 1.474 and 1.391 GHz. Full polarization was observed.

5.2.1 Data reduction

The calibrator sources will not be affected by the bandwidth smearing as they will be located at the pointing centre. The calibration procedure was therefore carried out on an average of the central 75% of the data, called the Channel 0 data set, as this is much less computationally intensive. The resulting calibration table was then copied over to the multi–channel dataset.

The calibration process was carried out following the methods outlined in the previous section. The flux densities of 3C286 and 3C147 were set using the scale of Baars et al. (1977). The

initial antenna gain solutions were then derived, using a restricted uv–range of 0–18 as the point source calibrator was resolved on the longer baselines. The flux density of the phase calibrator was then calculated and used to derive the final calibration. Finally, this was interpolated to cover the full time–period of the observations. The calibrated science data were then inspected to check the results and to identify and remove bad data; it was sufficient here to merely clip all (u, v) points above 0.5 Jy.

Since sources located at all positions in the final radio image need to be considered, the non–coplanar array wide–field imaging techniques, incorporated into the task IMAGR, were used. The field was split into facets, centred on the positions of each source from the A–array observations and the centre was shifted to the centre of each facet and imaged and deconvolved in turn. Each facet was 256 by 256 pixels (with $1.0''$ per pixel).

The deconvolution, or CLEANing, of each facet was done using 5000 iterations and nearly natural weighting to minimise the noise in the resulting CLEAN image. No self–calibration was carried out due to the weakness of the sources. The final noise level reached for all the facets was $\sim$50μJy/beam, with a resolution of $5.36''$ by $4.67''$. Finally a primary beam correction was applied to each image to account for the attenuation of the beam away from the pointing centre.

5.2.2 Source detection and results

All the sources in the Lynx field complete sample were detected in these observations. Their flux densities were, as with the A–array data, measured with *tvstat* if they showed extension or with *imfit* if they appeared compact; the method used for each source in the complete sample, along with the resulting flux densities and primary beam correction factors, can be found in Table 5.2. The corresponding radio contour maps (without primary–beam corrections applied) can be found in Figure 5.1. The results for sources not in the complete sample can be found in Table 5.1 and Figure 5.2.

Name	$S_{1.4\mathrm{GHz}}$ (mJy)	C_{PB}	Measure
55w119	1.97 ± 0.36	3.86	I
55w125	18.87 ± 4.04	12.01	I
55w126	4.13 ± 0.90	6.37	I

Table 5.1: The primary–beam corrected flux densities for the sources not included in the Lynx complete sample, along with the correction factors used. An *I* in the final column indicates an *imfit* measured flux density; a *T* indicates a *tvstat* measurement. A primary beam correction error of 20% of the difference between the corrected and un–corrected flux density has been incorporated into the quoted errors.

Name	$S_{1.4\mathrm{GHz}}$ (mJy)	C_{PB}	Measure
55w116	2.05 ± 0.43	2.22	T
55w118	0.85 ± 0.13	1.92	I
55w120	1.91 ± 0.43	2.68	T
55w121	1.24 ± 0.14	1.60	I
55w122	0.76 ± 0.18	1.45	I
55w123	1.09 ± 0.14	1.33	I
55w124	2.58 ± 0.10	1.35	I
55w127	1.72 ± 0.11	1.36	I
55w128	4.10 ± 0.56	2.05	T
55w131	1.20 ± 0.20	1.48	T
55w132	1.83 ± 0.36	2.05	T
55w133	2.17 ± 0.13	1.47	I
55w135	2.61 ± 0.37	1.98	T
55w136	0.90 ± 0.11	1.10	I
55w137	1.70 ± 0.17	1.29	T
55w138	1.81 ± 0.12	1.37	I
55w140	0.58 ± 0.09	1.06	I
55w141	0.60 ± 0.60	1.19	I
55w143a	2.22 ± 0.11	1.34	I
55w143b	0.65 ± 0.17	1.33	I
55w147	2.24 ± 0.14	1.82	I
55w149	7.63 ± 1.14	3.20	T
55w150	0.60 ± 0.14	1.88	I
55w154	12.90 ± 0.44	1.13	T
55w155	1.63 ± 0.15	1.55	I
55w156	4.02 ± 0.26	1.19	T
55w157	1.61 ± 0.13	1.68	I
55w159a	6.61 ± 0.21	2.69	I
55w159b	1.08 ± 0.31	2.55	I
55w160	0.77 ± 0.09	1.32	I
55w161	0.87 ± 0.16	1.87	I
55w165a	17.51 ± 1.33	2.06	T
55w165b	1.40 ± 0.23	1.99	I
55w166	2.26 ± 0.17	2.07	I
60w016	0.57 ± 0.15	1.52	I
60w024	0.25 ± 0.08	1.29	I
60w032	0.29 ± 0.10	1.51	I
60w039	0.64 ± 0.15	1.38	I
60w055	0.80 ± 0.27	2.34	I
60w067	0.65 ± 0.11	1.70	I
60w071	0.59 ± 0.19	1.42	I
60w084	0.54 ± 0.16	2.08	I

Table 5.2: The primary–beam corrected flux densities for the (complete sample) Lynx field B–array observations along with the correction factors used. An *I* in the final column indicates an *imfit* measured flux density; a *T* indicates a *tvstat* measurement. A primary beam correction error of 20% of the difference between the corrected and un–corrected flux density has been incorporated into the quoted errors.

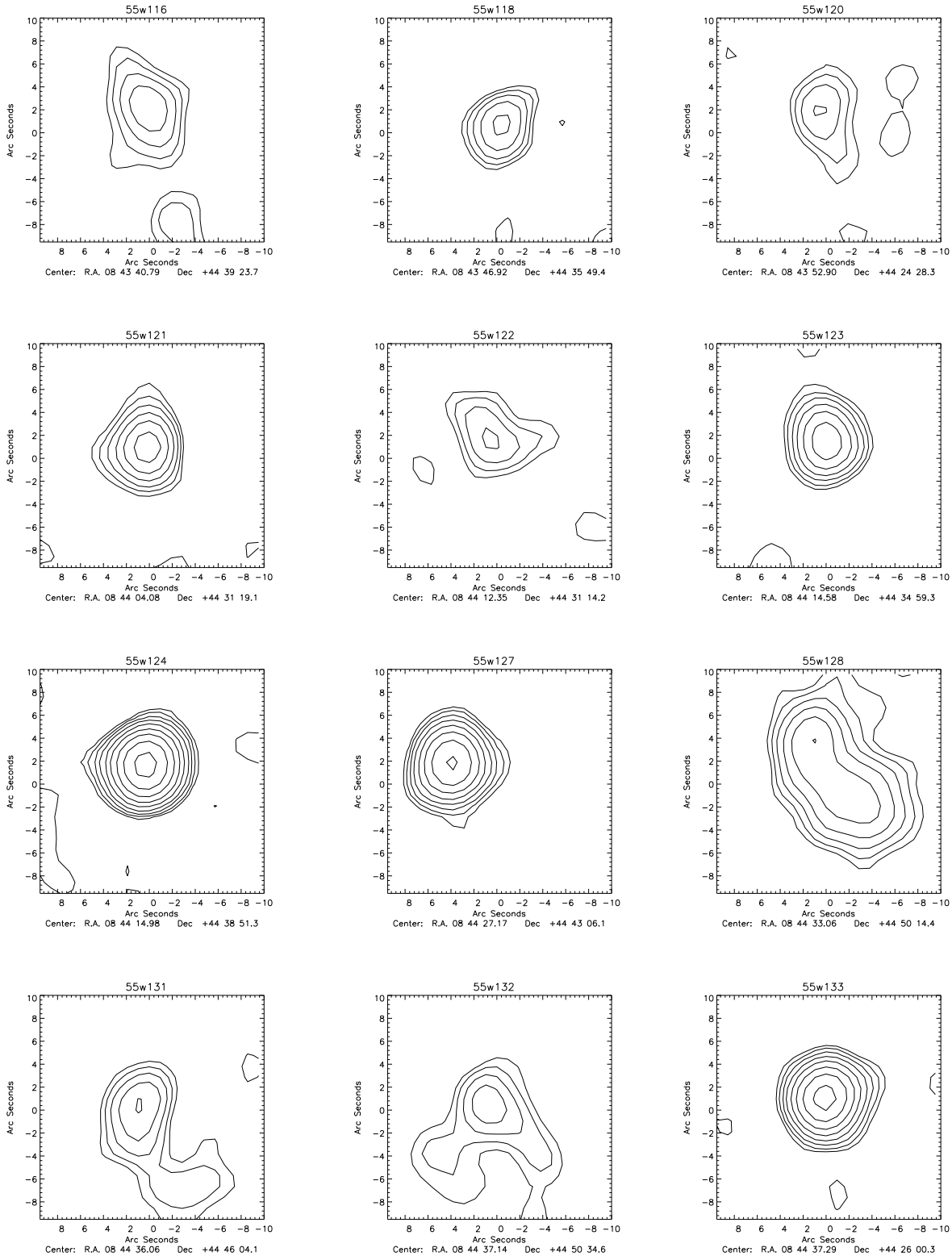

Figure 5.1: The radio contour images, for the Lynx field complete sample, from the VLA 1.4GHz B–array observations. The beam size is $5.36'' \times 4.67''$. Contours start at 50μJy/beam and are separated by factors of $\sqrt{2}$. The images are centred on the optical host galaxy positions from Chapter 3 if available.

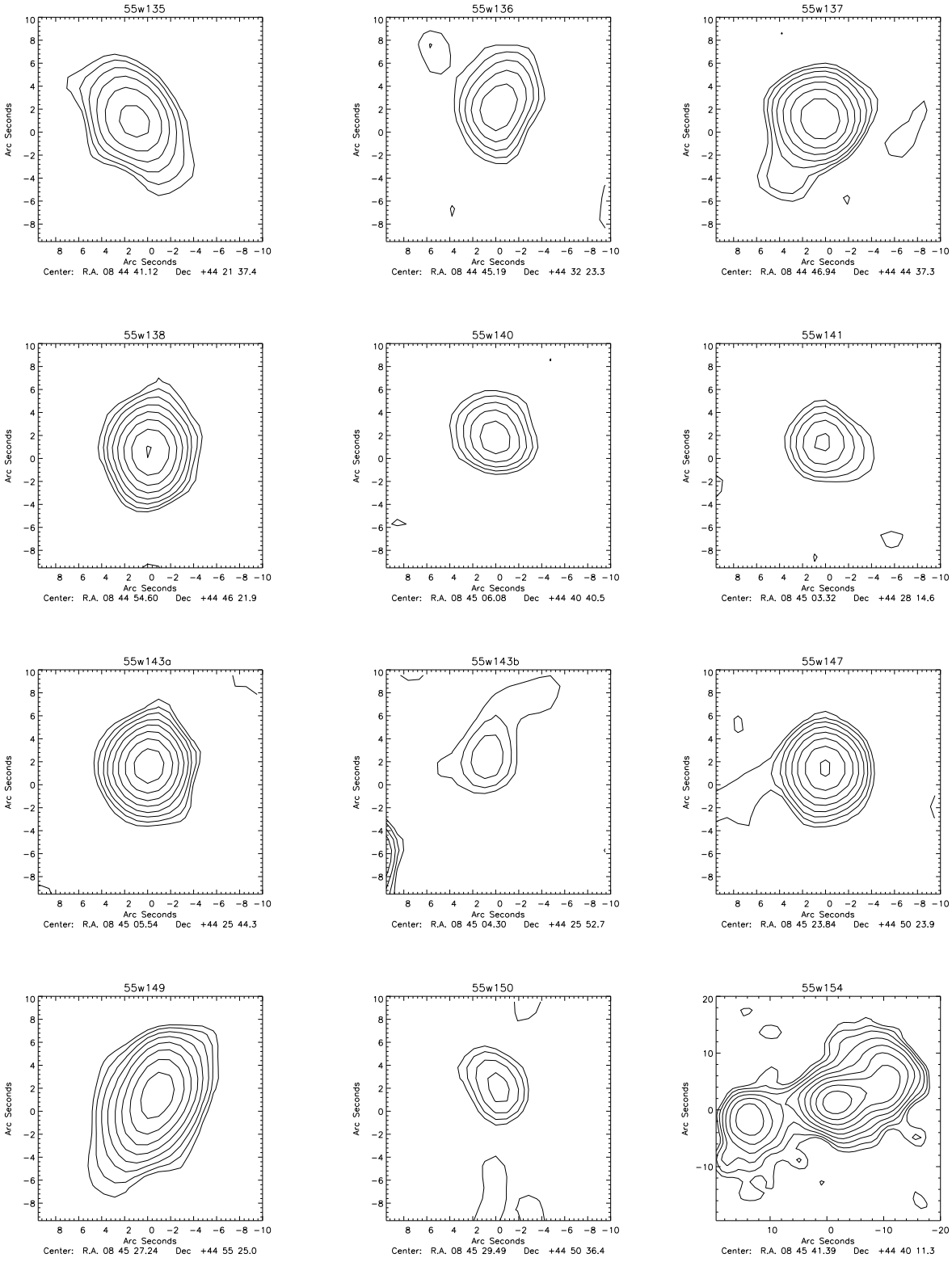
55w135
Arc Seconds
Arc Seconds
Center: R.A. 08 44 41.12 Dec +44 21 37.4
55w136
Arc Seconds
Arc Seconds
Center: R.A. 08 44 45.19 Dec +44 32 23.3
55w137
Arc Seconds
Arc Seconds
Center: R.A. 08 44 46.94 Dec +44 44 37.3
55w138
Arc Seconds
Arc Seconds
Center: R.A. 08 44 54.60 Dec +44 46 21.9
55w140
Arc Seconds
Arc Seconds
Center: R.A. 08 45 06.08 Dec +44 40 40.5
55w141
Arc Seconds
Arc Seconds
Center: R.A. 08 45 03.32 Dec +44 28 14.6
55w143a
Arc Seconds
Arc Seconds
Center: R.A. 08 45 05.54 Dec +44 25 44.3
55w143b
Arc Seconds
Arc Seconds
Center: R.A. 08 45 04.30 Dec +44 25 52.7
55w147
Arc Seconds
Arc Seconds
Center: R.A. 08 45 23.84 Dec +44 50 23.9
55w149
Arc Seconds
Arc Seconds
Center: R.A. 08 45 27.24 Dec +44 55 25.0
55w150
Arc Seconds
Arc Seconds
Center: R.A. 08 45 29.49 Dec +44 50 36.4
55w154
Arc Seconds
Arc Seconds
Center: R.A. 08 45 41.39 Dec +44 40 11.3

Figure 5.1

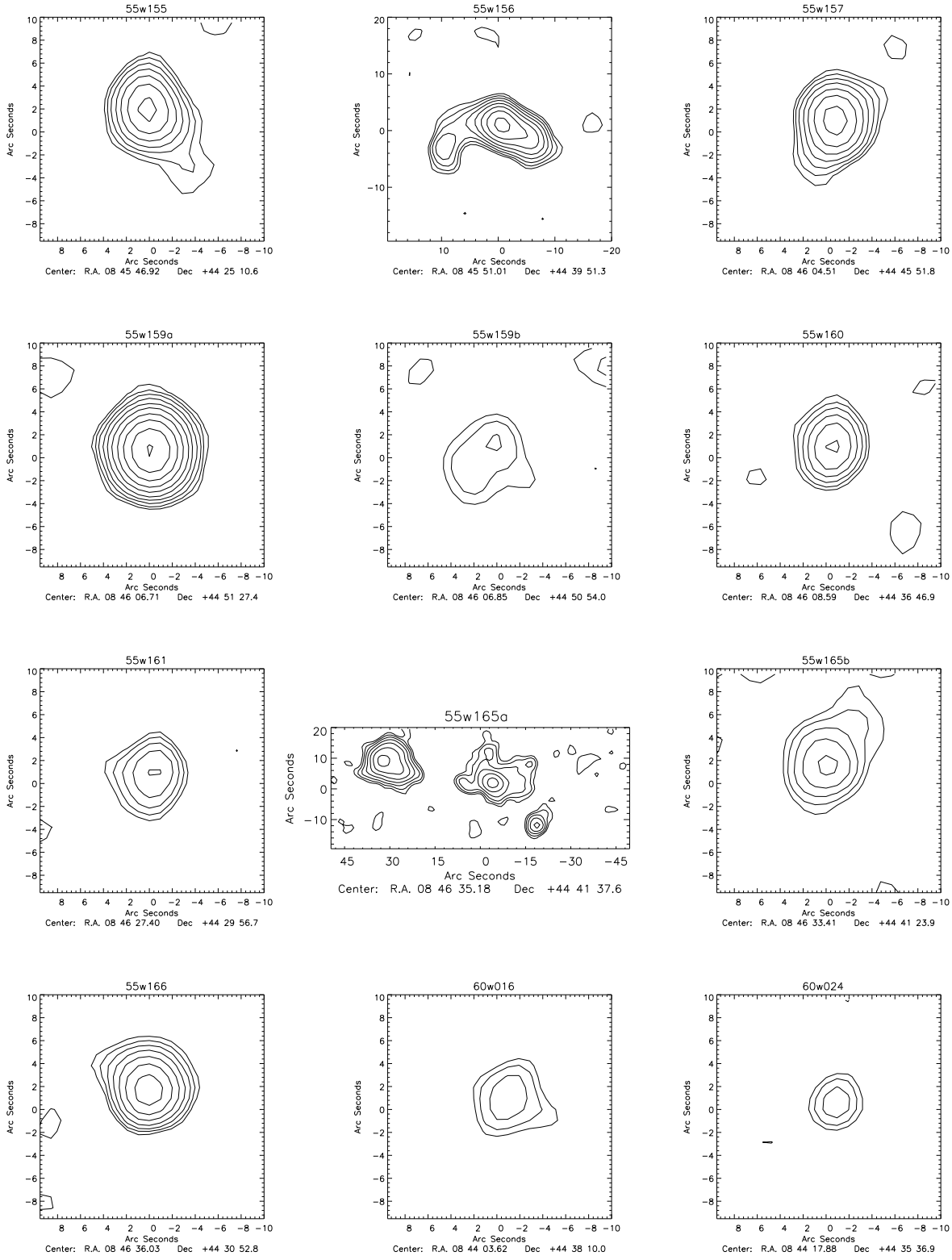
55w155
Arc Seconds
Center: R.A. 08 45 46.92 Dec +44 25 10.6
55w156
Arc Seconds
Center: R.A. 08 45 51.01 Dec +44 39 51.3
55w157
Arc Seconds
Center: R.A. 08 46 04.51 Dec +44 45 51.8
55w159a
Arc Seconds
Center: R.A. 08 46 06.71 Dec +44 51 27.4
55w159b
Arc Seconds
Center: R.A. 08 46 06.85 Dec +44 50 54.0
55w160
Arc Seconds
Center: R.A. 08 46 08.59 Dec +44 36 46.9
55w161
Arc Seconds
Center: R.A. 08 46 27.40 Dec +44 29 56.7
55w165a
Arc Seconds
Center: R.A. 08 46 35.18 Dec +44 41 37.6
55w165b
Arc Seconds
Center: R.A. 08 46 33.41 Dec +44 41 23.9
55w166
Arc Seconds
Center: R.A. 08 46 36.03 Dec +44 30 52.8
60w016
Arc Seconds
Center: R.A. 08 44 03.62 Dec +44 38 10.0
60w024
Arc Seconds
Center: R.A. 08 44 17.88 Dec +44 35 36.9

Figure 5.1

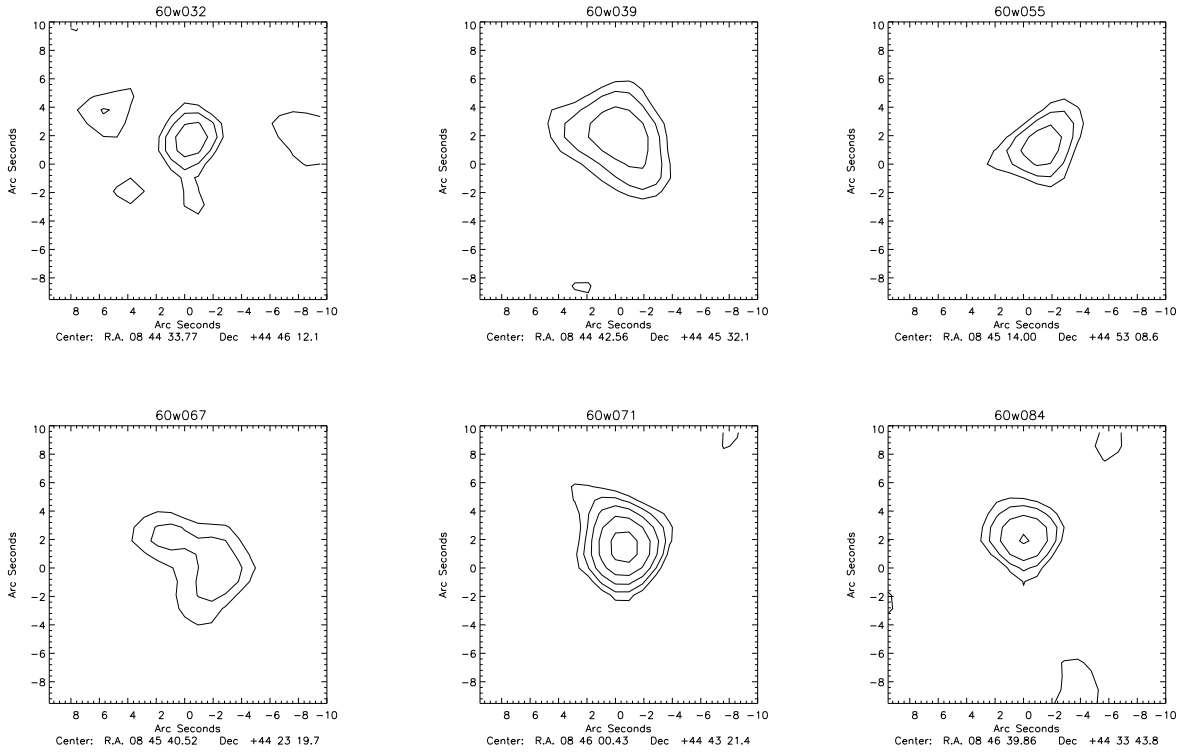

Figure 5.1

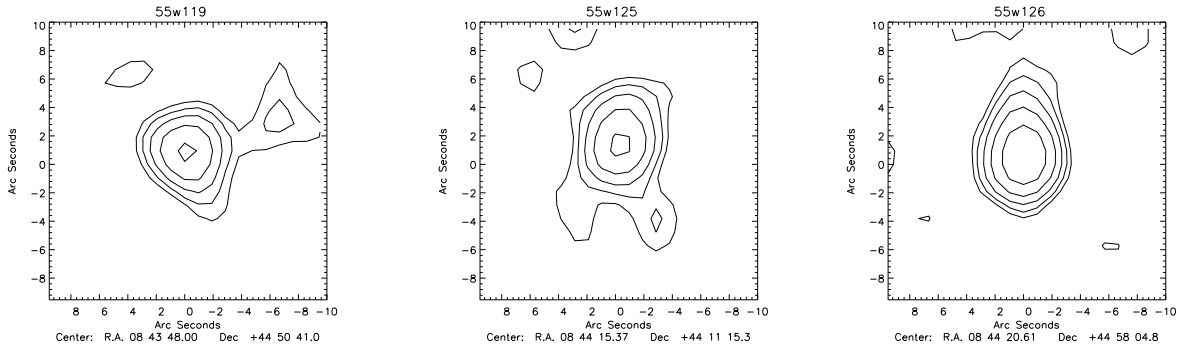

Figure 5.2: The B–array radio contour images, for the sources not included in the Lynx field complete sample. The beam size is $5.4'' \times 4.5''$. Contours start at 50μJy/beam and are separated by factors of $\sqrt{2}$. The images are centred on the optical host galaxy positions from Chapter 3 if available.

5.3 FRI candidate selection

The high–resolution radio observations were, by necessity, limited to the best high–redshift FRI candidates only; the next step therefore, was to select these candidate sources from the sample. The candidate criteria were, firstly, that their estimated redshifts were $\gtrsim 1.0$ and, secondly, that extended emission was visible in their radio image; this extension was defined, by inspection, as structure that deviated from a compact form. Since the high–resolution observations took place using two different instruments, the VLA+PieTown (VLA+Pt) link (§5.4.1) and the MERLIN (Multi Element Radio Linked Interferometer) array (§5.4.2), with slightly different characteristics, as described below, two different subsamples of these candidates were observed. Where possible, candidate sources were included in both observations to increase the possibility of detecting significant extended emission. Three of the high–redshift candidates were not able to be included in either observation due to time constraints; these were 53w081 in Hercules and 55w155 and 55w166 in Lynx.

5.4 High resolution observations

5.4.1 VLA A+PieTown observations

The 27 radio antennae of the VLA can be linked with one of the antennas of the Very Long Baseline Array (VLBA) located 50km away from the array centre at Pie Town. The extra baselines this adds means that the VLA+Pt can reach sub–arcsecond resolution at 1.4 GHz.

The candidate sources in the Hercules field, listed in Table 5.3, were observed on 26th September 2004 with the VLA+Pt at 1.4 GHz (L band). The candidate Lynx sources were observed similarly on 18th February 2006. Unlike the previous VLA A and B array observations, the wide field mode was not used, since off–centre sources were not necessary for the results. One channel, of 50 MHz bandwidth, and two IFs, of 1.385 and 1.465 GHz, were used for both observations. The details of the exposure times for each source can be found in Table 5.3. The flux and point calibrator calibrator for both fields was 3C286 and the phase calibrators were 1727+455 for the Hercules and 0832+492 for the Lynx field.

Hercules			
Source Name	Exposure Time (s)	$S_{1.4\mathrm{GHz}}$ (mJy)	rms (μJy)
53w054a	2600	1.82 ± 0.07	29
53w054b	2600	2.58 ± 0.07	29
53w059	2580	21.23 ± 0.21	30
53w061	2580	1.68 ± 0.06	28
53w065	2590	6.26 ± 0.09	33
53w069	2570	3.50 ± 0.18	36
53w087	2600	4.19 ± 0.17	28
53w088	2590	14.11 ± 0.09	30
Lynx			
55w116	2550	0.91 ± 0.16	49
55w120	2570	0.98 ± 0.13	47
55w121	2560	1.32 ± 0.11	43
55w128	2570	2.94 ± 0.45	47
55w132	2560	1.02 ± 0.19	45
55w133	2570	2.23 ± 0.14	44
55w136	2580	0.76 ± 0.17	44
55w138	2570	1.74 ± 0.18	45

Table 5.3: Details of the VLA+Pt exposure times for the Lynx and Hercules high–redshift candidate sources, along with the resulting flux densities and noise limits.

Data reduction and results

The flux density of 3C286 was set using the scale of Baars et al. (1977) and then, for each dataset, CALIB was run on 3C286 to derive the initial gain solutions, restricting the uv–range to 0–18 and including the inner 4 antennas on each arm only to prevent it from being resolved. The flux densities for 1727+455 and 0832+492 were adjusted to the right scale for the respective observations, using the flux density of 3C286, and then they were used to derive the final calibration solutions. Again, to prevent resolution, the uv minimum for 1727+455 was set to 6 and to 3 for 0832+492. These were again interpolated to cover the full length of the observations.

Each calibrated source observation was edited to remove bad data and then CLEANed using 10000 iterations, with a pixel size of $0.15''$ and nearly pure uniform weighting to avoid down-weighting the longest, PieTown, baselines and thus achieve high resolution images. The noise level reached for each source observation is given in Table 5.3 above and the resolution of the images was typically $1.1'' \times 0.6''$ with the highest resolution direction determined by the location of the PieTown antenna.

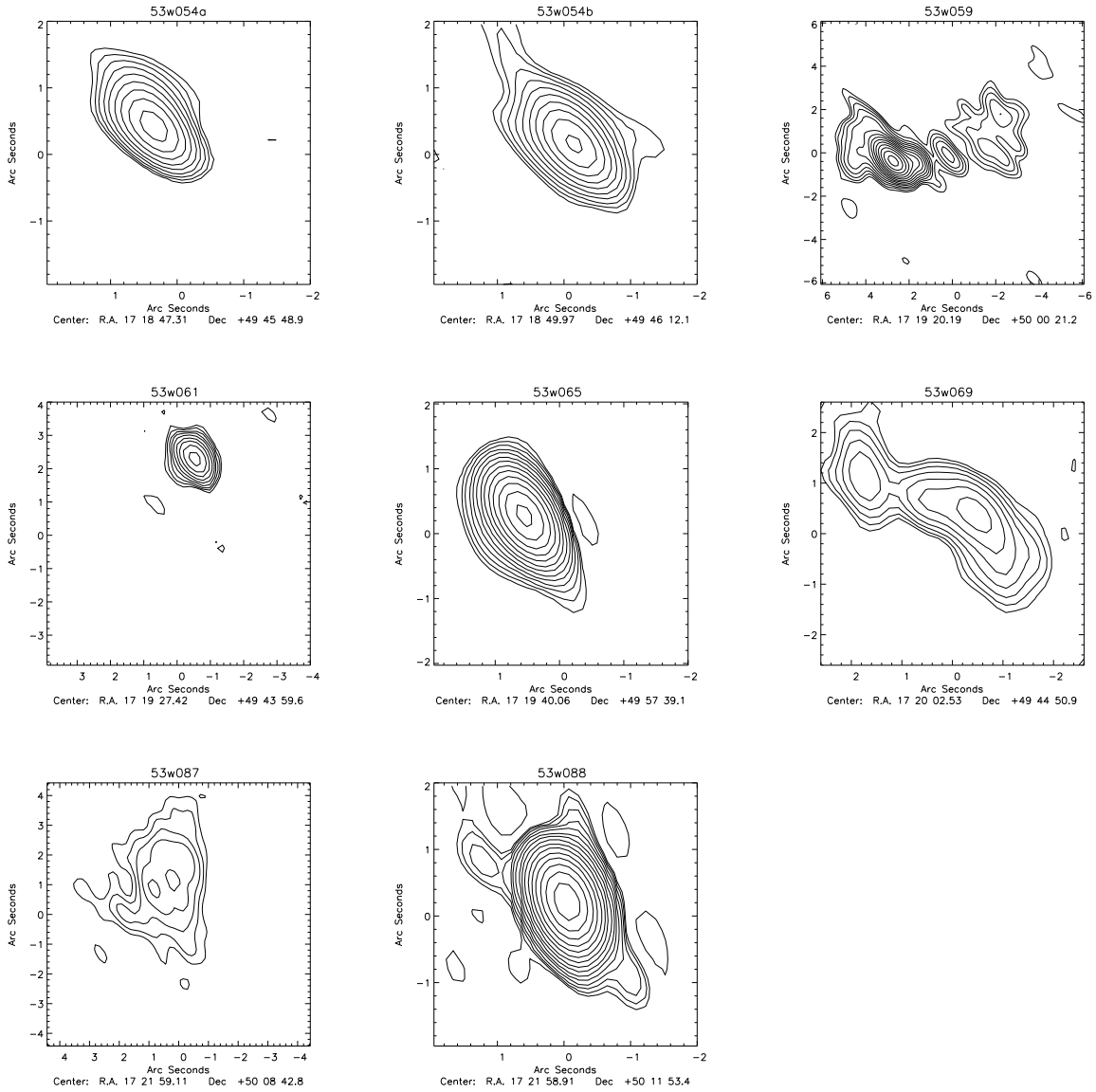

Figure 5.3: The radio contour maps, for the Hercules field, from the VLA+Pt 1.4 GHz observations, centred on the optical host galaxy positions where available. The beam size is typically $1.1'' \times 0.6''$. Contours start at 40μJy/beam and are separated by factors of $\sqrt{2}$.

All the candidate sources included in the VLA+Pt observations were detected and their flux densities were then measured with *tvstat*; these can be found in Table 5.3. The corresponding contour plots can be found in Figure 5.3 and 5.4.

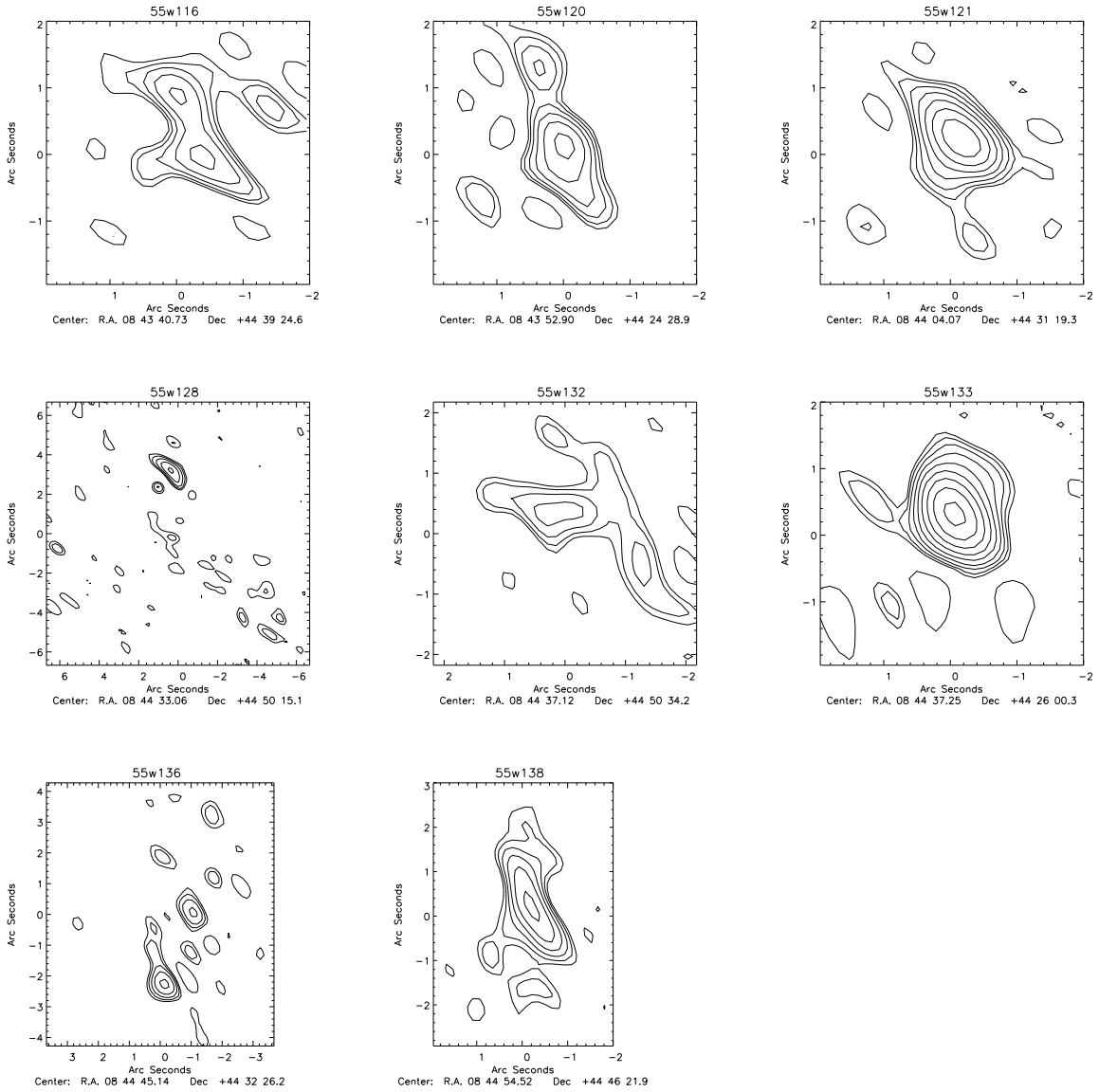

Figure 5.4: The radio contour maps, for the Lynx field, from the VLA+Pt 1.4 GHz observations, centred on the optical host galaxy positions where available. The beam size is $1.1'' \times 0.6''$. Contours start at 47μJy/beam and are separated by factors of $\sqrt{2}$.

5.4.2 MERLIN observations

The MERLIN observations were done in wide–field mode, with an individual field size of about $2.5'$ radius. Consequently, the pointing positions were designed such that the maximum number of non–candidate sources could also be observed whilst still including most of the candidates. Whilst these extra sources were not selected as high–redshift FRI candidates, observing them at higher–resolution may help to classify some of the lower redshift objects in the sample. It

should be noted that 53w091, one of the sources not included in the complete sample, was also included in the MERLIN observations as a result of this process.

MERLIN consists of up to 7 antennas spread across the UK, giving baselines up to 217km and a resolution, at L–band, of $\sim$0.15″. The sources were observed with MERLIN on 11th March 2005 for the Hercules and on 13th, 19th, 20th, 28th and 29th May 2006 for the Lynx field, both using 32 channels, with a combined bandwidth of 15.5 MHz. Three 2.5′ sub–fields were used in the Hercules field and 4 in the Lynx field; at this distance from the pointing centre the bandwidth smearing is $< 10\%$. It should be noted that due to technical problems the Lovell telescope, the largest antenna in the array, was only included in the observations of Lynx B, C and D; this increased the sensitivity for these subfields by a factor of $\sim$2.2.

For the Hercules subfields, the flux calibrators used were 3C286 and OQ208 and the phase calibrator was 1734+508. For three of the Lynx subfields (B, C and D), the flux calibrators were again 3C286 and OQ208; for Lynx A however 3C286 and 2134+004 were used. The Lynx phase calibrator was 0843+463. Two flux calibrators are necessary as 3C286 is resolved on all but the shortest MERLIN baselines. All subfields were observed for 12 hours.

Data reduction and results

The reduction of MERLIN data is slightly different from the methods already described for the VLA. In particular, the initial data editing and calibration must be done at Jodrell Bank, using local software specifically written for the array. The advantage of this is that MERLIN staff are available for consultation; these data were reduced with the help of Tom Muxlow and Peter Thomasson for the Hercules and Lynx subfields respectively.

The visibilities for the flux and phase calibration sources which were corrupted because of individual telescope faults or radio interference, were flagged and removed using the local tool *dplot*. The flux, S_P of OQ208 or 2134+004, depending on the observation, was then roughly calculated using

$$S_{\rm P} = S_{\rm 3C286}\frac{A_{\rm P}}{A_{\rm 3C286}} \tag{5.3}$$

where $S_{\rm 3C286}$ is the assumed flux density of 3C286 in the scale of Baars et al. (1977) and $A_{\rm P}$ and $A_{\rm 3C286}$ are the raw amplitudes of the two calibrators measured on the shortest baselines. For these observations, the flux density value of 3C286 used was 13.63 Jy; this resulted in flux densities for 2134+004 of 5.11 Jy and 1.18 Jy for OQ208, which were then used to apply rough calibrations to the relevant subfields. Finally the data were converted into the FITS format and loaded into AIPS.

Once in AIPS the first step was to check the data for the calibrators and flag any remaining bad visibilities. The target data for Hercules and Lynx were then fully calibrated in phase and amplitude using the phase calibrator source. This was done using the MERLIN pipeline (Diamond et al., 2003) which uses the AIPS calibration tasks with MERLIN specific inputs to produce the best results. Data which included the Lovell telescope were then reweighted to account for the different sensitivities of the instruments in the array.

Finally each subfield was Fourier transformed and deconvolved to form the final CLEANed image. To minimise the non–coplanar array effects the centre of each subfield was again shifted to the position of each source it contained and treated separately. Each source facet was 512 by 512 pixels with $0.045''$/pixel. The rms noise reached for each source can be found in Tables 5.4 and 5.5. This process was then repeated for Lynx subfields B, C and D, with all baselines including the Lovell telescope removed from the data. This was done as, without Lovell, an 76m diameter dish, the MERLIN antennae are all comparable in size (similar to those of the VLA) and so a simple primary beam correction method can be applied. The non–Lovell images were therefore used to measure the primary–beam corrected flux densities of the sources but the deeper, Lovell included, images were used for the morphological classification. The rms noise reached in the non–Lovell images can also be found in Table 5.5.

For the Hercules sources, one candidate and one of the 'extra' sources were resolved out; the rest were all detected. In the Lynx subfields all the candidates were detected and 3 of the 'extra' sources were resolved out. A primary beam correction was then applied to correct for the attenuation of the primary beam on the off–centre sources and the flux densities were measured; the resulting values can be found in Tables 5.4 and 5.5. The corresponding contour maps can be found in Figures 5.5 and 5.6.

Hercules				
Sub–field	Name	$S_{1.4\mathrm{GHz}}$ (mJy)	C_{PB}	rms (μJy)
A	53w054a	1.47 ± 0.13	1.03	41
A	53w054b	1.83 ± 0.13	1.02	41
A	53w057	2.04 ± 0.14	1.00	40
B	53w059	18.87 ± 0.62	1.06	46
A	53w061	1.06 ± 0.10	1.03	34
B	53w065	4.62 ± 0.18	1.05	46
B	53w066	3.32 ± 0.18	1.00	47
B	53w070	2.29 ± 0.15	1.08	46
C	53w087	*		43
C	53w088	10.80 ± 0.18	1.05	49
Extra sources				
C	53w082	2.40 ± 0.15	1.09	45
C	53w089	*		42
C	53w091	32.81 ± 1.00	1.04	47

Table 5.4: The primary beam corrected flux densities and un–primary beam corrected noise levels found from the Hercules MERLIN observations. A * indicates a source which was resolved out. All flux densities were measured using *tvstat*. A primary beam correction error of 20% of the difference between the corrected and un–corrected flux density has been incorporated into the quoted errors.

Lynx						
Sub–field	Name	$S_{1.4\mathrm{GHz}}$ (mJy)	C_{PB}	Measure	rms (Lovell) (μJy)	rms (no Lovell) (μJy)
C	55w116	1.68 ± 0.34	1.06	T	30	68
C	55w121	0.97 ± 0.14	1.05	I	32	71
B	55w128	1.52 ± 0.32	1.04	T	29	67
B	55w132	1.29 ± 0.31	1.01	T	28	65
D	55w133	1.63 ± 0.17	1.04	I	30	68
D	55w136	0.44 ± 0.19	1.04	T	28	68
B	55w138	1.16 ± 0.26	1.01	T	30	67
D	55w143a	1.73 ± 0.20	1.05	T	37	62
A	55w159a	4.71 ± 0.18	1.04	I	–	98
Extra sources						
C	55w118	0.77 ± 0.19	1.01	I	32	68
C	55w122	0.32 ± 0.15	1.07	I	30	67
C	55w123	1.01 ± 0.12	1.03	I	33	70
C	55w124	3.26 ± 0.14	1.05	I	32	76
B	55w127	1.31 ± 0.31	1.08	T	27	64
B	55w131	*			28	65
B	55w137	1.14 ± 0.17	1.02	T	28	63
D	55w141	0.26 ± 0.10	1.02	I	32	66
D	55w143b	0.31 ± 0.11	1.04	I	33	67
A	55w150	*			–	102
A	55w157	2.51 ± 0.30	1.04	I	–	108
A	55w159b	*	1.04		–	96
C	60w016	0.48 ± 0.16	1.02	T	33	72

Table 5.5: The primary beam corrected flux densities and un–primary beam corrected noise levels, both with and without the Lovell telescope in the array, found from the Lynx MERLIN observations. A * indicates a source which was resolved out. A primary beam correction error of 20% of the difference between the corrected and un–corrected flux density has been incorporated into the quoted errors. A 'T' indicates a *tvstat* measurement and an 'I' indicates an *imfit* measurement.

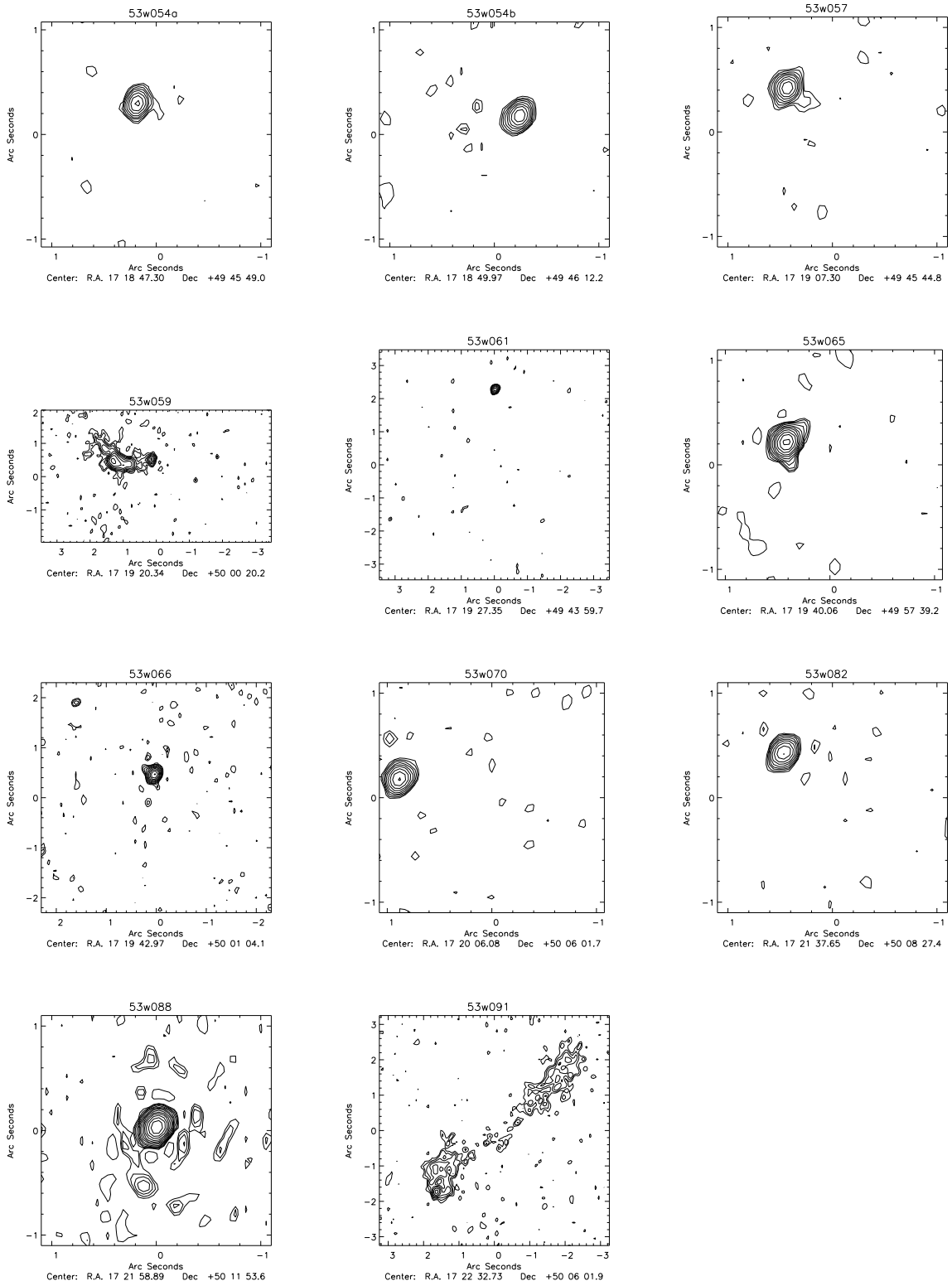

Figure 5.5: The radio contour maps, for the Hercules field, from the MERLIN 1.4 GHz observations, centred on the host galaxy position where available. The small scale ($\sim 1'' \times 1''$) of these images, combined with the optical astrometric error, results in the offsets seen here. The beam size is $0.19'' \times 0.15''$. Contours start at 50μJy/beam and increase by factors of $\sqrt{2}$.

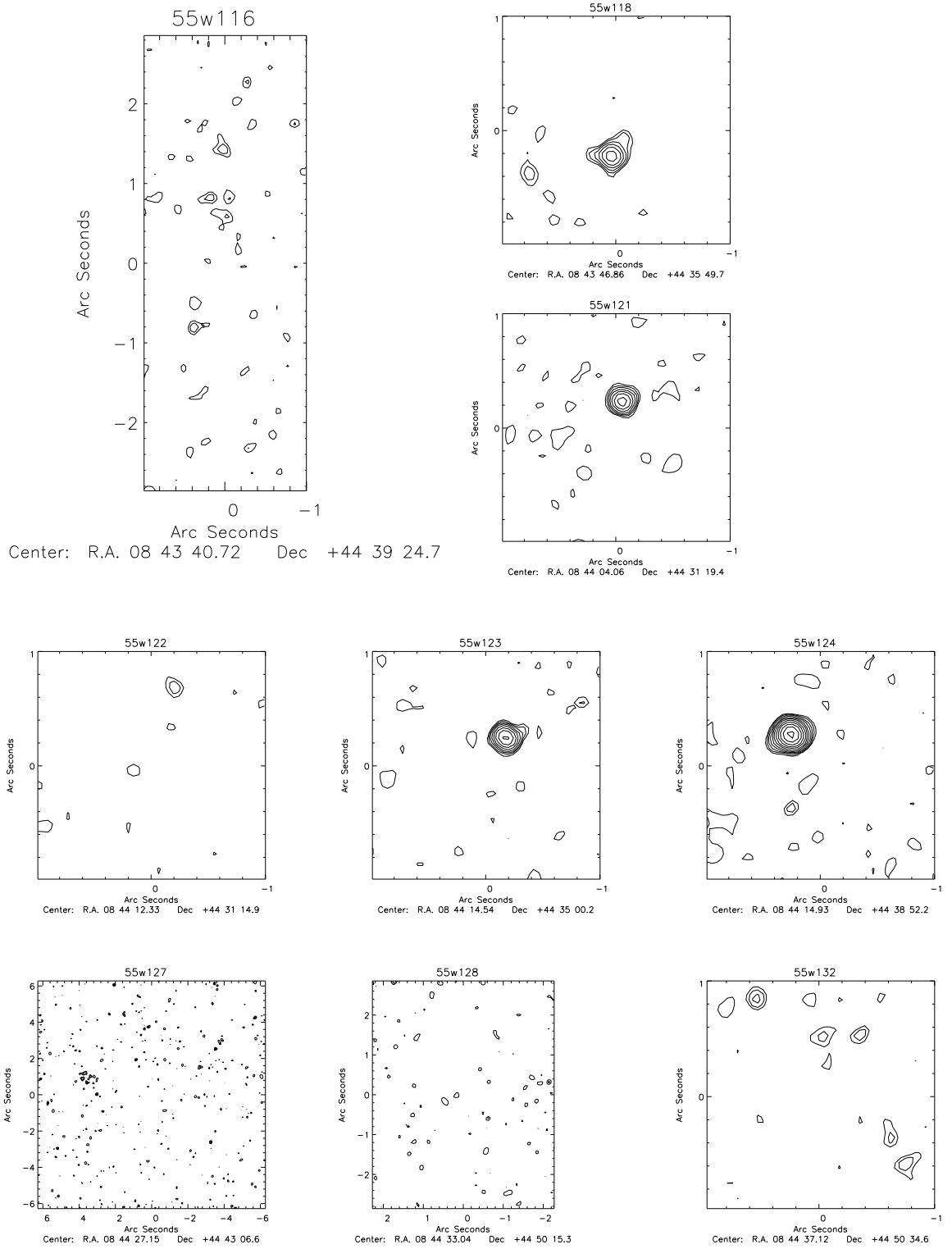

Figure 5.6: The radio contour maps, including the Lovell telescope, for the Lynx field, from the MERLIN 1.4 GHz observations, centred on the optical host galaxy position if available. The small scale ($\sim 1'' \times 1''$) of these images, combined with the optical astrometric error, results in the offsets seen here. The beam size is $0.19'' \times 0.15''$. Contours start at 33μJy/beam (apart from the sources in subfield A, 55w157 and 55w159a, which start at 90 μJy/beam) and increase by factors of $\sqrt{2}$.

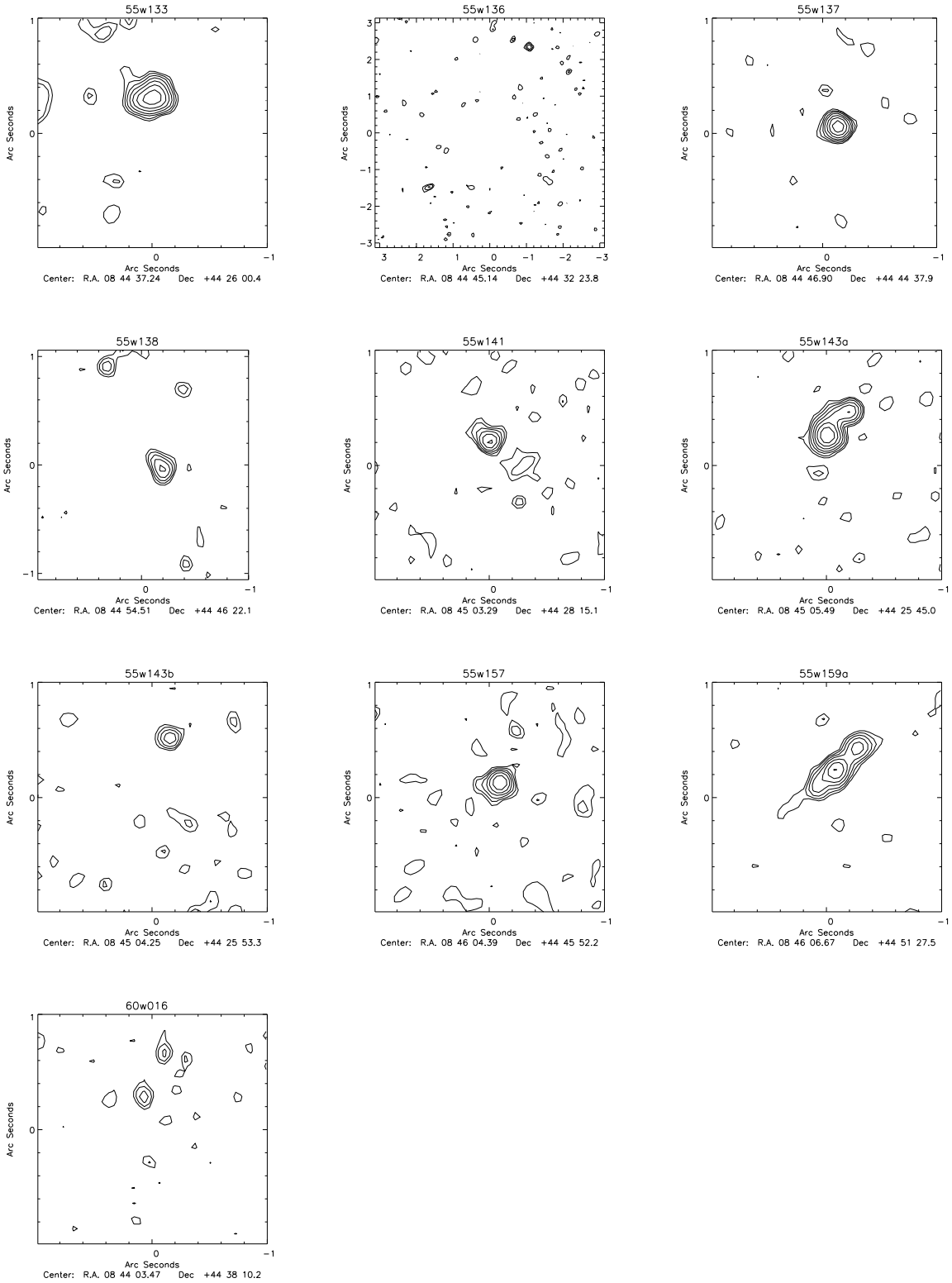
55w133
Arc Seconds
Arc Seconds
Center: R.A. 08 44 37.24 Dec +44 26 00.4
55w136
Arc Seconds
Arc Seconds
Center: R.A. 08 44 45.14 Dec +44 32 23.8
55w137
Arc Seconds
Arc Seconds
Center: R.A. 08 44 46.90 Dec +44 44 37.9
55w138
Arc Seconds
Arc Seconds
Center: R.A. 08 44 54.51 Dec +44 46 22.1
55w141
Arc Seconds
Arc Seconds
Center: R.A. 08 45 03.29 Dec +44 28 15.1
55w143a
Arc Seconds
Arc Seconds
Center: R.A. 08 45 05.49 Dec +44 25 45.0
55w143b
Arc Seconds
Arc Seconds
Center: R.A. 08 45 04.25 Dec +44 25 53.3
55w157
Arc Seconds
Arc Seconds
Center: R.A. 08 46 04.39 Dec +44 45 52.2
55w159a
Arc Seconds
Arc Seconds
Center: R.A. 08 46 06.67 Dec +44 51 27.5
60w016
Arc Seconds
Arc Seconds
Center: R.A. 08 44 03.47 Dec +44 38 10.2

Figure 5.6

5.5 Comparison of results

The flux densities for the sources in the sample in all the different radio observations are gathered together in Tables 5.6 and 5.7. Comparing the values, it is clear that, for some sources, significantly more flux was detected in the A or B–array observations than in the, lower resolution, Oort et al. (1987; 1985) data, as shown in Figure 5.7. This discrepancy occurred because of the different measurement methods used; Oort et al. determined all their flux densities using a two dimensional elliptical Gaussian fitting routine, which works well for pointlike sources, but fails for sources which are even slightly extended. The A and B–array flux densities on the other hand were measured with the Gaussian fitting task *imfit* or the total flux density measuring task *tvstat*, depending on the amount of source extension present, thus resulting in more accurate results.

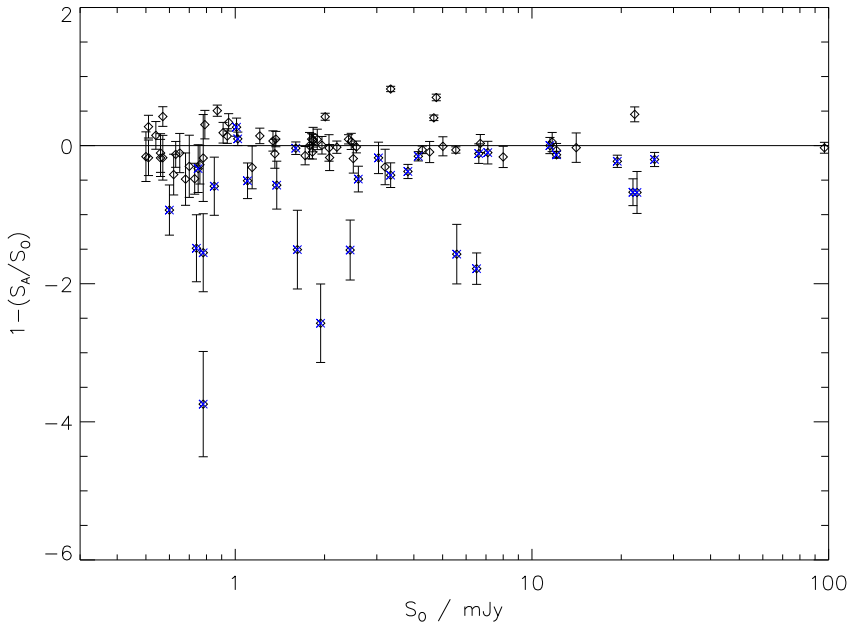

Figure 5.7: A comparison of the VLA A–array ($S_{\rm A}$) and Oort et al. (1985; 1987; $S_{\rm O}$) flux densities for both fields. Compact, *imfit* measured, sources are shown as diamonds and extended, *tvstat* measured, sources are overplotted with blue crosses.

The second point to be noted when comparing the values is that, for many of the sources, the measured flux density decreases as the resolution of the observations increases; this is illustrated in Figures 5.8 and 5.9. For the non–quasar sources, it is likely that this loss indicates the presence of resolved–out, extended emission, which in the absence of hotspots may indicate an FRI–type structure. Quasars are often variable so any flux density loss they exhibit is likely to be due to this.

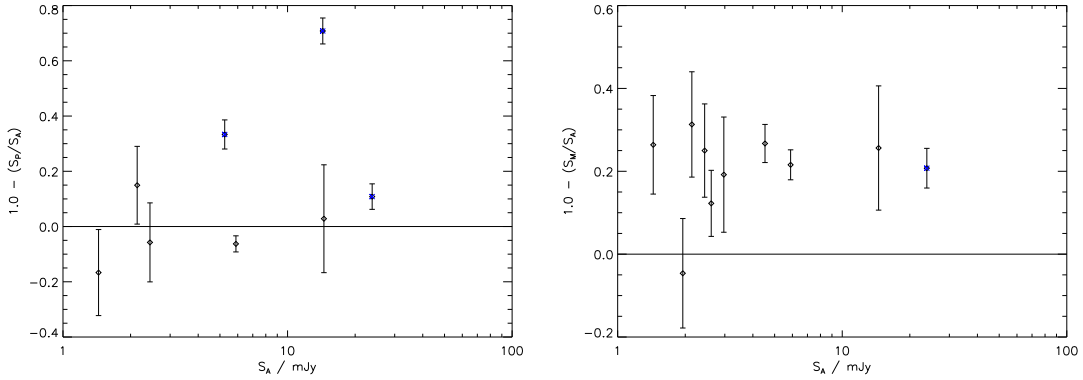

Figure 5.8: The flux density loss between the A–array ($S_{\rm A}$) and PieTown ($S_{\rm P}$) and MERLIN ($S_{\rm M}$) observations for the Hercules field.

Since the resolutions of the four radio observations are so different, it is hard to gain an overview of the structure of individual sources in the sample from considering Figures 2.2, 2.3, 5.1, 5.3, 5.4, 5.5 and 5.6 alone. Therefore, Figures 5.10 and 5.11 show, for the sources included in the VLA+Pt or MERLIN observations, all the radio contour maps at the same scale, centred on the optical host galaxy positions, if available, or the A–array position if not[1]; collecting the images together like this illustrates the power of the high resolution observations in differentiating FRI objects from FRIIs. For example, the Hercules field source 53w059 is an FRI candidate in the A–array data but it is only in the MERLIN map, showing its inner jet and resolved out lobes, that it can be firmly classified as such. On the other hand, the A–array image of the Lynx field source 55w138 does not show any clear structure and whilst the VLA+Pt map indicates that it is extended, the MERLIN map is needed to show the location of the jet hotspots.

[1]The starburst galaxy 55w127 is not included in this Figure as it is not an FRI candidate

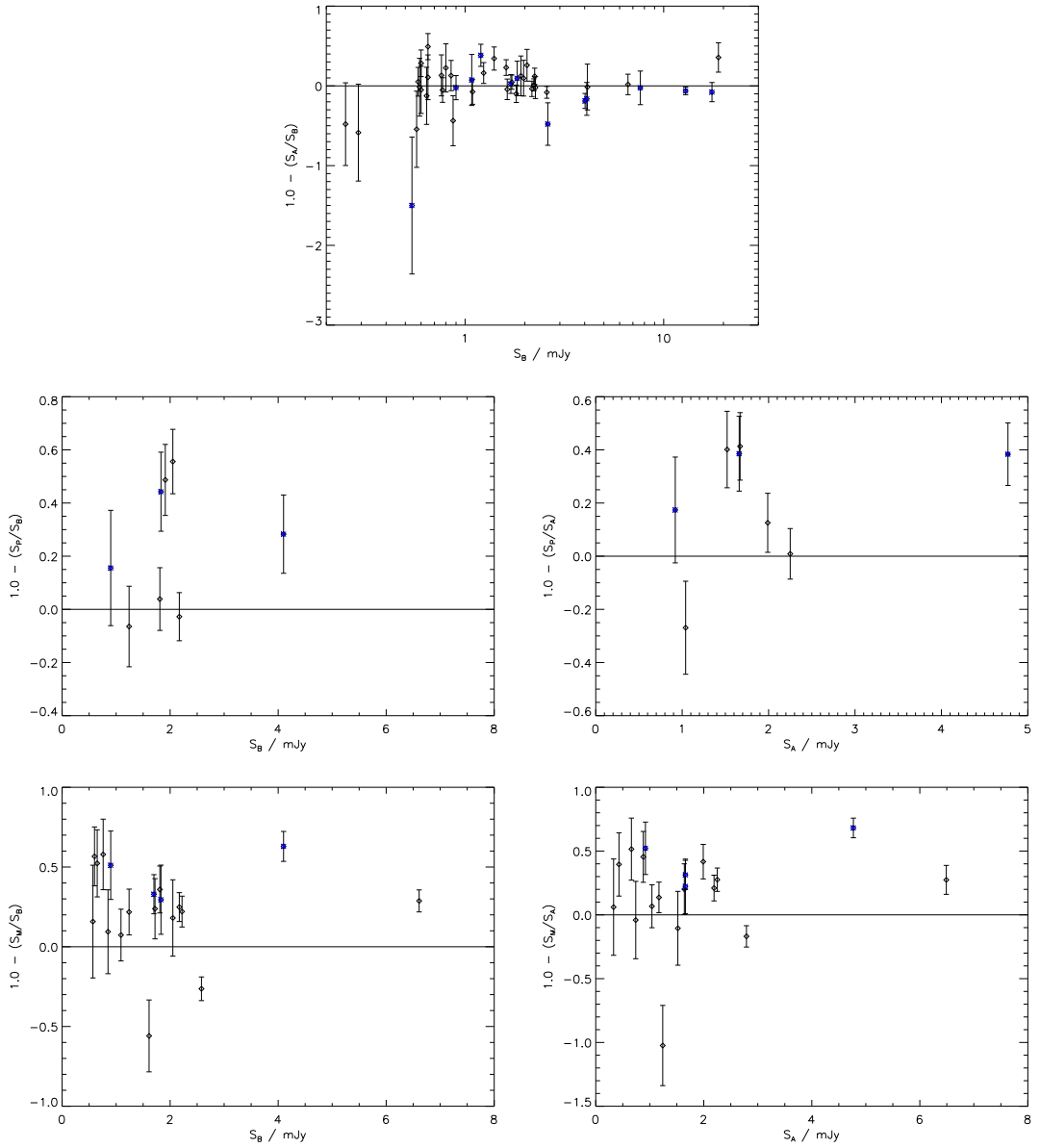

Figure 5.9: The flux density loss between the A ($S_{\rm A}$) or B–array ($S_{\rm B}$) and the PieTown ($S_{\rm P}$) or MERLIN ($S_{\rm M}$) observations for the Lynx field.

Name	$S_{\rm Oort}$	$S_{\rm A}$	$S_{\rm Pt}$	$S_{\rm Mer}$
53w052	8.00 ± 0.34	9.31 ± 1.17		
53w054a	2.07 ± 0.19	2.14 ± 0.35	1.82 ± 0.07	1.47 ± 0.13
53w054b	2.08 ± 0.19	2.44 ± 0.32	2.58 ± 0.07	1.83 ± 0.13
53w057	1.96 ± 0.14	1.95 ± 0.21		2.04 ± 0.14
53w059	19.40 ± 1.00	23.81 ± 1.21	21.23 ± 0.21	18.87 ± 0.62
53w061	4.76 ± 0.43	1.44 ± 0.18	1.68 ± 0.06	1.06 ± 0.10
53w062	0.73 ± 0.10	1.08 ± 0.07		
53w065	5.54 ± 0.20	5.89 ± 0.14	6.26 ± 0.09	4.62 ± 0.18
53w066	4.27 ± 0.17	4.53 ± 0.15		3.32 ± 0.18
53w067	21.90 ± 0.90	36.68 ± 3.97		
53w069	3.82 ± 0.17	5.25 ± 0.31	3.50 ± 0.18	
53w070	2.56 ± 0.14	2.61 ± 0.17		2.29 ± 0.15
53w075	96.80 ± 3.30	99.82 ± 6.83		
53w076	1.94 ± 0.17	6.93 ± 0.92		
53w077	6.51 ± 0.39	18.11 ± 1.01		
53w078	0.74 ± 0.12	1.84 ± 0.20		
53w079	11.70 ± 0.50	11.10 ± 1.56		
53w080	25.90 ± 0.90	31.11 ± 2.42		
53w081	12.10 ± 0.50	12.93 ± 1.08		
53w082	2.50 ± 0.19	2.97 ± 0.47		2.40 ± 0.15
53w083	5.01 ± 0.25	5.06 ± 0.64		
53w084	0.68 ± 0.12	1.01 ± 0.19		
53w085	4.52 ± 0.22	4.94 ± 0.65		
53w086a	1.62 ± 0.30	4.06 ± 0.54		
53w086b	2.44 ± 0.30	6.13 ± 0.74		
53w087	5.58 ± 0.35	14.35 ± 2.23	4.19 ± 0.17	*
53w088	14.10 ± 0.70	14.52 ± 2.92	14.11 ± 0.09	10.80 ± 0.18
53w089	3.04 ± 0.26	3.58 ± 0.62		*
66w009a	1.14 ± 0.21	1.50 ± 0.22		
66w009b	0.70 ± 0.21	0.91 ± 0.16		
66w014	3.34 ± 0.51	0.60 ± 0.09		
66w027	0.57 ± 0.11	0.67 ± 0.13		
66w031	0.76 ± 0.14	0.97 ± 0.12		
66w035	0.63 ± 0.09	0.71 ± 0.06		
66w036	0.78 ± 0.11	3.70 ± 0.29		
66w042	0.78 ± 0.14	1.99 ± 0.26		
66w047	0.60 ± 0.10	1.16 ± 0.10		
66w049	1.38 ± 0.27	2.17 ± 0.22		
66w058	1.89 ± 0.16	1.72 ± 0.24		

Table 5.6: The complete set of flux densities for the sources in the Hercules field complete sample. A '*' indicates a source which has been resolved out.

Name	$S_{\rm Oort}$	$S_{\rm B}$	$S_{\rm A}$	$S_{\rm Pt}$	$S_{\rm Mer}$
55w116	1.36 ± 0.12	2.05 ± 0.43	1.52 ± 0.25	0.91 ± 0.16	1.68 ± 0.34
55w118	0.91 ± 0.09	0.85 ± 0.13	0.74 ± 0.11		0.77 ± 0.19
55w120	1.83 ± 0.16	1.91 ± 0.43	1.67 ± 0.29	0.98 ± 0.13	
55w121	1.21 ± 0.09	1.24 ± 0.14	1.04 ± 0.11	1.32 ± 0.11	0.97 ± 0.14
55w122	0.56 ± 0.08	0.76 ± 0.18	0.66 ± 0.12		0.32 ± 0.15
55w123	2.01 ± 0.10	1.09 ± 0.14	1.17 ± 0.08		1.01 ± 0.12
55w124	4.67 ± 0.17	2.58 ± 0.10	2.79 ± 0.16		3.26 ± 0.14
55w127	1.81 ± 0.10	1.72 ± 0.11	1.64 ± 0.11		1.31 ± 0.31
55w128	3.34 ± 0.18	4.10 ± 0.56	4.77 ± 0.54	2.94 ± 0.45	1.52 ± 0.32
55w131	1.01 ± 0.10	1.20 ± 0.20	0.74 ± 0.11		*
55w132	1.10 ± 0.11	1.83 ± 0.36	1.66 ± 0.23	1.02 ± 0.19	1.29 ± 0.31
55w133	2.20 ± 0.11	2.17 ± 0.13	2.25 ± 0.16	2.23 ± 0.14	1.63 ± 0.17
55w135	2.60 ± 0.14	2.61 ± 0.37	3.86 ± 0.44		
55w136	1.02 ± 0.07	0.90 ± 0.11	0.92 ± 0.08	0.76 ± 0.17	0.44 ± 0.19
55w137	1.60 ± 0.09	1.70 ± 0.17	1.66 ± 0.11		1.14 ± 0.17
55w138	1.82 ± 0.10	1.81 ± 0.12	1.99 ± 0.15	1.74 ± 0.18	1.16 ± 0.26
55w140	0.79 ± 0.20	0.58 ± 0.09	0.55 ± 0.06		
55w141	0.87 ± 0.07	0.60 ± 0.11	0.43 ± 0.06		0.26 ± 0.10
55w143a	2.41 ± 0.11	2.22 ± 0.11	2.19 ± 0.13		1.73 ± 0.20
55w143b	0.57 ± 0.09	0.65 ± 0.17	0.33 ± 0.06		0.31 ± 0.11
55w147	1.72 ± 0.11	2.24 ± 0.14	1.97 ± 0.19		
55w149	7.10 ± 0.32	7.63 ± 1.14	7.82 ± 1.11		
55w150	0.95 ± 0.10	0.60 ± 0.14	0.63 ± 0.10		*
55w154	12.10 ± 0.40	12.90 ± 0.44	13.71 ± 0.40		
55w155	1.83 ± 0.10	1.63 ± 0.15	1.70 ± 0.14		
55w156	4.14 ± 0.16	4.02 ± 0.26	4.78 ± 0.21		
55w157	1.37 ± 0.10	1.61 ± 0.13	1.24 ± 0.12		2.51 ± 0.30
55w159a	6.70 ± 0.29	6.61 ± 0.21	6.49 ± 0.82		4.71 ± 0.43
55w159b	0.75 ± 0.13	1.08 ± 0.31	1.00 ± 0.19		*
55w160	0.94 ± 0.08	0.77 ± 0.09	0.81 ± 0.07		
55w161	1.34 ± 0.14	0.87 ± 0.16	1.25 ± 0.15		
55w165a	18.12 ± 0.54	17.51 ± 1.33	18.88 ± 1.54		
55w165c	0.78 ± 0.40	1.40 ± 0.23	0.92 ± 0.14		
55w166	2.46 ± 0.14	2.26 ± 0.17	2.31 ± 0.26		
60w016	0.62 ± 0.08	0.57 ± 0.15	0.88 ± 0.14		0.48 ± 0.16
60w024	0.51 ± 0.09	0.25 ± 0.08	0.37 ± 0.05		
60w032	0.54 ± 0.09	0.29 ± 0.10	0.46 ± 0.08		
60w039	0.65 ± 0.09	0.64 ± 0.15	0.72 ± 0.16		
60w055	0.51 ± 0.08	0.59 ± 0.19	0.60 ± 0.09		
60w067	0.56 ± 0.09	0.80 ± 0.27	0.62 ± 0.12		
60w071	0.50 ± 0.08	0.65 ± 0.11	0.58 ± 0.15		
60w084	0.85 ± 0.17	0.54 ± 0.16	1.35 ± 0.23		

Table 5.7: The complete set of flux densities for the sources in the Lynx field complete sample. A '*' indicates a source which has been resolved out.

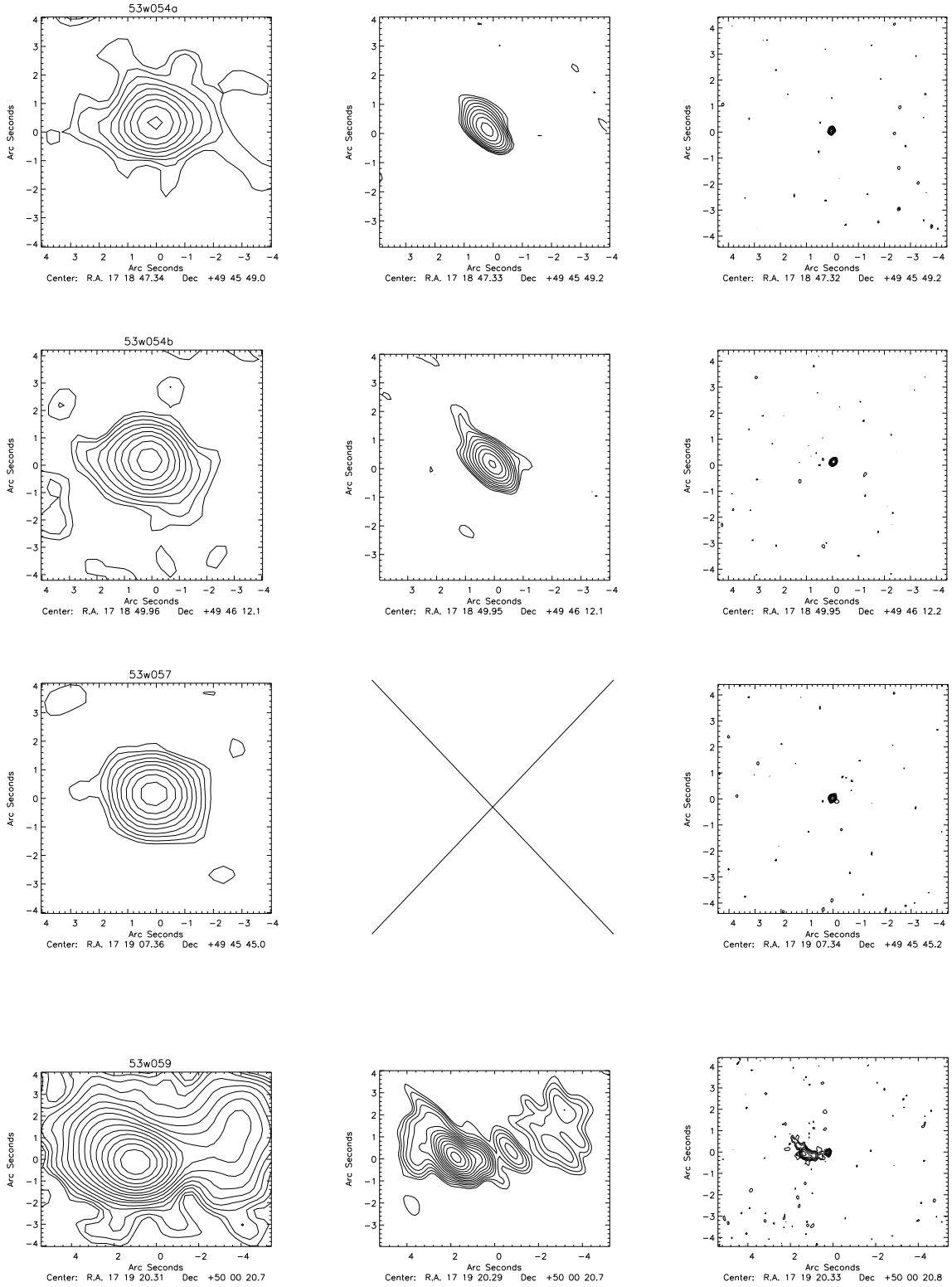

Figure 5.10: The A–array, A+Pt and MERLIN contour maps for the sources in the Hercules field, included in the A+Pt or MERLIN observations, all centred on the optical host galaxy position if available, with the aim of comparing the source morphologies at the three different resolutions, $\sim 1.5''$ $\sim 0.5''$ and $\sim 0.18''$. The contour maps for each source are all of equal size and all contours increase by a factor of $\sqrt{2}$.

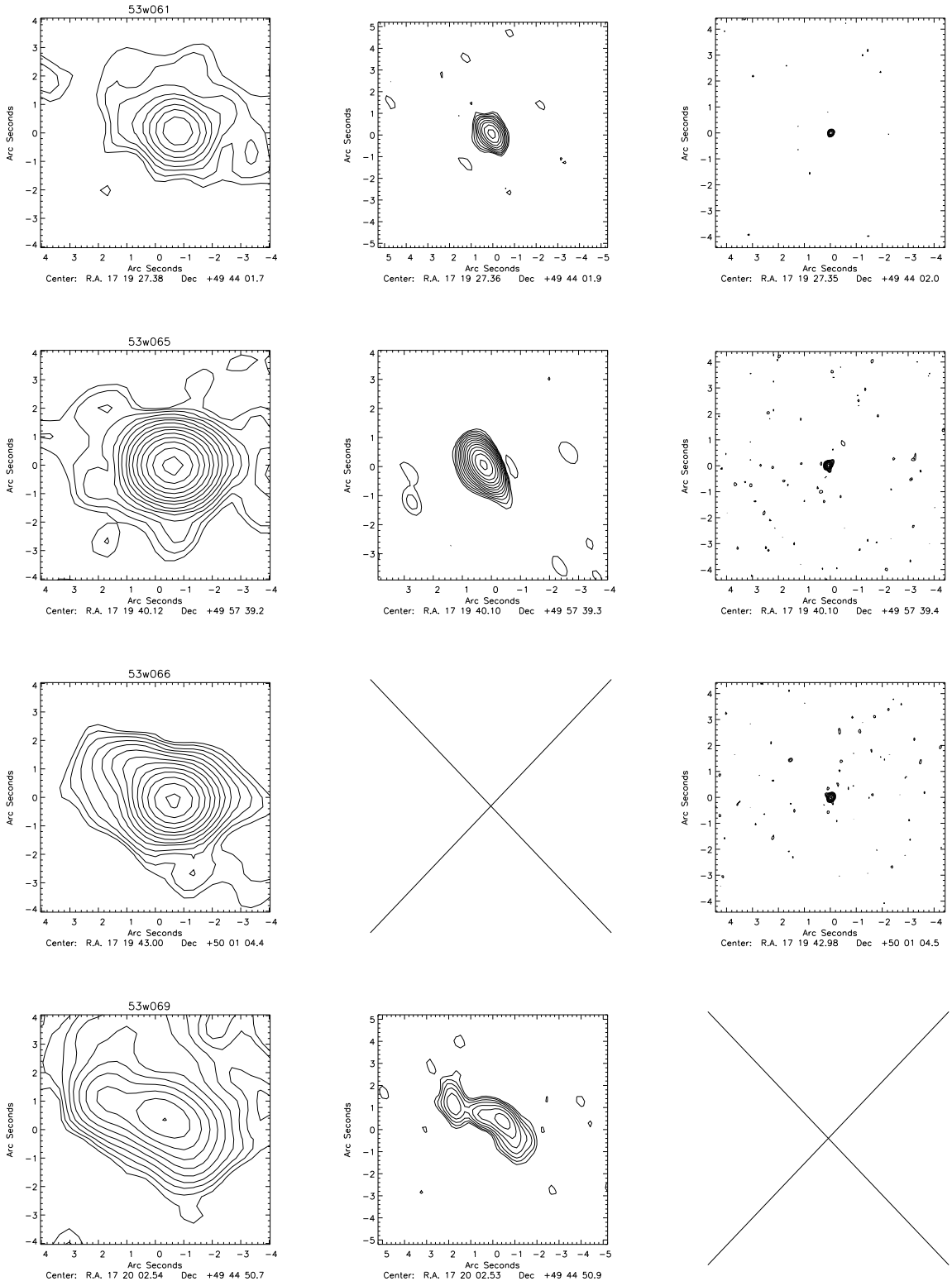
53w061
Arc Seconds
Arc Seconds
Center: R.A. 17 19 27.38 Dec +49 44 01.7
Arc Seconds
Arc Seconds
Center: R.A. 17 19 27.36 Dec +49 44 01.9
Arc Seconds
Arc Seconds
Center: R.A. 17 19 27.35 Dec +49 44 02.0
53w065
Arc Seconds
Arc Seconds
Center: R.A. 17 19 40.12 Dec +49 57 39.2
Arc Seconds
Arc Seconds
Center: R.A. 17 19 40.10 Dec +49 57 39.3
Arc Seconds
Arc Seconds
Center: R.A. 17 19 40.10 Dec +49 57 39.4
53w066
Arc Seconds
Arc Seconds
Center: R.A. 17 19 43.00 Dec +50 01 04.4
Arc Seconds
Arc Seconds
Center: R.A. 17 19 42.98 Dec +50 01 04.5
53w069
Arc Seconds
Arc Seconds
Center: R.A. 17 20 02.54 Dec +49 44 50.7
Arc Seconds
Arc Seconds
Center: R.A. 17 20 02.53 Dec +49 44 50.9

Figure 5.10

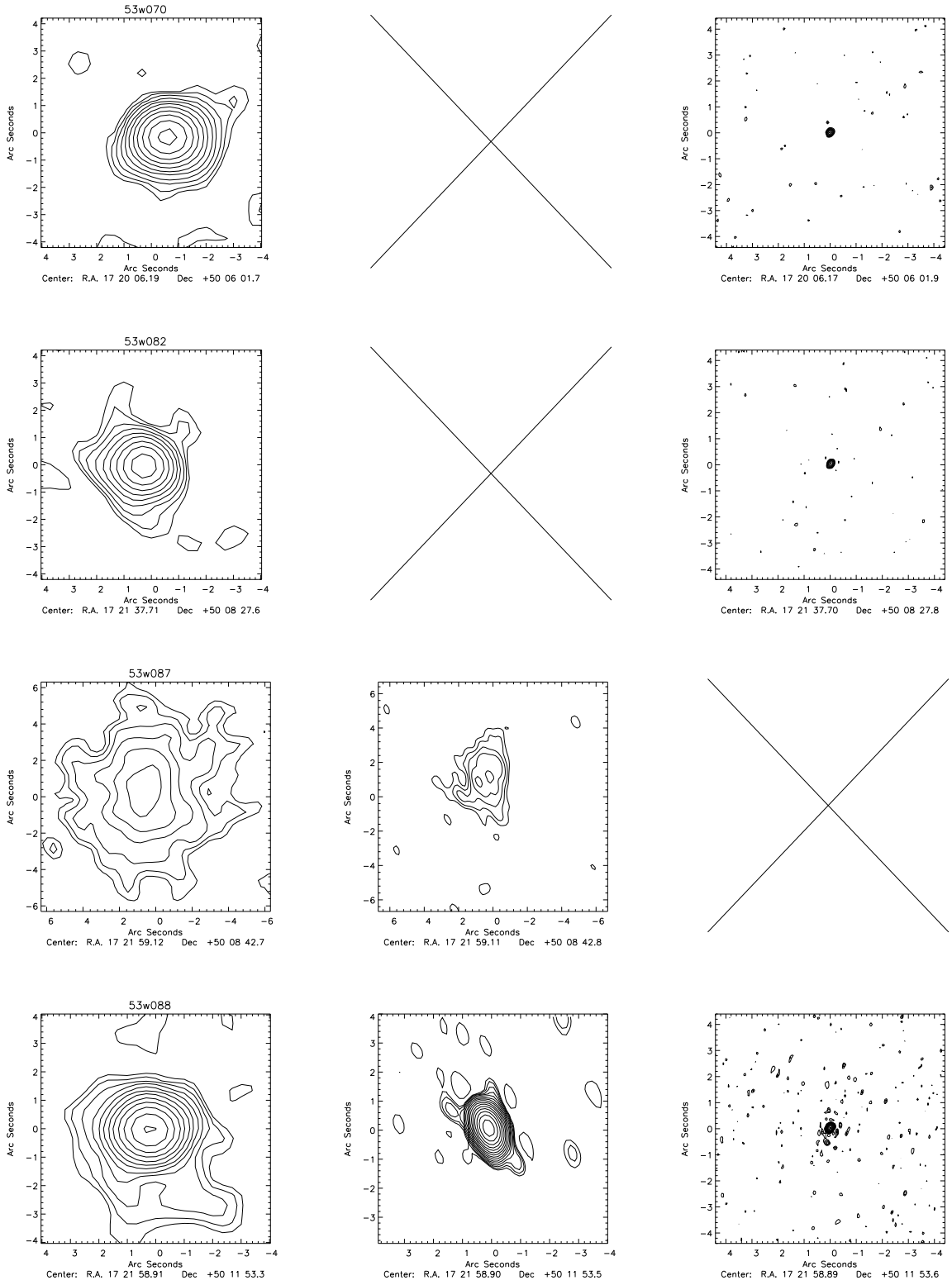
53w070
Arc Seconds
Center: R.A. 17 20 06.19 Dec +50 06 01.7
Center: R.A. 17 20 06.17 Dec +50 06 01.9
53w082
Center: R.A. 17 21 37.71 Dec +50 08 27.6
Center: R.A. 17 21 37.70 Dec +50 08 27.8
53w087
Center: R.A. 17 21 59.12 Dec +50 08 42.7
Center: R.A. 17 21 59.11 Dec +50 08 42.8
53w088
Center: R.A. 17 21 58.91 Dec +50 11 53.3
Center: R.A. 17 21 58.90 Dec +50 11 53.5
Center: R.A. 17 21 58.89 Dec +50 11 53.6

Figure 5.10

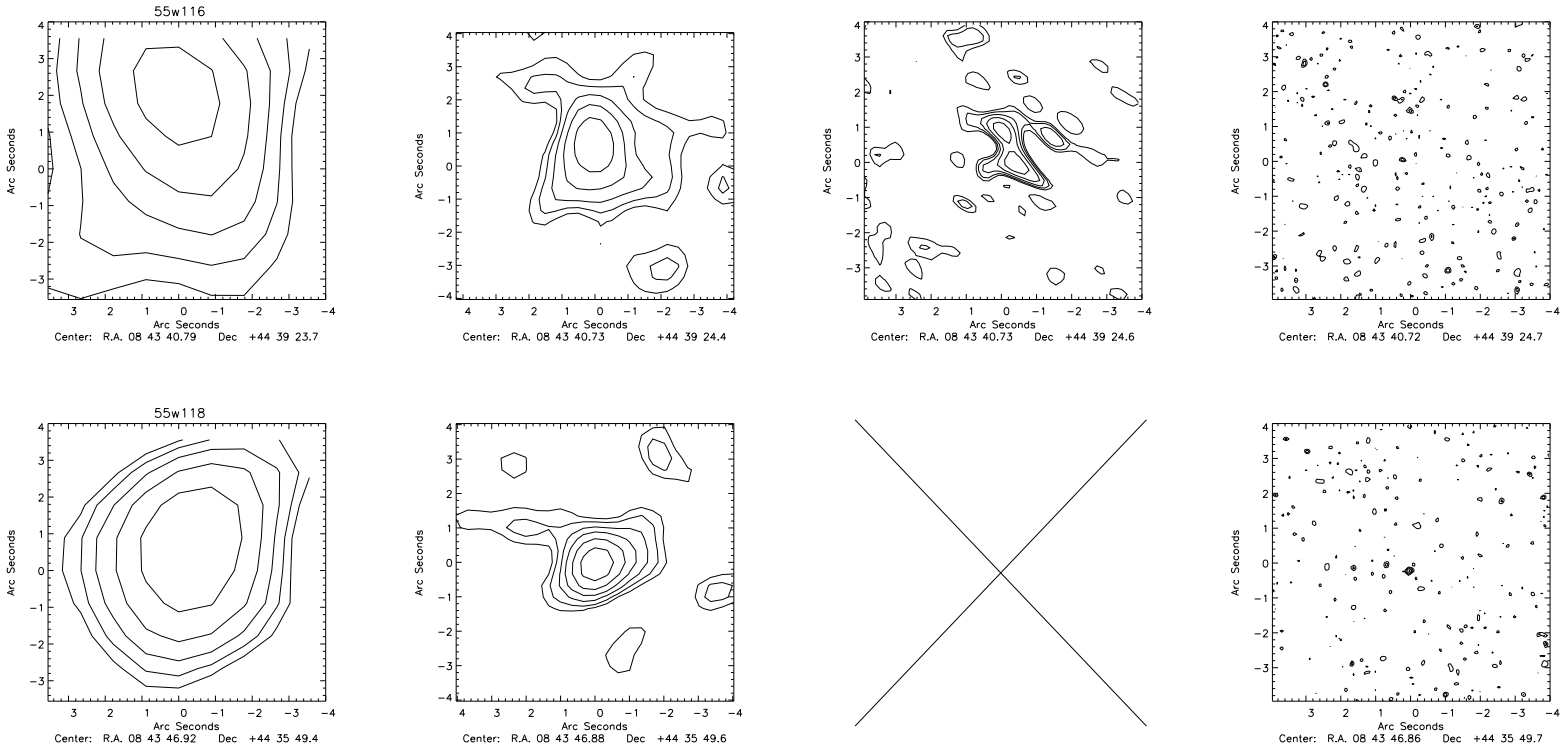

Figure 5.11: The B–array, A–array, A+Pt and MERLIN contour maps for the sources in the Lynx field, included in the A+Pt or MERLIN observations, all centred on the optical host galaxy position if available, with the aim of comparing the source morphologies at the four different resolutions, $\sim 5''$ $\sim 1.5''$ $\sim 0.5''$ and $\sim 0.18''$. The contour maps for each source are all of equal size and all contours increase by a factor of $\sqrt{2}$.

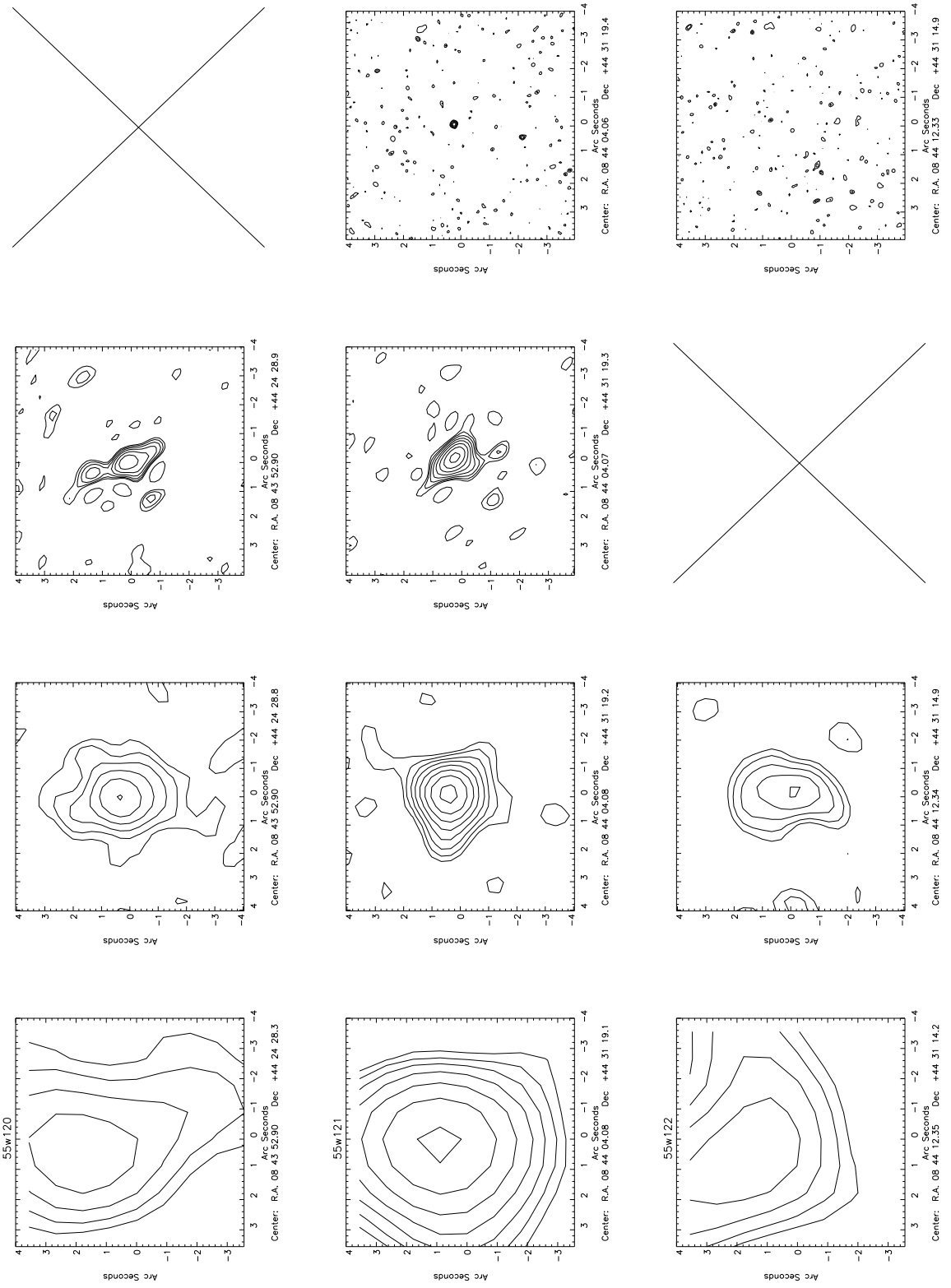
55w120
55w121
55w122
Arc Seconds
Center: R.A. 08 43 52.90 Dec +44 24 28.3
Center: R.A. 08 44 04.08 Dec +44 31 19.1
Center: R.A. 08 44 12.35 Dec +44 31 14.2
Center: R.A. 08 43 52.90 Dec +44 24 28.8
Center: R.A. 08 44 04.08 Dec +44 31 19.2
Center: R.A. 08 44 12.34 Dec +44 31 14.9
Center: R.A. 08 43 52.90 Dec +44 24 28.9
Center: R.A. 08 44 04.07 Dec +44 31 19.3
Center: R.A. 08 44 04.06 Dec +44 31 19.4
Center: R.A. 08 44 12.33 Dec +44 31 14.9

Figure 5.11

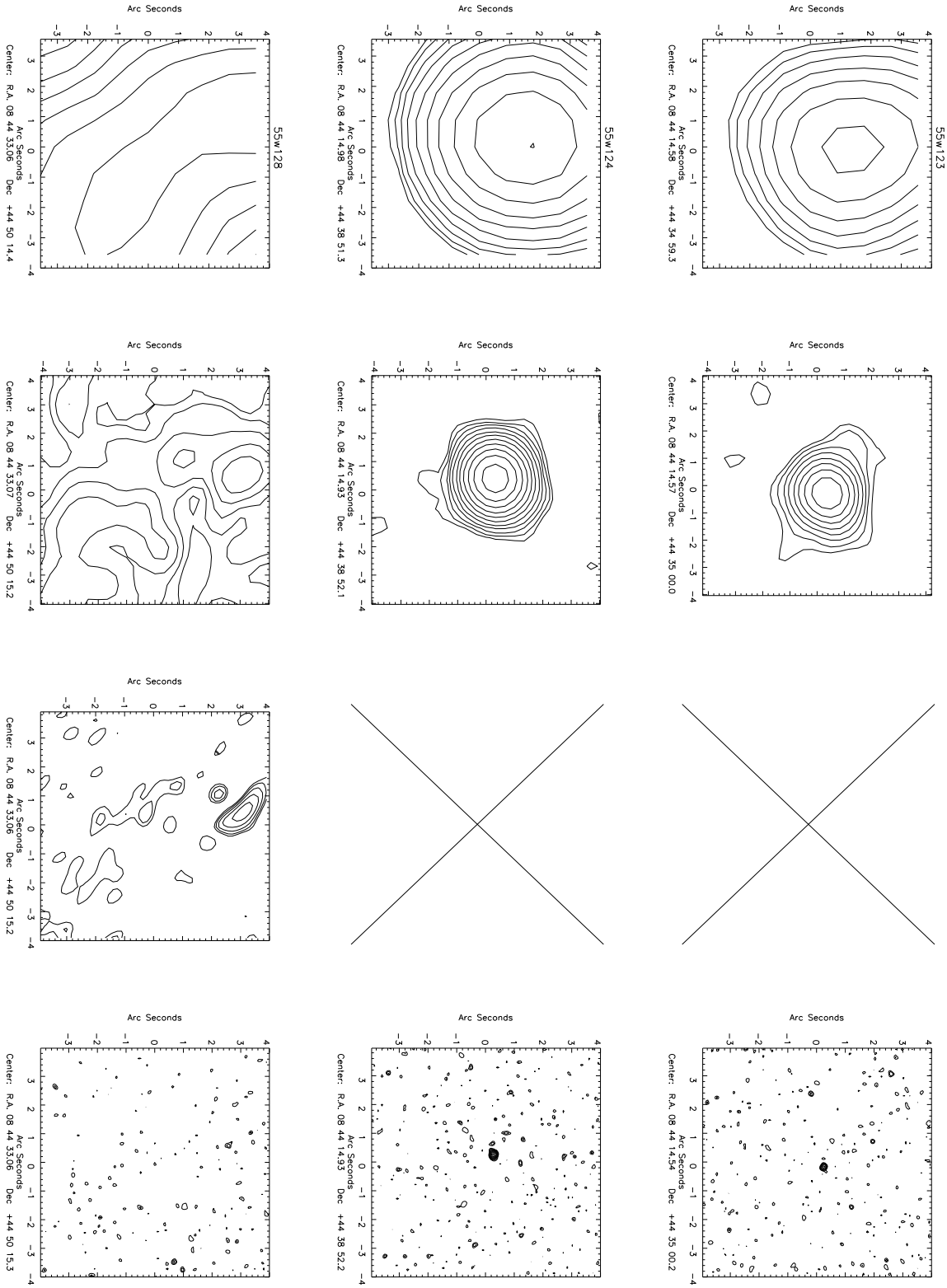
55w123
55w124
55w128
Arc Seconds
Center: R.A. 08 44 14.58 Dec +44 34 59.3
Center: R.A. 08 44 14.98 Dec +44 38 51.3
Center: R.A. 08 44 33.06 Dec +44 50 14.4
Center: R.A. 08 44 14.57 Dec +44 35 00.0
Center: R.A. 08 44 14.93 Dec +44 38 52.1
Center: R.A. 08 44 33.07 Dec +44 50 15.2
Center: R.A. 08 44 33.06 Dec +44 50 15.2
Center: R.A. 08 44 14.54 Dec +44 35 00.2
Center: R.A. 08 44 14.93 Dec +44 38 52.2
Center: R.A. 08 44 33.06 Dec +44 50 15.3

Figure 5.11

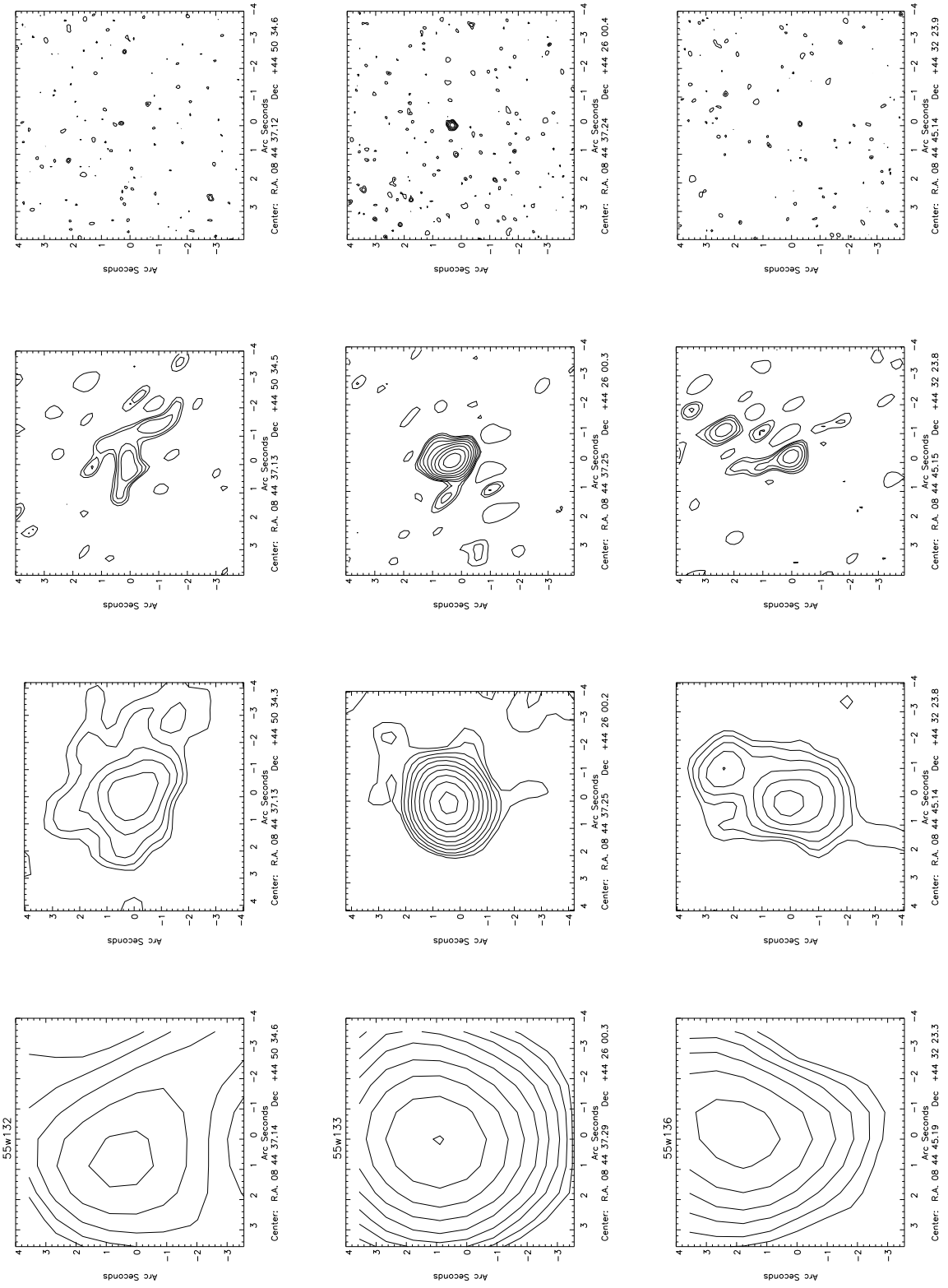
55w1.32
55w1.33
55w1.36
Arc Seconds
Center: R.A. 08 44 37.14 Dec +44 50 34.6
Center: R.A. 08 44 37.13 Dec +44 50 34.3
Center: R.A. 08 44 37.13 Dec +44 50 34.5
Center: R.A. 08 44 37.12 Dec +44 50 34.6
Center: R.A. 08 44 37.29 Dec +44 26 00.3
Center: R.A. 08 44 37.25 Dec +44 26 00.2
Center: R.A. 08 44 37.25 Dec +44 26 00.3
Center: R.A. 08 44 37.24 Dec +44 26 00.4
Center: R.A. 08 44 45.19 Dec +44 32 23.3
Center: R.A. 08 44 45.14 Dec +44 32 23.8
Center: R.A. 08 44 45.15 Dec +44 32 23.8
Center: R.A. 08 44 45.14 Dec +44 32 23.9

Figure 5.11

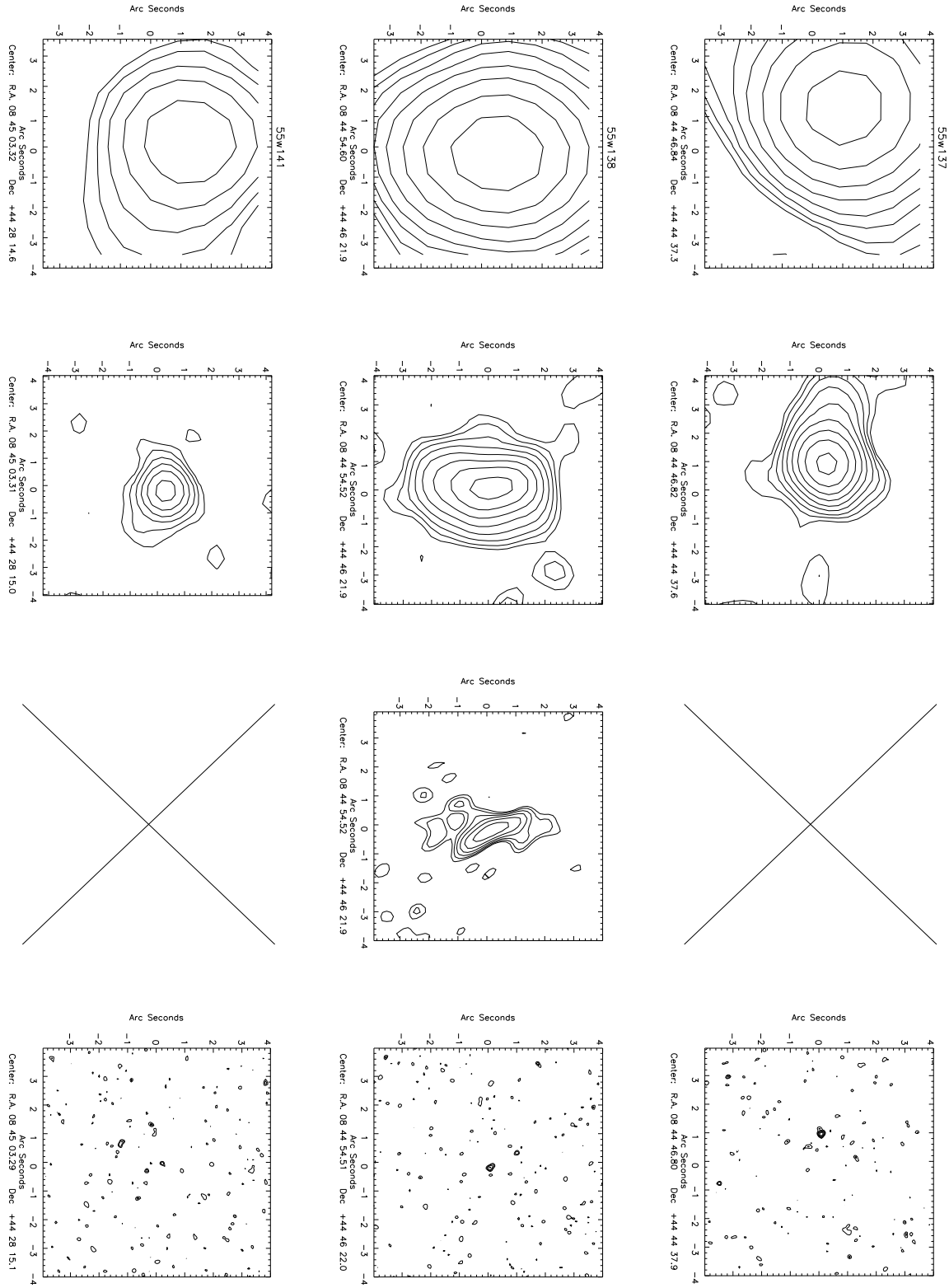
55w137
55w138
55w141
Arc Seconds
Center: R.A. 08 44 46.84 Dec +44 44 37.3
Center: R.A. 08 44 54.60 Dec +44 46 21.9
Center: R.A. 08 45 03.32 Dec +44 28 14.6
Center: R.A. 08 44 46.82 Dec +44 44 37.6
Center: R.A. 08 44 54.52 Dec +44 46 21.9
Center: R.A. 08 45 03.31 Dec +44 28 15.0
Center: R.A. 08 44 54.52 Dec +44 46 21.9
Center: R.A. 08 44 46.80 Dec +44 44 37.9
Center: R.A. 08 44 54.51 Dec +44 46 22.0
Center: R.A. 08 45 03.29 Dec +44 28 15.1

Figure 5.11

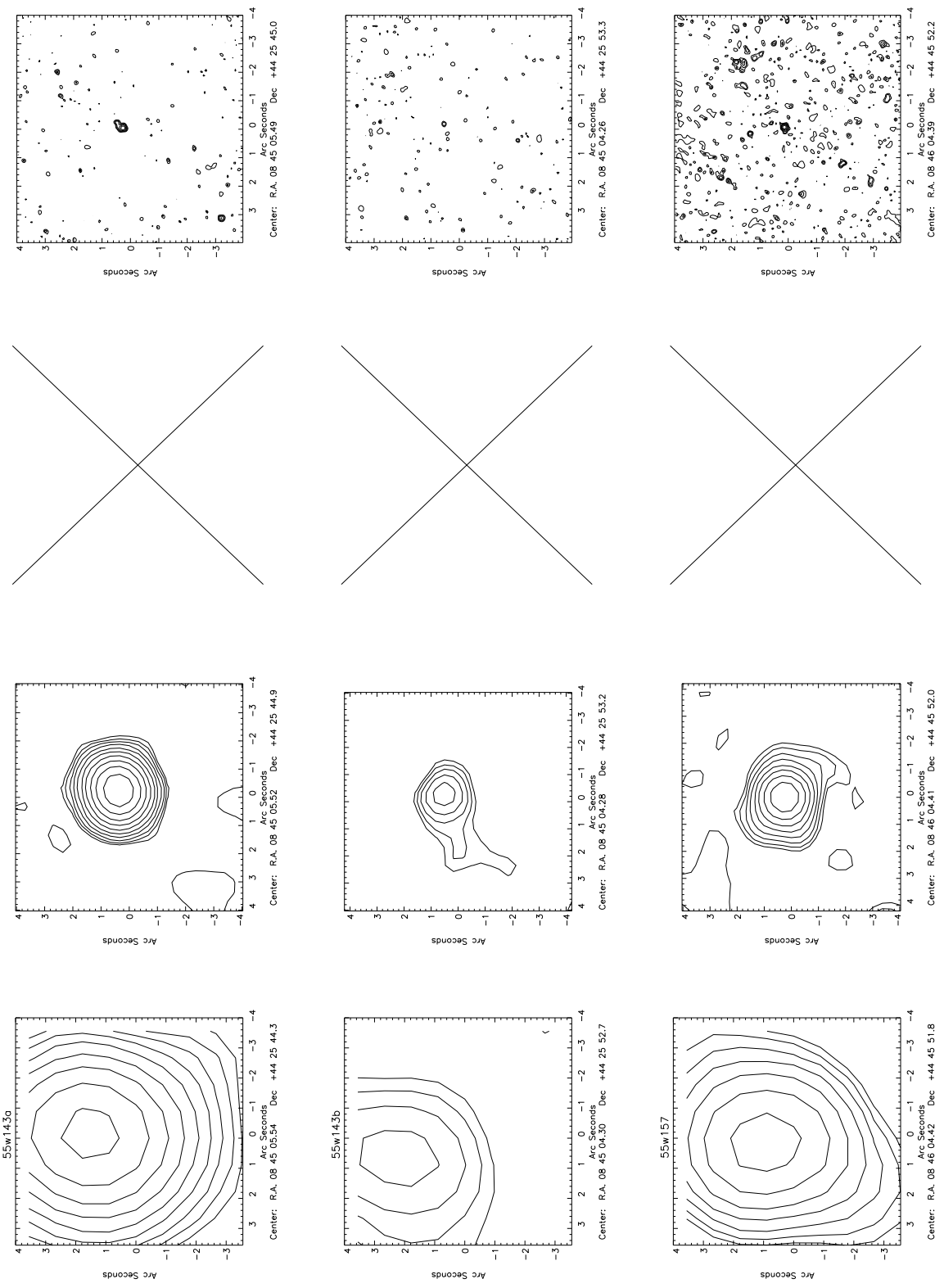
55w143a
55w143b
55w157
Arc Seconds
Center: R.A. 08 45 05.54 Dec +44 25 44.3
Center: R.A. 08 45 05.52 Dec +44 25 44.9
Center: R.A. 08 45 05.49 Dec +44 25 45.0
Center: R.A. 08 45 04.30 Dec +44 25 52.7
Center: R.A. 08 45 04.28 Dec +44 25 53.2
Center: R.A. 08 45 04.26 Dec +44 25 53.3
Center: R.A. 08 46 04.42 Dec +44 45 51.8
Center: R.A. 08 46 04.41 Dec +44 45 52.0
Center: R.A. 08 46 04.39 Dec +44 45 52.2

Figure 5.11

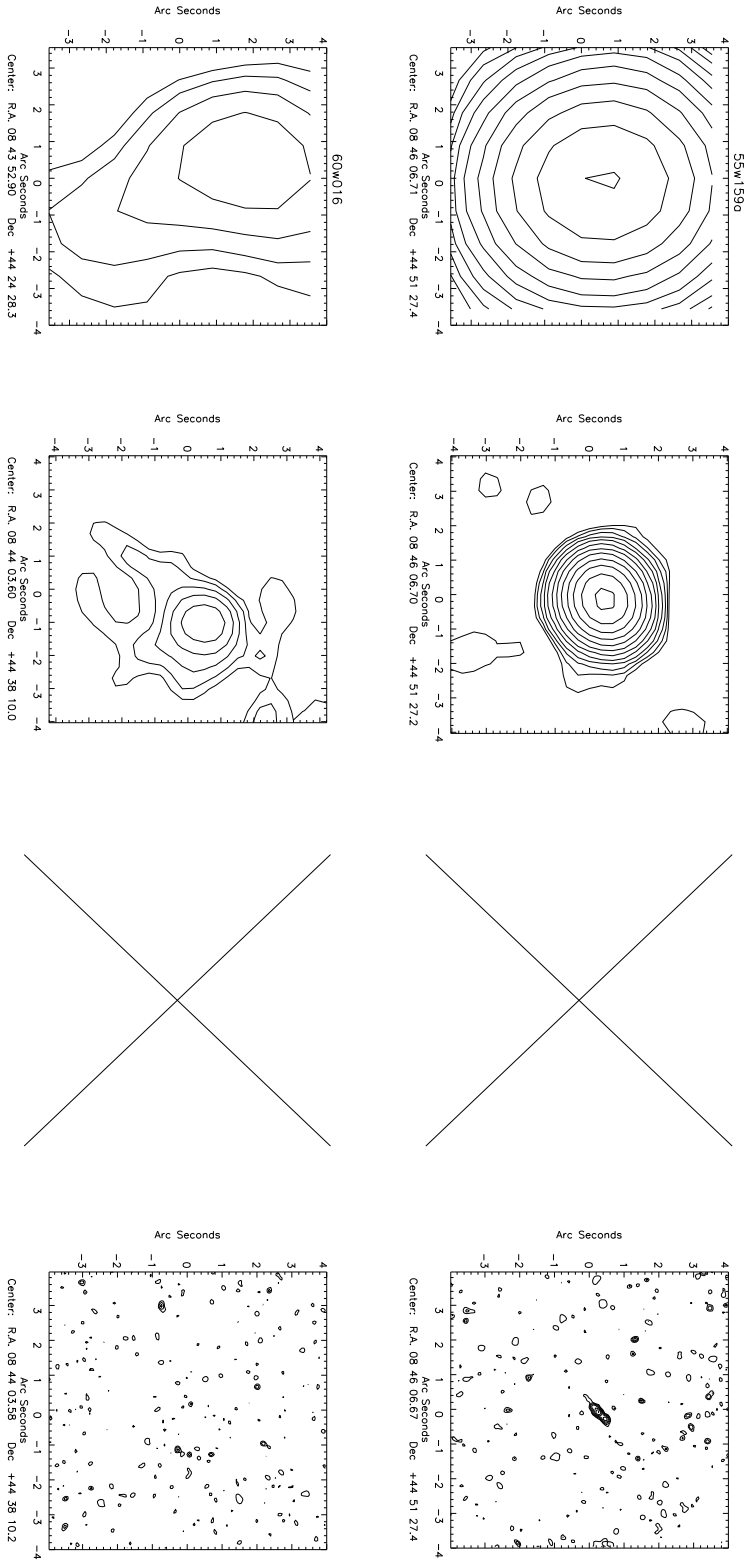
Arc Seconds
55w159a
Center: R.A. 08 46 06.71 Dec +44 51 27.4
Arc Seconds
60w016
Center: R.A. 08 43 52.90 Dec +44 24 28.3
Arc Seconds
Center: R.A. 08 46 06.70 Dec +44 51 27.2
Arc Seconds
Center: R.A. 08 44 03.60 Dec +44 38 10.0
Arc Seconds
Center: R.A. 08 46 06.67 Dec +44 51 27.4
Arc Seconds
Center: R.A. 08 44 03.58 Dec +44 38 10.2

Figure 5.11

5.6 FRI identification and classification

The most secure method of FRI classification, the detection of weak extended emission relative to compact cores, is impossible for the majority of the sample sources due to the lack of firm jet detections. FRI–type, as described above, can also be inferred by comparing the source flux densities at the low and high resolutions; a drop in flux density indicates the presence of resolved–out, extended emission, which in the absence of hotspots is likely to be due to an FRI.

The classifications were therefore done by inspecting the source morphologies where possible, and by using the flux–loss method where not, ignoring the possibly variable quasars. However, since the comparison between the Oort et al. (1987; 1985) and the A–array data cannot be relied upon to determine flux density loss, as discussed above, the only loss comparison that could be done for the Hercules field was between the A–array and VLA–Pt or MERLIN data. As a result, Hercules sources which were not covered by the higher–resolution observations, and which showed no obvious FRI–type jets in the A–array radio maps, could not be firmly classified. For the Lynx field sources, the existence of the B–array observations, which are of a similar resolution to the Oort et al. (1985), meant that these could be used for a more internally consistent comparison with the A–array, MERLIN and VLA–Pt data, instead.

Considering all these factors, five classification groups were defined for the sample. Group:

1. = Certain FRIs – these clearly show typical weak, edge–darkened, FRI jets and compact cores,
2. = Likely FRIs – these show some morphological extension consistent with an FRI structure, but not enough to be definite FRIs, along with a flux loss of 3σ or greater at higher resolution,
3. = Possible FRIs – either no extension is seen for these sources but they still lose $\geq 3\sigma$ of their flux when going to higher resolution, or some extension consistent with an FRI structure is seen but little flux is lost,
4. = Not FRIs – this group consists of sources which either have no flux loss or have bright FRII-type jets,
5. = Unclassifiable sources – this group is for sources in the Hercules field which are compact in the A–array maps, lose no flux between the Oort et al. and A–array data and were not included in the higher resolution observations.

The flux density loss between all the different observations was calculated using $(1 - \frac{S_{\rm hr}}{S_{\rm lr}})$,

where $S_{\rm hr}$ and $S_{\rm lr}$ are the flux densities measured in the higher and lower resolutions respectively. The σ values for these losses were then found by dividing the loss by its corresponding error; these can be found in Tables 5.8 and 5.9 with $>3\sigma$ losses highlighted in bold. Each source was classified into one of the groups in turn using the flowchart shown in Figure 5.12. For the sources that were classified by morphology alone, the process was repeated by two further, independent, testers to ensure that the results were consistent. If there was a disagreement between the three testers, the median grouping value was taken. The results given by each tester, along with the final groups assigned to these, and the rest of the sample, can be found in Tables 5.8 and 5.9.

5.7 Chapter summary

In this Chapter the flux densities resulting from the reduction of the low–resolution Lynx–field B–array and high–resolution VLA+Pt and MERLIN observations were presented. These values, along with those for the VLA A–array and the previously published Oort et al. (1985; 1987) were then used to sort the complete sample into 5 classification groups. The final numbers were 8, 10, 24, 33 and 6 sources in classification groups 1–5 respectively.

Name	$\sigma_{\rm P/A}$	$\sigma_{\rm M/A}$	Test 1	Test 2	Test 3	Final
			Group			Group
53w052						3
53w054a	1.06	2.46				4
53w054b	-0.40	2.22				4
53w057		-0.35				4
53w059	2.35	**4.33**	1	1	1	1
53w061^{Q}	-1.07	2.22				3
53w062						5
53w065	-2.16	**5.96**				2
53w066		**5.81**	3	3	2	3
53w067			1	2	1	1
53w069	**6.33**		2	1	1	1
53w070		1.54				4
53w075^{Q}						4
53w076			2	2	1	2
53w077			4	4	4	4
53w078						3
53w079						5
53w080^{Q}			4	4	4	4
53w081						5
53w082		1.38				4
53w083						5
53w084						5
53w085						3
53w086a			2	3	2	2
53w086b			3	3	2	3
53w087	**15.08**	*				2
53w088	0.14	1.71				3
53w089		*				3
66w009a						4
66w009b^{SB}						4
66w014						4
66w027^{SB}						4
66w031						3
66w035			3	3	2	3
66w036			2	3	1	2
66w042			2	2	1	2
66w047						3
66w049						4
66w058						5

Table 5.8: The σ flux density loss and classification groups for the sources in the Hercules field complete sample with values of $>3\sigma$ highlighted in bold. A, P and M represent the VLA A–array, VLA A+Pt and MERLIN observations respectively. A '*' indicates a source which was resolved out in the MERLIN observations. Sources previously classified as starburst galaxies and quasars are labeled with the superscripts 'SB' and 'Q' respectively. 'Test 1' etc. refers to the classifications assigned by each independent tester.

Name	$\sigma_{\rm A/B}$	$\sigma_{\rm P/B}$	$\sigma_{\rm P/A}$	$\sigma_{\rm M/B}$	$\sigma_{\rm M/A}$	Test 1	Test 2	Test 3	Final
						Group			Group
55w116	1.30	**4.59**	2.79	0.75	-0.36	4	3	3	3
55w118	0.68			0.36	-0.13				4
55w120	0.50	**3.64**	**3.26**			2	3	2	2
55w121	1.23	-0.43	-1.54	1.52	0.40				3
55w122	0.51			2.62	2.12				3
55w123	-0.47			0.45	1.14				4
55w124^{Q}	-1.10			-3.55	-2.01				4
55w127^{SB}	0.52			1.26	1.01				4
55w128	-0.79	1.92	**3.26**	**6.71**	**8.86**	1	2	1	1
55w131	2.77			*	*	2	2	1	2
55w132	0.43	2.98	2.74	1.36	1.04	4	3	3	3
55w133	-0.38	-0.31	0.09	2.75	**3.01**				2
55w135^{SB}	-1.80								4
55w136	-0.15	0.72	0.87	2.38	2.54	4	4	3	4
55w137	0.20			2.69	2.74				3
55w138	-0.91	0.33	1.13	2.78	**3.08**	3	4	2	3
55w140^{Q}	0.29								4
55w141	1.70			**3.07**	1.59				3
55w143a	0.18			2.28	2.08	3	3	2	3
55w143b	**3.01**			2.49	0.16				3
55w147	1.19								4
55w149	-0.12					1	1	1	1
55w150	-0.17								4
55w154	-1.31					1	1	1	1
55w155	-0.33								4
55w156	-2.01					1	1	1	1
55w157	2.34			-2.48	-3.26				4
55w159a	0.14			**4.17**	2.42	2	2	2	2
55w159b	0.23			*	*				3
55w160	-0.34								4
55w161	-1.39								3
55w165a	-0.65					1	1	1	1
55w165b	2.36								4
55w166	-0.16								4
60w016	-1.14			0.45	2.28				3
60w024	-0.93								4
60w032	-0.97								4
60w039^{SB}	-0.35								4
60w055	-0.05								4
60w067	0.74								4
60w071	0.38								4
60w084	-1.75								3

Table 5.9: The σ flux density loss and classification group for the sources in the Lynx field complete sample with values of $>3\sigma$ highlighted in bold. B, A, P and M represent the VLA A and B–array, VLA A+Pt and MERLIN observations respectively. A '*' indicates a source which was resolved out in the MERLIN observations. Sources previously classified as starburst galaxies and quasars are labeled with the superscripts 'SB' and 'Q' respectively. 'Test 1' etc. refers to the classifications assigned by each independent tester.

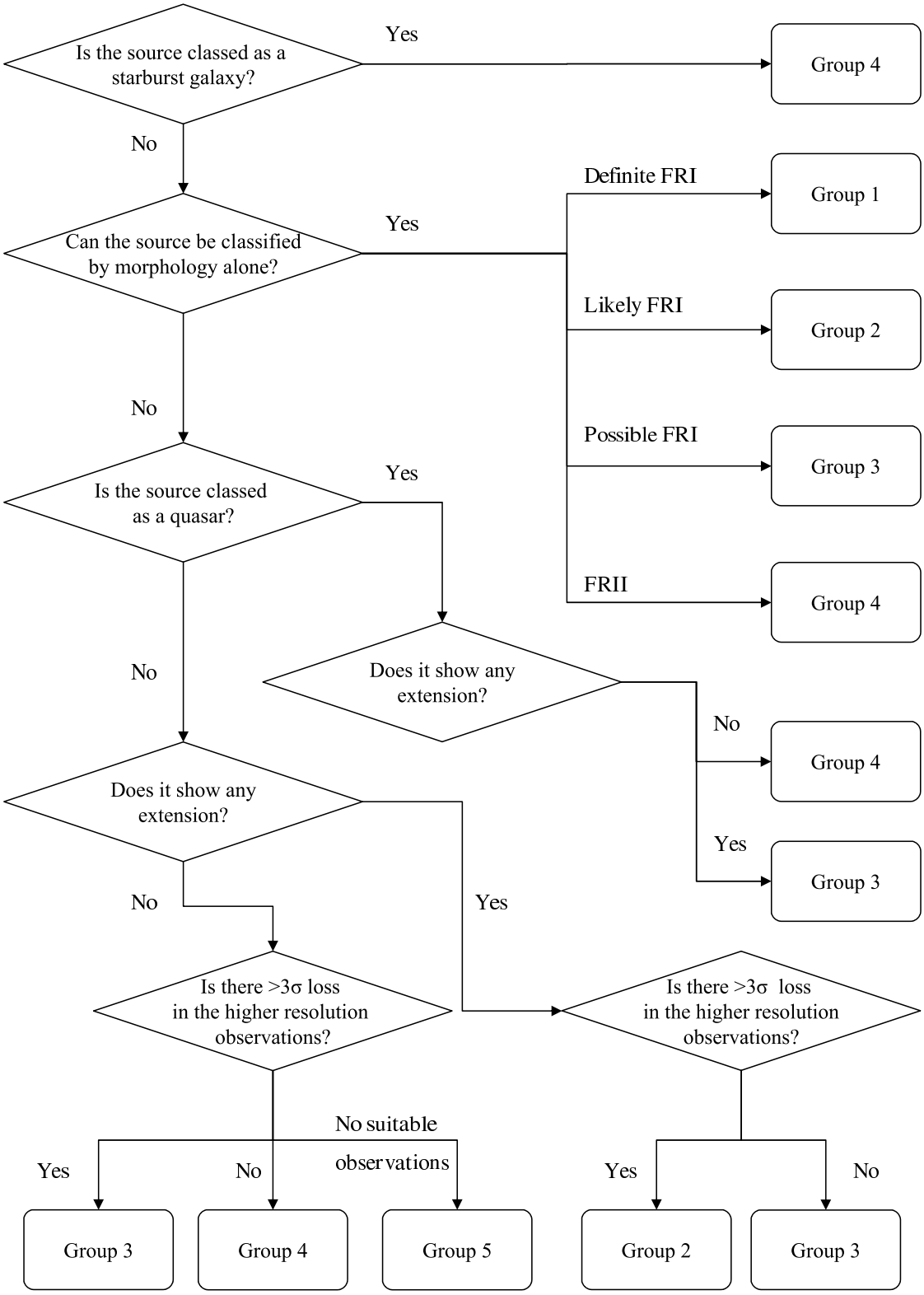

Figure 5.12: The procedure followed for the source morphological classification.

CHAPTER 6

Investigating the FRI subsample

Now that the radio sample has been classified, the sources in groups 1–3 (the certain, likely and possible FRIs) can be used to investigate the changes in co–moving space density over the redshift range of the sample. Alongside this, since the optical magnitudes of the sample have been determined, a first attempt can be made at determining the behaviour of the FRI/FRII dividing luminosity at different cosmic epochs. This chapter, therefore, outlines the methods which were employed to achieve these two measurements, along with the results obtained.

6.1 Measuring the co–moving space density

This section describes the steps taken to measure the minimal and maximal co–moving space density of the three FRI groups in the sample. Firstly, the parameters used for the measurement are defined, followed by the methods used to determine the local FRI space density, and finally, the space–density calculation is described.

6.1.1 Setting up the measurement

For the radio sample considered here the number and width of redshift bins used depends on the 0.5 mJy flux density limit of the sample, since the total radio power of an object is a function

of both z and S; this is illustrated in Figure 6.1 for powers $10^{23} \leq P_{1.4\mathrm{GHz}} \leq 10^{25}$ W/Hz (calculated assuming an α of 0.8 – the typical average value for radio galaxies). It is clear from this that whilst a sample source with a radio power of 10^{23} W/Hz can be seen out to a redshift of 0.26 with this flux density limit, a source with a higher power of 10^{25} W/Hz can be seen out to higher distances; in this case to a redshift of 1.86. Therefore, to ensure accurate space density calculations over a wide redshift range, a limiting power, P_{lim}, of 10^{25} W/Hz was imposed on the FRI subsample; this corresponds to a maximum redshift, z_{max}, of 1.86 for sources of $\alpha = 0.8$, at the sample flux density limit.

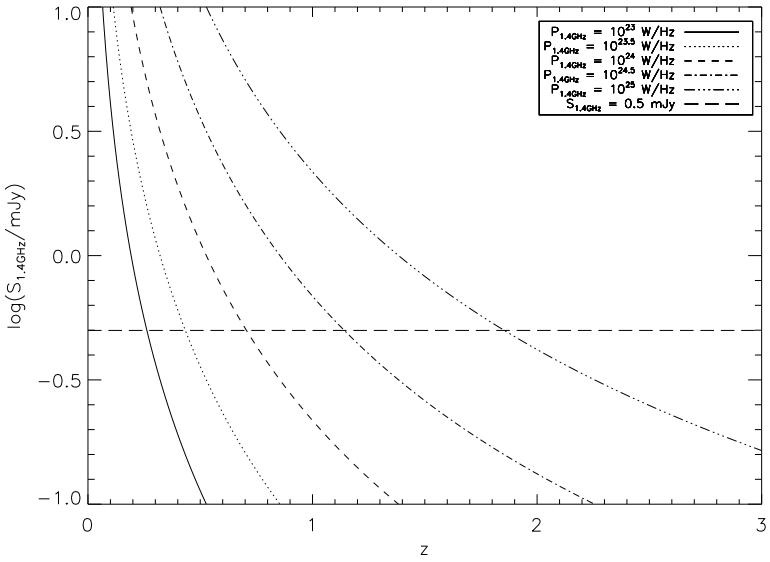

Figure 6.1: The variation of flux density, S, with redshift for five different radio powers. The flux density sample limit of 0.5 mJy is indicated by the long dashed line.

The space densities were calculated in 4 redshift bins of width 0.5, covering the range $0.0 < z \leq 2.0$. The upper end of the final, $z = 1.5$ – 2.0, bin exceeded the value of z_{max} corresponding to the limiting flux density for $\alpha = 0.8$; as a result the individual maximum redshifts of the sources in this bin were determined, so that only the volumes over which each source could be observed were used to find the density here.

It should be noted that the redshift limit strongly depends on the value of α used. This is illustrated by Figure 6.2, in which is plotted the variation of flux density with redshift for a radio power of 10^{25} W/Hz, calculated using values in the range $0.5 \leq \alpha \leq 1.5$; as the spectral index steepens, z_{max} decreases from 2.16 to 1.43. It is important to stress that α needs to be ≥ 1.37 before z_{max} falls below the start of the final redshift bin, for the limiting power of 10^{25} W/Hz. This spectral index is steeper than that found for essentially all radio sources which suggests that the space density results in the $z < 1.5$ bins are robust to changes in the assumed value of α.

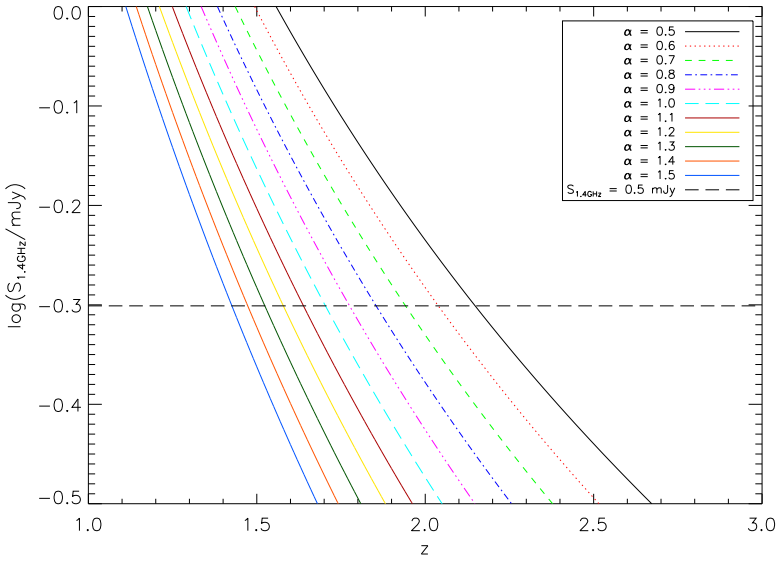

Figure 6.2: The variation of flux density with redshift, for $P_{1.4\mathrm{GHz}} = 10^{25}$ W/Hz, calculated using 11 different values of α.

The three different FRI classification groups used meant that a minimum (group 1 only), maximum (groups 1, 2 and 3) and probable (groups 1 and 2) FRI space density could be calculated. Additionally, the two HDF+FF sources were incorporated into group 1 and the HDF+FF area was added into the Hercules and Lynx areas determined by the optical imaging. The flux densities used to calculate the source radio powers are those resulting from the A–array observations, and sources that were previously classified as starburst galaxies have been removed from the sample. The spectral indices for 51% of the Hercules field sources were taken from Waddington et al. (2000); for the remainder of the sample α was assumed to be 0.8. The validity of this assumption was tested by recalculating the radio powers using two extreme α values of 0.5 and 1.8 for all the sources in the sample. Up to and including these limits, the number of sources in each bin does not change. Tables 6.1 and 6.2 summarises the magnitudes, redshifts, FRI grouping and radio power for the complete sample, and indicates which sources were included in the space density calculations here.

6.1.2 The local FRI space density

An accurate measurement of the local FRI space density is vital for determining whether the sample described here demonstrates a density enhancement at high redshift. This can be obtained by directly measuring the FRI numbers in two different local, complete, radio samples.

The first local measurement was carried out using a complete subsample of the 3CR galaxy

Hercules								
Name	r (63.9 kpc)	i (63.9 kpc)	K (63.9 kpc)	z	Origin	$\log P$	FRI Grouping	In ρ?
53w052	21.19	20.74	–	0.46	1a	24.82	3	
53w054a	23.58	23.46	18.17	1.51	3	24.95	4	
53w054b	–	–	19.75	3.50	3	25.53	4	
53w057	24.53	–	–	1.85	4	25.06	4	
53w059	24.17	–	–	1.65	4	26.60	1	X
53w061	21.13	20.77	–	2.88	1b	25.34	3	
53w062	21.67	20.80	–	0.61	1a	24.08	5	
53w065	22.84	23.14	–	1.185	1a	25.75	2	X
53w066	–	–	–	1.82	1b	25.99	3	X
53w067	21.94	21.22	–	0.759	1a	25.94	1	X
53w069	24.97	–	–	1.432	1a	25.78	1	X
53w070	22.05	21.21	–	1.315	2	25.06	4	
53w075	21.12	20.69	–	2.150	1a	27.44	4	
53w076	19.41	18.75	–	0.390	1a	24.55	2	
53w077	21.69	20.80	–	0.80	1a	25.71	4	
53w078	18.29	17.54	–	0.27	1a	23.57	3	
53w079	20.54	19.62	–	0.548	1a	24.94	5	
53w080	18.37	18.00	–	0.546	1a	25.53	4	
53w081	23.64	23.01	–	2.060	1a	26.54	5	
53w082	24.86	–	–	2.04	4	26.17	4	
53w083	21.94	21.28	–	0.628	1a	24.86	5	
53w084	24.61	–	19.29	2.73	3	25.70	5	
53w085	22.01	21.77	–	1.35	1a	25.85	3	X
53w086a	20.10	19.32	–	0.46	4	24.47	2	
53w086b	21.69	20.56	–	0.73	2	25.01	3	X
53w087	–	–	–	>3.7	3	>27.1	2	
53w088	–	–	–	1.773	1a	26.02	3	X
53w089	23.84	–	–	0.635	1a	24.85	3	
66w009a	22.68	21.93	16.51	0.65	3	24.39	4	
66w009b	17.19	16.67	13.26	0.156	1a	22.76	4	
66w014	–	–	–	–	–	–	4	
66w027	17.99	17.46	–	0.086	2	22.07	4	
66w031	22.45	22.23	17.76	0.812	2	24.43	3	
66w035	23.31	22.95	18.94	2.26	3	25.35	3	
66w036	22.60	21.63	17.26	0.924	2	25.15	2	X
66w042	21.16	20.96	–	0.65	4	24.51	2	
66w047	19.38	18.87	–	0.37	4	23.71	3	
66w049	22.41	21.98	–	0.95	4	24.95	4	
66w058	–	–	–	>2.3	4	>25.8	5	

Table 6.1: The magnitudes, redshifts, FRI groupings and radio power for the Hercules field. An 'X' in the last column indicates that a source is included in the $\geq 10^{25}$ W/Hz space density calculations and the corresponding photometric errors can be found in Table 3.5. For the 'Origin' column, (1a) and (1b) indicates a previously published redshift, (a – spectroscopic (Waddington et al., 2000; Bershady et al., 1994), b– photometric (Waddington et al., 2001)), (1c) indicates the redshift came from the SDSS, (2) indicates a DOLORES spectroscopic value, (3) is a K–z estimate, (4) is a r–z estimate. The FRI groupings are: (1) – certain FRI; (2) – likely FRIs; (3) – possible FRIs; (4) – not FRIs; (5) – unclassifiable sources.

Lynx Name	r (63.9 kpc)	i (63.9 kpc)	K (63.9 kpc)	z	Origin	$\log P$	FRI Grouping	In ρ?
55w116	21.84	20.97	–	0.851	2	24.68	3	
55w118	21.24	20.84	–	0.66	4	24.10	4	
55w120	–	–	17.96	1.35	3	25.20	2	X
55w121	22.98	–	19.17	2.57	3	25.65	3	
55w122	20.66	20.47	–	0.55	4	23.86	3	
55w123	22.71	22.79	17.10	0.87	3	24.59	4	
55w124	21.16	21.22	–	1.335	2	25.41	4	
55w127	13.45	13.39	–	0.04	4	22.14	4	
55w128	–	–	–	1.189	2	25.52	1	X
55w131	23.02	21.62	–	1.124	2	24.65	2	
55w132	–	–	–	$>$4.4	3	$>$26.4	3	
55w133	25.15	–	–	2.24	4	25.84	2	
55w135	–	–	13.12	0.090	1c	22.88	4	
55w136	23.45	–	18.81	2.12	3	25.40	4	
55w137	–	–	–	0.151	2	22.99	3	
55w138	–	–	19.34	2.81	3	26.02	3	
55w140	20.75	20.96	–	1.685	2	24.94	4	
55w141	–	–	–	$>$1.8	4	$>$24.9	3	
55w143a	25.03	–	–	2.15	4	25.79	3	
55w143b	25.11	–	–	2.21	4	25.00	3	
55w147	22.90	–	17.51	1.07	3	25.03	4	
55w149	16.34	15.80	–	0.151	2	23.66	1	
55w150	20.70	20.00	–	0.470	2	23.68	4	
55w154	19.25	18.64	–	0.330	2	24.66	1	
55w155	–	–	–	$>$3.7	3	$>$26.2	4	
55w156	22.56	22.84	17.07	0.86	3	25.19	1	X
55w157	21.77	21.15	–	0.557	2	24.15	4	
55w159a	23.38	–	–	1.29	4	25.74	2	X
55w159b	18.74	18.15	–	0.311	1c	23.47	3	
55w160	21.33	20.17	–	0.600	2	24.04	4	
55w161	19.94	19.33	–	0.44	4	23.91	3	
55w165a	21.31	20.26	–	0.68	4	25.54	1	X
55w165b	21.62	20.86	–	0.75	4	24.33	4	
55w166	22.54	21.81	–	0.99	4	25.02	4	
60w016	22.55	21.38	–	0.840	2	24.43	3	
60w024	21.94	20.78	–	0.773	2	23.96	4	
60w032	–		–	$>$1.8	4	$>$24.9	4	
60w039	17.08	16.63	–	0.151	2	22.63	4	
60w055	21.63	20.57	–	0.718	2	24.11	4	
60w067	–	–	–	$>$1.8	4	$>$25.1	4	
60w071	23.28	–	–	1.25	4	24.67	4	
60w084	17.58	16.85	–	0.127	1c	22.74	3	

Table 6.2: The magnitudes, redshifts, FRI groupings and radio power for the Lynx field. An 'X' in the last column indicates that a source is included in the $\geq 10^{25}$ W/Hz space density calculations and the corresponding photometric errors can be found in Table 3.6. For the 'Origin' column, (1a) and (1b) indicates a previously published redshift, (a – spectroscopic (Waddington et al., 2000; Bershady et al., 1994), b– photometric (Waddington et al., 2001)), (1c) indicates the redshift came from the SDSS, (2) indicates a DOLORES spectroscopic value, (3) is a K–z estimate, (4) is a r–z estimate. The FRI groupings are: (1) – certain FRI; (2) – likely FRIs; (3) – possible FRIs; (4) – not FRIs; (5) – unclassifiable sources.

survey (Laing et al., 1983) which contains 30 FRI sources with $S_{178\mathrm{MHz}} \geq 10.9$ Jy (corresponding to $S_{1.4\mathrm{GHz}} \geq 2.09$ Jy, using $\alpha = 0.8$), in an area of 4.24 sr. A source with power $P_{\mathrm{lim}} = 10^{25}$ W/Hz and $\alpha = 0.8$, can be seen out to a redshift of 0.046 if it was in this survey. Converting the 3CR flux densities to 1.4 GHz using their published spectral indices (Laing et al., 1983), it was found that there were 4 FRIs with $P_{1.4\mathrm{GHz}} \geq P_{\mathrm{lim}}$ in the comoving volume of $V(\mathrm{z} \leq 0.046) \times (4.24/4\,\pi) = 1.0 \times 10^7$ Mpc^3, which gives a local space density of 402 $\pm$ 201 FRIs/Gpc^3.

The second local sample used was the equatorial radio galaxy survey of Best et al. (1999) which contains 178 sources, including 9 FRIs, with $S_{408\mathrm{MHz}} > 5$ Jy (corresponding to $S_{1.4\mathrm{GHz}} > 1.9$ Jy, again using $\alpha = 0.8$), in an area of 3.66 sr. In this survey a source at P_{lim} can be seen out to $z = 0.048$; there are 2 FRIs in this volume with powers greater or equal to this which gives a local density of 196 $\pm$ 139 FRIs/Gpc^3.

Combining the results from these two surveys gives a total of 6 FRI sources in a comoving volume of 2.0 $\times$ 10^7 Mpc and a corresponding comoving local FRI space density of 298 $\pm$ 122 FRIs/Gpc^3.

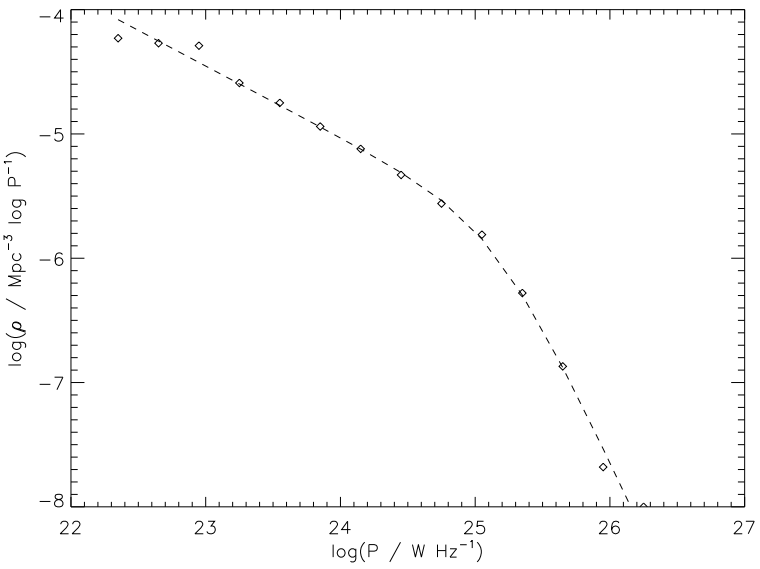

Figure 6.3: The radio luminosity function of Best et al. (2005) overplotted with the calculated best–fit line.

An alternative estimate can be obtained by integrating the local radio luminosity function of Best et al. (2005), which was calculated from a sample of 2215 radio–loud AGN, formed by comparing the SDSS with two radio surveys: the National Radio Astronomy Observatories (NRAO) Very Large Array (VLA) Sky Survey (NVSS) (Condon et al., 1998) and the Faint Images of the Radio Sky at Twenty centimetres (FIRST) survey (Becker et al., 1995). To

accurately calculate the number density, ρ, a broken power law of the form

$$\rho = \rho_0 \left[\left(\frac{P}{P_*} \right)^{\alpha} + \left(\frac{P}{P_*} \right)^{\beta} \right]^{-1}, \tag{6.1}$$

was fitted, where α and β are the power law slopes, P_* is the luminosity of the power–law break and ρ_0 is a density constant. The resulting fit is shown in Figure 6.3 and the final parameters were $\rho_0 = 10^{-5.70}$ Mpc^{-3}, $P_* = 10^{25.16}$ W/Hz, $\alpha = 0.57$ and $\beta = 2.31$. Using Equation 6.1 the total number of sources per Mpc^3, $\rho_{\rm tot}$ is therefore

$$\begin{aligned} \rho_{\rm tot} &= \int_{P_1}^{P_2} \frac{dn}{dP} dP & (6.2)\\ &= \int_{P_1}^{P_2} \rho \, \frac{\log_{10} e}{P} dP & (6.3)\\ &= \int_{P_1}^{P_2} \frac{\log_{10} e}{P} 10^{-5.70} \left[\left(\frac{P}{10^{25.16}} \right)^{0.57} + \left(\frac{P}{10^{25.16}} \right)^{2.31} \right]^{-1} dP, & (6.4)\\ & & (6.5) \end{aligned}$$

where $P_1 = P_{\rm lim}$ and P_2 are the luminosity limits of the integration.

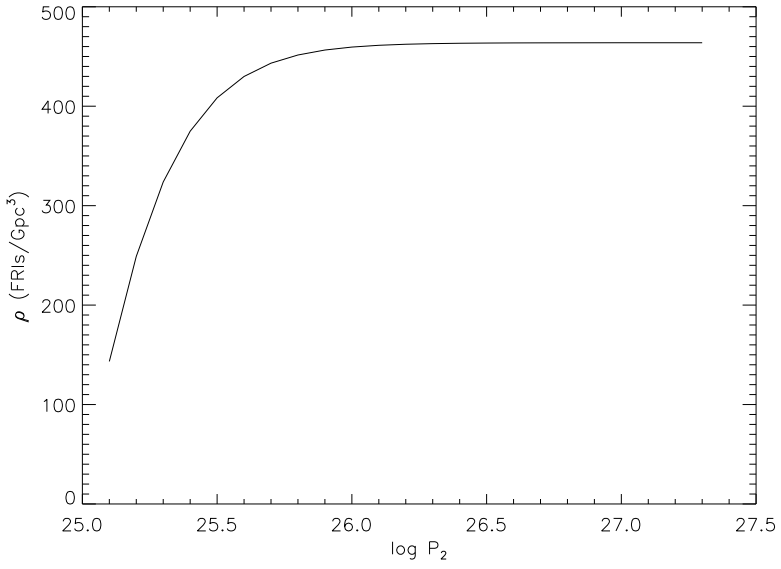

Figure 6.4: The values of $\rho_{\rm tot}$ resulting from different values of P_2.

Since the radio luminosity function decreases rapidly above $\log P = 24.5$, the calculated value of $\rho_{\rm tot}$ is not strongly dependent on the chosen value for P_2, as illustrated in Figure 6.4. Although there will be some FRIIs included, the majority of sources will be FRIs, and setting $P_2 = \infty$ will derive a maximal FRI space density which ought also to be close to the true

value. The calculation gives 460 FRIs/Gpc^3, which is in good agreement with the values calculated by the two direct measurements.

6.1.3 The space density calculation

The space density, ρ, of N sources in some redshift bin Δz is simply

$$\rho_{\Delta \mathrm{z}} = \sum_{i=0}^{N} \frac{1}{V_i} \tag{6.6}$$

where V_i is the volume over which a source i could be seen in a particular bin. In the case where source weights need to be considered, this can be rewritten as

$$\rho_{\Delta \mathrm{z}} = \sum_{i=0}^{N} \frac{w_i}{V_i} \tag{6.7}$$

where w_i are the weights previously calculated for the sources.

Figure 6.5 shows the results of this calculation for the 4 redshift bins, plotted at the bin midpoints; the numbers are given in Table 6.3. As discussed above, it is only in the final, $1.5 < z < 2.0$, bin that the values of V_i (and hence the density) depend on the assumed value of α; the V_is for sources in the other bins are all the full bin volume. In reality though, the 3 sources that do lie in the last bin have flux densities which are all much greater than the 0.5 mJy limit (the faintest is 4.53 mJy), and therefore the result does not change if α is varied.

	Minimum		Probable		Maximum	
Bin	No.	ρ (FRIs/Gpc^3)	No.	ρ (FRIs/Gpc^3)	No.	ρ (FRIs/Gpc^3)
$0.0 < z \leq 0.5$	0	0	0	0	0	0
$0.5 < z \leq 1.0$	3	1636	4	2492	5	3037
$1.0 < z \leq 1.5$	4	1331	7	2329	8	2662
$1.5 < z \leq 2.0$	1	276	1	276	3	829
$0.5 < z \leq 1.5$	7	1446	11	2391	13	2804

Table 6.3: The results of the space density calculations for both redshift bin sizes. 'No'. is the number of sources in each bin.

The space densities for the minimum, probable and maximum FRI groups show a high redshift comoving density enhancement for the FRIs in this sample, compared to the local FRI space density. The turnover in space density seen at $z \gtrsim 1.5$ is supported by the work of Waddington et al. (2001) who found evidence for a high redshift cut–off for their lower luminosity radio sources by $z \simeq 1$ – 1.5. However, since the values of V_i in the last bin can depend on assumed

spectral indices, the addition of a small number of steep spectrum sources, close to the luminosity limit, would result in a large increase in density; for example, ∼3 more sources of flux density $S_{\rm lim}$ and $\alpha = 1.0$ would be needed to give the same maximum value of ρ as in the previous $1.0 < z < 1.5$ bin.

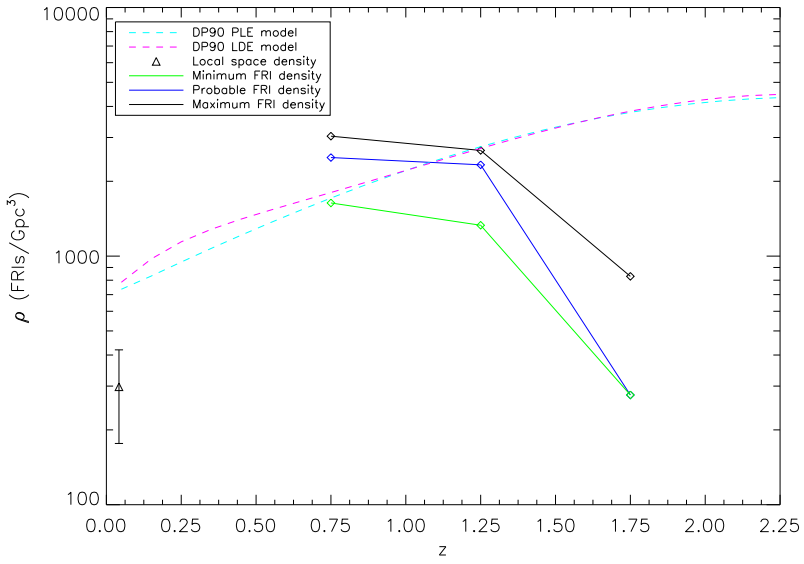

Figure 6.5: The space density changes in redshift bins of width 0.5, plotted at the bin midpoints. Also shown are the PLE and LDE models of DP90, converted to 1.4 GHz and to this cosmology, for comparison; see later for a full discussion of these models. Since no sources with $P > 10^{25}$ W/Hz were found in the first redshift bin, no space density value is plotted there.

Two potential concerns in calculating the space densities are the estimated redshifts and the assumed spectral indices of 0.8 used for some of the sample sources. Error in these could move sources between redshift bins, and simultaneously affect the radio power determinations. To investigate the effect of these on the results, two Monte Carlo simulations, with 10,000 iterations each, were performed. In the first simulation, in each iteration, the redshifts which were estimated were varied by a factor drawn randomly from a Gaussian distribution of width equal to 0.2 in $\log z$, the approximate spread in both the r–z and K–z relations. Similarly, in the second simulation, in each iteration, the assumed spectral indices were varied from 0.8 by a factor drawn randomly from a Gaussian distribution of width 0.5; this value was chosen as it represents a reasonable spread in α. Figures 6.6 and 6.7 show the results of the simulations, carried out for the probable FRIs (i.e. groups 1 and 2) only. Also shown are the errors on the densities calculated from the simple Poisson errors on the number of sources in each bin (for the bin containing no sources, an error of ± 1 source was assumed). These results are also given in numerical form in Table 6.4. It is clear from this that the major limiting factor for the results is the small number of sources in the sample, rather than the redshift estimates, or the assumed spectral indices, that were used for some of the sources. It should also be noted that the radio

FRI classifications are as comparably large a source of error as the redshift estimates.

	$0.0 < z \leq 0.5$	$0.5 < z \leq 1.0$	$1.0 < z \leq 1.5$	$1.5 < z \leq 2.0$
$\rho_{\rm prob}$	0	2492	2329	276
$\rho_{\rm max} - \rho_{\rm min}$	0	1401	1331	553
$z\ \sigma_{\rm mc}$	810	496	391	257
$\alpha\ \sigma_{\rm mc}$	0	345	124	0
$\sigma_{\rm p}$	2442	1246	880	276

Table 6.4: The errors calculated from the Monte Carlo simulations, $z\ \sigma_{\rm mc}$ and $\alpha\ \sigma_{\rm mc}$, along with the Poissonian, $\sigma_{\rm p}$, errors and the spread in the calculated space densities for each redshift bin ($\rho_{\rm max} - \rho_{\rm min}$); all values are in FRIs/Gpc^3. Also shown is the probable FRI space density, $\rho_{\rm prob}$.

Quantifying the space density enhancement

The calculations above showed that the uncertainty in the space density results is dominated by the Poissonian error. In order to better quantify the high redshift enhancements therefore, the density calculation was repeated using a single, large redshift bin spanning $0.5 < z < 1.5$, containing a minimum of 7 and a maximum of 13 FRI sources. The resulting densities can also be found in Table 6.3; they show enhancements of 3.2σ, 2.9σ and 2.1σ over the local FRI space density, for the maximum, probable and minimum groupings respectively.

Measuring these significance levels is not the best way of judging the reliability of the space density increase, however. A better method (previously described in §1.3) is to assume no evolution of the FRI population and then calculate the probability of detecting the numbers of minimum ($P_{>7}$), probable ($P_{>11}$) and maximum ($P_{>13}$) objects seen in the $0.5 < z < 1.5$ bin if this non–evolution scenario was correct. The volume contained within this bin is 0.005 Gpc^3 which, assuming no evolution occurs from a local density of 298 FRIs/Gpc^3, gives an expected number of 1.44 FRIs over this range. (For comparison, repeating this calculation for $z < 0.5$ suggests that 0.12 FRIs should have been detected in the sample, in this volume, for a constant co–moving space density.) The resulting probabilities are summarized in Table 6.5; these are all $\ll$1% which indicates that, as expected, the no–evolutionary scenario can be discounted.

	Expected Number	$P_{>7}$	$P_{>11}$	$P_{>13}$
No Evolution	1.44	0.07%	3.8×10^{-5}%	4.9×10^{-7}%
PLE	11.63	94%	61%	38%
LDE	11.67	95%	62%	39%

Table 6.5: The probabilities calculated for the no–evolution, PLE and LDE scenarios for the minimum, probable and maximum numbers of FRIs.

The DP90 pure luminosity evolution (PLE) and luminosity/density evolution (LDE) models, which fit the overall radio source population well, out to $z \sim 2$, can also be compared to the

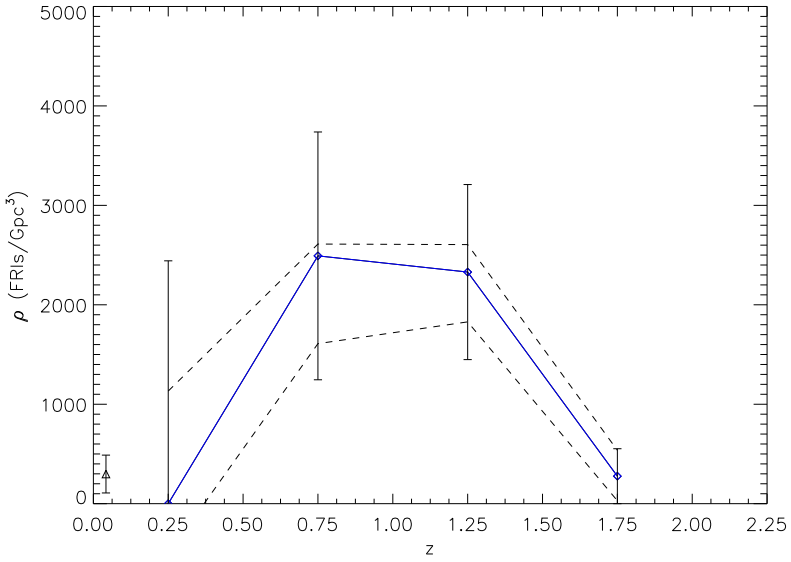

Figure 6.6: The space density changes of the probable group of objects, overplotted with the 1σ results of the redshift Monte Carlo simulations (dotted lines) and the Poisson errors on the calculated densities; this shows that it is the small number of sources in each bin that has the most effect on the results.

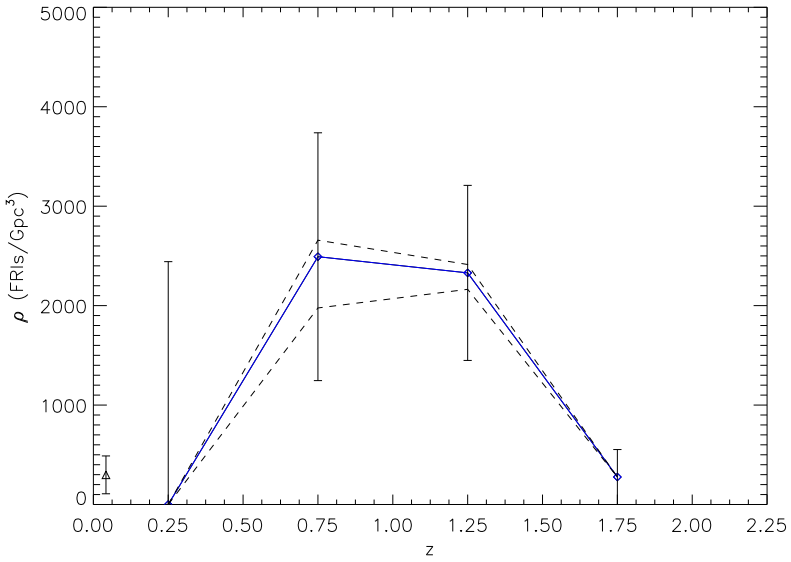

Figure 6.7: The space density changes of the probable group of objects, overplotted with the 1σ results of the spectral index Monte Carlo simulations (dotted lines) and the Poisson errors on the calculated densities; this again shows that it is the small number of sources in each bin that has the most effect on the results.

results using this method. If the behaviour of the FRIs here is consistent with these PLE and LDE models, this would suggest that they evolve in the same way as FRII objects of the same radio power.

In the PLE model, the local radio luminosity function (RLF) of Equation 6.1 shifts horizontally in the ρ–z plane only, and its overall shape does not change. These redshift changes were confined to the luminosity normalization, P_* only, and DP90 parameterized these as a quadratic in $\log z$:

$$\log\ P_*(z) = f(z) = a_0 + a_1 z + a_2 z^2, \tag{6.8}$$

where the a_0, a_1 and a_2 are the quadratic co–efficients.

Conversely, in the LDE model, the local RLF can move both horizontally and vertically and, therefore, can steepen or flatten. As a result, DP90 allowed the density normalization, ρ_0, to also vary with redshift with the form

$$\log\ \rho_0 = \sum_{i=0}^{5} c_i\ y_z^i, \tag{6.9}$$

where $y = 0.1\ z$ and c_0 to c_5 are the expansion co–efficients, and the variation of P_* was modified to be

$$\log\ P_*(z) = a_0 + \frac{a_1}{\eta}[1 - (1+z)^{-\eta}]. \tag{6.10}$$

For each of these two models, the total number of sources in the interval $0.5 < z < 1.5$ was found by integrating

$$N_{\rm tot} = \int_{0.5}^{1.5} \rho\ dV(z)\ d\Omega \tag{6.11}$$

$$= \Omega \int_{0.5}^{1.5} \int_{P1}^{P2} \frac{\log_{10} e}{P} \rho_0 \Big\{ \Big(\frac{P}{P_*(z)} \Big)^{\alpha} + \Big(\frac{P}{P_*(z)} \Big)^{\beta} \Big\}^{-1} dP\ dV(z) \tag{6.12}$$

where Ω is the area of the survey in steradians and the luminosity limits of the integration are $P1 = 10^{25}$ W/Hz and $P2 = 10^{27.5}$ W/Hz (note that Figure 6.4 has already shown that the value chosen for $P2$ does not strongly affect the final result). The co–efficients used in these calculations, determined originally by DP90, can be found in Table 6.6. Where necessary these values were converted from their original 2.7 GHz to 1.4 GHz, the frequency used here, again assuming an average α of 0.8. Changing this assumption does not significantly alter the final results.

The parameters calculated for the PLE and LDE models were originally determined using Einstein de Sitter cosmology. Whilst the value of $N_{\rm tot}(S)$, between these redshift limits, is

PLE model		LDE model	
α	0.69	α	0.73
β	2.17	β	2.22
a_0	24.89	a_0	24.55
a_1	1.26	a_1	3.17
a_2	-0.26	η	1.37
$\log \rho_0$	-6.91	c_0	-6.62
		c_1	-10.97
		c_2	97.91
		c_3	-338.51
		c_4	434.38
		c_5	-186.92

Table 6.6: The co–efficients determined at 2.7 GHz, for the PLE and LDE evolution models (Dunlop & Peacock, 1990).

not affected by cosmological changes (as this is a direct property of the basic data from which DP90 derived their models), the concordance cosmology power limits, $P1 = 10^{25}$ W/Hz and $P2 = 10^{27.5}$ W/Hz, will alter. Taking this into account, Equation 6.12 was calculated over 96 redshift steps, between $z = 0.5$ and $z = 1.5$, and at each step $P1$ and $P2$ were re–evaluated using

$$P1_{1.4GHz} = 10^{25}\Big(\frac{\mathbf{d_{eds}}(z)}{\mathbf{d_{\Lambda cdm}}(z)}\Big)^2 \text{ W/Hz}, \quad (6.13)$$

$$P2_{1.4GHz} = 10^{27.5}\Big(\frac{\mathbf{d_{eds}}(z)}{\mathbf{d_{\Lambda cdm}}(z)}\Big)^2 \text{ W/Hz}, \quad (6.14)$$

where $\mathbf{d}_{\Lambda\mathrm{cdm}}$ and $\mathbf{d}_{\mathrm{eds}}$ are the luminosity distances in concordance and Einstein de Sitter cosmologies respectively.

Carrying out the integrations results in $N_{\mathrm{tot}} \sim 11$ for both models, over this redshift range, and corresponding enhancements over the local value used here of ∼8. This expected number agrees very well with the observed numbers of 7, 11 and 13 for the minimum, probable and maximum samples, confirming that these space densities can be consistent with these models. This is further supported by Figure 6.5, in which the density values predicted by the PLE and LDE models are overplotted with the results previously calculated for the 4 redshift bins. The low redshift disagreement seen between the models and the local FRI space density is likely to arise from the poor constraints locally, at these radio powers, in the DP90 results. To illustrate this, Figure 6.8 compares the local RLF predicted by the DP90 PLE model with that found by Best et al. (2005); it clearly shows that the model overpredicts the value of ρ for $P_{1.4\mathrm{GHz}} > 10^{25}$ W/Hz.

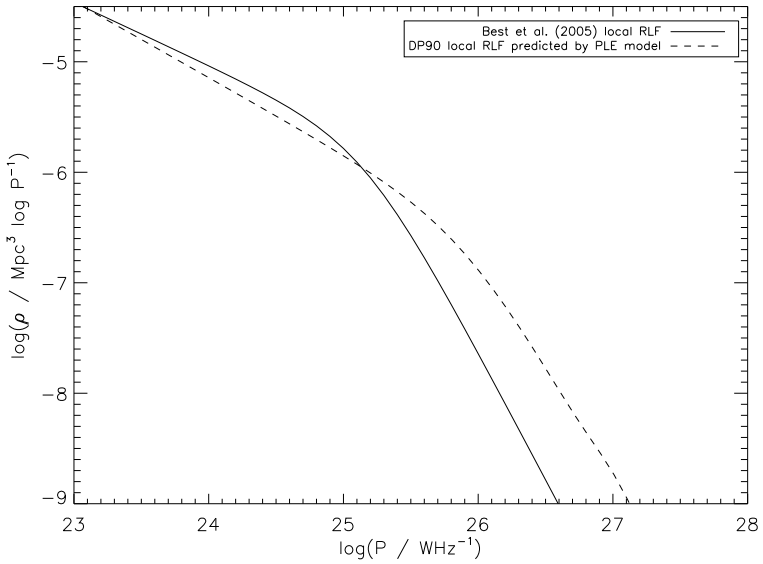

Figure 6.8: A comparison of the local RLFs measured by Best et al. (2005) and predicted by the PLE model of DP90, both plotted at 1.4 GHz, using concordance cosmology.

Including the lower luminosity FRIs

The space density calculation can be repeated using different luminosity limits to investigate the behaviour of the weaker sources in the sample. Figures 6.9 and 6.10 show the results of this for limits of 10^{24} and $10^{24.5}$ W/Hz and the density values are given in Table 6.7. The calculation was, in both cases, carried out for the minimum, maximum and probable numbers of FRI, using redshift bins of width 0.5, with the final bin dependent on the value of the limiting luminosity as discussed previously. The local values were again found using a combination of the 3CR and equatorial galaxy samples.

	Minimum		Probable		Maximum	
Bin	No.	ρ (FRIs/Gpc^3)	No.	ρ (FRIs/Gpc^3)	No.	ρ (FRIs/Gpc^3)
$P \geq 10^{24.0}$ W/Hz						
$0.0 < z \leq 0.5$	1	2442	3	7546	4	9988
$0.5 < z \leq 1.0$	3	1636	5	3370	10	6892
$P \geq 10^{24.5}$ W/Hz						
$0.0 < z \leq 0.5$	1	2442	2	4884	3	7326
$0.5 < z \leq 1.0$	3	1636	5	3370	8	5006
$1.0 < z \leq 1.5$	4	1331	8	2882	9	3215

Table 6.7: The results of the space density calculations using the luminosity limits $P \geq 10^{24}$ and $P \geq 10^{24.5}$ W/Hz, for the maximum, minimum and probable FRI numbers.

The comoving space densities for these two new limits indicate that the enhancement over the

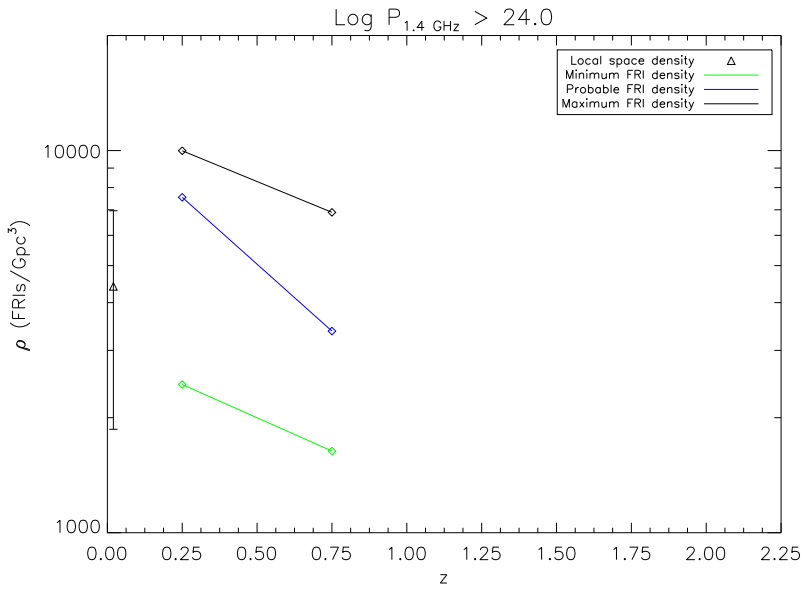

Figure 6.9: The space density changes in redshift bins of width 0.5, plotted at the bin midpoints for P$> 10^{24}$ W/Hz. For comparison the redshift axis is plotted with the same range as in Figure 6.5.

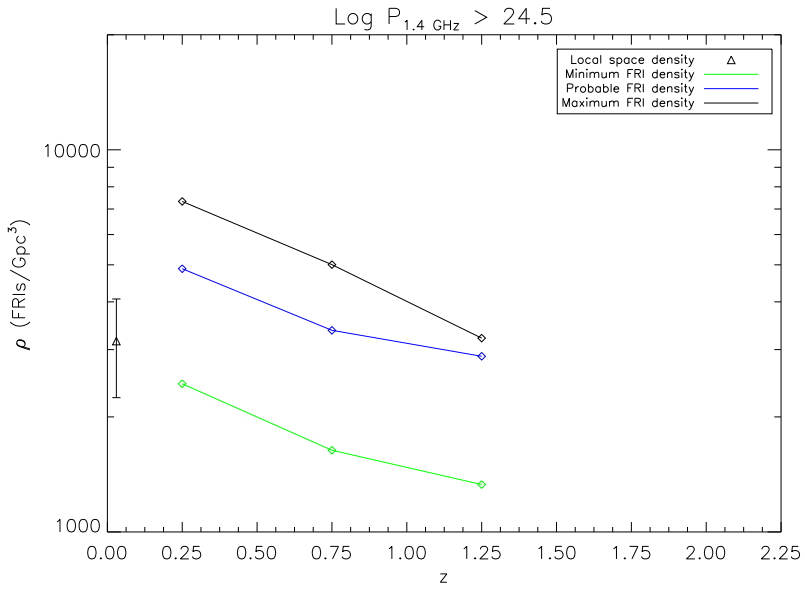

Figure 6.10: The space density changes in redshift bins of width 0.5, plotted at the bin midpoints for P$> 10^{24.5}$ W/Hz. For comparison the redshift axis is plotted with the same range as in Figure 6.5.

local values in both cases is smaller than that seen when $P_{\rm lim} = 10^{25}$ W/Hz (Figure 6.5). These results are supported by the work of Sadler et al. (2007) who found that the cosmic evolution of their low power ($10^{24} \leq P_{1.4\rm GHz} < 10^{25}$ W/Hz) population was significant but less rapid than that seen for their higher powered sources.

Inspection of Figures 6.9 and 6.10 also suggests that the peak comoving density moves to lower redshifts at lower luminosities, though the errors on these results, and the restricted redshift range needed at these low powers, are too large to draw any significant conclusions.

6.1.4 Discussion of the results

Now that the space density enhancements of this sample have been determined, as discussed in the previous section, it is useful to compare them to the results of previous work. Sadler et al. (2007), for instance, found increases in space density, out to $z = 0.7$, by a factor of $\sim$ 2 – 10 for the high ($P_{1.4GHz} > 10^{25}$ W/Hz) luminosity radio galaxies in their sample; these are consistent with the range of enhancements ($\sim$5 – $\sim$9) to $z \sim 1$ seen in the large redshift bin here. Jamrozy et al. (2004) also find that positive evolution, this time PLE, of the form $\rho(z) = \rho(0)\exp(M(L)\tau)$ (where $\tau = 1-(1+z)^{-1.5}$ and the evolution rate, $M(L)$, was found to be 5.0), is necessary to fit the number counts of the highest luminosity, morphologically selected, FRIs in their sample. At $z = 1$ this corresponds to an enhancement of 25 which is significantly higher than that seen here. Additionally, Willott et al. (2001) see a rise of about one dex, between $z \sim 0$ and $z \sim 1$, in the comoving space density of their low luminosity, weak emission line, population which contains mainly FRI sources, along with some FRIIs. It should be noted that other studies of radio galaxy evolution do not directly measure the amount of space density evolution present in their samples; instead they test for evolution using the $V/V_{\rm max}$ statistic[1] and therefore cannot be directly compared to the results of this work.

In general, all the previous studies of radio galaxy evolution conclude that the more luminous sources undergo more cosmic evolution. For samples in which the FRI population was determined by a luminosity cut, this tends to imply little or no evolution for these sources (e.g. the lower luminosity sources of Clewley & Jarvis (2004) show no evolution, whereas evolution is seen for sources of comparable luminosity to those here). However, for samples which either morphologically classify their sources or which apply a different dual–population scheme (e.g. the low/high luminosity division based on line luminosity of Willott et al. (2001)), evolution of at least some of the FRIs objects is typically seen. It would seem, therefore, that the previous models in which all FRIs have constant space density, whereas all FRIIs undergo strong, positive, cosmic evolution, are too simplistic and do not accurately represent the behaviour of the FRI–type objects. A better representation of the FRI/II space density evolution seen here and in other work, is the picture in which as the luminosity of a source increases, so does the amount of positive evolution it undergoes between z $\sim$0 and 1–2. It should be noted though

[1]This statistic is equal to 0.5 if the sample sources are uniformly distributed, $>$0.5 if there are more sources located at larger distances and $<$0.5 if there are more sources nearby. For more details see Appendix A

that the behaviour of the low power FRIs is not really investigated here, but the evolution seen for higher power objects is consistent with this model.

The detection in this work of FRI space density enhancements for sources with $P_{1.4\mathrm{GHZ}} \geq 10^{25}$ W/Hz, along with the previous studies which find essentially luminosity dependent evolution for the FRI population, strongly suggests that neither the intrinsic or the extrinsic difference models can fully explain the observed FRI/II differences. When radio galaxies are divided according to their line luminosities, as in Willott et al. (2001), there are both FRI and FRII sources in the low excitation, low luminosity, population; this implies that these FRIIs may also have inefficient accretion flows similar to those previously proposed for FRIs (e.g. Ghisellini & Celotti 2001). Jets produced by low accretion flow sources are generally weak with the majority having an FRI type structure, whereas higher accretion flows give rise to stronger, mainly FRII type jets. In this scenario therefore, both low and high accretion flows are capable of producing both FR jet structures and the morphological differences between the two classes can be explained extrinsically, as a function of their individual environments, whilst the differences in line luminosity can be explained intrinsically, as a function of their black hole properties (e.g. Hardcastle et al., 2006).

6.1.5 Predictions for future surveys

The space densities calculated for this sample can be used to make predictions of the numbers of sources likely to be seen, per redshift bin per square degree, in future surveys to be carried out with new instruments like the Low Frequency ARray (LOFAR) and the Square Kilometre Array (SKA); the method used for this calculation, along with the results, are described in this section.

The first step was to fit a model radio luminosity function, $\Phi(P \geq P_{\mathrm{lim}})$, to the 'probable FRI' redshift, z, and luminosity, P, data points for the three limiting powers, $\mathrm{P_{lim}} = 10^{24}$, $10^{24.5}$ and 10^{25} W/Hz. The errors were taken to be the difference between the maximum and minimum FRI values and the local density values were taken as the combination of the 3CR and equatorial sample results. As has been previously discussed in §6.1.3, the reality of the high–redshift cut–off seen in the data is uncertain due to the assumed spectral indices. To ensure that this caution is incorporated into the fitting process the errors on the final points in each luminosity group were doubled.

Previous studies (e.g. DP90, Best et al. (2005)) have shown that $\Phi(P \geq P_{\mathrm{lim}}, 0) = \Phi_0 P^{-\alpha}$ since essentially all of the FRIs lie below the break in the local luminosity function. The higher redshift turnovers seen in the data, on the other hand, can be best parameterized by

an exponential with the same form as that of the models of Willott et al. (2001) for the high luminosity population. Combining these factors therefore, the model used was of the form

$$\Phi(P \geq P_{\rm lim}, z) = \Phi_0 P^{-\alpha} f(P \geq P_{\rm lim}, z), \tag{6.15}$$

where the evolution function $f(P \geq P_{\rm lim})$ is either

$$f(P \geq P_{\rm lim}, z) = (1+z)^{\beta} \text{ for } z < z_{\rm max} \text{ or} \tag{6.16}$$

$$f(P \geq P_{\rm lim}, z) = (1+z_{\rm max})^{\beta} \exp[\gamma(z - z_{\rm max})^2] \text{ for } z \geq z_{\rm max}, \tag{6.17}$$

and where the peak redshift, $z_{\rm max}$, is given by

$$z_{\rm max} = z_0 \Big(\frac{P}{10^{24} W/Hz} \Big)^{\delta}. \tag{6.18}$$

This model RLF has six free parameters, $\Phi_0, \alpha, \beta, \gamma, z_0$ and δ, which, given the small number of data points available from the space density calculations is a reasonable number. Physically, α is the slope of the local RLF, z_0 is the value of $z_{\rm max}$ at 10^{24} W/Hz, β is a measure of the rate of increase of space density in the local universe and γ controls the steepness of the high–redshift decline. If more data were available then the model could be refined by allowing γ to also vary with z; this may improve the parameterisation of the high–redshift turnover.

Parameter	Best fit value
$\log \Phi_0$	31.39
α	1.16
β	3.91
γ	2.06
z_0	0.21
δ	0.60

Table 6.8: The parameter values for the best–fit model

Equation 6.15 was fitted to the data using the IDL routine `mpfit` (Markwardt, 2007) which uses the method of least squares to determine the best values for the six free parameters; these can be found in Table 6.8 and the best–fit model is illustrated in Figure 6.11. The χ^2 for this result is 6.8 which, since there are six degrees of freedom, gives an acceptable reduced χ^2 of 1.1. The fitted value of α is steeper than that previously determined for the low luminosity population (e.g. Willott et al. (2001)); this is likely to have occurred because the 10^{24} – 10^{25} W/Hz regime, in which the data are fitted, is at the break in the RLF, where the gradient is indeed steeper than at lower powers. This suggests that whilst the model fits the data here well, it will overpredict the numbers of local sources.

The next step in calculating the predictions was to calculate dN/dz, the number of sources

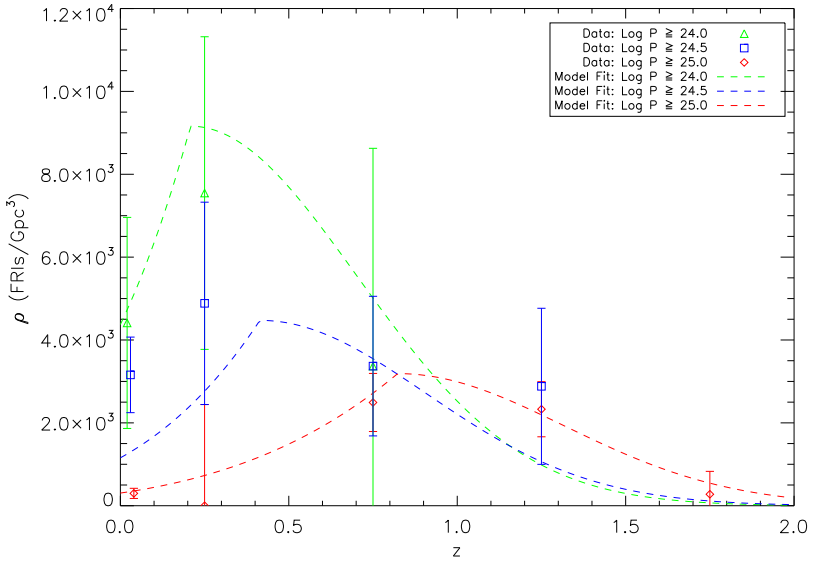

Figure 6.11: The data points for the $P_{\rm lim} = 10^{24}$, $10^{24.5}$ and 10^{25} W/Hz space density measurements overplotted with the model RLF constructed from the best fitting parameters.

per redshift bin, for the best fitting result. This was done by integrating the model RLF as in Equation 6.12, over the interval $0.0 < z < 0.1$ to give the total number of sources in this volume, and then dividing by 0.1 – the width of the redshift bin. The upper and lower redshift limits were then increased and the calculation repeated; this process continued until $z = 2.0$. In all cases, the upper limit (P_2) of the luminosity integral was taken to be $10^{27.5}$ W/Hz, whereas the lower limit was calculated at each redshift from the flux density limit of the proposed survey under investigation. Ω, the survey area, was taken to be 1 square degree in all cases. It should also be noted that the lower luminosity limit of the integration was restricted to 10^{22} W/Hz since the model fitting is not robust at lower luminosities as previously discussed.

The survey limit considered here is $S_{\rm lim} = 1\mu$Jy; this sensitivity is equivalent to the proposed 200 MHz 'LOFAR–deep' survey (Best, 2007). Figure 6.12 shows the predicted dN/dz values arising from this flux density limit. The 1σ uncertainty on this prediction was estimated by determining the value of γ which would result in a fit where the χ^2 is 7.04 higher than that found for the best–fit model (Press et al., 1992). Only γ was used for this as it controls the steepness of the exponential fall–off and thus its maximal value will give the upper limit of the numbers of sources at higher redshift. The resulting error prediction is also shown in Figure 6.12 for comparison.

The SKA will be a significantly more sensitive instrument than LOFAR and, as such, the surveys that it will undertake will have flux density limits at the tens of nJy level (Jarvis and Rawlings, 2004). Extrapolating the best–fit model to these limits would result in a prediction

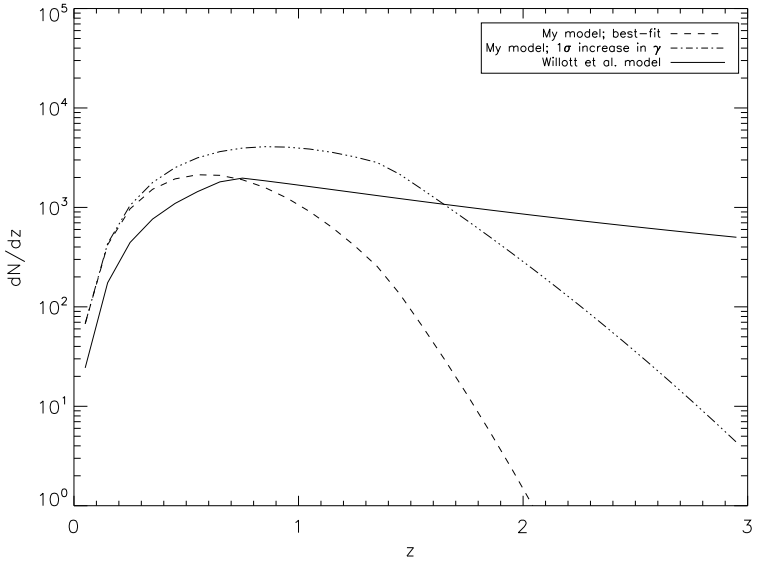

Figure 6.12: The changes in dN/dz predicted by both the best–fit model and model C of Willott et al. (Willott et al., 2001), for a survey with a flux density limit of 1 μJy and an area of 1 square degree. Also shown is the uncertainty on the prediction arising from the model fit.

with a high level of uncertainty due to the poor low luminosity constraints. Consequently, the predictions were only carried out for the hypothetical 1 μJy survey.

The dN/dz predictions for this sample can also be compared with those arising from previous determinations of the RLF. The model C parameterisation of Willott et al. (2001) was chosen for this as it accurately reproduces the PLE results of DP90, but, as discussed in §6.1.4, has a better physical basis. For low luminosity sources, it has the form

$$\rho_l(P,z) = \rho_{l0}\Big(\frac{P}{P_{l*}}\Big)^{-\alpha_l}\exp\Big(\frac{-P}{P_{l*}}\Big)(1+z)^{k_l} \text{ for } z < z_{l0} \quad (6.19)$$

$$\rho_l(P,z) = \rho_{l0}\Big(\frac{P}{P_{l*}}\Big)^{-\alpha_l}\exp\Big(\frac{-P}{P_{l*}}\Big)(1+z_{l0})^{k_l} \text{ for } z \geq z_{l0} \quad (6.20)$$

where $\log\rho_{l0} = -7.120, \alpha_l = 0.539, \log P_{l*} = 26.10, z_{l0} = 0.706$ and $k_l = 4.30$ at 151 MHz and in Einstein de Sitter cosmology. This was converted to 1.4 GHz and then integrated in the same way as before, but, in this case, the luminosity integral limits were re–evaluated at each redshift step to convert them to ΛCDM cosmology, using the same procedure described in Equation 6.14; the resulting prediction is overplotted in Figure 6.12.

The comparison between the two models shows that at redshifts $\gtrsim 2.5$ the FRI numbers predicted by the space densities found for this sample, are consistently lower than those for the 'low luminosity' model C population. Since the Willott et al. (2001) model was based on source number counts, this suggests that at high–z not all of the radio sources in their sam-

ple are FRIs. It should be noted here that the increase over the Willott et al. line seen in the best–fitting model at low redshifts, is likely to again result from the high fitted value of the α parameter.

In conclusion, therefore, it is clear that the space density results for the sample are not yet accurate enough to make robust high redshift predictions of the FRI behaviour. To do this would require a deeper survey with a flux density limit lower than the 0.5 mJy one used here; this would then allow sources with luminosities lower than 10^{24} W/Hz to be included in the fitting.

6.2 The FRI/FRII dividing luminosity

Ledlow & Owen (1996) demonstrated that, locally, the luminosity dividing FRI and FRII objects is a function of the host galaxy absolute magnitude (as shown in Chapter 1, Figure 1.5). This section describes how the radio sample here was used to look for changes in this dividing luminosity at different cosmological epochs.

6.2.1 K and Evolutionary corrections

All the sources in the sample were observed at the same wavelength, determined by the filters of the telescopes used. However, since observed wavelength, λ_0, is related to emitted wavelength, λ_1, by $\lambda_0 = (1 + z)\lambda_1$, the actual region of the source spectral energy distribution (SED) probed depends on the source redshift. The K correction is applied to the magnitudes of the sample to correct all the measurements to the same rest frame wavelength (Poggianti, 1997).

A similar problem arises since the source fluxes also change with time as the galaxy ages; a sample of objects at different redshifts, and different formation ages, will therefore not all be observed at the same evolutionary stage. Since the aim here is to see if galaxies that lie on the FRI/II dividing line at $z = 1$ are consistent with those on the dividing line at $z = 0$, the evolutionary, or e, correction needs to be applied to ensure that, at each redshift, sources can be accurately compared.

The need for these two corrections is illustrated by Figure 6.13, which shows the spectral evolution of an elliptical galaxy with cosmic time. It clearly shows that, firstly, as a source ages it loses significant amounts of flux (especially at bluer wavelengths), and, secondly, that there is a large variation of flux with wavelength, and hence redshift, indicating therefore, the

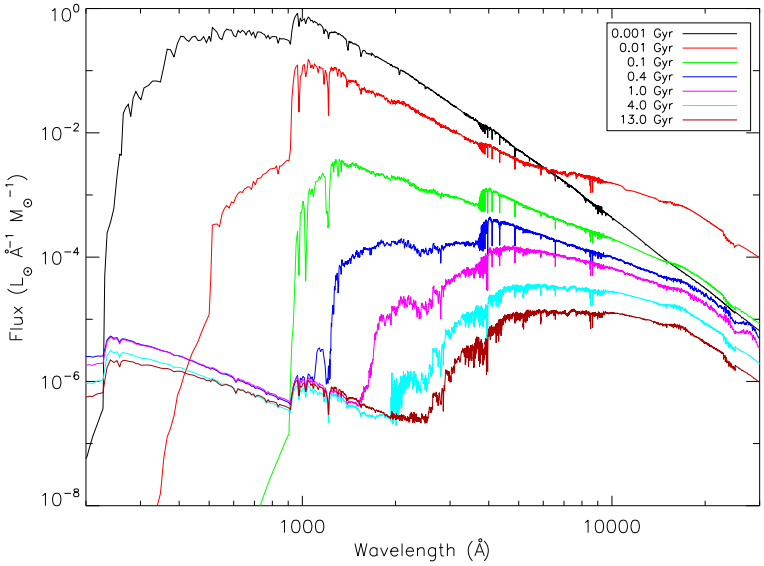

Figure 6.13: The spectral energy distributions for an elliptical galaxy model with seven different formation ages. The model used is that of Bruzual & Charlot (2003) with an single, instantaneous burst of star formation, followed by passive evolution thereafter.

necessity of correcting all sources to the same rest frame wavelength.

For the sample sources, the corrections were calculated using the GALAXEV code of Bruzual & Charlot (2003). This code allows the spectral evolution of several different stellar population models to be computed for different ages and metallicities, using a large number of filters. As the actual star formation history of the sources is unknown, the corrections were calculated for two likely models – passive evolution following an initial, instantaneous burst at $z = 5$ (Figure 6.13) and exponentially declining star formation, with an e–folding time of 1 Gyr, beginning at $z = 10$. The filter used for both models was that of the *r*–band WFC. The corrections calculated using the two models are of a similar magnitude at low redshift, as shown in Figure 6.14 and only significantly diverge at $z \gtrsim 1$

6.2.2 The high–redshift Ledlow & Owen diagram

Now that the K and evolutionary corrections have been calculated for the two star formation histories, the high–redshift Ledlow & Owen diagram for the AGN in the full sample, ignoring sources classified as quasars because of their non–thermal AGN emission, can be constructed. The resulting radio luminosity versus absolute magnitude diagrams are presented in Figures 6.15 (for the burst model) and 6.16 (for the exponentially declining star formation model), split into redshift slices of width 0.5 so that changes with increasing distance are immediately

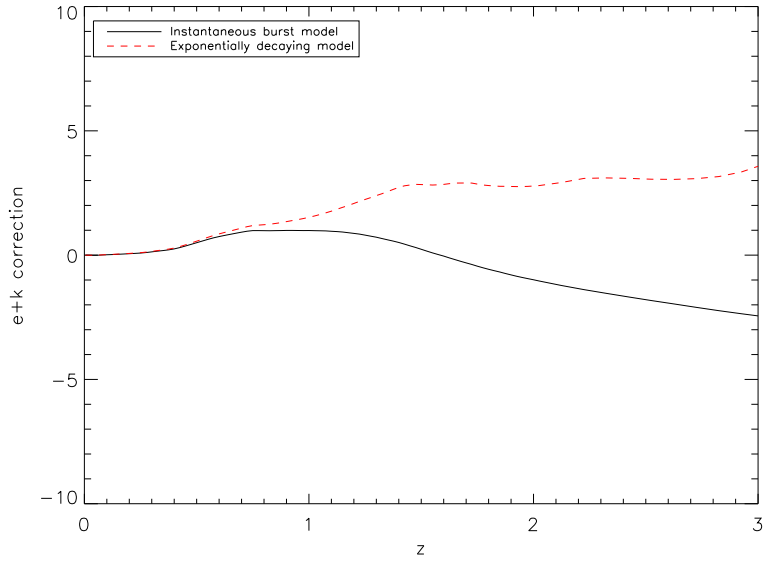

Figure 6.14: A comparison of the K+evolutionary (e) corrections for the two stellar evolution models.

apparent. Redshifts higher than 2.5 are ignored because of the small number of sources located beyond this. Sources with photometric redshift estimates are coloured blue to indicate that they have uncertain positions in these two Figures as a result of the redshift dependence of both their absolute magnitude and their radio power; these uncertainties ($\Delta(\log z) = 0.2$, as before), are illustrated in Figures 6.17 and 6.18 for clarity.

It is immediately obvious from inspecting Figures 6.15, 6.16, 6.17 and 6.18 that the lack of higher powered objects in the radio sample leads to underpopulation of the upper regions of the diagrams. There also seems to be no clear FRI/II separation in e.g. the $0.5 < z < 1.0$ bin, but this is not unexpected given the small ranges of P and M_r covered. The results do indicate however, that the position of the low redshift FRI/II dividing line does not appear to shift to brighter absolute magnitudes up to redshifts of $\sim$1, but the conclusions that can be drawn about the behaviour of the line at redshifts greater than this are severely limited by the differences in the two stellar population models used to correct the data. If the exponentially decaying model is correct, then the $1.0 < z < 1.5$ bin suggests that FRIs may move above the local dividing line, indicating that the division may have been at lower (evolutionary corrected) absolute magnitudes at high redshift. This could be understood if the host galaxies of both FR types were intrinsically fainter in the *r*–band here, and is supported by the observation that radio galaxies in the 6C survey tend to be smaller than the more powerful 3CR objects at $z \sim 1$ (Roche et al., 1998). Sources at higher redshift may also be in denser environments and so be able to produce the same radio luminosity for a lower host galaxy, evolutionary corrected, absolute magnitude, also causing the FRI/II dividing line to shift. However, without additional spectroscopy to properly determine the stellar populations of the sample sources, any evolution

in the line can not be determined.

6.3 Chapter summary

In this Chapter the methods for calculating the FRI space density enhancement and the high–redshift Ledlow & Owen diagrams have been described and the results presented. Space density enhancements of factors ∼5–9 over the local density were found for the $P_{1.4\mathrm{GHz}} \geq 10^{25}$ W/Hz FRI subsample. These values were inconsistent with a constant density/no–evolution scenario at a >99.9% confidence level, and in good agreement with the PLE and LDE models of DP90. The uncertainty in these results was dominated by the low number of sources used. The turnover in space density seen at $z \gtrsim 1.5$ is less secure due to the assumed α value of 0.8; it is however, consistent with the observations of Waddington et al. (2001).

Conclusions about the behaviour of the FRI/II dividing luminosity are harder to draw, however: a shift to brighter magnitudes at higher redshift seems inconsistent with the data, but a shift to fainter magnitudes may be possible. A larger sample, combined with high quality spectroscopic observations to allow accurate K+e corrections to be determined, is required to confirm or deny this.

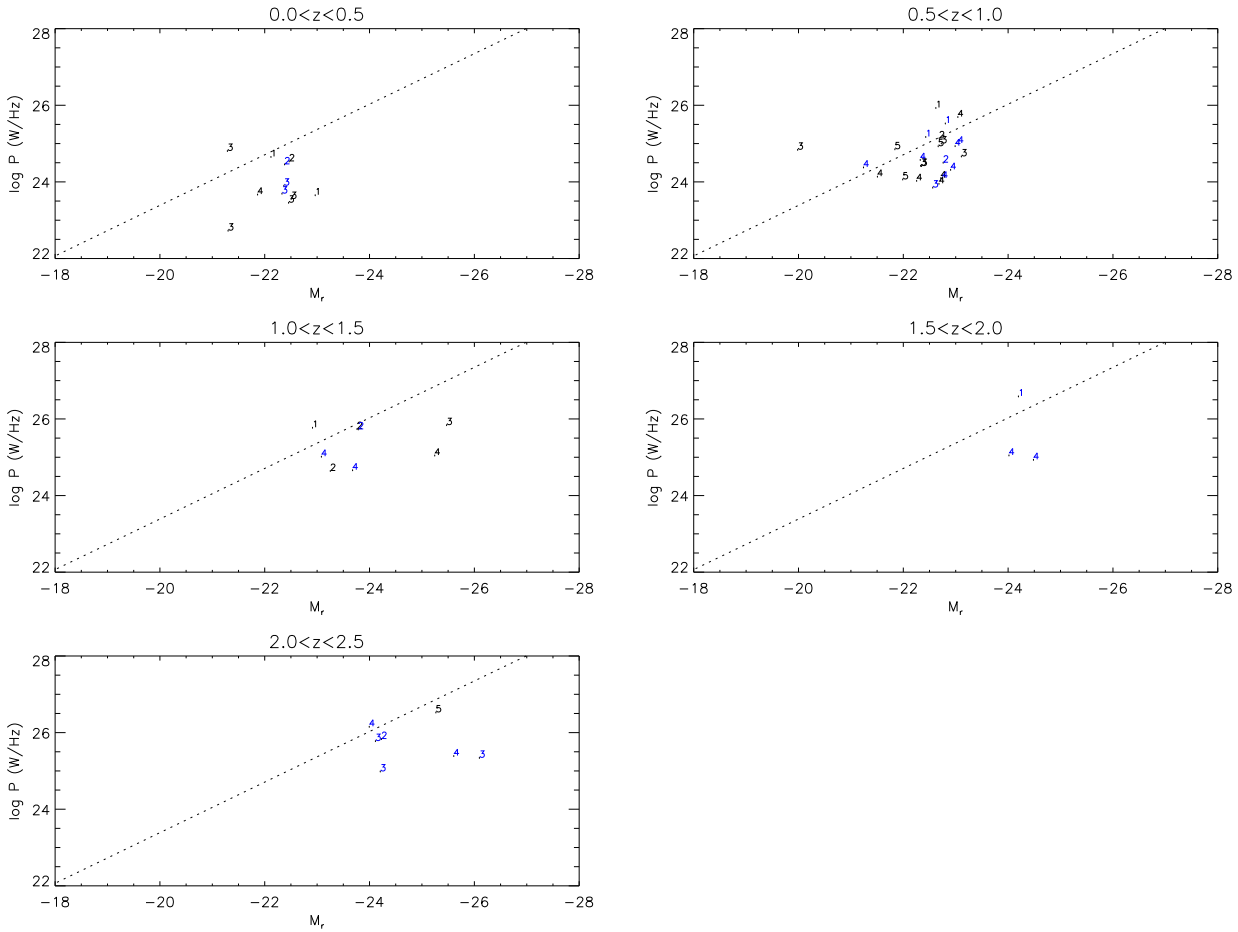

Figure 6.15: Absolute *r*–band magnitude, corrected using the passive evolution model, versus total radio power for the sample. Numbers indicate the radio classification assigned in the previous Chapter; 1–3 indicate FRIs of differing certainty whereas 4 and 5 are a mixture of FRIIs, compact objects and unclassifiable sources. The dotted line is an approximation to the dividing line found by Ledlow & Owen (1996) and sources with photometric redshift estimates are coloured blue.

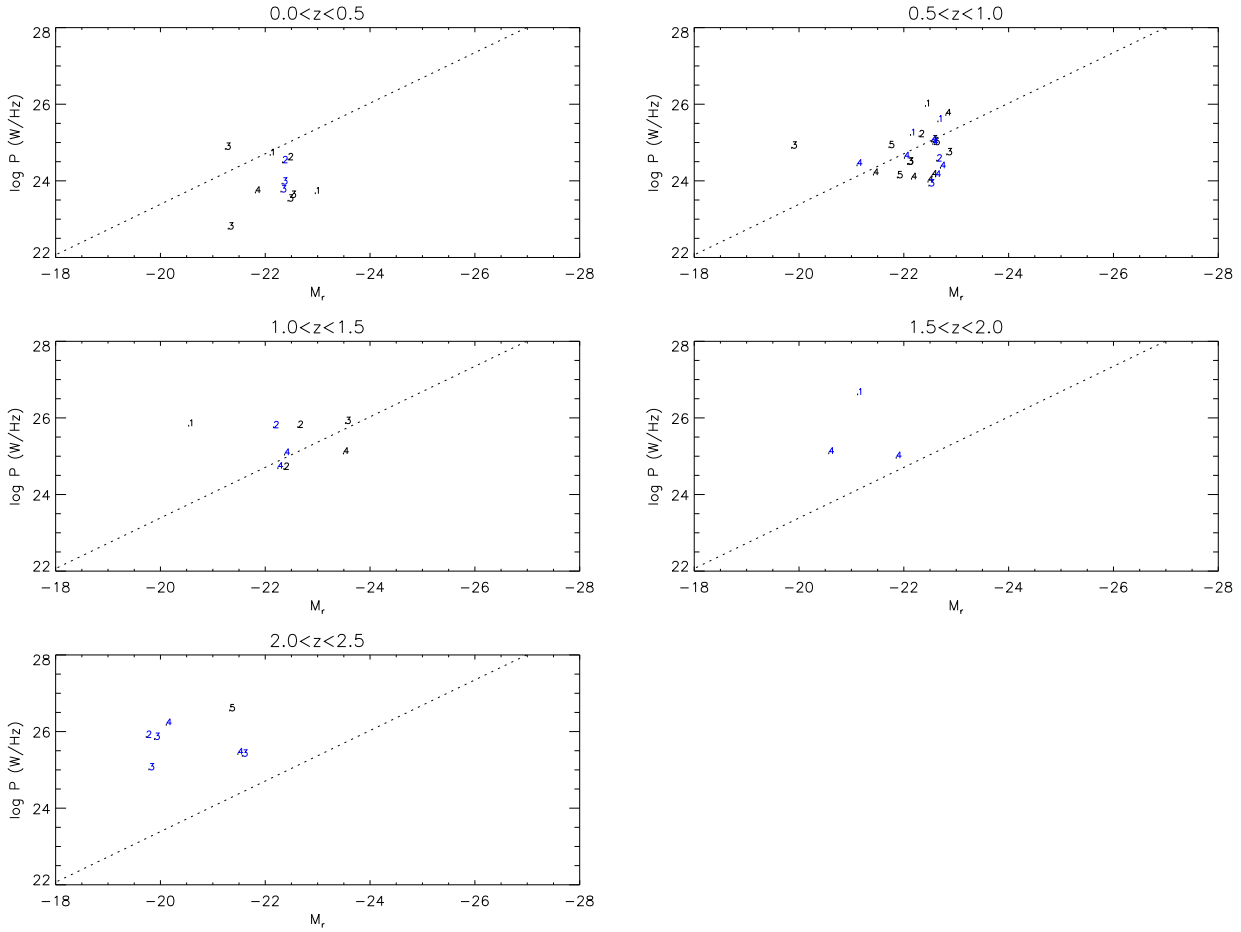

Figure 6.16: Absolute *r*–band magnitude, corrected using the exponentially declining star formation model, versus total radio power for the sample. Numbers indicate the radio classification assigned in the previous Chapter; 1–3 indicate FRIs of differing certainty whereas 4 and 5 are a mixture of FRIIs, compact objects and unclassifiable sources. The dotted line is an approximation to the dividing line found by Ledlow & Owen (1996) and sources with photometric redshift estimates are coloured blue.

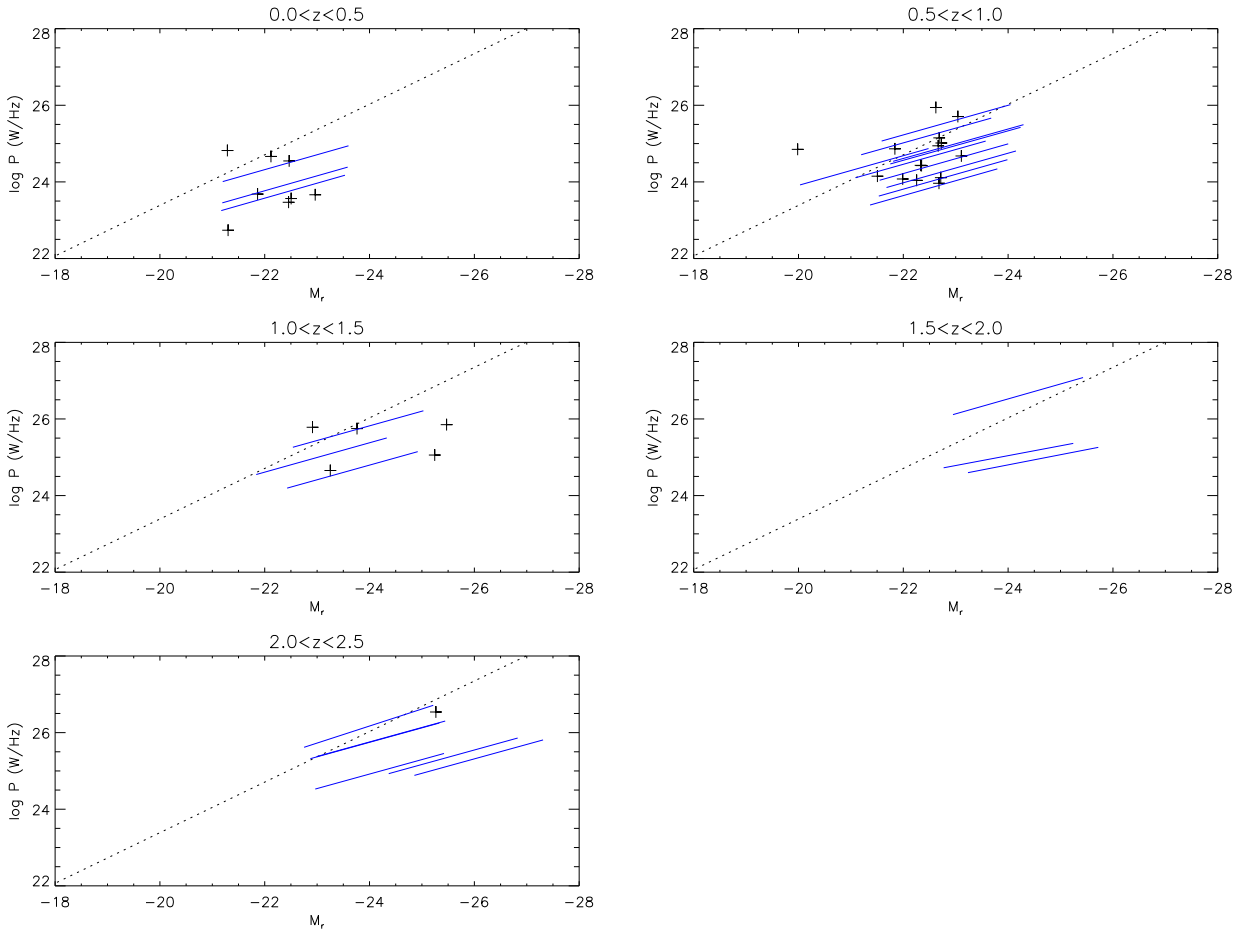

Figure 6.17: Absolute *r*–band magnitude, versus total radio power for the sample, as in Figure 6.15, but now showing the effect of the error of 0.2 in $\log z$ on the photometric redshift estimates.

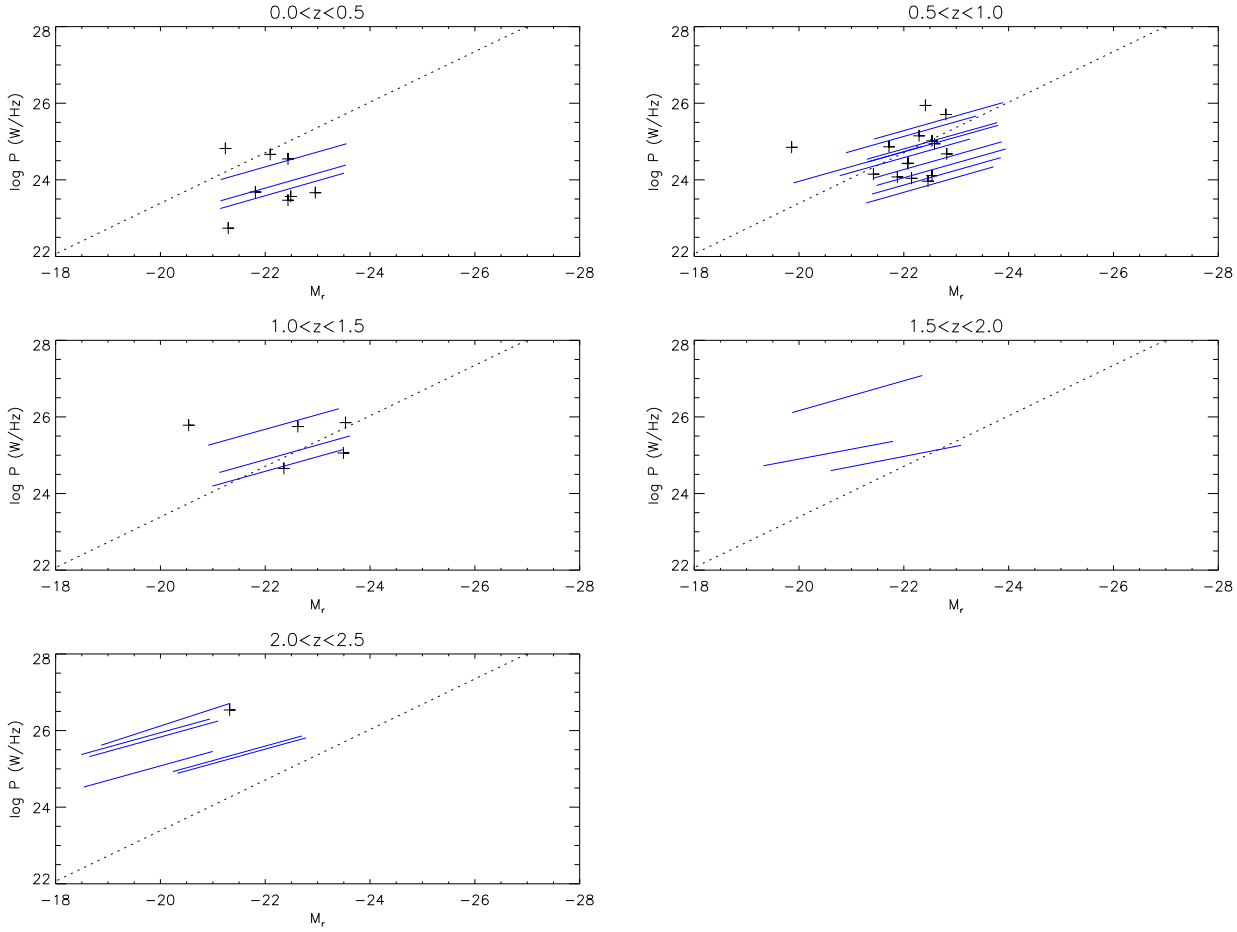

Figure 6.18: Absolute *r*–band magnitude, versus total radio power for the sample, as in Figure 6.16, but now showing the effect of the error of 0.2 in $\log z$ on the photometric redshift estimates.

CHAPTER 7

Conclusions and future work

The main aim of this thesis was to directly measure the high redshift space density of FRI radio sources and thus attempt to improve the understanding of the underlying differences between the two FR types. This was achieved using multi–wavelength observations of a complete sample of 81 radio galaxies, above a limiting flux density of $S_{1.4\mathrm{GHz}} > 0.5$ mJy, selected using wide–field, 1.5″ resolution, VLA A–array radio observations of two fields in Lynx and Hercules. These were previously observed, at lower resolution, by Oort et al. Oort and van Langevelde (1987); Oort and Windhorst (1985).

Optical (INT) and infra–red (UKIRT) imaging was used to identify the host galaxies corresponding to the radio sources in the sample. These observations reached limiting magnitudes of $r \geqslant 25.2$ for the Hercules field, $r \geqslant 24.4$ for the Lynx field and $K \gtrsim 20$ for those sources included in the UKIRT data. The identification fraction was 85% for both fields combined and the magnitude and colour distributions were in good agreement with previous results.

Spectroscopic data were then taken for the best candidate high–redshift sources in the sample that did not already have a previously published redshift value. 56% and 62% of the Lynx and Hercules field sources respectively (41 sources in total), were included in these observations and this resulted in 20 redshifts (65% from emission lines and the remainder from absorption lines only). Once the previously published redshifts were included, the final spectroscopic completeness of the sample was 49%. The K–z and r–z relations were then used to photometrically estimate redshifts for the remaining sources in the sample with a host galaxy detection; this left $<$10% of the sample without redshift information. These results were also used to

clean the sample by identifying the 5 quasars and 5 starburst galaxies present.

The classification of the sample was then done with the aid of further radio observations of the two fields. Lower, $\sim 5''$ resolution, VLA B–array data were obtained for the Lynx field alone so that a measure of the total flux density of those sources could be obtained. Following this, the 21 best FRI candidates were then observed with either VLA+Pt at $1.1'' \times 0.6''$ resolution, or MERLIN at $0.19'' \times 0.15''$ resolution or both. An additional 16 sources were also observed as they fell within the MERLIN subfields. The radio sources in the sample were then sorted into 5 classification groups: Group 1 was for secure, morphologically classified, FRIs; Group 2 for sources with indications of FRI–type extension, alongside a flux density loss of 3σ or more; Group 3 for sources with either flux density loss or some extension, and Groups 4 and 5 for sources which were either definitely not FRIs or which were unclassifiable.

Finally, the maximum, probable and minimum space densities of the FRIs in groups 1–3, together with the two FRIs in the Hubble Deep and Flanking Fields, were calculated using redshift bins of width 0.5, over the range $0.0 < z < 2.0$. These showed clear density enhancements by a factor 5–9, at $z \sim 1.0$, over the local FRI value. The probable density values were used to estimate the errors arising from the redshift estimates used; these showed that the dominant source of error is the low number of sources in the sample and that the result is secure. The possible decline in space density seen at $z \gtrsim 1.5$ is less clear due to a combination of the flux limit and the uncertainties in spectral index.

A larger bin, spanning $0.5 < z < 1.5$, was then used to quantify the observed enhancement; this ruled out the no–evolution scenario at the $>$99.9% confidence limit. The FRI evolution was also found to be consistent with the PLE and LDE models of DP90 which suggests that, at a particular radio power, FRIs evolve like FRIIs.

The dividing line found by Ledlow & Owen (1996) between FRIs and FRIIs in the $P_{\rm rad}$ vs. $P_{\rm opt}$ plane was also investigated and found to apparently not move to brighter absolute magnitudes at higher redshift. This conclusion is very weak, however, due to the underpopulation of the FRII section of the high redshift Ledlow & Owen diagram and the inaccuracy of the K and evolutionary corrections applied to the data.

The clear density enhancements seen in the FRIs here shows that, for sources $\geq 10^{25}$ W/Hz at least, the FRI population does undergo cosmic evolution. This suggests that the observed FRI/II differences cannot fully be explained by assuming that they are two discrete, unrelated, types of object. It is clear that further work, as described in the next section, is vital for understanding the underlying differences between the two types.

7.1 Improving the FRI space density measurement

The accuracy of the results in this thesis is limited by three major factors: (i) the radio classifications, (ii) the low spectroscopic completeness of the sample and (iii) the small numbers of definite FRIs present. The second of these can be addressed simply with, for example, a GEMINI GMOS proposal to obtain spectra for the remaining high–redshift FRI candidates with only estimated redshifts; the solution for the first and third is outlined below.

The need in the current sample to work largely object–by–object, for both the optical spectroscopy and the high–resolution radio imaging, inevitably limits the final space density values. This can be remedied by utilising the data from the several large, deep, wide–field imaging surveys currently underway. Surveys such as the UKIDSS UDF ($\sim$1 sq. degree) or the Hubble COSMOS field (2 sq. degrees) with their high–quality multi–band imaging, spectroscopy and low–resolution radio imaging will enable the selection of many suitable high–redshift FRI candidates for further radio follow–up observations and thus refine the space density calculations using a much larger area. It should be noted here that the dN/dz predictions for the FRI numbers calculated in §6.1.5 suggests that a survey of at least 1 sq. degree is needed to ensure that sufficient sources are detected to draw firm conclusions on the high redshift space density enhancement. This criteria is adaquately satisfied by both the UDF and COSMOS areas. Planned surveys for future instruments such as the LOFAR and, more distantly, the SKA will cover much wider areas than this, and at greater senstivities, thus further improving the quality of the data and, therefore, the space density measurement.

The COSMOS field in particular will be covered by a 1.4 GHz VLA A–array radio survey which will be excellent for selecting candidates for FRI follow–up. It should be noted that these radio observations being undertaken of the COSMOS field, are being done with the aim of constraining the evolution of the low–luminosity radio sources. However, since there is no fixed radio luminosity which divides the FRIs and FRIIs, luminosity selection alone, without morphological classification will not separate FRIs and FRIIs. Thus follow–up high resolution radio studies are required to provide an accurate picture of the cosmic evolution of the FRI radio galaxies themselves and refine the conclusions about the intrinsic/extrinsic differences between the two classes.

Accurate morphological classification of radio sources as FRIs is very difficult due to the high sensitivities and resolutions needed to detect these low–luminosity objects. Currently the high–resolution radio observations have been taken using the VLA+Pietown and MERLIN arrays but their sensitivities and narrow fields has limited the numbers of objects searched. The quality

of the future observations can be improved by using the enhanced technological capabilities of the new eMERLIN and eVLA facilities, both of which offer high angular resolution across large fields and which are expected to be operational from late 2007. The increased sensitivity (by a factor of $\sim$5 for eVLA and by $\sim$8 for eMERLIN) of these arrays will also enable deeper observations to be taken which will lead to the classification of sources from the fainter end of the radio luminosity function, instead of being limited to the brighter FRI candidates only; this will be ideal for investigating the apparent luminosity dependent evolution of the FRIs. eMERLIN in particular will operate in wide–field mode (10 arcmin diameter at 1.4 GHz) as standard thus enabling many FRI candidates to be observed simultaneously. In the future this can be extended to include data from the large–sky surveys planned for the LOFAR array; its low frequency, arcsecond resolution, imaging capabilities will be ideal for detecting the extended emission that is vital for accurate morphological classification. Such surveys will obviously facilitate the FRI detection and make it possible to properly classify all radio galaxies present, not just the best candidates.

A new, larger, sample of fully classified radio galaxies (both FRIs and FRIIs) will also enable the construction of more detailed, better populated, higher redshift, Ledlow & Owen diagrams, with the aim of properly investigating changes in the FRI/II dividing luminosity. Furthermore the quantity of multi–band optical and infra–red imaging data will also enable the other properties of these objects to be investigated. In particular, differences in triggering mechanisms could be shown by comparing the incidence of mergers and interactions in the local environments of the two classes. Alongside this, the availability of full colours for the FRI and FRII host galaxies will enable the stellar populations to be reconstructed and the star formation histories of the two classes to be compared. The deep, high resolution X–ray observations of the COSMOS field with Chandra will also allow the central engines of the FRIs detected to be probed, to investigate possible differences in their radiative efficiency compared with the FRIIs. All these factors will play an important role in understanding the links between the two types.

References

Baars, J. W. M., Genzel, R., Pauliny-Toth, I. I. K., and Witzel, A.: 1977, *A&A* **61**, 99

Barbaro, G. and Poggianti, B. M.: 1997, *A&A* **324**, 490

Baum, S., Zirbel, E., and O'Dea, C.: 1995, *ApJ* **451**, 88

Becker, R. H., White, R. L., and Helfand, D. J.: 1995, *ApJ* **450**, 559

Bershady, M. A., Hereld, M., Kron, R. G., Koo, D. C., Munn, J. A., and Majewski, S. R.: 1994, *AJ* **108**, 870

Best, P. (ed.): 2007, *LOFAR-UK: A science case for UK involvement in LOFAR*, Chapt. 5, LOFAR-UK consortium

Best, P. N., Kaiser, C. R., Heckman, T. M., and Kauffmann, G.: 2006, *MNRAS* **368**, L67

Best, P. N., Kauffmann, G., Heckman, T. M., and Ivezić, Ž.: 2005, *MNRAS* **362**, 9

Best, P. N., Röttgering, H. J. A., and Lehnert, M. D.: 1999, *MNRAS* **310**, 223

Best, P. N., van Dokkum, P. G., Franx, M., and Röttgering, H. J. A.: 2002, *MNRAS* **330**, 17

Bolzonella, M., Miralles, J.-M., and Pelló, R.: 2000, *A&A* **363**, 476

Bridle, A. H. and Perley, R. A.: 1984, *ARA&A* **22**, 319

Bruzual, G. and Charlot, S.: 2003, *MNRAS* **344**, 1000

Burke, B. F. and Graham-Smith, F.: 2002, *An Introduction to Radio Astronomy*, CUP

Cao, X. & Rawlings, S.: 2004, *MNRAS* **349**, 1419

Casali, M. & Hawarden, T.: 1992, *UKIRT Newsletter* **4**, 33

Clewley, L. and Jarvis, M. J.: 2004, *MNRAS* **352**, 909

Condon, J. J., Cotton, W. D., Greisen, E. W., Yin, Q. F., Perley, R. A., Taylor, G. B., and Broderick, J. J.: 1998, *AJ* **115**, 1693

Condon, J. J. and Yin, Q. F.: 1990, *ApJ* **357**, 97

Diamond, P. J., Garrington, S. T., Gunn, A. G., Leahy, J. P., McDonald, A., M., B., T. W., Richards, A. M. S., and Thomasson, P.: 2003, *The MERLIN User Guide*

Donley, J. L., Rieke, G. H., Rigby, J. R., and Pérez-González, P. G.: 2005, *ApJ* **634**, 169

Dunlop, J.S. & Peacock, J.: 1990, *MNRAS* **247**, 19

Dunn, R.: 2005, *An Introduction to X-ray Astronomy*, `http://www-xray.ast.cam.ac.uk/xray_introduction/`

Eales, S., Rawlings, S., Law-Green, D., Cotter, G., and Lacy, M.: 1997, *MNRAS* **291**, 593

Fanaroff, B.L. & Riley, J.: 1974, *MNRAS* **167**, 31P

Gawroński, M. P., Marecki, A., Kunert-Bajraszewska, M., and Kus, A. J.: 2006, *A&A* **447**, 63

Ghisellini, G. and Celotti, A.: 2001, *A&A* **379**, L1

Gopal-Krishna and Wiita, P. J.: 2000, *A&A* **363**, 507

Hardcastle, M.: 1995, *Jets in nearby FRII radio galaxies*, `www.mrao.cam.ac.uk/yerac/hardcastle/ hardcastle.htm`

Hardcastle, M. J., Evans, D. A., and Croston, J. H.: 2006, *MNRAS* **370**, 1893

Högbom, J. A.: 1974, *A&AS* **15**, 417

Hogg, D. W.: 1999, *astro-ph/9905116*

Irwin, M.: 2002, *Wide Field Survey – Astrometric Calibration*, `http://www.ast.cam.ac.uk/~wfcsur/astrometry.php`

Jackson, C. and Wall, J.: 1999, *MNRAS* **304**, 160

Jamrozy, M.: 2004, *A&A* **419**, 63

Jarvis, M. J. and Rawlings, S.: 2004, *New Astronomy Review* **48**, 1173

Jorgensen, I.: 1994, *PASP* **106**, 967

Kauffmann, G., Heckman, T. M., Tremonti, C., Brinchmann, J., Charlot, S., White, S. D. M., Ridgway, S. E., Brinkmann, J., Fukugita, M., Hall, P. B., Ivezić, Ž., Richards, G. T., and Schneider, D. P.: 2003, *MNRAS* **346**, 1055

Koo, D. C. and Kron, R. G.: 1982, *A&A* **105**, 107

Krolik, J. H.: 1999, *Active Galactic Nuclei*, Princeton University Press

Kron, R. G., Koo, D. C., and Windhorst, R. A.: 1985, *A&A* **146**, 38

Laing, R. A., Jenkins, C. R., Wall, J. V., and Unger, S. W.: 1994, in G. V. Bicknell, M. A. Dopita, and P. J. Quinn (eds.), *ASP Conf. Ser. 54: The Physics of Active Galaxies*, p. 201

Laing, R. A., Riley, J. M., and Longair, M. S.: 1983, *MNRAS* **204**, 151

Landolt, A. U.: 1992, *AJ* **104**, 340

Ledlow, M. J. and Owen, F. N.: 1996, *AJ* **112**, 9

Leggett, S.: 2005, *Extinction Measurements*, `http://www.jach.hawaii.edu/UKIRT/astronomy/calib/phot_cal/cam_zp.html`

Longair, M.: 1966, *MNRAS* **133**, 421

Markwardt, C. B.: 2007, *Markwardt IDL Library*, `http://cow.physics.wisc.edu/~craigm/idl/idl.html`

McCarthy, P. J.: 1993, *ARA&A* **31**, 639

McCarthy, P. J., van Breugel, W., Spinrad, H., and Djorgovski, S.: 1987, *ApJ* **321**, L29

McLure, R. J. and Dunlop, J. S.: 2002, *MNRAS* **331**, 795

Miller, L., Peacock, J. A., and Mead, A. R. G.: 1990, *MNRAS* **244**, 207

Monet, D. G., Levine, S. E., Canzian, B., Ables, H. D., Bird, A. R., Dahn, C. C., Guetter, H. H., Harris, H. C., Henden, A. A., Leggett, S. K., Levison, H. F., Luginbuhl, C. B., Martini, J., Monet, A. K. B., Munn, J. A., Pier, J. R., Rhodes, A. R., Riepe, B., Sell, S., Stone, R. C., Vrba, F. J., Walker, R. L., Westerhout, G., Brucato, R. J., Reid, I. N., Schoening, W., Hartley, M., Read, M. A., and Tritton, S. B.: 2003, *AJ* **125**, 984

Mushotzky, R.: 2004, in A. Barger (ed.), *Supermassive Black Holes in the Distant Universe*, Chapt. 2, Kluwer

Muxlow, T. W. B., Richards, A. M. S., Garrington, S. T., Wilkinson, P. N., Anderson, B., Richards, E. A., Axon, D. J., Fomalont, E. B., Kellermann, K. I., Partridge, R. B., and Windhorst, R. A.: 2005, *MNRAS* **358**, 1159

Oort, M. J. A. and van Langevelde, H. J.: 1987, *A&AS* **71**, 25

Oort, M. J. A. and Windhorst, R. A.: 1985, *A&A* **145**, 405

Owen, F. N., Ledlow, M. J., Keel, W. C., and Morrison, G. E.: 1999, *AJ* **118**, 633

Owen, F. N. & Laing, R. A.: 1989, *MNRAS* **238**, 357

Peacock, J. A.: 1999, *Cosmological Physics*, Cambridge University Press

Peebles, P. J. E.: 1993, *Principles of Physical Cosmology*, Princeton University Press

Perley, R. A.: 1999, in P. R. Taylor G.B., Carilli C.L. (ed.), *Synthesis Imaging in Radio Astronomy II*, Vol. 180, p. 383

Peterson, B. M.: 1997, *An introduction to active galactic nuclei*, CUP

Poggianti, B. M.: 1997, *A&AS* **122**, 399

Press, W., Flannery, B., Teukolsky, S., and Vetterling, W.: 1992, *Numerical Recipes in C: The Art of Scientific Computing, 2nd ed.*, CUP

Roche, N., Eales, S., and Rawlings, S.: 1998, *MNRAS* **297**, 405

Rowan-Robinson, M.: 1968, *MNRAS* **138**, 445

Ryle, M. & Clarke, R.: 1961, *MNRAS* **122**, 349

Sadler, E. M., Cannon, R. D., Mauch, T., Hancock, P. J., Wake, D. A., Ross, N., Croom, S. M., Drinkwater, M. J., Edge, A. C., Eisenstein, D., Hopkins, A. M., Johnston, H. M., Nichol, R., Pimbblet, K. A., de Propris, R., Roseboom, I. G., Schneider, D. P., and Shanks, T.: 2007, *MNRAS* pp 787–+

Sandage, A.: 1972, *ApJ* **173**, 485

Schmidt, M.: 1968, *ApJ* **151**, 393

Smith, J. A., Tucker, D. L., Kent, S., Richmond, M. W., Fukugita, M., Ichikawa, T., Ichikawa, S.-i., Jorgensen, A. M., Uomoto, A., Gunn, J. E., Hamabe, M., Watanabe, M., Tolea, A., Henden, A., Annis, J., Pier, J. R., McKay, T. A., Brinkmann, J., Chen, B., Holtzman, J., Shimasaku, K., and York, D. G.: 2002, *AJ* **123**, 2121

Snellen, I. A. G. and Best, P. N.: 2001, *MNRAS* **328**, 897

Snellen, I. A. G., Bremer, M. N., Schilizzi, R. T., Miley, G. K., and van Ojik, R.: 1996, *MNRAS* **279**, 1294

Snellen, I. & Best, P.: 2003, *New Astron Rev* **47**, 225

Spergel, D. N., Bean, R., Dore', O., Nolta, M. R., Bennett, C. L., Hinshaw, G., Jarosik, N., Komatsu, E., Page, L., Peiris, H. V., Verde, L., Barnes, C., Halpern, M., Hill, R. S., Kogut, A., Limon, M., Meyer, S. S., Odegard, N., Tucker, G. S., Weiland, J. L., Wollack, E., and Wright, E. L.: 2006, *astro-ph/0603449*

Stoughton, C., Lupton, R. H., Bernardi, M., Blanton, M. R., Burles, S., Castander, F. J., Connolly, A. J., Eisenstein, D. J., Frieman, J. A., Hennessy, G. S., Hindsley, R. B., Ivezić, Ž., Kent, S., Kunszt, P. Z., Lee, B. C., Meiksin, A., Munn, J. A., Newberg, H. J., Nichol, R. C., Nicinski, T., Pier, J. R., Richards, G. T., Richmond, M. W., Schlegel, D. J., Smith, J. A., Strauss, M. A., SubbaRao, M., Szalay, A. S., Thakar, A. R., Tucker, D. L., Vanden Berk, D. E., Yanny, B., Adelman, J. K., Anderson, Jr., J. E., Anderson, S. F., Annis, J., Bahcall, N. A., Bakken, J. A., Bartelmann, M., Bastian, S., Bauer, A., Berman, E., Böhringer, H., Boroski, W. N., Bracker, S., Briegel, C., Briggs, J. W., Brinkmann, J., Brunner, R., Carey, L., Carr, M. A., Chen, B., Christian, D., Colestock, P. L., Crocker, J. H., Csabai, I., Czarapata, P. C., Dalcanton, J., Davidsen, A. F., Davis, J. E., Dehnen, W., Dodelson, S., Doi, M., Dombeck, T., Donahue, M., Ellman, N., Elms, B. R., Evans, M. L., Eyer, L., Fan, X., Federwitz, G. R., Friedman, S., Fukugita, M., Gal, R., Gillespie, B., Glazebrook, K., Gray, J., Grebel, E. K., Greenawalt, B., Greene, G., Gunn, J. E., de Haas, E., Haiman, Z., Haldeman, M., Hall, P. B., Hamabe, M., Hansen, B., Harris, F. H., Harris, H., Harvanek, M., Hawley, S. L., Hayes, J. J. E., Heckman, T. M., Helmi, A., Henden, A., Hogan, C. J., Hogg, D. W., Holmgren, D. J., Holtzman, J., Huang, C.-H., Hull, C., Ichikawa, S.-I., Ichikawa, T., Johnston, D. E., Kauffmann, G., Kim, R. S. J., Kimball, T., Kinney, E., Klaene, M., Kleinman, S. J., Klypin, A., Knapp, G. R., Korienek, J., Krolik, J., Kron, R. G., Krzesiński, J., Lamb, D. Q., Leger, R. F., Limmongkol, S., Lindenmeyer, C., Long, D. C., Loomis, C., Loveday, J., MacKinnon, B., Mannery, E. J., Mantsch, P. M., Margon, B., McGehee, P., McKay, T. A., McLean, B., Menou, K., Merelli, A., Mo, H. J., Monet, D. G., Nakamura, O., Narayanan, V. K., Nash, T., Neilsen, Jr., E. H., Newman, P. R., Nitta, A., Odenkirchen, M., Okada, N., Okamura, S., Ostriker, J. P., Owen, R., Pauls, A. G., Peoples, J., Peterson, R. S., Petravick, D., Pope, A., Pordes, R., Postman, M., Prosapio, A., Quinn, T. R., Rechenmacher, R., Rivetta, C. H., Rix, H.-W., Rockosi, C. M., Rosner, R., Ruthmansdorfer, K., Sandford, D., Schneider, D. P., Scranton, R., Sekiguchi, M., Sergey, G., Sheth, R., Shimasaku, K., Smee, S., Snedden, S. A., Stebbins, A., Stubbs, C., Szapudi, I., Szkody, P., Szokoly, G. P., Tabachnik, S., Tsvetanov, Z., Uomoto, A., Vogeley, M. S., Voges, W., Waddell, P., Walterbos, R., Wang, S.-i., Watanabe, M., Weinberg, D. H., White, R. L., White, S. D. M., Wilhite, B., Wolfe, D., Yasuda, N., York, D. G., Zehavi, I., and Zheng, W.: 2002, *AJ* **123**, 485

Taylor, G., Carilli, C., and R.A., P. (eds.): 1999, *Synthesis Imaging in Radio Astronomy II*, Vol. 180

Taylor, M.: 2000, *Astrometric calibration for INT Wide Field Camera images*, `http://www.star.bris.ac.uk/~mbt/wfc/calibrate/`

Waddington, I., Dunlop, J. S., Peacock, J. A., and Windhorst, R. A.: 2001, *MNRAS* **328**, 882

Waddington, I., Windhorst, R. A., Dunlop, J. S., Koo, D. C., and Peacock, J. A.: 2000, *MNRAS* **317**, 801

Wall, J.: 1980, *Phil Trans R Soc* **A296**, 367

Willott, C. J., Rawlings, S., Blundell, K. M., Lacy, M., and Eales, S. A.: 2001, *MNRAS* **322**, 536

Willott, C. J., Rawlings, S., Jarvis, M. J., and Blundell, K. M.: 2003, *MNRAS* **339**, 173

Windhorst, R., Mathis, D., and Neuschaefer, L.: 1990, in R. G. Kron (ed.), *ASP Conf. Ser. 10: Evolution of the Universe of Galaxies*, pp 389–403

Windhorst, R. A., van Heerde, G. M., and Katgert, P.: 1984, *A & A Supplement Series* **58**, 1

York, D. G., Adelman, J., Anderson, Jr., J. E., Anderson, S. F., Annis, J., Bahcall, N. A., Bakken, J. A., Barkhouser, R., Bastian, S., Berman, E., Boroski, W. N., Bracker, S., Briegel, C., Briggs, J. W., Brinkmann, J., Brunner, R., Burles, S., Carey, L., Carr, M. A., Castander, F. J., Chen, B., Colestock, P. L., Connolly, A. J., Crocker, J. H., Csabai, I., Czarapata, P. C., Davis, J. E., Doi, M., Dombeck, T., Eisenstein, D., Ellman, N., Elms, B. R., Evans, M. L., Fan, X., Federwitz, G. R., Fiscelli, L., Friedman, S., Frieman, J. A., Fukugita, M., Gillespie, B., Gunn, J. E., Gurbani, V. K., de Haas, E., Haldeman, M., Harris, F. H., Hayes, J., Heckman, T. M., Hennessy, G. S., Hindsley, R. B., Holm, S., Holmgren, D. J., Huang, C.-h., Hull, C., Husby, D., Ichikawa, S.-I., Ichikawa, T., Ivezić, Ž., Kent, S., Kim, R. S. J., Kinney, E., Klaene, M., Kleinman, A. N., Kleinman, S., Knapp, G. R., Korienek, J., Kron, R. G., Kunszt, P. Z., Lamb, D. Q., Lee, B., Leger, R. F., Limmongkol, S., Lindenmeyer, C., Long, D. C., Loomis, C., Loveday, J., Lucinio, R., Lupton, R. H., MacKinnon, B., Mannery, E. J., Mantsch, P. M., Margon, B., McGehee, P., McKay, T. A., Meiksin, A., Merelli, A., Monet, D. G., Munn, J. A., Narayanan, V. K., Nash, T., Neilsen, E., Neswold, R., Newberg, H. J., Nichol, R. C., Nicinski, T., Nonino, M., Okada, N., Okamura, S., Ostriker, J. P., Owen, R., Pauls, A. G., Peoples, J., Peterson, R. L., Petravick, D., Pier, J. R., Pope, A., Pordes, R., Prosapio, A., Rechenmacher, R., Quinn, T. R., Richards, G. T., Richmond, M. W., Rivetta, C. H., Rockosi, C. M., Ruthmansdorfer, K., Sandford, D., Schlegel, D. J., Schneider, D. P., Sekiguchi, M., Sergey, G., Shimasaku, K., Siegmund, W. A., Smee, S., Smith, J. A., Snedden, S., Stone, R., Stoughton, C., Strauss, M. A., Stubbs, C., SubbaRao, M., Szalay, A. S., Szapudi, I., Szokoly, G. P., Thakar, A. R., Tremonti, C., Tucker, D. L., Uomoto, A., Vanden Berk, D., Vogeley, M. S., Waddell, P., Wang, S.-i., Watanabe, M., Weinberg, D. H., Yanny, B., and Yasuda, N.: 2000, *AJ* **120**, 1579

Zirbel, E.L. & Baum, S.: 1995, *ApJ* **448**, 521

APPENDIX A

The $V/V_{\rm max}$ test

The $V/V_{\rm max}$ statistic (Rowan-Robinson, 1968; Schmidt, 1968) provides a useful test of the evolution of a sample, as it is not dependent on assumptions as to the form of the evolution involved.

In a survey with some flux density limit, $S_{\rm lim}$, a source at redshift z, with flux density, $S > S_{\rm lim}$, would still have been included in the sample out to a higher redshift, $z_{\rm max}$. $V/V_{\rm max}$ is therefore, for each object in a sample, the ratio of the volume, V, enclosed by z, to the maximum volume, $V_{\rm max}$ enclosed by $z_{\rm max}$. If the sample sources are uniformly distributed (i.e. if there is no evolution of the population with cosmic time) then the values of the ratio will also be uniformly distributed, between 0 and 1, and

$$\left\langle \frac{V}{V_{\rm max}} \right\rangle = \frac{1}{N} \sum_{i=1}^{N} \frac{V_i(z)}{V_i(z_{\rm max})} = 0.5, \tag{A.1}$$

where N is the total number of objects in the sample. If the population undergoes positive cosmic evolution then $\langle V/V_{\rm max} \rangle > 0.5$, and if the evolution is negative then $\langle V/V_{\rm max} \rangle < 0.5$. The error in this is given by $\sigma_{V/V_{\rm max}} = (12N)^{-1/2}$ (Peterson, 1997).

In a sample with strong, positive, low redshift, evolution and weak, negative, high redshift evolution, the $V/V_{\rm max}$ test, as described above, would mask the high redshift behaviour. To avoid this, the test is modified to a banded version, in which only sources above some limiting redshift, z_0 are considered, for several values of z_0. In other words, for a non–evolving

population,

$$\left\langle \frac{V - V_0}{V_{\rm max} - V_0} \right\rangle = 0.5. \tag{A.2}$$

where V_0 is the limiting volume enclosed by z_0.